Smart Wind Turbine: Analysis and Autonomous Flap

Smart Wind Turbine: Analysis and Autonomous Flap

Proefschrift

ter verkrijging van de graad van doctor
aan de Technische Universiteit Delft,
op gezag van de Rector Magnificus prof. ir. K. C. A. M. Luyben,
voorzitter van het College voor Promoties,
in het openbaar te verdedigen op maandag 12 oktober 2015 om 10:00 uur

door

Lars Oliver BERNHAMMER

Ingenieur Luchtvaart en Ruimtevaart
geboren te Gießen, Duitsland.

This dissertation has been approved by the promotors:

Prof. dr. G.A.M. van Kuik
Prof. dr. M. Karpel
Copromotor: Dr. R. De Breuker

Composition of the doctoral committee:

Rector Magnificus,	chairperson	
Prof. dr. G.A.M van Kuik,	promotor	Delft University of Technology
Prof. dr. M. Karpel	promotor	Technion - Israel Institute of Technology
Dr. R. De Breuker,	copromotor	Delft University of Technology

Independent members:

Prof. dr. F. van Keulen	Delft University of Technology
Prof. dr. L.L.M. Veldhuis	Delft University of Technology
Prof. dr. C.L. Bottasso	Technische Universität München
Prof. dr. P. Marzocca	Royal Melbourne Institute of Technology
Prof. dr. ir. R. Benedictus,	Technische Universiteit Delft, reservelid

Keywords: Wind Energy, Aeroelasticity, Structural Dynamics, Adaptive Structures

Printed by: Ipskamp Drukkers in The Netherlands

Front & Back: Design by Kiki Kraak

ISBN 978-94-6259-827-0

PREFACE

This dissertation is the result of four years of Ph.D. studies. Conducting Ph.D. research has been a very enriching experience, which, at times, delivered a good deal of frustration, but also a great amount of pleasure. During this journey, I could consistently rely on friends and colleagues helping me through the difficult phases and sharing the joyful ones.

First of all, my thanks go to my promoters, who did not only serve me as academic but also as personal mentors. I had the good fortune to have three supervisors with a very different personality, such that I could seek supervision as it fitted my needs. Moti Karpel, Gijs van Kuik and Roeland De Breuker did not only provide academic supervision, but also helped me prepare the next steps in my career. On top of that I got various philosophical and political discussions, a deep insight to Israel and, of course, a private sculpturing class.

My gratitude extends to the other members of the Wind Energy research group, especially to Gerard van Bussel, who supported me no matter what research visit I was planning, and Carlos, with whom I shared many discussions not only about wind turbine aeroelasticity. The same thanks go to my fellow Ph.D. candidates, who were my regular lunch company but also helped to solve an uncountable number of little, daily problems. Thanks to Ricardo, Etana, Maarten, Lorenzo, Cyril, Giuseppe, Ye, Daniel, Rene, Wei, Claudia and Ben in particular.

I was very lucky that I was part of a second research group as well, namely Aerospace Structures and Computational Mechanics. First of all, I would like to thank my fellow diver, Jurij, for supporting me in the design and building process of my wind tunnel experiments. Furthermore, I profoundly appreciated the rest of the aeroelasticity and morphing group, for their feedback, collaboration and of course travel company when it came to conferences and road trips: Noud, Erik, Kristofer, Daniel and Fardin.

I am in deep debt to the members of the Delft Center for Systems and Control. Since I started my Master thesis, you have regularly been a major contributor to my research in general, and to my wind tunnel experiments in particular. I appreciate these efforts even more as I know how ignorant I am still about model identification and controller design. Thanks to Jan-Willem, Gijs, Edwin and Sachin for making so many of my publications possible.

A word of thanks is also due to Alex Shousterman, who shared his office at Technion with me, for all of his help during my numerical simulations and for his efforts to teach me Russian. I am also in debt to Joost Sterenboorg, whose wind tunnel experiment I adapted for my experiments; and to Thijs Gillebaart for his valuable comparison studies of the aerodynamic models I used. My thanks extend to my Master students, especially to Jeroen, whose work found its way into this dissertation. I am also in debt to Jonathan Berg, who co-authored one of my papers and provided experimental data as comparison for a second one.

Of course, my thanks extends to the technicians in the aircraft hall, the wind tunnels and at the Faculty of Mechanical Engineering who provided measurement equipment, helped in the construction of model and much more. I am also grateful to Sylvia and Laura to keep paperwork away from me as much as possible, and naturally also to all the people who helped me in completing this dissertation, be it by translating, spell and grammar checking or the design of the cover: Sachin, Kiki, Jaco, Daniel, Hieu, Siebe and Noud.

But most of all, I am grateful for my friends and family.

SUMMARY

Smart Wind Turbine: Analysis and Autonomous Flap

Wind turbines convert kinetic energy of the wind into electrical energy. Unfortunately, this process is everything but constant, as the wind source shows large fluctuations with high and low frequencies. This turbulence, together with the wind shear and yawed inflow, excites the turbine structure, thereby driving the loads and the design of turbines in general and blades in particular. In response to this, several control mechanisms have been applied to wind turbines since the generation of stall controlled machines in the 1980s. While collective pitch control was applied first, the control mechanisms have become more localised and act on individual turbine blades, rather than on the rotor as a whole. An advanced control scheme is termed 'smart wind turbine'. These type of wind turbine actively measures vibrations of its blades through a set of distributed sensors throughout the blades and then aims to counteract the vibrations using aerodynamic modifications around the blades' trailing edges close to the tips by means of control surface deflections.

This thesis investigates two aspects of the smart rotor concept: the analysis of smart rotors and the design of an autonomous flap concept. For the analysis, a wind turbine analysis tool with special focus on smart rotors and controller implementation has been developed. This code, the Delft University Smart Wind turbine Analysis Tool (DU-SWAT), has been benchmarked not only against conventional wind turbine codes, but a comparison study with the first utility-scale smart rotor experiment, the Sandia National Laboratories Smart Rotor, was performed. The experimentally obtained eigenfrequencies of the test turbine matched closely those of the numerical study. The difference in the first eigenfrequency is 2.7% or 0.1 Hz (4.4 Hz experimentally, 4.5 Hz numerically). A second comparison step was a time domain analysis of the wind turbine response to a step deflection input of the flaps. For the tower response, the frequencies and the amplitudes of the numerical and experimental responses agree very well. For blade vibrations, an increase in damping in the numerical simulations is observed. While for low flap deflection amplitudes, up to 5 degrees, the response amplitude is predicted

well. When high step deflections are modelled, the numerical simulations increasingly fail to accurately capture the dynamics of the turbine. In combination with the differences in damping, this leads to the conclusion that vortices, shed from the flap tips, interact with the larger tip vortices, possibly due to the proximity of the flaps to the blade tips. This inaccuracy of high flap deflection angles is however of limited importance, as it was demonstrated that the periodic (1P) load, the most dominant contributor to fatigue damage, could be alleviated effectively even with deflection angles up to 5 degrees.

The individual flap controller has been tuned to the NREL 5MW reference turbine and has been used to study both fatigue and extreme loads according to the certification regulations. Failure-free cases were included in the analysis, and loads have been monitored throughout the turbine. The fatigue load reduction of the blade root bending moment of 24% corresponds well with the findings of previous researchers. Besides this verification, it was also shown that the structural loads increase nowhere in the turbine, with the exception of the blade root torsional moment. Several other loads decrease, for example the tower torsion moments and the bending moments in the turbine shaft. The extreme load reduction is smaller than the fatigue load reduction. Still, the ultimate tip deflection and the ultimate blade root bending moment could be reduced by 7% and 8%, respectively. The moments in the tower are also reduced. Besides load alleviation, an additional functionality of the smart rotor was established. The flaps can be used to increase the power production of the turbine by responding to fluctuations in the wind speed and the delays in the adjustment of the rotor speed due to the rotor inertia.

An intermediate step of the wind turbine analysis was the development of a suitable structural model. The developed structural dynamics model, which is based on modal equations of motion, is not limited to wind turbine structures, but rather applicable to a broad range of engineering problems concerning structural vibrations. The model closes the gap between modal reductions, which are typically used in linear vibration analysis, and non-linear geometry. For that purpose the structure is segmented and the segments are joined by rigid-body displacements in a co-rotational framework, which introduces geometric non-linearities. This allows modelling of the structural dynamics for large deformations, while maintaining linear stress information of the finite element model of all segments. The basic assumption underlying this approach is that the structural displacement is large, but the strains remain small, which is typically the case for slender structures such as wind turbine blades.

The second major topic, which has been addressed in this dissertation, is the physical implementation of a flap system. The described flap system is fully autonomous and is mounted as a free-floating flap, which means that the flap can freely rotate around a hinge axis. The flap is controlled by a trailing edge tab and driven by servo actuators. The flap is mass underbalanced and aeroelastically

unstable in interaction with one of the main structural modes. This renders the flap system highly responsive to control inputs, but also to external excitations. When vibrating, the kinetic energy of the flap is converted by electromagnetic harvesters into electric energy. This energy is either stored in a battery or used to power the sensors and the actuators. It was demonstrated that the instability of the flap dramatically increases the amount of harvested energy by, in case of the experiment, a factor of 225 for wind speeds just below and above the flutter speed. The flap system measures the vibrations through accelerometers. When unstable, the vibration amplitude is either limited by structural delimiters or can be actively controlled by the control system. It was shown, that the flap system can be self-sufficient during the controlled limit cycle oscillation. Id est the power produced during limit cycle oscillation is greater than the power consumed to keep the oscillation amplitude constant.

The main advantage of the autonomous flap is its improved replaceability compared with non-autonomous ones. As it neither needs a connection to a central control unit and a power system, nor is an integral part of the wind turbine blades like seamless solutions, it can be exchanged easily in case of failure.

In conclusion, smart wind turbines have a great potential to improve the cost efficiency by reducing loads for most turbine components as has been shown in this dissertation. This can be achieved using the novel flap concept, which helps, due to its plug-and-play nature, to reduce maintenance costs.

SAMENVATTING

Slimme Windturbine: Rotoranalyse en Autonome Klep

Windturbines zetten kinetische energie van de wind om in elektrische energie. Helaas is dit proces verre van constant aangezien de wind sterk fluctueert met zowel hoge als lage frequenties. Deze turbulentie, maar ook windschering en scheve aanstroming, exciteert de windturbineconstructie en is daarom essentieel bij het ontwerp van windturbines in het algemeen of, meer specifiek: het ontwerp van turbinebladen. Om de fluctuaties tegen te gaan zijn er sinds de generatie van op overtrek geregelde machines in de tachtiger jaren al vele besturingsmechanismen toegepast. In het begin werd collectieve bladhoekregeling toegepast, later echter werd de besturing meer plaatselijk door individuele turbinebladen te regelen in plaats van de rotor in zijn geheel. De meest geavanceerde optie is de 'smart rotor', welke actief de vibraties van de bladen meet door middel van over de bladen verdeelde sensoren. Vervolgens moeten aerodynamische modificaties zoals kleppen aan de achterrand vlakbij de tip van de bladen, deze vibraties tegengaan.

Deze thesis onderzoekt een tweetal aspecten van het smart rotorprincipe. Zowel de analyse van dergelijke systemen als het ontwerp van een klep worden behandeld. Voor de analyse is een wind turbine analyse tool ontwikkeld, waarbij er extra aandacht is besteed aan smart rotors en de besturingsimplementatie. Deze code, gedoopt DU-SWAT (Delft University Smart Wind turbine Analysis Tool), is niet alleen geijkt met conventionele windturbinecodes, maar is ook vergeleken met het eerste smart rotor-experiment op industriële schaal: de Sandia National Laboratories Smart Rotor. De eigenfrequenties van de proefturbine komen goed overeen met die uit de numerieke studie. Het verschil in de eerste eigenfrequentie is 2.7% of 0.1 Hz (4.4 Hz in het experiment, 4.5 Hz numeriek). Een tweede vergelijking is gemaakt op basis van de respons van de rotor in het tijdsdomein op een stapbeweging van de kleppen. Experiment en numerieke simulatie komen goed overeen wat betreft de frequentie en amplitude van de torenrespons. Bij de bladvibraties geeft de code een grotere demping dan experimenteel geobserveerd. Voor de lagere klepamplitudes tot 5 graden komt de respons amplitude nog goed overeen, maar het verschil tussen experiment en simulatie wordt steeds groter

al naar gelang er een grotere stapbeweging wordt gemodelleerd. Ook gezien de verschillen in de demping is de conclusie dat dit komt doordat de wervels die van de uiteinden van de kleppen afkomen, de sterke wervel die van de nabije bladtip afkomt beinvloeden. Deze onnauwkeurigheid is echter niet heel erg van belang, aangezien het reeds werd aangetoond dat de 1P belasting, welke het meest bijdraagt aan vermoeiingsschade, al doeltreffend kon worden verminderd met een klepuitwijking van 5 graden.

Deze individuele klep regeling is afgestemd op de NREL 5MW referentieturbine, en is vervolgens ingezet om zowel vermoeiingskrachten als extreme krachten te bestuderen zoals de norm voor certificatie voorschrijft. Faalvrije belasting gevallen zijn meegenomen in de analyse en de belastingen zijn op meerdere plekken in de turbine gemonitord. De vermindering van de vermoeiingsbelasting van het buigmoment in de bladwortel met 24% komt goed overeen met bevindingen van andere onderzoekers. Naast deze verificatie is het ook aangetoond dat de kleppen de structurele belastingen in de turbine niet vergroten in de turbine, het torsiemoment in de bladwortel uitgezonderd. Enkele andere belastingen verminderen, zoals de torsiebelastingen in de toren en de buigmomenten in de turbine-as. De reductie van de extreme belasting is minder uitgesproken dan die van de vermoeiingsbelasting. Desalniettemin konden de uiterste tipdeflectie en het uiterste bladwortelbuigmoment worden verminderd met respectievelijk 7% en 8%. Ook de momenten in de toren zijn minder. Naast de lastenverlichting is er een aanvullende functie van de smart rotor vastgesteld. De kleppen zijn gebruikt om de elektriciteitsproductie van de turbine te verhogen door ze enerzijds te laten reageren op fluctuaties van de windsnelheid, en anderzijds op de vertragingen in rotorsnelheid als gevolg van rotortraagheid.

Als tussenstap naar een succesvolle wind turbine analyse is er een geschikt structural model gemaakt. Het ontwikkelde model voor structurele dynamica is gebaseerd op modale bewegingsvergelijkingen en is qua applicatie niet gelimiteerd tot alleen windturbinestructuren, maar toepasbaar op een weids spectrum aan ingenieursvraagstukken waarbij structurele trillingen aan bod komen. Het model dicht de kloof tussen modale reducties, welke typisch gebruikt worden voor lineaire vibratieanalyse, en niet-lineaire geometrie. Hiervoor wordt de structuur in segmenten verdeeld welke met starre lichaamverplaatsingen in een meedraaiend assenstelsel met elkaar worden verbonden zodat geometrische niet-lineariteiten worden geïntroduceerd. Op deze manier kan de structurele dynamica voor grote vervormingen worden gemodelleerd terwijl alle segmenten van het eindige-elementenmodel lineair verlopende spanningen bevatten. Deze methodologie stoelt op de aanname dat, hoewel de structurele verplaatsingen groot zijn, de rekken toch klein blijven. Dit is typisch het geval voor slanke structuren zoals windturbinebladen.

Het tweede hoofdonderwerp behandeld in deze dissertatie is de fysieke implementatie van een klepsysteem. Het beschreven systeem werkt volledig autonoom en is gemonteerd als een vrij beweegbare klep, wat betekent dat deze vrij om zijn scharnieras kan draaien. De klep wordt bestuurd door een tab op de achterrand die wordt aangedreven met servomotoren. De klep is qua massaverdeling ondergebalanceerd en aeroelastisch onstabiel in de interactie met een belangrijke structurele eigenbeweging. Dit maakt dat het klepsysteem erg gevoelig is voor zowel besturingssignalen als externe excitaties. Wanneer de klep vibreert, wordt de aanwezige kinetische energie door elektromagnetische apparatuur omgezet in elektrische energie, welke ofwel in een batterij wordt opgeslagen, ofwel als voeding voor de sensoren en actuatoren wordt gebruikt. Het is aangetoond dat de klepinstabiliteit de hoeveelheid gewonnen energie van het klepsysteem met een factor 225 laat toenemen bij windsnelheden dichtbij de flutter snelheid. Het klepsysteem meet de trillingen met accelerometers. Wanneer de trilling instabiel is, wordt de trillingsamplitude ofwel begrensd door structurele begrenzers, ofwel actief beheersd door het regelsysteem. Tevens is het aangetoond dat het klepsysteem zelfvoorzienend kan zijn tijdens de actief begrensde oscillatie, met andere woorden, de verkregen energie gedurende deze beweging is groter dan de benodigde energie om de bewegingsamplitude constant te houden.

Het belangrijkste voordeel van de autonome klep is dat hij gemakkelijker te vervangen is dan niet-autonome exemplaren. Aangezien het systeem noch een verbinding met een centraal besturings- en voedingssysteem nodig heeft, noch een integraal deel uitmaakt van het windturbineblad zoals het geval is bij volledig geïntegreerde oplossingen, kan het in geval van storing gemakkelijk vervangen worden.

De conclusie is dat de slimme windturbines een grote potentie hebben hun kosteneffectiviteit te verbeteren door de belasting op alle turbinecomponenten te verminderen zoals in deze dissertatie is aangetoond. Dit kan worden bereikt door het nieuwe klep concept toe te passen dat door zijn plug-and-play karakter ook de onderhoudskosten helpt verminderen.

ACADEMIC CONTRIBUTION OF THIS DISSERTATION

Smart wind turbines, in the context of this dissertation, have built-in active load alleviation capacity that improves their efficiency and life-cycle cost. Such a system is comprised of distributed sensors, a control system and aerodynamic effectuators like trailing edge flaps. This dissertation advances the research on these wind turbines both by developing and applying load analysis methodologies and by the design and testing of an innovative flap concept.

The first significant contribution of this dissertation is the numerical analysis of a smart wind turbine:

- An aeroservoelastic wind turbine analysis tool has been created using state-of-the-art low fidelity wind turbine aerodynamic modeling including an unsteady aerodynamic section model combined with a multi-body structural model. This was a required step as commercial and open-source aeroelastic wind turbine codes cannot model distributed flaps along the blades. The resulting code has been verified for conventional turbines with commercially available and open-source aeroelastic wind turbine tools. A validation case with the first utility scale smart rotor, the Sandia National Laboratories Smart Rotor experiment, has been performed. The time domain results show that the analysis tool can capture relevant aeroelastic turbine dynamics. In the numerical simulations, the damping of blade vibrations are overpredicted, which is attributed to the assumption of the blade element momentum method of independent annuli.

- An advanced non-linear structural model has been developed. This model is based on the modal reduction from a full finite element model. For that purpose, the structure has been segmented and the segments have been re-joined in a co-rotational framework such that geometrically non-linear structural dynamics could be adequately modelled with a strongly reduced number of degrees of freedom as compared with the full finite element model.

- The validated analysis tool has been used to predict the reduction of fatigue and extreme loads for the design load cases considering the power production and the turbine start-up cases, as prescribed by the International Electrotechnical Commission. It was shown that the forces and bending moments throughout the turbine can be significantly reduced or remain unaltered by the loads alleviation system. The most significant resulting load reductions can be found for the flapwise bending moment, the shaft moments and the tower torsional moment. Additionally, it was demonstrated that the smart rotor can be controlled such that it maximizes the average power output by responding to fluctuations in the inflow velocity.

The second major contribution of this dissertation is the development of an autonomous flap for load alleviation purposes:

- The main advantage of the autonomous flap concept is that the flap is fully independent from the main wind turbine and can be used as plug-and-play unit, which only requires a simple clip attachment to the blade. The flap is free-floating and mass underbalanced such that it becomes aeroelastically unstable in interaction with a bending mode. The kinetic energy of the flap vibration is converted into electrical energy, which supplies power to all sensors and the actuation system of a trailing edge tab, which aerodynamically controls the flap.
- It was demonstrated experimentally and numerically that the aeroelastic instability can be transformed into tolerable limit-cycle oscillations, both through structural delimiters and through control activity. Furthermore, it was shown by an energy balance that the system can be fully autonomous, as the generated energy is higher than the energy required to maintain the limit cycle oscillation.

NOMENCLATURE

ROMAN SYMBOLS

a’	Tangential induction factor
a	Axial induction factor
A_i	Amplitude of indicial fucntion
$\mathbf{A}$	State matrix
$\mathbf{B}$	Input matrix
b_{hc}	Length in half chord
b_i	Exponent of indicial function
$\bar{\mathbf{B}}$	Generalized damping matrix
c_D	Drag coefficient
c_L	Lift coefficient
c_M	Moment coefficient
c	Chord
$\mathbf{C}$	Output matrix
$C_{D_{ax}}$	Axial force coefficient
C_{ip}	Tangential force coefficient
CG	Center of gravity
D	Drag
D_T	Tower diameter
$\mathbf{D}$	Feed-through matrix
D_T	Tower diameter
d	Distance
d_{hub}	Distance tower to hub
E	Young’s modulus
$\mathbf{e}$	Unit vector
F	Force
f	Separation weight function
$\mathbf{F}$	Aerodynamic force vector
$\mathbf{f_c}$	Vector of centrifugal force
$\mathbf{f_g}$	Vector of gravitational force
f_p	Prandtl tip loss factor
$\mathbf{f}_\omega$	Vector of rotational force

F_{dydx}	Shape coefficient flap
F_y	Shape coefficient flap
G_{dydx}	Shape coefficient flap
G	Shear modulus
$\mathbf{g}$	Gravity vector
H_y	Shape coefficient flap
I	Moment of inertia
$\mathbf{I}$	Identity matrix
J	Polar moment of Inertia
K	Stiffness
$\bar{\mathbf{K}}$	Generalized stiffness matrix
l	Length
L	Lift
L_i	Impedance
M	Moment
m	Mass
$\bar{\mathbf{m}}$	Mass vector
$\bar{\mathbf{M}}$	Generalized mass matrix
$\mathbf{M_f}$	Mass matrix only containing fictitious masses
$\bar{\mathbf{M}}_\mathbf{f}$	Generalized mass matrix including fictitious masses
N	Number
n	Number of coils
P	Power
p	Polynomial coefficient
$\mathbf{q}$	Auxiliary vector
r	Local radius
$\mathbf{r}$	Position vector
R	Rotor radius
R_e	Electrical resistance
$\mathbf{R}$	Rotation matrix
RC	Center of rotation
Re	Reynolds number
S	Shear force
t	Time
$\mathbf{T}$	Transformation matrix
$\mathbf{u}$	Nodal coordinates
U	Voltage
$\mathbf{u}$	Displacement vector
$\mathbf{u_r}$	Rotation vector
$\mathbf{u}$	Input vector
v	Bending displacement
V	Velocity
w	Downwash
$\mathbf{x}$	State vector

y	Vertical displacement
z	State variable

GREEK SYMBOLS

α_0	Zero lift angle of attack
α	Angle of attack
β	Flap deflection angle
γ	Magnetic field strength
ϵ	Distance from aerodynamic center
ζ	Damping coefficient
θ	Azimuth angle
Θ	Pitch angle
ϑ	Torsion angle
λ	Tip speed ratio
μ	Dynamic viscosity
ξ	Generalized displacement
ρ	Density
τ	Time coefficient
ϕ_{in}	Inflow angle
ϕ	Generalized coordinates
Φ	Generalized coordinates of system with fictitious masses removed
χ	Indicial function
Ψ	Rotation angle
ψ	Rotation magnitude
Ω	Rotation vector
ω	Angular velocity
ω_n	Natural frequency

COORDINATE SYSTEMS

g	Global coordinate system
i	Initial coordinate system
b	Body attached coordinate system
e	Elastic body fixed coordinate system

SUB/SUPERSCRITPS

ac	Actuator
ae	Aeroelastic
aero	Aerodynamic
AF	Airfoil-flap intersection
ax	Axial
att	Attached
B	Boundary layer
bat	Battery
c	Control
coil	Coil
dyn	Dynamic
hc	Half chord
EA	Elastic Axis
e	Elastic
edge	Edgewise
FA	Fore-aft
fs	Fully seperated
fol	Follower
fit	Fitted
fict	Fictitious
h	hinge
hub	Hub
lag	Lag terms
LE	Leading Edge
local	Local velocity
m	Mass
open	Open-circuit
p	Pressure
pot	Potential
r	Rigid-body
res	Resulting
qs	Quasi steady
SS	Side-side
st	Steady
str	Torsion rate
tan	Tangential
TE	Trailing Edge
tr	Transport
ts	Tower shadow
tube	Streamtube
var	Variable

sv	Successive vortices
x	Vertical flow velocity
y	Axial direction

ABBREVIATIONS

ATEFlap	Adaptive Trailing Edge Flap
BEM	Blade Element Momentum
CFD	Computational Fluid Dynamics
DFT	DDiscrete Fourier Transform
DLC	Design Load Cases
DOWEC	Dutch Offshore Wind Energy Convertor Project
ECD	Extreme Coherent Gust with Direction Change
EDC	Extreme Direction Change
EOG	Extreme Operational Gust
ETM	Extreme Turbulence Model
FEM	Finite Element Method
FFF	Free-Floating Flap
GDW	Generalized Dynamic Wake
HPF	High-Pass Filter
IBC	Individual Blade Control
IEC	International Electrotechnical Commission
IMU	Inertial Measurement Unit
IBC	Individual Blade Control
IPC	Individual Pitch Control
LCO	Limit Cycle Oscillation
LQ	Linear-Quadratic
LTC	Look-up Table Controller
MBS	Multi-Body Simulation
MIMO	Multiple Input Multiple Output
MPC	Model Predictive Controller
NREL	National Renewable Energy Laboratory
NWP	Normal Wind Profile
NTW	Normal Turbulence Model
OJF	Open Jet Facility
PD	Proportional-Derivative Controller
PID	Proportional-Integral-Derivative Controller
PSD	Power Spectral Density
RANS	Reynolds-Averaged Navier-Stokes
SISO	Single Input Single Output
VLM	Vortex Lattice Method

CONTENTS

When the winds of change blow, some people build walls
and others build windmills.
Chinese proverb

1

INTRODUCTION

1.1 RECENT DEVELOPMENTS IN WIND ENERGY

During the last decades, wind energy has developed from a niche technology into one of the main energy sources. In 2013, wind energy provided 13% of the European power consumption (Corbetta and Miloradovic, 2014), outperforming other renewable energy sources such as photovoltaic plants (9%) and biomass (1%). From all renewable energy sources, only hydroelectric power, with a share of 16%, contributes more to the EU power mix. While the percentage of wind energy might seem small, one has to bear in mind that wind energy is a relatively new energy source and still in the process of catching up with conventional power generation. In the same year, the capacity of power plants using renewable energy sources accounted for 72% of the total energy installation. With 44% of the installed renewable power, wind energy is the single largest power source installed.

Together with the growth of the wind energy industry, the size of wind turbines has increased uninterruptedly during the last three decades, as shown in Figure 1.1. This increase in size is an effort to reduce the cost of energy. These costs, per quantity of energy generated by the turbine, do not purely depend on the construction costs, but also on the costs of investment and maintenance. The latter typically amount to 20-25% of the total life cycle costs (International Renewable Energy Agency, 2012), even though these costs per kilowatt have declined since the 1980s. The last factor has been efficiently addressed by increasing the turbine

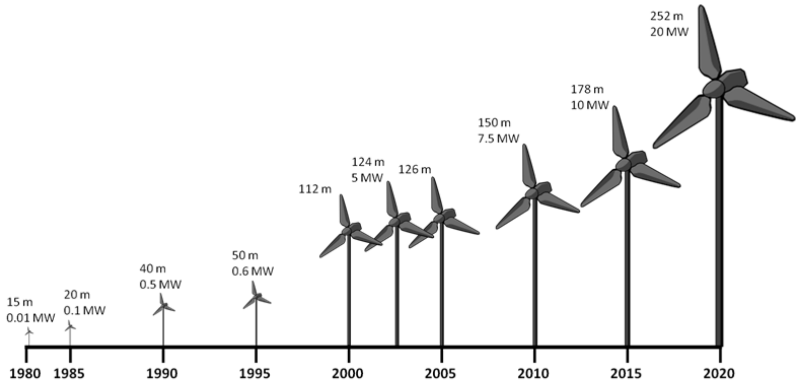

Figure 1.1: Increase in turbine size over the last three decades[1]

size, because larger and fewer turbines lead to a reduction in the total number of inspections. The number of inspections is particularly critical in offshore applications of wind energy as the turbines can only be accessed with specialised, costly equipment and when the weather is good.

As a result of the increase in turbine size, all its components, such as the blades, the nacelle and the hub, are exposed to higher wind, wave and gravitational loads. The increase in aerodynamic and hydrodynamic loads imposed on the turbine have traditionally been matched by increasing structural stiffness by adding material or by using stronger and stiffer, but also more expensive materials. This has resulted in heavier structures, which also yield higher gravitational loads on all components. Ashuri (2012) concluded that traditional upscaling methods using a conventional approach to wind turbine design will not be cost-effective for the size of next generation wind turbines. He identified the ratio between the increase of mass and the blade stiffness as a bottleneck in the development of future wind turbines.

A possible approach that can be taken to improve turbine blades is the alleviation of the aerodynamic loading either with passive or active aeroelastic solutions. Both approaches aim at reducing vibrational and ultimate loads, thereby enabling lighter blade designs and reducing requirements on other turbine parts. Passive load alleviation approaches typically involve bend-twist coupling of a rotor blade or mass-damper systems. In the twist-bend approach, the blade is designed in such a way that an increase in blade loads and the resulting bending would introduce torsion of the blade, which would limit the increase in blade loads. Active approaches refer to actively changing aerodynamic loads on the turbine blades to

---

[1] Case Western Reserve University Cleveland, Worlds First Carbon Nanotube Reinforced Polyurethane Wind Blades, http://engineering.case.edu/emac/news/Carbon-Nanotube-Reinforced, June 2015

alleviate fatigue and extreme loads.

1.2 SMART ROTORS

An example of such an active approach are smart rotors, which are a novel approach to wind turbine design. They exploit active aerodynamic devices such as flaps or tabs to adapt the flow field around the wind turbine blade. Many different concepts can be classified as smart rotors. A smart rotor in its broadest sense consists of a set of sensors, a control system, actuators and aerodynamic effectuators. The sensors, accelerometers or strain gauges measure the dynamic response of the blade structure. The measurements serve as input to a control system, which then determines the response of the aerodynamic device.

A wide range of aerodynamic concepts can be used to change the aerodynamic loads on a wind turbine blade. Barlas and van Kuik (2010) provide a comprehensive overview on different technologies. The most traditional way is to pitch the blade for control. In this case the entire blade is rotated to reduce the lift, and, thereby, loads. While collective pitch control, which means that all blades are pitched by the same amount, has been used for a long time to limit generator loads, recent developments show the emergence of individual pitch controllers that address asymmetric blade loads. These controllers address cyclic variations of loads and set the pitch angle for each blade individually depending on the orientation of the blades. As pitch controllers are slow due to the large inertia they need to overcome, these controllers can only mitigate low frequency loads. Other local technologies can control higher frequency vibrations and are therefore more suitable to address loads caused by turbulent wind. Examples of such load alleviation devices are suction or blowing, plasma actuation, micro tabs or trailing edge flaps.

Because of their large frequency bandwidth and control authority, trailing edge flaps are natural candidates for smart rotor control. Indeed, they have gained a dominant position in smart rotor research. Either rigid flaps or adaptive trailing edges are used. Normally, these devices are placed close to the blade tip so that maximum control forces can be generated, and thus the impact on the root bending moment can be maximised. These forces are used to reduce dynamic loads such that a lighter turbine design can be realised.

1.3 RESEARCH QUESTIONS

Significant research efforts have been made by van Wingerden (2008), Andersen (2010), Hulskamp (2011), Barlas (2011), Bæk (2011) and Bergami (2013) to model a wind turbine with trailing edge flaps, including a first estimate of the load reduction for selected load cases. Even though these results give a first indication of the potential of smart rotors, a more complete analysis is required, studying all certification load cases, such as ultimate and fatigue load cases during power production, turbine start-up and shut-down. For smart wind turbine analyses, dedicated aerodynamic models for airfoils with adaptive trailing edges have been developed at the Danish Technical University DTU (Andersen (2010); Bæk (2011); Bergami (2013)). While the research focus in the field of smart rotors has been on aerodynamic modeling, structural dynamics have received little attention. Wind turbine blades normally are subjected to distributed loading. This allows for rapid solving of the structural dynamics using modal or beam approaches. The aerodynamics of the flaps on smart rotors, and the inertial loads due to flap motion, however, cause a more localised load distribution. The traditional approaches are therefore either inaccurate or show a strong increase in computational time.

This thesis presents an effort to advance the stateof the art in structural dynamics such that these loads can be included efficiently in the formulations of the structural dynamics. An aeroelastic tool, which has been developed including the novel structural approach, is used to expand the number of analysed design load cases to form a broad basis for a qualitative judgment on the impact that smart rotors can have on the design of a wind turbine. This can be expressed as the first objective of this dissertation:

Determine to what extent smart rotors can be used to overcome limits on the upscaling of current, traditional wind turbine blades.

Based on these simulations, requirements on the flap have been derived and compared with requirements from previous studies (Barlas (2011); Bergami (2013)). These requirements have been paired with the most critical offshore requirement, namely durability of a flap system. So far, in all smart rotor designs, the flap system is an integral part of the wind turbine structure in an effort to decrease the failure probability of the flaps. This dissertation proposes an alternative approach to smart rotor design such that flaps can be used as plug-and-play devices that can be easily connected to an existing blade structure. As a result, only the smart element needs to be replaced in case of failure. This translates into the second objective of this thesis:

Develop a flap system that is suitable for offshore applications.

1.4 THESIS OUTLINE

The structure of the thesis reflects the two objectives as formulated in the previous section. The dissertation is divided into two parts to address both thesis objectives. The parts are further divided into five and three chapters, respectively. An overview of this outline is found in Figure 1.2.

The first part focuses on the analysis of smart rotors. Chapter 2 forms an introduction to this part. It discusses the limitations of current practice in aeroelastic analysis of wind turbines and potential improvements thereto. Chapter 3 explains the aerodynamic, structural and wind models that form part of the aeroservoelastic in-house tool 'Delft University Smart Wind Turbine Analysis Tool (DU-SWAT)'. The tool is benchmarked against commercially available, aeroelastic codes for conventional wind turbines. Chapter 4 presents a novel approach to formulate the structural dynamics of a wind turbine. Chapter 5 extends the validity study to the modelling capabilities of smart rotors of the new aeroservoelastic tool. The first utility scale smart rotor at Sandia National Labs is used as benchmark case for the simulations. A comparison is done in terms of spectral analysis and time domain simulations with step inputs in flap deflection. Part I is concluded by assessing the load alleviation potential of smart rotors for all failure-free design load cases. Chapter 6 presents these findings together with an investigation on using the smart rotor for secondary purposes such as increasing power production.

Part II investigates the physical design of a smart rotor system. This part begins with a literature review on requirements of smart rotors and possible design solutions (Chapter 7). The concept of free-floating flaps is proposed and analysed in detail. A new smart rotor concept is proposed based on the list of requirements. The concept of the autonomous flap is developed in the last two chapters. While Chapter 8 focuses on exploiting free-floating flaps as an energy harvester, in Chapter 9, previous research on free-floating flaps, used for load alleviation, is integrated with the energy harvesting potential demonstrated in Chapter 8. These functionalities can be combined into an autonomous unit as described in Chapter 9.

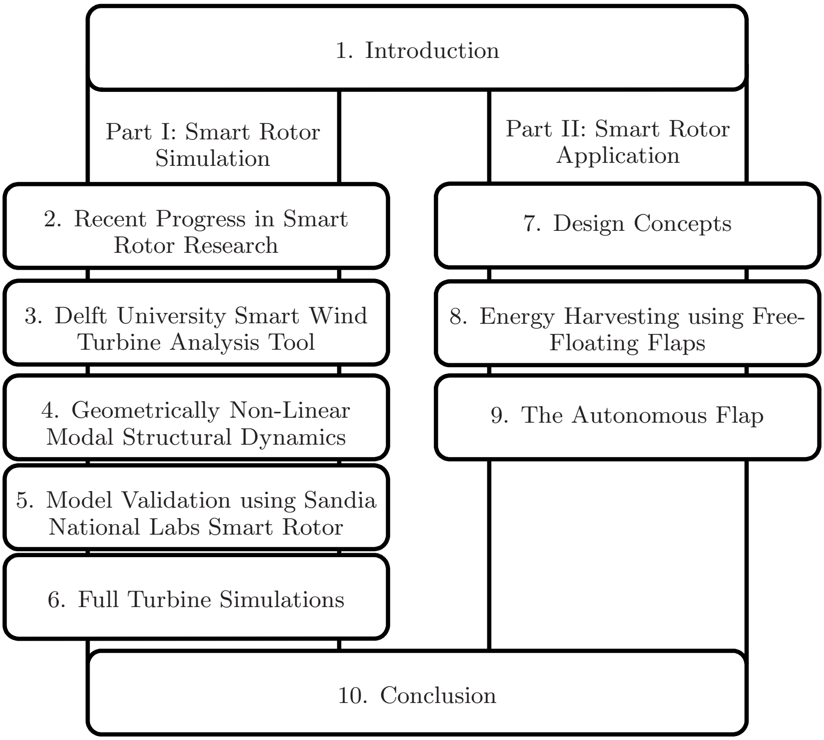

Figure 1.2: Thesis outline

Part I

Smart Wind Turbine: Analysis

Science is not only a discipline of reason but, also, one of romance and passion.
Stephen Hawking

2

RECENT PROGRESS IN SMART ROTOR RESEARCH

2.1 INTRODUCTION

Motivated by the limits of upscaling that have been outlined in Chapter 1, significant research has been performed on smart rotors. This chapter provides a comprehensive overview of this research, analyses the progress made, and indicates what steps need to be taken for efficient full-turbine simulations and building a full-scale prototype.

The chapter[1] is divided into three sections. Firstly, a brief discussion of smart rotor concepts is presented, including a trade-off to identify the best concept. This is followed by an analysis of the aeroelastic models that are currently used for time domain simulation of smart rotors. Finally, control models are investigated and a synopsis is presented.

---

[1] This chapter is an adaptation of the journal paper 'How far is smart rotor research and what steps need to be taken to build a full-scale prototype?' by Bernhammer, van Kuik and De Breuker (2014).

2.2 ACTIVE AERODYNAMIC DEVICE SELECTION

As illustrated in the last chapter, smart rotors are a potential solution to the challenge of increasing turbine size. During the last decade, the idea of the smart rotor has matured from an abstract concept to the proof-of-concept stage. Due to the nature of the problem, a multidisciplinary approach needs to be chosen, that requires research in aerodynamics, control theory, material science and wind turbine structures. The technology in each of these fields needs to be developed to a sufficient technology readiness level before the implementation of a full-scale turbine can be made feasible.

Various research institutes, including DTU Risø, Delft University of Technology, University Stuttgart and Sandia National Laboratories, have investigated the smart rotor concept and its subdomains, leading to advances in the design and analysis of such wind turbines. During the last decade, several Ph.D. theses have been devoted to this topic. In this chapter the research progress is analysed and it is highlighted how the present dissertation contributes to addressing the open questions in smart rotor research.

The first step in the development of a novel technology is the generation of concepts. In the early stages of the research on smart turbines, many different concepts for active aeroelastic devices were considered. Among these are geometric and fluidic devices. Johnson et al. (2010), Johnson et al. (2008), Barlas and van Kuik (2010) and Buhl et al. (2007) provide a very comprehensive overview of the different concepts.

2.2.1 GEOMETRIC DEVICES

Geometric devices can change the shape and dimensions of an airfoil, thereby altering the flow field around it. These devices may either be discrete, as in the case of trailing edge flaps, or deform the airfoil in a continuous way. Both concepts are illustrated in Figure 2.1. The discrete concept has the advantage that it is easily replaceable, whereas continuous, compliant structures provide a smooth deformation and a lower drag coefficient. The continuous deformation can be extended to seamlessly morphing shapes, which protect the mechanisms in offshore environments from moisture penetration.

Besides trailing edge flaps, other systems have been studied for wind turbines. The most prominent system is microtabs. These tabs, which typically extend 1 or 2% of the chord length into the flow, are mounted close to the trailing edge, thereby altering the Kutta condition. The advantage of microtabs is that a small amount of energy is required to obtain a very high acutation frequency. However, for control purposes, their suitability is limited as consequence of their binary position, which can either be fully retracted or extended. An example of such a

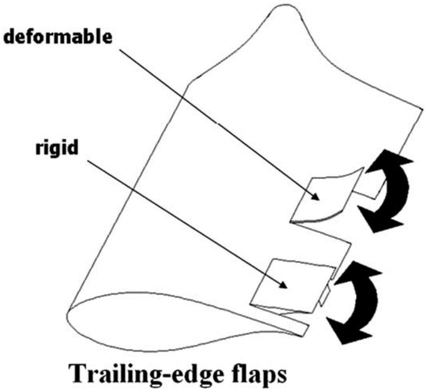

Figure 2.1: Rigid flaps and deformable trailing edges (Barlas, 2011)

tab is shown in Figure 2.2.

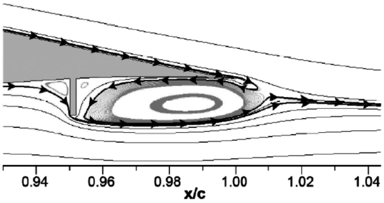

Figure 2.2: Schematic of a microtab close to the trailing edge (Zayas et al., 2007)

A third type of system are span or chord extensions. In these concepts, either the blade span or chord can be varied to generate additional power below the rated wind speed or to decrease loads above the rated wind speed. Johnson et al. (2008) summarize research activities on span extension that have been performed a decade ago on small utility scale turbines with a power rating of 120kW.

A further approach, which also involves varying the blade shape, is active twist. By introducing torsional moments into the structure, the blade twists with respect to its undeformed configuration. This twist leads to a change in the angle of attack distribution over the blade and, consequently, also results in a changed load distribution.

As demonstrated by the the aerospace industry, it is also possible to combine several of these concepts to achieve particularly high changes in lift coefficient. An example thereof is the 'Fowler flap', which combines a change in camber, through flap deflection, with chord extension.

2.2.2 FLUIDIC DEVICES

The second type of active devices that can be installed on wind turbines are fluidic devices. As the name indicates, these devices directly influence the flow by acting on the boundary layer. As such, these devices are particularly powerful in the region of flow separation.

Blowing of air injects momentum into the flow either through holes or through slats, while suction aims at removing the zone of low momentum close to the airfoil surface. Both methods help overcoming adverse pressure gradients, which are the source of flow separation. Circulation control extends this research to the region with attached flow. In this case, air is blown tangentially over a rounded trailing edge of the airfoil. This jet causes the airflow to follow the curvature of the rounded trailing edge. The resulting change in rear stagnation point increases the lift an airfoil generates.

While suction and blowing change the mass flux of the flow, synthetic jets do not require an air source for their operation. A synthetic jet consists of a cavity, with a variable volume. The volume of the cavity is varied using either a piston oscillation or a diaphragm. The volume change results in an increase in pressure in the cavity, causing air to be ejected through a small orifice. The pulsing air jet interacts with the flow around an airfoil, changing its apparent shape (de Vries, 2013). Figure 2.3 displays the effect of such an actuator on the flow field surrounding the trailing edge.

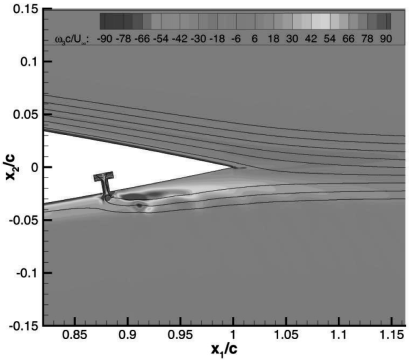

Figure 2.3: Synthetic jet actuation, streamlines and iso-contours of dimensionless velocity de Vries (2013)

Similar to the synthetic jets, plasma actuators are zero net mass flux devices. They create a voltage potential between two electrodes. Ions are created at the electrodes and start to travel as a result of the voltage difference. The ions collide with neutral particles in the region between the electrodes. Consequently, momentum is transfered to the flow close to the surface. Plasma actuators, therefore, help control the boundary layer shape and postpone separation.

2.2.3 CONTROL AUTHORITY OF DIFFERENT CONCEPTS

Despite the variety of concepts, most research has focused on trailing edge flaps or microtabs. Barlas (2011) attributes this to the fact 'that the maximum control authority can be achieved by using trailing edge flaps in combination with mechanically amplified smart material actuation'. Bæk (2011) discards options that act on the boundary layer, because the wind turbine airfoils are operating in the linear regime of the lift curve. Consequently, the control authority achievable with those methods remains limited. This is documented in Table 2.1, which shows that the effect of flaps and tabs on the lift coefficient is significantly higher than for fluidic devices.

Table 2.1: Comparison of aerodynamic control devices (Barlas (2011))

Aerodynamic device	Type	ΔC_L
Trailing edge flap	Geometric	0.4
Microtab/microflap	Geometric	0.3
Morphing airfoil	Geometric	0.4
Active twist	Geometric	0.2
Suction/blowing	Fluidic	0.2
Circulation control	Fluidic	0.2
Synthetic jets	Fluidic	0.05
Plasma actuators	Fluidic	0.02

In fact, all research institutes that are investigating smart rotors have opted for trailing edge flaps. Smart rotors offer, besides the high steady aerodynamic effect, also a bandwidth that is larger than the range of frequencies of interest of up to 4.0 Hz, depending upon the actuation type. Following this trend, research in this field has focused on developing analytical and numerical tools to simulate such control devices. Among this are the studies of aerodynamic models, and control, and actuation methods of blades with trailing edge flaps. In the following section, the readiness of these methods will be discussed.

2.3 AEROELASTIC ANALYSIS TOOLS

Aeroservoelastic analysis tools for wind turbines need to be fast in execution as a large number of different of load cases has to be analysed for certification and design purposes. With current numerical procedures, neither computational fluid dynamic (CFD) simulations nor vortex methods can fulfill this requirement, especially not when used in combination with high fidelity finite element approaches to analyze the structural dynamics. A trend towards one of two approaches is visible. The first trend involves the usage of structural mode shapes such as in GH Bladed (Bossanyi (2003*b*)). The second one is the exploitation of multi-body formulations such as HAWC2 (Larsen and Hansen (2012)), FAST (Jonkman and Buhl (2005)) or the first generation of the aeroservoelastic tool of Delft University of Technology (Barlas (2011)). Alternative structural formulations could also be based on beam models.

2.3.1 AERODYNAMIC MODELLING

In aerodynamic modelling, most research tools have opted for the blade element momentum (BEM) method. A summary of typical BEM methods can be found in any introductory book on wind turbines such as the 'Wind Energy Handbook' (Burton et al., 2001). The BEM method is computationally very cheap, but involves several assumptions and corrections. The main assumption is that the aerodynamic loads can be modelled by considering blade sections independently. Due to its popularity, the blade element momentum method has been extended over the last two decades by using engineering corrections for a finite number of blades, tip and root flow, and dynamic inflow.

In the BEM method, the angle of attack of each blade section is computed. This is done based on the geometric relationship between the incoming wind, structural deformations and velocities, and induction. For each section, the lift coefficient is determined based on (corrected) two-dimensional airfoil data. This is done using a look-up table of airfoil data in simple codes.

In aeroelastic codes, however, the unsteady aerodynamic effects on the turbine loads are considered. Therefore, adequate models for unsteady aerodynamics of airfoils in rotary wings need to be used. Models for flapping airfoils have been established by Leishman (1994), ONERA (McAlister et al. (1984)) and Gaunaa (2006). The model of Leishman only provides an approximate solution as it was originally derived for helicopters and exploits corrected flat plate aerodynamic formulations. These poorly capture the dynamics of very thick airfoils that are used for wind turbine blades. The model is also only valid in the linear part of the lift curve. The model formulated by ONERA is a dynamic stall model. Similarly, the model of Gaunaa, has been expanded by Andersen et al. (2009) to use a Beddoes-Leishman type dynamic stall model (Leishman and Beddoes (1986)). This model is especially suitable for thick airfoils with deformable trailing edges (Bergami and Gaunaa (2012)). All the aforementioned models have been benchmarked against 2D test data. Andersen (2010) further combines these models with a dynamic inflow model and a near wake model, resulting in a tool that can be used to calculate loads quickly.

Furthermore, these models have been verified by means of wind tunnel testing. Both the ONERA and the Gaunaa model have been verified for two-dimensional flow (McAlister et al. (1984), Bæk (2011)), with the latter being compared to the experimental results obtained with a flapped airfoil. Good agreement was found in both cases. A next step would be to quantify the effect of radial components in the flow, especially with regard to stall.

The latest research efforts to apply CFD to the field of smart rotors are still limited to two-dimensional simulations. Wolff et al. (2014) used Reynolds-Averaged Navier-Stokes (RANS) to optimize trailing edge geometries. The unsteady behavior caused by prescribed trailing edge oscillation of the optimised design was then compared to steady results obtained using time resolved RANS. Bergami (2013) compare EllipSys 2D, a CFD code, with a viscous-inviscid interaction method and the Adaptive Trailing Edge Flap (ATEFlap) model of Andersen et al. (2009). The engineering model captures the dynamic behavior well for attached flow, but has difficulties reproducing separation dynamics. The research on smart rotors conducted using two-dimensional CFD has been extended by Heinz et al. (2011) and Zhu et al. (2014), who demonstrated numerically that deformable trailing edges can be used for load alleviation of gusts.

One of the few research institutes that deviate from the BEM approach is Imperial College London. They have recently developed an unsteady vortex lattice method (VLM), coupled to a geometrically non-linear beam model (Ng et al. (2013)). During these simulations they use a prescribed helicoidal wake. The formulation has been cast in a state-space format, which is very convenient for controller design (Ng et al., 2015, 2014). This approach provides a great improvement in accuracy as it is the first time that the interaction of the flap vortices with their surroundings is modelled. Another research group focussing on the vortex methods is found at Delft University of Technology, who use their code for non-linear aeroelastic design studies (Hegberg et al., 2013).

2.3.2 STRUCTURAL MODELLING

While the aerodynamic modelling of smart rotors has received a lot of attention, no dedicated structural models have been developed. This focus on aerodynamics is explained partially by the fact that structural models are more easily transferable between aerospace research and wind energy. However, this focus on aerodynamics is due to the fact that transient loads must be computed first before they can be applied to a structure. The interchangeability between the aeronautic and wind energy domains has led to mature structural models for wind turbines without much effort.

Multi-body codes are widely used for structural analysis, and commercial packages such as ADAMS are readily available. Two types of models can be distinguished: rigid multi-body approaches and flexible multi-body approaches. The first employs a combination of springs and rigid bodies providing a fast, easy to use approach to solving structural problems. If modelled in a co-rotational framework, such models can include geometric non-linearities that accurately represent large deflections of a rotor blade. The downside of the approach is that, by concentrating the stiffness of a model in springs, information about the stress distribution is lost. Only models of moderate complexity can be analysed and stress concentrations cannot be identified.

Newer approaches involve models consisting of multiple flexible bodies, which yields a more accurate representation of the structural behaviour. A complete overview of such models is given by Bachau (2011). The most notable framework of wind turbine analysis, optimization and design tools, the combination of $C_p - lambda$ (Bottasso et al., 2013, 2006) and $C_p - Max$ (Bottasso, Campagnolo, Croce, Dilli, Gualdoni and Nielsen (2014)), utilises multi-body structural formulations. This framework has been used for several aeroservoelastic research efforts such as the development of an aeroelastically scaled rotor experiment (Bottasso, Campagnolo and Petrovic, 2014; Campagnolo et al., 2014) and turbine optimization (Bottasso, Croce, Sartori and Grasso, 2014)). However, smart rotor modelling is not addressed by these codes.

Another concept is, therefore, to use modal reduction to solve the equations of motion. A direct solution of the full finite element model is very time consuming. The modal approach provides detailed information about the stress distribution of a structure of arbitrary complexity. The inherent disadvantage is that modal formulations use linear superposition to calculate displacements. This makes modal formulations inaccurate when dealing with large deflections and rotations, which start to play a more significant role when considering large wind turbines. It is suspected that these non-linearities lead to load alleviations and deflection reductions. The use of modal based codes during the design phase will, therefore, most likely lead to a conservative design.

The challenge in code development is to provide a concept that can accomodate high fidelity, with non-linear formulations, in a time efficient way. In literature, this problem has not been solved yet. All standard codes opt for either one of the two options presented above: GH Bladed uses modal formulations and FAST and HAWC 2 and the aeroelastic code of Delft University of Technology use multi-bodies as shown in Table 2.2.

Very little research has been published on the structural dynamics of smart wind turbine rotors, for which accurate modelling of localised, impulsive forces as caused by flaps, is crucial. In terms of load alleviation efforts, the largest focus has been on passive systems that use the bend-twist coupling of rotor blades (among others Capellaro (2012); Fedorov and Berggreen (2014); Gœzcue and Kayran (2014)).

Table 2.2: Selected aeroelastic analysis tools

Code	Aerodynamic model	Structural model
GH Bladed	BEM, GDW	Modal, FEM
HAWC2	BEM	MBS, FEM
FAST	BEM, GDW	MBS, FEM
Flex5	BEM	Modal, FEM
DU-SWAT	BEM	MBS

BEM - Blade Element Momentum Method
GDW - Generalized Dynamic Wake
FEM - Finite Element Method
MBS - Multi-body Simulation

2.3.3 CHALLENGES FOR SMART ROTOR SIMULATION

The assumption of independent annuli might hold true for conventional blades, which have a smooth twist distribution and no discontinuities, but the validity of this method still needs to be proven for smart rotors. Actuation of discrete flaps, however, causes shedding of trailing vortices. The effect of this on the aerodynamic loads still has to be quantified. As the deformable trailing edges are typically located between 70 and 95% of the blade span, the vortices shed during operation may interact with the tip vortices. Even though the strength of tip vortex is much larger in magnitude, the vortices from the flaps might have a significant effect on the tip vortex breakdown in the turbine wake. In fact, research interest on the field of aerodynamics has slowly shifted to more advanced simulation methods to predict both of these phenomena. Research efforts on the high fidelity modelling of smart rotors have been initiated by DTU, Imperial College and Delft University of Technology. With advances in computational power, a transition from BEM to more advanced aerodynamics codes can be expected in the next decade.

Another further research question which has still not been addressed, is how to apply the smart rotor loads to the subsequent structural analysis. A method should be developed that converts the aeroservoelastic response into structural loads with a level of accuracy that is equivalent to the typical modal-based loads analyses conducted in aerospace industry. It is desirable to be able to include non-linear effects in the structural dynamic formulation to make them suitable for downwind turbines with large blade deformations.

2.4 SMART ROTOR EXPERIMENTS

When this project started, the experimental work being performed on smart rotors had only reached the proof-of-concept level. In the Open Jet Facility (OJF) of

Delft University of Technology, which is a recirculating wind tunnel with an open test section, a smart rotor prototype has been tested under controlled conditions (Barlas, van Wingerden, Hulskamp, van Kuik, Verhaegen and Bersee (2010); Hulskamp et al. (2010); van Wingerden et al. (2010)). This first full rotor experiment was a follow-up to earlier non-rotating experiments (van Wingerden et al., 2008). The smart rotor experiment was a collaboration of three Ph.D. students investigating the control, materials and simulation aspects of a smart rotor design. In such a controlled environment with low turbulence, the smart rotor was able to reduce the standard deviation of the flapwise root bending moment by more than 50% (Barlas et al. (2013)) for yaw angles below 5 degrees. For higher yaw angles, the reduction in standard deviation was less, but still remained above 30%.

In 2011 and 2012, Sandia National Laboratories implemented the smart rotor concept on a small utility scale turbine of 110kW (Berg et al. (2011, 2012)). Each of the three blades is equipped with three individually controllable flaps close to the blade tip. This experiment will be analysed in more detail in Chapter 5. Vestas has taken, in collaboration with DTU Risø, a similar approach by equipping one blade of a Vestas V27 with a 70 cm long flap (Castaignet et al., 2014). Frequency model predictive control for the flap was both simulated (Castaignet et al., 2013) and experimentally investigated. Using these flaps, load reductions in the order of 14% could be achieved. This is significant, considering that only 5% of the blade span was equipped with flaps.

2.5 CONTROLLER

As in the case with the aerodynamics the subject of controller design is also a very active research field. During the past years, the theoretical foundation for the controller domain has been established. Barlas has studied a number of control schemes numerically (Barlas, 2011), which included decentralised individual flap control (IFC), IFC using a Coleman transform, and multiple feedback flap control. All of these control schemes use decoupled single input single output feedback loops, resulting in 15%, 9% and 19% blade root moment reduction, respectively, for a free wind speed of 8.0 m/s. However, these values decrease as the wind speed increases, eventually ending up at reduction values that are significantly smaller than what can be reached with individual pitch control.

With the established control schemes (Bossanyi, 2003*a*; van Wingerden, 2008), the simulation of smart rotors has been developed to a sufficient level to extend the research to the next level, id est the application of the technology in a prototype. In fact, the development of a prototype has been done for the smart rotor experiment of Delft University of Technology by van Wingerden et al. (2010) and the MPC controller, which Castaignet et al. (2011) used for his numerical studies. This controller has been used for the test turbine (Castaignet et al., 2013).

A linearised system for controller design can be obtained numerically using aeroservoelastic codes such as GH Bladed, FAST or the DU-SWAT. For experiment-based controller designs, a more appropriate method is system identification. van Wingerden (2008) has developed a method to obtain models by novel subspace Linear-Parameter-Varying system identification algorithms both for open-loop and closed-loop systems. Due to the large number of parameters, these systems are complex to identify. Therefore, a linear time invariant solution has been derived that is based on parameter dependent dynamics. These methods have been successfully demonstrated in wind tunnel tests (van Wingerden et al. (2008)). For a specific non-rotating experiment a 90% reduction of the root bending moment has been achieved. For the rotationary experiment the amplitudes of the one- and three-per-revolution (1P and 3P) modes were reduced by 37% and 55%, respectively.

Recent research has focused on adding more advanced control approaches to improve the fatigue load reduction and extreme load mitigation. Instead of using a controller analogous to IPC, Bergami and Poulsen (2015) have developed a linear quadratic controller; Houtzager et al. (2011, 2013) use a controller that rejects repetitive and non-repetitive wind disturbances. During experiments on a single, non-rotating blade, this controller achieved load reductions of more than 40% at low turbulence levels. Tutty et al. (2014) present a numerical study on iterative learning control for an airfoil simulated using CFD. The pressure distribution around the trailing edge is used as the control variable. Barlas et al. (2012) constructs a multiple-input-multiple-output controller that is based on local flow measurements reaching fatigue load reductions of 27%. van Parys et al. (2014) and Ng et al. (2012) relate this to the gust load reduction using the aeroelastic model presented in more detail by Ng et al. (2015).

A further challenge in controller design lies in the high number of control inputs and outputs, which requires the development of computationally efficient algorithms. Rice and Verhaegen (2008) provide an overview of the advances in this field.

2.6 CHALLENGES AND OPPORTUNITIES

Until this point, research has been focused on creating a control system that takes over the functionality of individual pitch control, thereby reducing the root bending moment of the rotor blades. However, it may be possible that other components of the turbine, such as gear boxes or generators, are more sensitive to high-cycle fatigue than the blade root section is. Therefore, it is unclear whether the possible increase in annual energy production of 2.5% estimated by Bæk (2011) for a possible blade size increment of up to 3.0%, should be seen as low when compared to the costs of applying active aerodynamic devices, that only consider the blade root moment as design criterion. These costs might partially be offset by cost savings for other wind turbine components due to reduced loads on them. Bæk (2011) did a first analysis of the load spectrum of the main turbine components, showing that the maximum hub and tower fatigue loads decrease significantly when individual flap control is used. This trail needs to be followed to fully understand the impact of the application of smart rotors. Bæk's findings (Bæk (2011)) are more conservative than previous research, which predicted a possible increase in blade length of up to 10% (Berg et al. (2009)). Together with the work by Resor et al. (2012), who report a fatigue load reduction on drive train bearings of 7%, this calls for a more in-depth analysis, including the consideration of the full design load case spectrum.

Smart rotor control systems with deflectable trailing edges can cover the entire vibration frequency range that is of interest for a wind turbine, as identified by Barlas (2011). This range is between 0.0 and 6.0 Hz and cannot be covered by an individual pitch system. Consequently, individual pitch control is not suited for the suppression of aeroelastic instabilities like flutter. For the current generation of wind turbines, flutter is typically not critical. However, when the wind turbine diameter is increased to obtain a higher higher energy output, flutter may become problematic (Berring et al. (2006); Bir and Jonkman (2007)). The use of trailing-edge flaps can increase the likelihood of flutter occuring for smart rotors (Bergami and Gaunaa (2010)). Apart from flutter suppression, other unsteady effects due to fluctuating inflow can be corrected more effectively by active aerodynamic devices, as the frequencies at which excitation occurs, for example due to wake meandering, are too high to be corrected by pitch controlled systems (Markou et al. (2011)). Bossanyi (2000) states, in a similar fashion, that individual pitch control can experience difficulties in handling stochastic components in the wind inflow. Thus individual flap control can form a complementary control scheme to individual pitch control. Lackner and van Kuik (2010) have studied the combination of individual flap control and individual pitch control. The conclusion was reached that individual pitch control shows a greater load alleviation capacity than individual flap control for low frequency vibration. Notably the peak in the Power Spectral Density (PSD) of 1P can be further reduced. While the individual pitch control limits its effectiveness to a region around the 1P mode, distributed control can also alleviate loads that occur at higher frequencies. Plumley et al. (2014) have performed a similar comparison concluding that the power requirements for flap operation are only 1% of that of an individual pitch controller with comparable load alleviation potential.

Finally, another topic that has been given very little attention until this point is the inclusion of smart rotors in the design spectrum. Up till now, all applications have involved the modification of existing turbines. There are weight and cost penalties associated with including a set of sensors and control devices to an already existing design. Besides the required devices adding to the overall blade mass, the structure also needs to be locally reinforced to withstand the forces generated by the flaps. The full benefit of smart rotors can only be realised, when such control systems are accommodated in the design right from the very beginning. This will allow weight benefits to be achieved, which in turn would lower the gravitational loads, thereby allowing a further reduction in weight. Efficiently combining a smart rotor with other technologies under development, like torsion-bending coupling of rotor blades as developed by the university of Stuttgart (Barlas, Lutz, Bak, Hulskamp and Apinaniz (2010)), might enhance the control authority of a localised control systems. Benefits can especially be expected with regards to the tip deflection of the rotor, an issue that is gaining importance with increasing rotor size. Local control systems with high bandwidth may be able to manipulate the tip path, thereby reducing the requirements on tower clearance. The rotor blade could be used, in combination with torsion-bending coupling, to lever-up the effect of the forces generated by the control devices so that large tip displacement reductions become feasible.

2.6.1 CHOICES FOR THIS DISSERTATION

This dissertation will follow the same approach as most research institutes and will treat smart wind turbine rotors that have trailing edge flaps. The main reasons are the high control authority, the maturity of this technology readiness level and the frequency bandwidth that it can control. At the beginning of this dissertation, several steps necessary in smart rotor development were identified. These steps will be addressed in this dissertation, such as experimental validation using the Sandia National Laboratories Smart Rotor, a load assessment and modelling of structural dynamics of smart rotors. These topics will form the body of the first part of the dissertation. Developments related to other topics, such as aerodynamic modelling, have been highlighted in the literature review presented above.

While the fundamentals of smart rotor analysis have been established, the main remaining challenge lies the practical implementation of the smart rotor concept. This dissertation aims at advancing this concept to a practical solution. The design and analysis choices, which will be made in the various chapters, should therefore be viewed with this in mind.

2.7 SYNOPSIS

Smart rotor research is currently in the initial stages of implementation in full scale wind turbines.

- Current research mostly focuses on smart rotors with discrete trailing edge flaps.

- The control effectiveness of trailing edge flaps is superior to fluidic load alleviation devices such as suction/blowing, synthetic jets and plasma actuators.
- Two-dimensional, unsteady engineering models have been created and validated. These models have been integrated with aeroelastic BEM based wind turbine aeroelastic tools.
- The load reduction potential has been shown for selected load cases, but a full turbine analysis, meeting the certification load cases, still needs to be made.
- There is a need for validation of the assumption of independent annuli when considering smart rotors.
- Different control strategies have been developed and root bending moment fatigue load reduction potentials of 20-30% were found in numerical simulations.
- Little research has been done to account for smart rotor forces in structural dynamics.
- Validation data from full-scale smart rotor experiments is needed to assess the quality of the load reduction predictions.
- A smart turbine should be designed from the beginning, instead of applying smart elements to an existing turbine.

What was most significant about the lunar voyage was not that men set foot on the moon, but that they set eye on the earth.
Norman Cousins

3

DELFT UNIVERSITY SMART WIND TURBINE ANALYSIS TOOL (DU-SWAT)

3.1 INTRODUCTION

A shortcoming that was identified in Chapter 2 is the emphasis of current smart rotor research on the blade root bending moment. In order to analyze the impact that a smart rotor has on all turbine components, such as the drive train, the generator or the tower, an aeroservoelastic analysis tool has been created that focuses on distributed flaps, sensors and controller implementation. The Delft University Smart Wind Turbine Analysis Tool (DU-SWAT) is presented in this chapter and validated against commercially available aeroelastic software for conventional wind turbines.

First, the coordinate systems that are used in this dissertation are defined. Then DU-SWAT is described in detail, starting with an overview of the code structure, followed by the modules of the code. This consists of a description of the wind model, and an explanation of the aerodynamic model and the controller design is provided. The model of the structural dynamics, as implemented in the code, obtained using multi-body formulations is then given. Finally, the presented aeroservoelastic tool is compared to GH Bladed and FAST.

3.2 DEFINITION OF COORDINATE SYSTEMS

When analysing aeroelastic systems, defining suitable coordinate systems is of utmost importance. Structures undergo deformations and the aerodynamic forces are coupled to these deformations. This also applies to wind turbines. In fact, when analyzing wind turbines, one often has to deal with a number of different coordinate systems simultaneously. Figure 3.1 gives an overview of the two most relevant coordinate systems for wind turbines. The global coordinate system serves as fixed reference frame in the aeroelastic analysis and is chosen to coincide with the base of the tower. Foundation models are not considered in the current turbine analysis. It is therefore assumed that there is not translation or rotation at the base of the tower. Both the structural deformations and the wind input are expressed in the global coordinate system.

Besides the global coordinate system, a second coordinate system is specified: a local, body-attached coordinate systems, that follows the translation and deformation of the structure at a certain point. This local coordinate system is used to compute aerodynamic forces. The local coordinate system can be further split into an inertial orientation frame, a body-attached frame and an elastic body-attached frame, as shown in Figure 3.2. The difference between the latter two reference frames is that the body-attached coordinate frame is purely based on rigid-body translation and rotation from the inertial orientation frame, whereas the elastic body-attached frame also includes translations and rotations originating from elastic deformation of the structure. The initial orientation frame coincides with the local orientation frame of blades, shaft and tower segments when each simulation is initialised and the structure is still undeformed.

Rotation matrices transform displacements and rotations from one coordinate system to another. For this purpose, the coordinate systems are defined by normalised, orthogonal vectors, $\mathbf{e}$. In the case of the global coordinate system the unit vectors $\mathbf{e}^{\mathbf{g}}$ are simply the unit vectors of the undeformed coordinates system. For the other coordinate systems, defining unit vectors is slightly more complex. First, one of the unit vectors is specified based on the undeformed structure. The unit vector is defined along either the tower or the blades such that:

$$\mathbf{e}_3^i = \mathbf{u}_{2,z} - \mathbf{u}_{1,z} \tag{3.1}$$

where $\mathbf{u}$ is the vector of the nodal coordinates of the undeformed structure. The subscripts $1, z$ denote the location in axial direction of a root boundary grid point, while $2, z$ denotes a position at unit distance along the axis. In the case of the initial coordinates system, without structural deformation, the remaining two unit vectors can be obtained in the same manner. If small strains are assumed and the cross-section remains perpendicular to the axis of the tower and blades, this is also

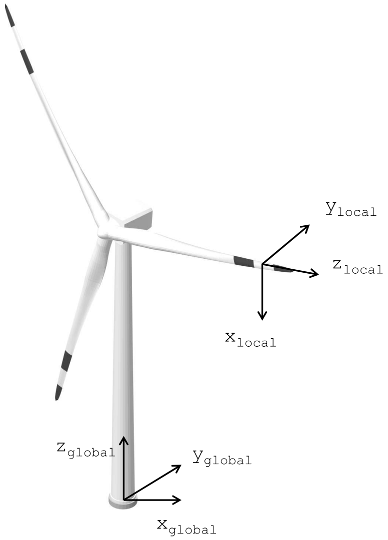

Figure 3.1: Global coordinate system

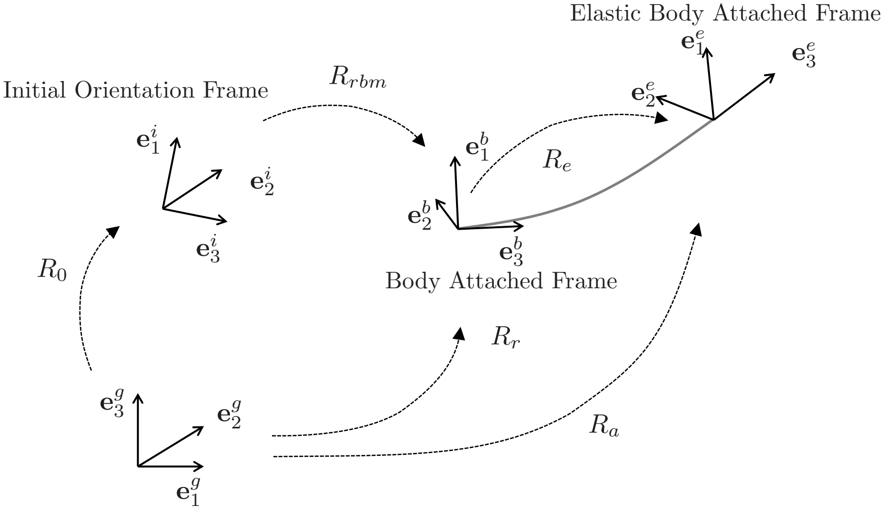

Figure 3.2: Rotation between coordinate systems

true for both the body-attached and the elastic body-attached reference frame. In the case of large strains and warping, the second and third vector need to be defined in a different manner. In that case, an auxiliary vector $\mathbf{q}_0$ is defined that is orthogonal to $\mathbf{e}_3^i$. It is convenient for the blades to specify $\mathbf{q}_0$ in the edgewise direction. The vectors, $\mathbf{e}_3^i$ and $\mathbf{q}_0$, span a plane, to which a perpendicular vector is defined. When the vector $\mathbf{q}_0$ is normalised, the second vector of the coordinate system can be obtained.

$$\mathbf{e}_2^i = \mathbf{q}_0 \times \mathbf{e}_3^i \tag{3.2}$$

The remaining unit vector of the coordinate system is the directional vector that is perpendicular to the plane spanned by $\mathbf{e}_2$ and $\mathbf{e}_3$. It can be computed by a cross product analogue to Equation 3.2.

3.2.1 ROTATION MATRICES

Rotation matrices map the displacements, velocities, accelerations and forces in different coordinate frames to another. In this dissertation, the rotating vector approach of Battini (2008) is followed. This total rotation parametrization has the advantage, that it circumvents the updating procedure associated with compound rotations. The disadvantage of this method is that the angle of rotation is limited to 2π rad.

The orthogonal rotation matrix for a node is obtained using three independent parameters. A vector of rotation angles, Ψ_1 to Ψ_3, each defined around a corresponding direction vector of the body-attached coordinate system, is used to describe the orientation of the segment. These rotation angles are used to define a rotation vector, $\mathbf{u_r}$, and rotation magnitude, ψ.

$$\mathbf{\Psi} = \begin{pmatrix} \Psi_1 \\ \Psi_2 \\ \Psi_3 \end{pmatrix} = \mathbf{u_r}\psi \tag{3.3}$$

The rotation magnitude can be obtained from the rotation angles Ψ_1 to Ψ_3.

$$\psi = \sqrt{\Psi_1^2 + \Psi_2^2 + \Psi_3^2} \tag{3.4}$$

Finally, the rotation matrix can be constructed.

$$\mathbf{R_{sub}} = \mathbf{I} + \frac{sin\psi}{\psi}\tilde{\Psi} + \frac{1}{2}\left[\frac{2sin\frac{\psi}{2}}{\psi}\right]^2 \tilde{\Psi}^2 \tag{3.5}$$

with $\mathbf{R_{sub}} = \mathbf{I}$ when $\boldsymbol{\Psi} = \mathbf{0}$ and

$$\tilde{\Psi} = \begin{bmatrix} 0 & -\Psi_3 & \Psi_2 \\ \Psi_3 & 0 & -\Psi_1 \\ -\Psi_2 & \Psi_1 & 0 \end{bmatrix}$$

$$\mathbf{I} = \begin{bmatrix} 1 & 0 & 0 \\ 0 & 1 & 0 \\ 0 & 0 & 1 \end{bmatrix}$$

Rotation matrices can be defined with respect to any coordinate system. In this dissertation, the primary coordinate system is the global coordinate system in which both structural dynamics and the inflowing wind are defined. The rotation matrices between the coordinate frames can be obtained through pre-multiplication of the individual rotation matrices. Exempli gratia the rotation matrix, from the body-attached frame to the body-attached elastic frame, can be linked by each individual rotation matrix with respect to the global frame.

$$\mathbf{R}_e = \mathbf{R}_a^{-1}\mathbf{R}_r \tag{3.6}$$

3.3 STRUCTURE OF THE DU-SWAT

The commercially available wind turbine analysis tool, GH Bladed, and the open-source code FAST, do not have smart rotor modelling capabilities. Therefore it was necessary to develop an analysis tool that can accomodate smart wind turbine systems. The code has been named Delft University Smart Wind Turbine Analysis Tool (DU-SWAT) and is a sequel to DU-SWAMP (Barlas, 2011), which stands for Delft University Smart Wind turbine Aeroelastic Modular Processing. Both codes share the same Simulink platform, but the DU-SWAT incorporates more advanced aerodynamic and structural models. The controller design and the wind models are similar in both codes. The DU-SWAT has been developed with special focus on smart rotor research and controller implementation. A flow chart of the code is given in Figure 3.3.

As shown in Figure 3.3, the DU-SWAT consists out of three main modules, namely aerodynamics (Sections 3.5 and 3.6), structural dynamics (Section 3.7) and a control module (Section 3.8). The theory behind all of the modules will be discussed in this chapter. Each module is linked to the others by a set of defined parameters that are transfered between them.

The wind module (Section 3.4) supplies wind data, as a function of time, to the aerodynamic module. This data can be obtained using commercially available or open-source software and is preprocessed to adapt it to the input format of the

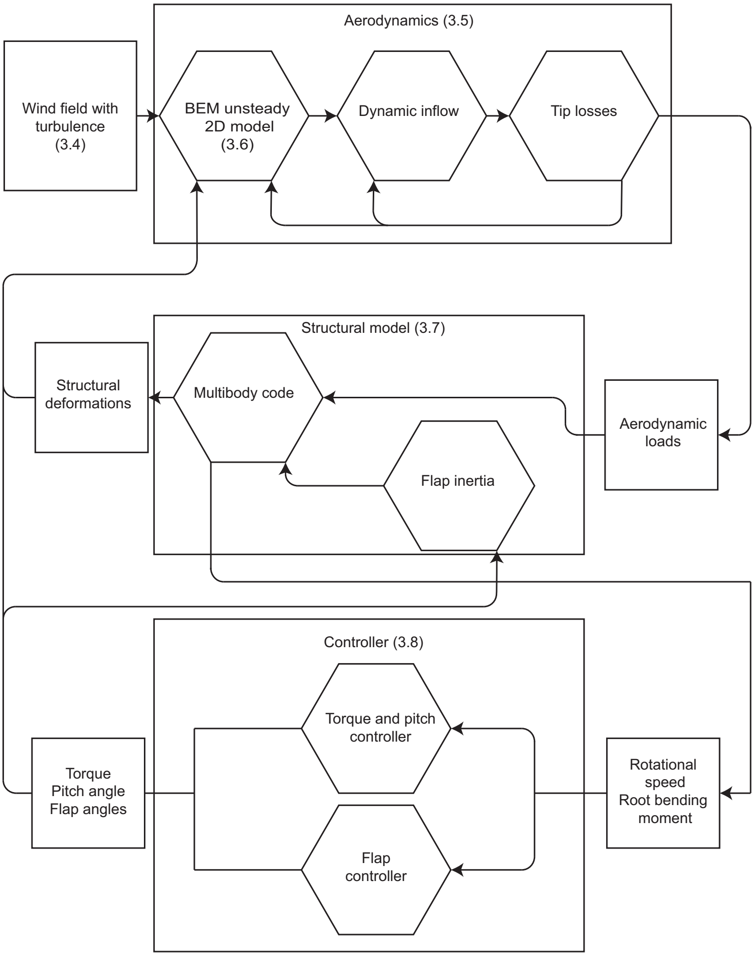

Figure 3.3: Flow chart of the DU-SWAT

aerodynamic module. The aerodynamic module provides a force and moment distribution along the span of each wind turbine blade. This serves as input to the structural module, which in turn feeds back structural deformations, velocities and accelerations to both the aerodynamic module and the control module. Also, the rotation speed of the turbine is passed to the control module. The code was structured in such a way, that this list of inputs can easily be extended if needed for more advance control studies. For the case of individual flap control, the root bending moment in the flapwise direction has been added to the interface between the structural module and controller. The controller provides the reaction torque, pitch angle and flap angles to both the structural and aerodynamic modules. The code is fully modular meaning that all modules can be easily interchanged.

During a simulation, the aeroservoleastic modules are solved using a closed coupled integration scheme. The time-domain response is computed with a variable time step by means of the built in ordinary differential equation solver of Simulink, based on the Dormand-Prince algorithm. The relative accuracy of the solver is 0.1%. In the current set-up, the wind turbine analysis code is able to simulate a 10 minute design load case, defined according to specifications, in less than two hours.

3.4 WIND MODELLING

As shown in Figure 3.3, the first model component is the wind input. The required wind input for design load cases are specified by the International Electrotechnical Commission (IEC). These load cases cover a variety of power production, start-up, shut down and emergency conditions (International Electrotechnical Commission, 2005). The wind input files need to be supplied as time history files for the aeroelastic simulation.

3.4.1 GENERATION OF WIND FILES

The DU-SWAT uses two freely available research tools to create the wind files. The first tool is the National Renewable Energy Laboratory (NREL) developed TurbSim (Jonkman, 2009). TurbSim provides a stochastic time history signal of wind sheets. On each wind sheet, which is defined in terms of grid coordinates, wind speed components are provided in three directions as shown in Figure 3.4. The grid size and resolution can be defined by the user, and should be chosen such that the smallest length scale and time scale of interest is captured in the wind time data. The area covered by the wind sheet should contain the wind turbine rotor.

TurbSim offers a great range of options, ranging from different turbulence models (e.g. Kaimal or van Karman) to wind turbine classes and turbulence types, as defined by the IEC standards (International Electrotechnical Commission, 2005). Different wind shear models can be used (e.g. potential profile, logarithmic profile, jet profile, etc.) to cover all stochastic load cases in the certification regulations.

While TurbSim was already used in the previous generation of aeroelastic codes at Delft University of Technology (Barlas, 2011), a second wind generator has been included to extend the research to deterministic load cases. Similar to TurbSim, IECwind is an open-source tool created by the NREL (Buhl, 2014).

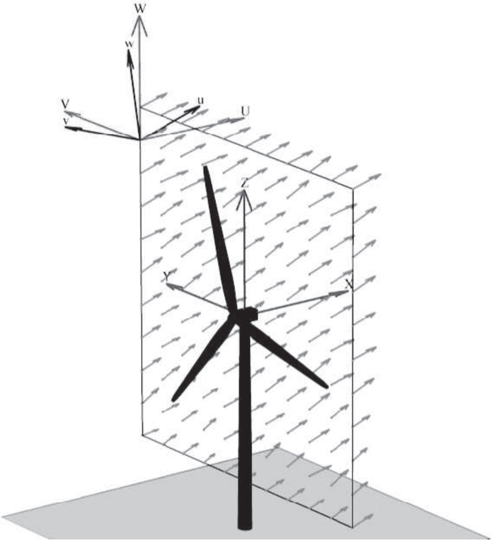

Figure 3.4: Coordinates

IECwind can generate wind histories for extreme changes of direction, extreme operational gusts, normal wind profiles, extreme wind shear and extreme coherent gusts with direction change. The code uses wind turbine and turbulence classes, as well as the hub height, as input. The output is a time series of wind direction and magnitude. A Matlab script is used to convert this information into the same format as provided by TurbSim.

3.4.2 PREPARATION OF WIND FILES FOR AEROSERVOELASTIC ANALYSIS

Both the wind files obtained by TurbSim and by IECwind are loaded as data files into the time-domain simulation. The wind components are provided for a Cartesian grid of nodes. To speed up computations, the wind speeds for the Cartesian nodes are interpolated onto a circular grid as shown in Figure 3.5. The wind speed components, however, still remain defined in the original, global reference frame as shown in Figure 3.1.

The DU-SWAT calculates the wind speed components for all spanwise section locations specified in the BEM module. The wind speed distribution is interpolated from a Cartesian coordinate system to a Cylindrical coordinate system reduces the interpolation efforts that have to be made when performing the time-domain simulations. The interpolation in the preprocessor, from a grid defined in x and y coordinates to an azimuth dependent grid, causes a smoothing of the wind field, thereby reducing its spatial resolution. This can be compensated for by increasing the number of nodes in the grid, which is still computationally more efficient.

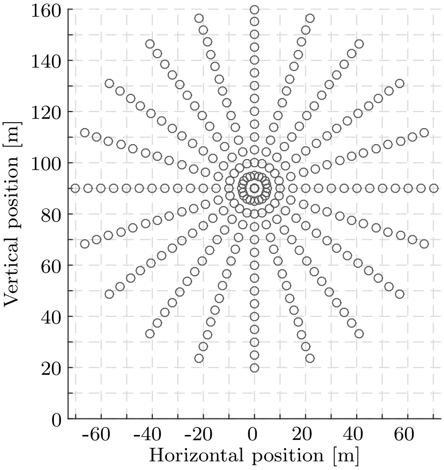

Figure 3.5: Cartesian vs circular grid

The obtained wind distribution is corrected using a tower shadow model (Burton et al., 2001). This model introduces a velocity deficit in the axial direction, in front of the tower, to obtain the axial wind speed including tower shadow V_{ts},

$$V_{ts} = V_{ax} \frac{\left(\frac{D_T^2}{2}\right)^2 \left(x_{hub}^2 - r_i^2 sin^2(\theta)\right)}{\left(x_{hub}^2 - r_i^2 sin^2(\theta)\right)^2} \tag{3.7}$$

where r_i is the radial location of each blade section, x_{hub} is the axial distance between the blade and the hub and D_T is the tower diameter. For each airfoil section in the BEM model, the resulting wind speed components are converted to the local, elastic body attached reference frame by means of the coordinate transformation:

$$\mathbf{V}_{local} = \mathbf{R}_a \mathbf{V}_{inflow} \tag{3.8}$$

3.5 UNSTEADY BLADE ELEMENT METHOD

Spatially distributed wind information is used as input to the aerodynamic module, which in the DU-SWAT is an unsteady BEM model. The code incorporates a dynamic inflow model and an unsteady sectional model into the classical BEM formulations. This section presents the mathematical formulation used in the DU-SWAT.

3.5.1 LOADS PER STREAMTUBE

The starting point for the load estimation is the computation of the sectional angle of attack. For this purpose, the structural velocities are superimposed onto the rotational velocity and the components of the wind speed as defined in the previous section. The axial and tangential velocity components of the wind speed, V_{ax} and V_{tan}, are then computed for each blade section.

$$V_{tan} = (\omega r + V_x)(1 + a') - V_{edge} \tag{3.9}$$

$$V_{ax} = (V_y)(1 + a) - V_{flap} \tag{3.10}$$

where a and a' are the axial and tangential induction factors, respectively. Both coefficients are obtained through iteration with the dynamic inflow model as described in section 3.5.3. The subscripts $'edge'$ and $'flap'$ denote the edgewise and flapwise components of the structural blade velocities, respectively. Equations 3.9 and 3.10 are combined to obtain the inflow angle ϕ.

$$\phi = \left(\frac{V_{tan}}{V_{ax}}\right) \tag{3.11}$$

This inflow angle, in turn, is combined with the pitch angle, Θ, and the torsional angle of the blades, $\vartheta_{torsion}$, to obtain the angle of attack of each individual rotor section.

$$\alpha = \phi - \Theta - \vartheta_{torsion} \tag{3.12}$$

The section freestream velocity is obtained by combining the axial and tangential velocity components.

$$V_{local} = \sqrt{V_{ax}^2 + V_{tan}^2} \tag{3.13}$$

The time history of the angle of attack is used to compute the unsteady lift, drag and moment coefficients as described in section 3.6. These coefficients are converted into sectional lift and drag forces and pitching moments. The force that the wind turbine blade exerts on the free flow is computed by the axial components of lift and drag forces.

$$F_{ax} = Lcos(\phi) + Dsin(\phi) \tag{3.14}$$

This force, F_{ax}, is integrated over the length of the blade. In the DU-SWAT, the force is assumed to be constant over each section and can therefore simply be summed.

$$F_{ax,section} = \sum_{i=1}^{N_{blades}} F_{ax,i} \tag{3.15}$$

The subscript 'section' indicates that the load is computed per streamtube. This force is non-dimensional and represented by the coefficient $C_{D_{ax}}$, while the in-plane component of the lift force is denoted C_{ip}.

$$\begin{aligned} C_{D_{ax}} &= \frac{F_{ax,tube}}{\frac{1}{2}\rho V_y^2 \Delta r_i \pi} \\ C_{ip} &= c_L sin\phi \end{aligned} \tag{3.16}$$

These coefficients are used to determine the induction factors as described for the dynamic inflow model.

3.5.2 TIP CORRECTIONS

The code incorporates a Prandtl tip correction factor (Burton et al. (2001)). The tip loss factor, f_p, is computed using the distance between successive vortices, d_{sv}:

$$d_{sv} = \frac{2\pi R}{N_{blades}} \left(\frac{V_\infty (1-a)}{V_{res}} \right) \tag{3.17}$$

where N_{blades} is the number of blades in the turbine and R is the rotor radius. The resulting velocity, V_{res}, can be computed using Equation 3.18.

$$V_{res} = \sqrt{(\omega r)^2 + V_\infty^2 (1-a)^2} \tag{3.18}$$

The distance between the successive tip vortices is used to obtain the Prandtl correction factor f_p.

$$f_p = \frac{2}{\pi} cos^{-1} \left(e^{-\pi \frac{R-r}{d_{sv}}} \right) \tag{3.19}$$

The factor, f_p, is a function of the radial position of each section.

3.5.3 DYNAMIC INFLOW MODEL

The blade loads are computed iteratively using the dynamic inflow model. The tangential and axial induction factors are updated every time step according to the loads obtained for each stream tube. The implementation is analogous to the implementation in the DU-SWAMP (Barlas (2011)) and is based on the formulations of Snel (2001) and the Matlab implmentation of Marrant (2007). In this derivation, the wake is considered to be a vortex sheet. The dynamics of the wake development are modelled using a first-order differential equation that acts as a low-pass filter. The velocities of the trailing vortices, V_{tr}, are used as parameters in the time integration of the induction factors.

$$V_{tr} = V_y\,(1-a)$$

In the computation of the axial induction factor, a distinction is made between the 'normal windmill state' and the 'turbulent wake states' (Barlas (2011)). The derivative of the axial induction factor is based on the value of the axial induction factor itself from the previous time step and the axial force per stream tube.

$$\begin{aligned}\frac{da}{dt} &= \tfrac{V_y}{4R}\left(-a+0.5-0.5\sqrt{1-C_{D_{ax}}}\right) \quad C_{D_{ax}} \leq 1 \qquad (3.20)\\ \frac{da}{dt} &= \tfrac{V_y}{4R}\left(-a+1.991-\tfrac{2.7077}{C_{D_{ax}}}\right) \quad C_{D_{ax}} > 1\end{aligned}$$

For the tangential induction factor, the distinction between wake states is not made. The derivative of the axial induction factor is directly obtained from the in plane forces, C_{ip}.

$$\frac{da'}{dt} = \frac{V_{tr}}{4R}\left(\frac{N_{blades}c}{2\pi r}\frac{V_y^2}{V_y-V_{ax}}C_{ip}\right) \qquad (3.21)$$

Finally the induction factors are corrected according to the Prandtl induction factor, f_p, as computed in the previous section.

$$\begin{aligned}a_{corrrected} &= \frac{a}{f_p} \qquad (3.22)\\ a'_{corrected} &= \frac{a'}{f_p}\end{aligned}$$

Both induction factors are fed back as input to the load calculation module.

3.6 UNSTEADY SECTIONAL AERODYNAMIC MODEL

Flaps can be excited at a wide range of frequencies. These frequencies may be high enough that the flow around an airfoil section is unable to reach a steady state condition. This requires the modelling of unsteady aerodynamics at both the scales of the turbine and the airfoil. While the wake dynamics were discussed in the previous section, this section will elaborate on the unsteady sectional model used by the DU-SWAT.

3.6.1 PREPROCESSOR

A preprocessor to the unsteady two-dimensional aerodynamic model has been created in Rfoil (van Rooij (1996)). Rfoil is a software tool for airfoil analysis based on Xfoil (Drela (1989)) with improved stall prediction and corrections for rotational effects. For the airfoil analysis each section is analysed separately. First, the local sectional Reynolds number, Re, is

$$Re = \frac{\rho c \sqrt{V_{\infty,rated}^2 + \omega_{rated}^2 r^2}}{\mu} \tag{3.23}$$

where μ is the dynamic viscosity, c is the chord length and ρ is the density of air. For each section the lift, drag and moment polars have been obtained for angles of attack from -20 to 20 degrees in steps of 0.5 degrees. This procedure has been repeated for different flap deflection angles, creating lift, drag and moment surfaces, respectively. The flap deflection has been modelled as continuous by adding a camber line deformation described by the quadratic function

$$\begin{aligned} \Delta y\left(x,\beta\right) &= \quad 0 & x &< x_{AF} \\ \Delta y\left(x,\beta\right) &= -\left(x - x_{AF}\right)^2 \cdot \tfrac{\beta}{\left(x_{TE} - x_{AF}\right)} & x &\geq x_{AF} \end{aligned} \tag{3.24}$$

where $y\left(x,\beta\right)$ describes the addition to the camber line

Shortening of the airfoil due to flap deflection has been neglected because of the small flap rotation angle. As an example, the deformed flap shape used in Chapter 6 is displayed in Figure 3.6. The resulting surfaces have been approximated by a polynominal fit in order to speed up the numerical simulation. The polynomial function for the fit is:

$$c_{L,fit} = p_{0,0} + p_{1,0}\alpha + p_{0,1}\beta + p_{2,0}\alpha^2 + p_{1,1}\alpha\beta + \cdots + p_{5,0}\alpha^5 \tag{3.25}$$

Figure 3.7 shows the lift and drag coefficient data obtained from Rfoil and the polynomial surface fit for a NACA64618 airfoil profile. These coefficients are used as input to the unsteady, sectional aerodynamic model.

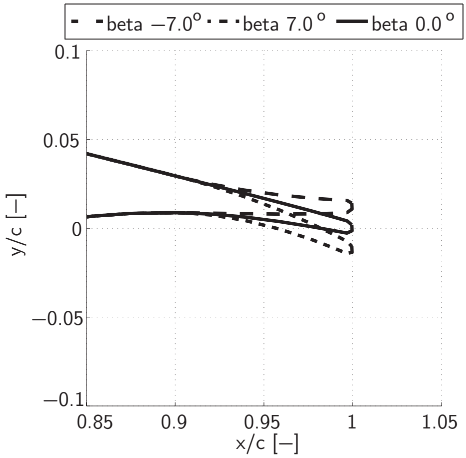

Figure 3.6: Flap deformation

3.6.2 ADPATIVE TRAILING EDGE FLAP MODEL (ATEFLAP)

Smart rotor airfoils can exploit the benefits of a continuously deforming trailing edge. A special aerodynamic adaptive trailing edge flap model has been developed by the Danish Technical University to model the aerodynamic response using state-space equations. This engineering model for the unsteady sectional aerodynamics is used in the DU-SWAT, where it is implemented based on the description by Bergami and Gaunaa (2012). It is the same model as used in HAWC2 (Larsen and Hansen (2012)).

3.6.3 STEADY TWO-DIMENSIONAL COEFFICIENTS

The starting point is the steady lift curve as obtained by the preprocessor. The lift curve is in reality a lift surface as not only the angle of attack, but also the flap deflection angle are input parameters to obtain the lift coefficient. An example of such a lift surface is shown in Figure 3.7. The ATEFlap model first splits the lift surface into an attached component and a separated component, as described in Equation 3.26.

$$c_L^{st} = c_L^{att} f^{st} + c_L^{fs} \left(1 - f^{st}\right) \tag{3.26}$$

The attached lift coefficients are simply obtained by computing the lift curve slope as a function of α and β, as well as the zero lift angle of attack. The corresponding linearization is given in Equation 3.27.

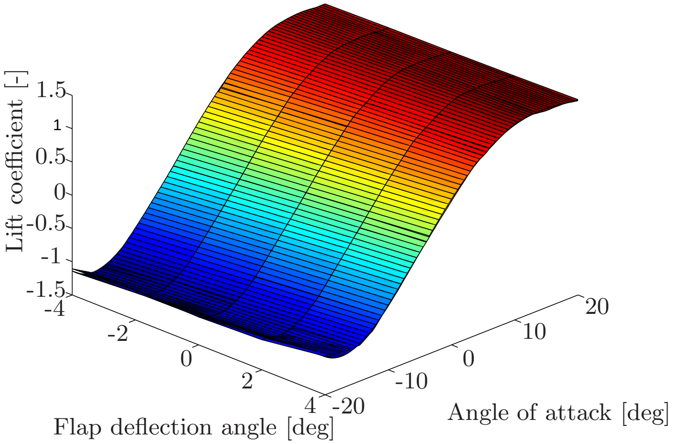

(a) Lift coefficient

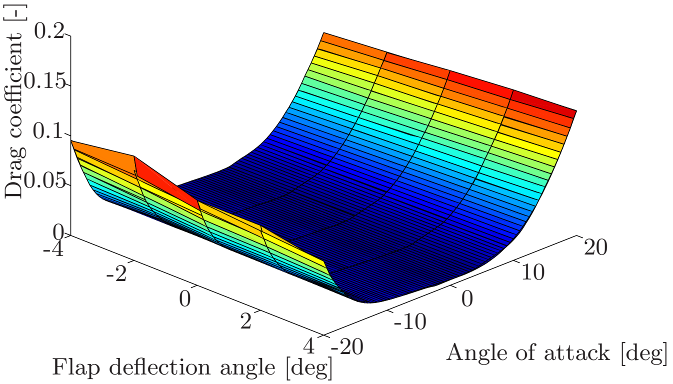

(b) Drag coefficient

Figure 3.7: Lift and drag polar NACA 64618: Data and fit

$$c_L^{att} \approx \frac{\partial c_L}{\partial \alpha}\left(\alpha - \alpha_0\right) + \frac{\partial c_L}{\partial \beta}\beta \tag{3.27}$$

The separation coefficient, f_{st}, is obtained by comparing the linear attached solution to the actual lift curve.

$$f^{st}\left(\alpha, \beta\right) = \left(2\sqrt{\frac{c_L^{st}}{c_L^{att}}} - 1\right)^2 \tag{3.28}$$

This allows the fully separated contribution to the lift to be computed.

$$c_L^{fs} = \frac{c_L^{st} - c_L^{att} f^{st}}{1 - f^{st}} \tag{3.29}$$

This coefficient, c_L^{fs}, is purely an auxiliary variable and does not have any physical meaning.

3.6.4 DYNAMIC CORRECTIONS FOR THE LIFT COEFFICIENT

The equations presented in the previous sections are aimed at calculating a steady aerodynamic solution. In order to obtain a dynamic solution, a quasi-steady angle of attack and a quasi-steady flap angle need to be computed. This angle of attack is computed for the 3/4 chord position and depends on both the geometric angle of attack, as well as the angle of attack induced by the plunge motion and the rotational velocity. The quasi-steady flap angle is computed in similar manner.

$$\begin{aligned} \alpha_{qs} = &\quad \alpha_{3/4} = \alpha_{st} - \tfrac{\dot{y}}{V_{local}} + \tfrac{(0.5-\epsilon_{EA}) b_{hc} \dot{\alpha}_{st}}{V_{local}} && (3.30) \\ \beta_{qs} = &\quad \beta - \tfrac{H_y \dot{\beta}}{V_{local} \frac{\partial c_L}{\partial \beta}} && (3.31) \end{aligned}$$

where α_{qs}, $\alpha_{3/4}$ and α_{st} denote the quasi-steady, the 3/4 chord and the static geometric angles of attack, respectively. The symbol $\dot{y}$ is the plunging velocity, ϵ_{EA} is the distance between elastic axis and aerodynamic center measured in half chords and b_{hc} is the half chord length. The variable H_y is an integral that depends on the geometry of the flap. The integral is derived by Gaunaa (2007). The quasi-steady angle of attack, α_{qs}, and the quasi-steady flap deflection angle, β_{qs}, are converted to an effective angle of attack, α_{eff}, and an effective flap deflection angle, β_{eff}, using the lag function:

$$\alpha_{eff} = \alpha_{qs} \chi(0) + \sum^{N_{lag}} z_i^{\alpha} \tag{3.32}$$

$$\beta_{eff} = \beta_{qs} \chi(0) + \sum^{N_{lag}} z_i^{\beta} \tag{3.33}$$

where z is a state variable that depends on the downwash time history. The variable χ is a lag function defined by the experimentally obtained coefficients, A_i and b_i. The values of these coefficients depend on the thickness of the wing section (Bergami et al., 2013).

$$\dot{z}_i = -\frac{V_{local}}{b_{hc}} b_i z_i + \frac{V_{local}}{b_{hc}} b_i A_i w_{qs} \tag{3.34}$$

$$\chi = 1 - \sum_{i=1}^{N_{lag}} A_i e^{b_i \tau} \tag{3.35}$$

where τ is a dimensionless time coefficient measured in terms of half chords travelled.

$$\tau = \frac{V_{local} t}{b_{hc}} \tag{3.36}$$

The potential lift is a sum of the circulatory and non-circulatory terms.

$$c_{L,pot} = c_{L,eff}\left(\alpha_{eff}, \beta_{eff}\right) + \pi \frac{b_{hc}}{V_{local}} \dot{\alpha} + \frac{F_{dydx}}{\pi} \frac{b_{hc}}{V_{local}} \dot{\beta} \tag{3.37}$$

Similarly to H_y, F_{dydx} is a coefficient that depends on the deformed shape of the flap. The potential lift is adjusted by a lag term to account for the time delay in the development of the pressure field.

$$\dot{c}_l^{lag} = c_L^{lag} \frac{V_{local}}{b_{hc}\tau_p} + c_{L,pot} \frac{V_{local}}{b_{hc}\tau_p} \tag{3.38}$$

The constant τ_p can be determined experimentally. In this dissertation a value of 1.5 is used for τ_p, which has been found experimentally by DTU Risø.

3.6.5 SEPARATION DYNAMICS

Up until this point, no separation dynamics have been considered. First, an equivalent separation point is computed based on the value of c_l^{lag}

$$\begin{aligned} f^{c_L,lag} &= f^{st}\left(\alpha^*, \beta^*\right) \\ \alpha^* &= \frac{c_{L,\beta=0}^{lag}}{\frac{\partial c_L}{\partial \alpha}} + \alpha_0 \\ \beta^* &= \frac{c_L^{lag} - c_{L,\beta=0}^{lag}}{\frac{\partial c_L}{\partial \beta}} \end{aligned} \tag{3.39}$$

A lag function is applied to the separation constant, f, but instead of using a pressure time constant, τ_p, as before, a boundary layer time constant τ_B is used. The resulting first order differential equation (Equation 3.40) is solved by time marching in the DU-SWAT. The separation point, f^{dyn}, represents the dynamic location of flow separation of the airfoil.

$$\dot{f}^{dyn} = \frac{V_{local}}{b_{hc}\tau_B}\left(f^{c_{L,lag}} - f^{dyn}\right) \tag{3.40}$$

This allows the computation of the dynamic circulatory terms, $c_{L,circ}^{dyn}$, in the lift coefficient.

$$c_{L,circ}^{dyn} = c_{L,att}\left(\alpha_{eff}, \beta_{eff}\right) f^{dyn} + c_l^{fs}\left(\alpha_{eff}, \beta_{eff}\right)\left(1 - f^{dyn}\right) \tag{3.41}$$

The circulatory component can be combined with the non-circulatory terms such that the full equation for the lift coefficient becomes:

$$c_L^{dyn} = c_{L,circ}^{dyn} + \pi\frac{b_{hc}}{V_{local}}\dot{\alpha}^{str} + \frac{F_{dydx}b_{hc}}{\pi V_{local}}\dot{\beta} \tag{3.42}$$

3.6.6 DRAG AND MOMENT COEFFICIENTS

The lift coefficient is the sum of the circulatory dynamic term and the non-circulatory term. The value of the drag and moment coefficients are based on steady data and depend on the sum of individual components that can easily be obtained as shown in Bergami and Gaunaa (2012).

$$\begin{aligned}
c_D &= && c_D^{eff} + c_{D,ind}^{\alpha} + c_{D,ind}^{\beta} + c_{D,ind}^{f} \\
c_D^{eff} &= && c_D\left(\alpha_{eff}, \beta_{eff}\right) \\
c_{D,ind}^{\alpha} &= && c_{L,circ}^{dyn}\left(\alpha_{qs} - \alpha_{eff}\right) \\
c_{D,ind}^{\beta} &= && c_{L,circ}^{dyn}\frac{\frac{\partial c_L}{\partial \beta}}{\frac{\partial c_L}{\partial \alpha}}\left(\beta_{st} - \beta_{eff}\right) f^{dyn} \\
c_{D,ind}^{f} &= && \left(c_d^{eff} - c_{D,\alpha_0,0}\right)\left[\left(\tfrac{1-\sqrt{f^{dyn}}}{2}\right)^2 - \left(\tfrac{1-\sqrt{f^{C_{L,lag}}}}{2}\right)^2\right]
\end{aligned} \tag{3.43}$$

The values of the angles of attack and flap deflection angles are identical to the values used for the computation of the lift coefficient. The total drag coefficient, c_D, is the sum of the effective drag coefficient, c_D^{eff}, the induced drag components caused by the unsteady lift component and the drag component from the separation dynamics. The moment coefficient is computed in a similar fashion, by summing up circulatory and non-circulatory terms.

$$\begin{aligned}
c_m &= && c_m^{qs} + c_m^{nc,\dot{\alpha}} + c_m^{nc,\dot{\beta}} \\
c_m^{qs} &= && c_m\left(\alpha_{eff}, \beta_{eff}\right) \\
c_m^{nc,\dot{\alpha}} &= && -0.5\pi\tfrac{b_{hc}}{V_{local}}\dot{\alpha}^{str} \\
c_m^{nc,\dot{\beta}} &= && \dot{\beta}\left[-0.5\tfrac{b_{hc}}{V_{local}\pi}\left(G_{dydx} + 0.5F_{dydx}\right) + 0.5\tfrac{1}{V_{local}}\left(\tfrac{F_y}{\pi} + \tfrac{H_y}{2}\right)\right]
\end{aligned} \tag{3.44}$$

The coefficients G_{dydx} and F_{dydx} depend on the trailing edge shape. For the flap configuration considered in this thesis, the coefficients of the adaptive trailing edge model of Gaunaa (2007) are:

$$\begin{aligned} F_{dydx} &= -8.988 \cdot 10^{-3} \\ F_y &= -7.44 \cdot 10^{-4} \\ G_{dydx} &= -3.958 \cdot 10^{-3} \\ H_y &= 4.352 \cdot 10^{-2} \end{aligned} \tag{3.45}$$

3.6.7 NUMERICAL COMPARISON TO COMPUTATIONAL FLUID DYNAMICS

The accuracy of the sectional unsteady aerodynamic model has been investigated by Gillebaart et al. (2014). Two different aerodynamic models are compared. The first model is the ATEFlap model presented in the previous section, while the second model is a computational fluid dynamic approach (URANS). In this section each aerodynamic model is coupled to a simple three degrees of freedom structural model as shown in Figure 3.8. The structural properties, which are provided in Table 3.1, have been chosen to approximate an airfoil section, located close to the tip of a wind turbine blade, both in terms of frequency and mass. The set-up of the structural model can be seen in Figure 3.8. The flap is implemented as described in section 3.6.1. The airfoil with flap is subjected to a two-dimensional flow containing a disturbance that represents a gust.

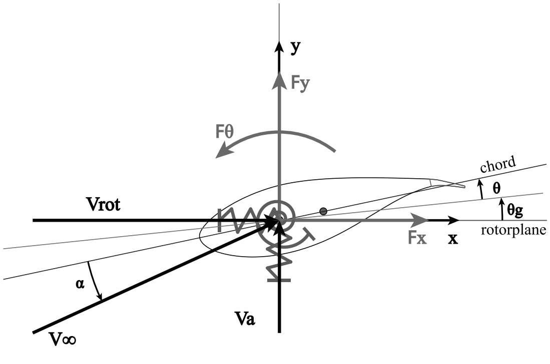

Figure 3.8: Illustration of structural model including a flap together with forces, inflow directions and angle definitions (Gillebaart et al. (2014))

A Proportional-Derivative (PD) controller, with the plunge velocity as input, has been added to the model to try to minimise the vertical deflection. A second

Table 3.1: Structural properties for three degrees of freedom model

Chord	1m	K_x	6316 N/m
RC (from LE)	0.3m	K_y	1579 N/m
CG (from LE)	0.35m	K_Ψ	8290 Nm/rad
Mass	40kg/m	Ψ	5 degrees
I_{CG}	$2kgm^2$		

order backward differencing scheme is used to integrate the URANS model. A Runge-Kutta algorithm is used by the ATEFlap model for time integration. The gain of the controller has in each case been manually tuned to the values shown in Equation 3.46.

$$\frac{d\beta}{dt} = -100\frac{dy}{dt} - 20\frac{d^2y}{dt^2} \tag{3.46}$$

Two different types of traveling gust have been simulated. The first one is a Mexican hat gust (Manwell et al., 2003) with an amplitude of 1.0 m/s and a frequency of 1.2 Hz. The second one is a (1-cos) gust with the same amplitude and frequency. Figures 3.9 and 3.10 show the results for the force and moment coefficients and deflections. In the uncontrolled case, the differences between the engineering model and the CFD method are in the order of 1% for both the plunging and horizontal movement. The rotational parameters show a larger relative error. However, the amplitude of the moment is very small, resulting in a 0.04 degrees difference in pitch angle.

In the controlled case, the relative differences between the two aerodynamic models increase. The amplitudes of the displacement and force are reduced by 83% (URANS) and 81% (ATEFlap) for the cosine gust, respectively. They are reduce, respectively, by 78% (URANS) and 76% (ATEFlap) for the Mexican hat gust. Both codes show a strong increase in moments and pitch angle. The relative difference between the corresponding values remains below 1%, except for the maximum pitching moment during the Mexican hat gust, which shows a difference of up to 3%. The unsteady sectional aerodynamic engineering model, ATEFlap, may thus be thus considered very accurate and can be used in a blade momentum approach without contributing to the uncertainty of the modelling approach. Possible discrepancies in unsteady aerodynamic behaviour between test turbines and simulations, can therefore not be attributed to the sectional model.

3.7 STRUCTURAL MODEL

Two different structural models have been implemented in the DU-SWAT. The first model is a multi-body formulation consisting of rigid bodies interconnected

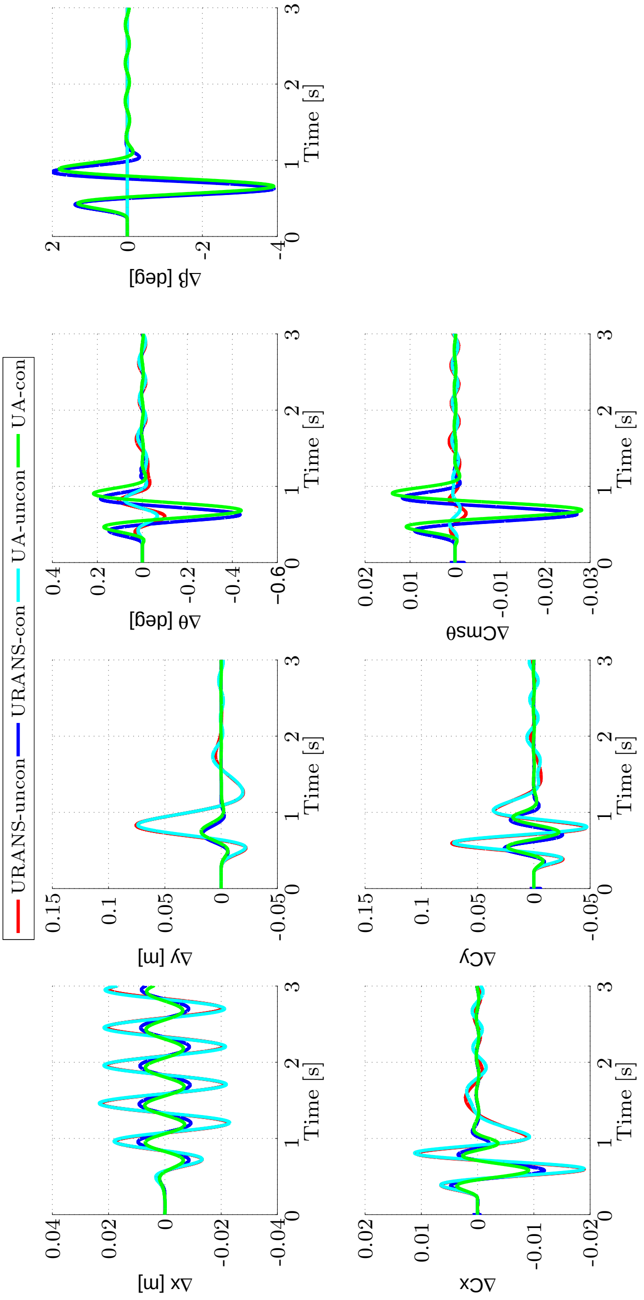

Figure 3.9: Response in time to a Mexican hat gust: unsteady aerodynamic (UA) model and the URANS model (URANS), for both the uncontrolled (uncon) and controlled case (con) (Gillebaart et al. (2014))

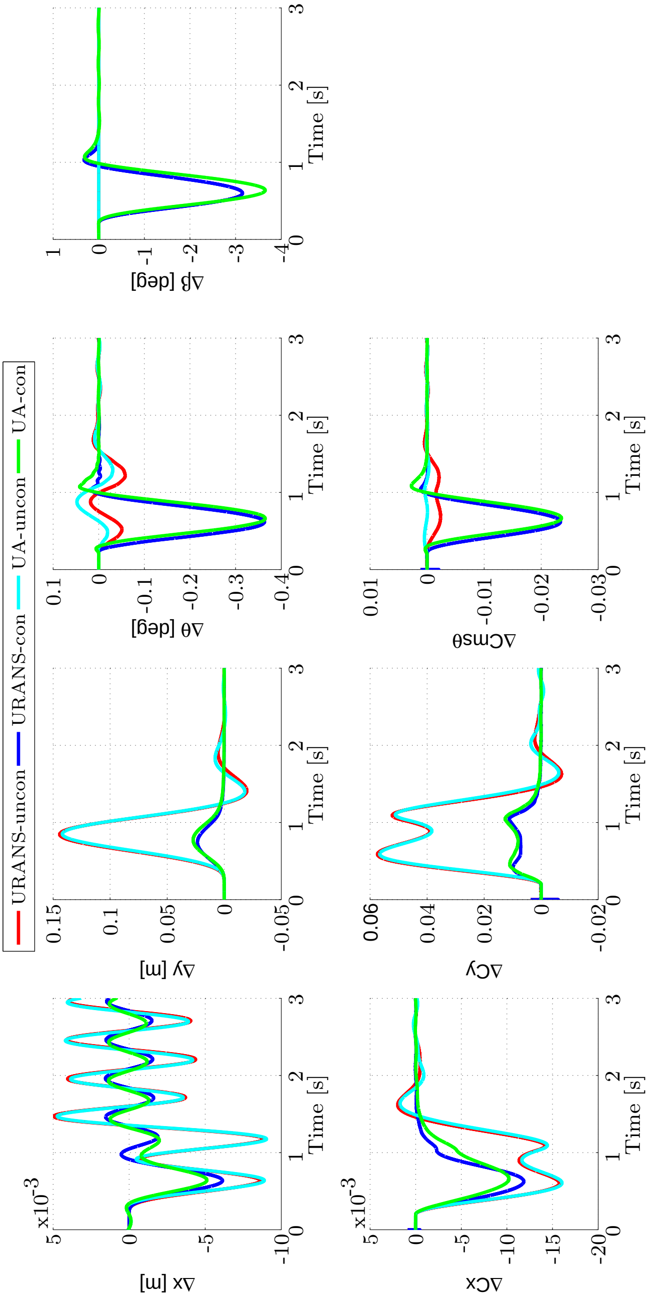

Figure 3.10: Response in time to a 1-cos gust: unsteady aerodynamic (UA) model and the URANS model (URANS), for both the uncontrolled (uncon) and controlled case (con) (Gillebaart et al. (2014))

with springs. This approach will be briefly discussed in this section. A second, more advanced modelling approach, using modal formulations, will be presented in Chapter 4.

3.7.1 MULTI-BODY DYNAMICS

The aerodynamic model was coupled to a multi-body system modelled in SimMechancis (The Math Works, 2011). SimMechanics is a simulation environment that employs rigid-body systems. It is a package for Matlab Simulink. A more complete description of the modelling capabilities of this tool can be found in the User's Guide (The Math Works, 2011). For this simple structural model, the turbine is segmented into rigid bodies that are interconnected by a spring-damper system as shown in Figure 3.11. In the current model, only rotational degrees of freedom are included. The three degrees of freedom between the elements are expressed in a co-rotational framework, so that geometric non-linearities can be captured. The mass and moment of each rigid body are positioned at its center of gravity.

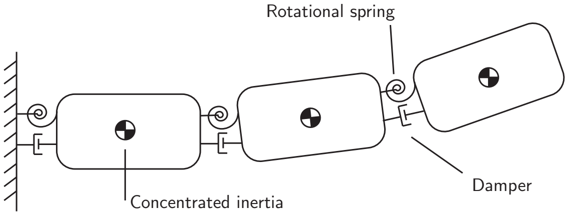

Figure 3.11: Rigid bodies in a co-rotational frame work with spring-damper connection

Each wind turbine blade is broken down into 18 elements of equal span interconnected with spring-damper elements. This number of elements was chosen for two reasons. Firstly, it includes a sufficient number of multi-bodies to approximate the shape of the first three flapwise and edgewise eigenmodes, thereby covering frequencies of turbulent excitation up to 6.0 Hz. These frequencies are the most relevant as higher frequencies contribute only very little to fatigue damage or ultimate loading. A second reason for choosing 18 elements was that the relative difference in stiffness, between adjacent springs, can be restricted to 10%. For the rotational springs, the spring stiffness has been selected based on the average stiffness EI and GJ of each body, where E is the Young's modulus, G is the shear modulus, and I and J are the moment of inertia and the polar moment of inertia, respectively. The tower is modelled using 12 rigid bodies. It is possible to use less rigid bodies for the tower as the stiffness of the tower is more uniform than the blade stiffness. Figure 3.12 shows the machine model used in SimMechanics. Using 18 bodies per blade results in each blade having 51 degrees of freedom and the tower having 33 degrees of freedom. The total of 186 degrees of freedom offered a suitable compromise between computational time and accuracy.

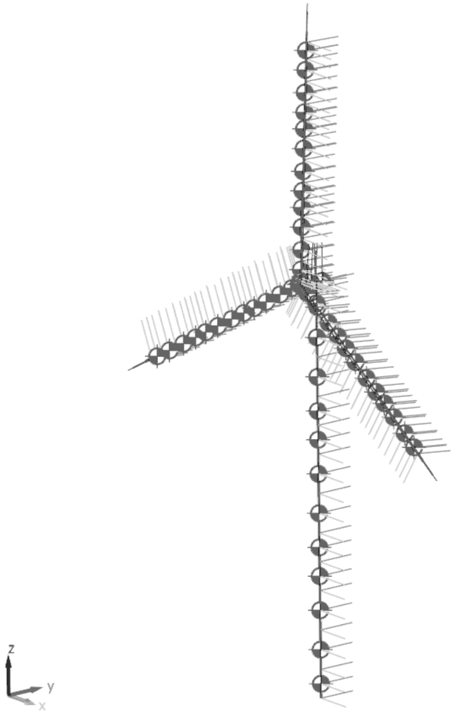

Figure 3.12: Multi-body representation in SimMechanics

SimMechanics automatically takes care of computing gravitational, centrifugal or Coriolis forces. The aerodynamic forces are interpolated onto each body and applied at the location of the aerodynamic center. SimMechanics also provides translation and rotation matrices, and the derivatives of these matrices with respect to the undeformed shape, such that the structural input to the aerodynamic model can easily be calculated. The rotational degree of freedom of the rotor is modelled using a revolute joint with the resistance torque obtained from the controller. The shaft is assumed as rigid.

3.7.2 ASSEMBLY OF EQUATIONS OF MOTION

SimMechanics assembles the equations of motion by itself and updates them every time step to include non-linearities. It assumes that both the blade and tower structure can be approximated by a beam model. This beam model is divided into elements and a stiffness matrix is constructed. Only bending deformations are included in the structural model. The stiffness matrix of each element is given by:

$$\left\{ \begin{array}{c} S_1 \\ M_1 \\ S_2 \\ M_2 \end{array} \right\} = \frac{EI}{L_i^3} \left[\begin{array}{cccc} 12 & 6L_i & \text{-12} & 6L_i \\ 6L_i & 4L_i^2 & -6L_i & 2L_i^2 \\ \text{-12} & -6L_i & 12 & -6L_i \\ 6L_i & 4L_i^2 & -6L_i & 2L_i^2 \end{array} \right] \left\{ \begin{array}{c} v_1 \\ \Psi_1 \\ v_2 \\ \Psi_2 \end{array} \right\} \tag{3.47}$$

where S is the shear force, M is the moment acting on the boundary of the element and v is the bending displacements of the boundary grid points. It is then assumed that the deformation of each individual element is small and that the overall deformation is dominated by the rotations and translations of the follower elements. This allows Equation 3.47 to be reduced to:

$$\left\{ \begin{array}{c} S_1 \\ M_1 \\ S_2 \\ M_2 \end{array} \right\} = \frac{EI}{L_i^3} \left[\begin{array}{cc} 6L_i & 6L_i \\ 4L_i^2 & 2L_i^2 \\ -6L_i & -6L_i \\ 4L_i^2 & 2L_i^2 \end{array} \right] \left\{ \begin{array}{c} \Psi_1 \\ \Psi_2 \end{array} \right\} \tag{3.48}$$

Different elements can be stitched together using continuity conditions. In the linear case, this would result in the following system matrix:

$$\left\{ \begin{array}{c} S_1 \\ M_1 \\ S_{app} \\ M_{app} \\ S_3 \\ M_3 \end{array} \right\} = \left[\begin{array}{ccc} \frac{6EI}{L_1^2} & \frac{6EI}{L_1^2} & 0 \\ \frac{4EI}{L_1} & \frac{2EI}{L_1} & 0 \\ -\frac{6EI}{L_1^2} & -\frac{6EI}{L_1^2} + \frac{6EI}{L_2^2} & \frac{6EI}{L_2^2} \\ \frac{2EI}{L_1} & -\frac{4EI}{L_1} + \frac{4EI}{L_2} & \frac{2EI}{L_2} \\ 0 & -\frac{6EI}{L_2^2} & -\frac{6EI}{L_2^2} \\ 0 & \frac{2EI}{L_2} & \frac{4EI}{L_2} \end{array} \right] \left\{ \begin{array}{c} \Psi_1 \\ \Psi_2 \\ \Psi_3 \end{array} \right\} \tag{3.49}$$

In the non-linear case, the force and displacement compatibility, between an elements and its follower, is ensured through the usage of rotation matrices such that

$$\left\{ \begin{array}{c} \Psi_{x,fol} \\ \Psi_{y,fol} \\ \Psi_{z,fol} \end{array} \right\} = R_a R_r^{-1} \left\{ \begin{array}{c} \Psi_x \\ \Psi_y \\ \Psi_z \end{array} \right\} \tag{3.50}$$

SimMechanics automatically takes care of this procedure at every time step. The damping matrix is assembled analogous to the stiffness matrix. The inertia tensor of each element is used to build the mass matrix. In the derivation of the linear stiffness matrix, only a single bending degree of freedom was taken into account. The DU-SWAT, however, incorporates all three rotational degrees of freedom of each element such that the stiffness, damping and mass matrices are block diagonal matrices of size 186 by 186. The equations of motion are thus a function of rotation angles only:

$$\mathbf{M_r}\left(\Psi\right)\begin{Bmatrix}\ddot{\Psi}_{x,1}\\ \ddot{\Psi}_{y,1}\\ \ddot{\Psi}_{z,1}\\ \vdots\\ \ddot{\Psi}_{x,n}\\ \ddot{\Psi}_{y,n}\\ \ddot{\Psi}_{z,n}\end{Bmatrix}+\mathbf{B_r}\left(\Psi\right)\begin{Bmatrix}\dot{\Psi}_{x,1}\\ \dot{\Psi}_{y,1}\\ \dot{\Psi}_{z,1}\\ \vdots\\ \dot{\Psi}_{x,n}\\ \dot{\Psi}_{y,n}\\ \dot{\Psi}_{z,n}\end{Bmatrix}+\mathbf{K_r}\left(\Psi\right)\begin{Bmatrix}\Psi_{x,1}\\ \Psi_{y,1}\\ \Psi_{z,1}\\ \vdots\\ \Psi_{x,n}\\ \Psi_{y,n}\\ \Psi_{z,n}\end{Bmatrix}=\left\{F_{app}\right\} \quad (3.51)$$

This differential equation is solved, together with the aerodynamic equations, using a variable step size using the Dormand-Prince algorithm.

3.7.3 INERTIAL FORCES OF FLAP DYNAMICS

The flaps have not been modelled as separate bodies, but the forces and moments associated with each flap motion have been included as a force input to the blade structure. Figure 3.13 shows a schematic overview of the forces acting on the main structure that are caused by flap operation. These forces can be approximated by Equation 3.52

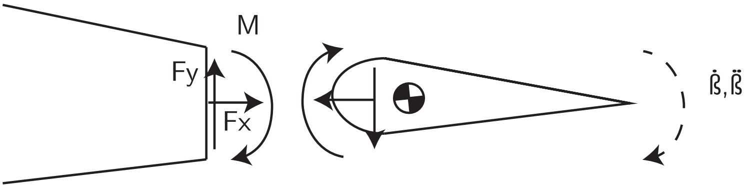

Figure 3.13: Reaction forces and moments

$$\begin{aligned}M_\beta = &\quad \ddot{\beta} I_m\\ F_x = &\quad m_{flap} d_{cog,h}\left(sin\left(\beta\right)\dot{\beta}^2 - cos\left(\beta\right)\ddot{\beta}\right)\\ F_y = &\quad m_{flap} d_{cog,h}\left(cos\left(\beta\right)\dot{\beta}^2 - sin\left(\beta\right)\ddot{\beta}\right)\end{aligned} \quad (3.52)$$

where I_m is the mass moment of inertia around the flap hinge, $d_{cog,h}$ denotes the distance between the center of gravity and the hinge position. In this model, the mass of the flap is lumped at its center of gravity. It should be noted that only centripetal and inertial forces are included. It is assumed that the Coriolis forces caused by the flap motion are small.

3.8 CONTROLLER DESIGN

The controller design is an implementation of the FAST turbine controller (Namik, 2008) in an analogous manner to the previous generation of aeroelastic wind turbine analysis codes of Delft University of Technology (Barlas, 2011). This implementation includes both a torque and pitch controller. As Figure 3.14 shows, the resistance torque is divided into five regions. The main ones are an idling region (region 1), an optimum power region (region 2) and the pitch controlled region (region 3). The control regions are connected by transition regions to allow progression from idling to power production. In region 1.5, the resistance torque is ramped up to the optimum resistance torque for power production. Region 2.5 models the transition from no pitch activity to pitch activity.

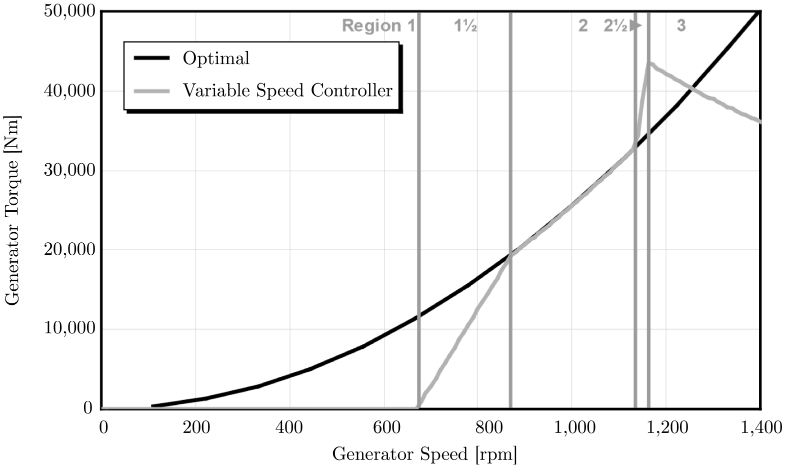

Figure 3.14: Torque vs speed response of variable speed controller (Jonkman et al., 2009)

The filtered generator speed serves as input to the controller. The resistance torque is then determined. A rate limiter and a saturation limit are applied before the torque is fed back to the structural model. The layout of the controller can be seen in Figure 3.15.

The pitch controller is a Proportional-Integral-Derivative (PID) controller combined with a rate and a saturation limiter. The coefficients of the controller are used as provided by Jonkman et al. (2009). As shown in Figure 3.16, the controller is active only above the rated generator speed.

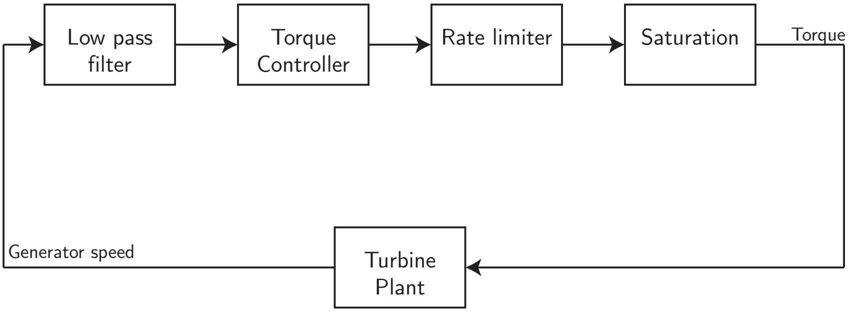

Figure 3.15: Layout of torque controller

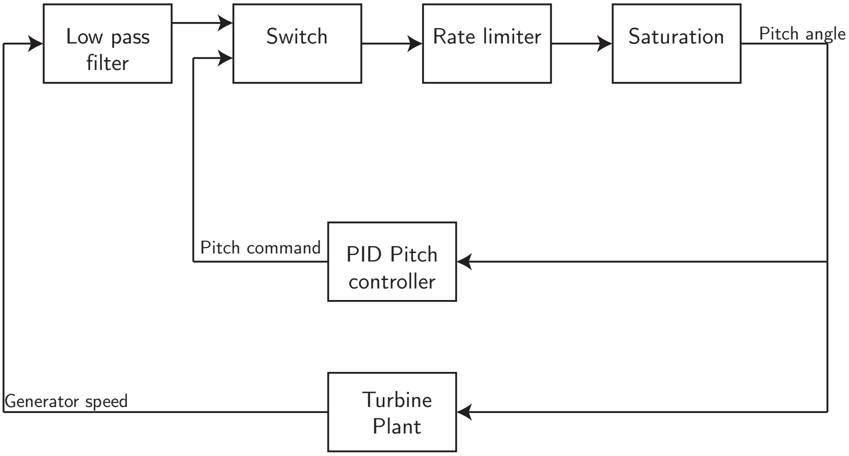

Figure 3.16: Layout of pitch controller

3.8.1 INDIVIDUAL FLAP CONTROL

Additionally to conventional wind turbine controllers, distributed flap control can be implemented. In this case, the flap setting is fed as input into both the aerodynamic module and the structural module. The resulting loads, associated with the flap dynamics, are included in the structural module through an equivalent force input.

As indicated, the DU-SWAT has been designed to allow for the easy implementation of a controller by first creating its source code in Simulink and then compiling it to C++. A controller can be directly included in the Simulink framework and then be compiled together with the structural and the aerodynamic modules. This also allows one to quickly adapt the control system to accommodate more advanced control strategies than collective pitch control. Individual

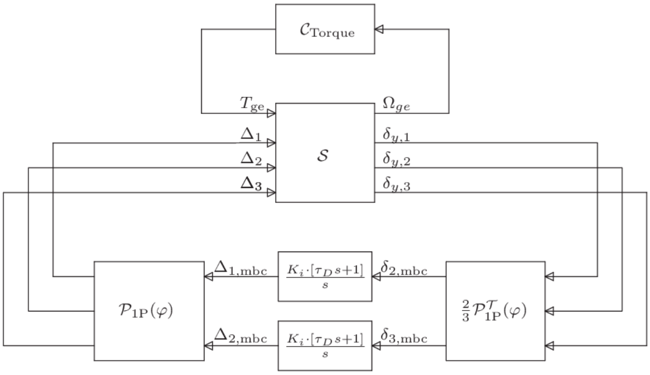

Figure 3.17: Layout of control system (Bernhammer, De Breuker, van Kuik, Berg and van Wingerden, 2013)

pitch controllers attenuate low frequency vibrations. Analogous to the individual pitch control (IPC), an individual flap controller has been developed. The main advantage of the flap control system, when compared to IPC, is that the actuation energy is significantly lower and the bandwidth is typically significantly higher. The normal practice for designing this type of controller is to decouple the system by using Coleman transformations in yaw and tilt directions (Bossanyi, 2009; Houtzager et al., 2013). The Coleman transform converts all parameters that are measured from the rotating reference frame to a fixed reference frame.

$$P^{-1} = \begin{bmatrix} \frac{1}{3} & \frac{1}{3} & \frac{1}{3} \\ \frac{2}{3}\sin\psi_1 & \frac{2}{3}\sin\psi_2 & \frac{2}{3}\sin\psi_3 \\ \frac{2}{3}\cos\psi_1 & \frac{2}{3}\cos\psi_2 & \frac{2}{3}\cos\psi_3 \end{bmatrix} \tag{3.53}$$

where ψ is the azimuth angle of the rotor blades. The decoupling allows the design of single-input-single-output (SISO) integral controllers for individual pitch control. Since multiple flaps can be applied on a single blade, the system could also use a multiple-input-multiple-output (MIMO) controller, e.g. to mitigate higher blade eigenmodes. The control system has been linearised and is considered time-invariant. A PI-controller has been used for the flap action without altering the original torque and pitch control designs as specified for the NREL 5MW reference turbine (Jonkman et al., 2009). Figure 3.17 displays the control system layout including the torque controller described above and the IFC. This controller design approach has been used to assess the load reduction potential of the Sandia National Labs Smart Rotors (Bernhammer, De Breuker, van Kuik, Berg and van Wingerden, 2013).

The control system was linearised by perturbing the steady state condition of the system by flap deflections at a wind speeds of 10.0 m/s. The variable monitored by the control system is the flapwise root bending moment. Periodic components have been filtered out. A Bode plot of the flap deflection versus the root bending moment is shown in Figure 3.18. A broad peak corresponding to the first flapwise eigenfrequency can be seen centered around 0.7 Hz. This first flapwise eigenmode is aerodynamically damped. The second and third flapwise eigenmodes are more clearly visible at just above 2.0 Hz and at 4.5 Hz, respectively. The perturbations in the magnitude plot and the small peaks in the phase plot, at 0.3 Hz and at 1.2 Hz, correspond to the tower mode and the first edgewise mode, respectively.

The gain of the controller has been tuned such that the flap deflections will remain below 5 degrees at rated wind speeds and also so that the resonance around the first flapwise eigenfrequency is slightly reduced. Gain scheduling, depending on the generator speed, was not applied. The Individual Flap Control (IFC) controller has been designed to eliminate the periodic components (1P) of the rotor and tuned so that it also reduces the resonance associated to the first flapwise bending frequency. It was chosen to control the periodic loads as these loads contribute most to the fatigue damage. The transfer function of the controller is:

$$C\left(z\right)=\frac{1.3686\cdot10^{-6}}{z} \tag{3.54}$$

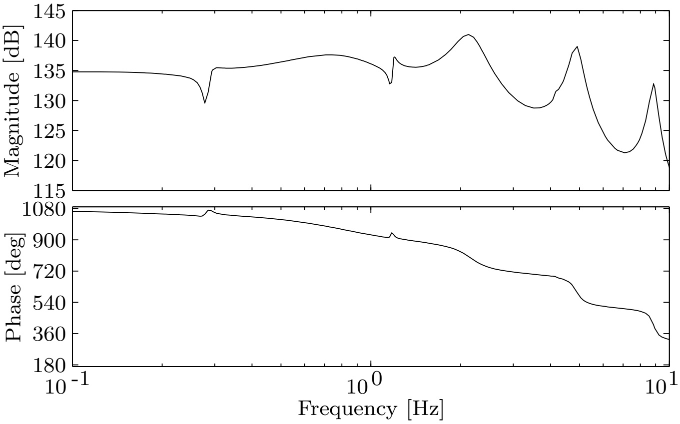

Figure 3.18: Bode plot of numerical system: Magnitude (1st plot) and phase (2nd plot) of flapwise tip deflection as a result of flap deflection

3.9 VERIFICATION WITH COMMERCIAL PROGRAMS

In order to validate the the DU-SWAT, a comparison analysis to two reference codes, GH Bladed and FAST, is performed. Both steady-state and frequency responses are compared.

3.9.1 STEADY VALIDATION DATA

The first validation case is a steady analysis of the 5 MW reference turbine of the NREL (Jonkman et al., 2009). The thrust of the turbine, the power production, the bending moment at the blade root and the blade tip deflection have been chosen as representative parameters. The comparison between these parameters is plotted a function of the wind speed in Figures 3.19 to 3.22. Excellent agreement is found for the power generated between all analysis types as shown in Figure 3.19. The data points of GH Bladed and FAST practically coincide with the data points of the DU-SWAT. The largest difference can be observed at the rated wind speed of 11.0 m/s. This can probably be attributed to differences in the implementation of the control schemes in region 2.5. In the case of the thrust, the difference between the models is larger. While the results of GH Bladed and the DU-SWAT correspond well, the thrust obtained by FAST is higher throughout the operational range. It is assumed that this is the result of the wake model included in FAST as other codes, such as DU-SWAMP (Barlas, 2011), were exhibiting similar differences. The same is found for the root bending moment and the tip deflection as shown in Figures 3.21 and 3.22. In all cases, similar trends can be observed with the values peaking at the rated wind speed. The difference between the values at the rated speed, calculated using GH Bladed and the DU-SWAT, are in the order of 3% for both the root bending moment and the tip deflection. The comparison with FAST shows larger differences, up to 7%. The crelatively large discrapancy can again be attributed to the wake model of FAST. It should also be noted that the differences between the calculated values, of GH Bladed and the DU-SWAT in Figure 3.21, increase with increasing wind speed. However, the differences between the computed values in Figures 3.20 and 3.22 remain small as the wind speed increases.

3.9.2 FREQUENCY RESPONSE

The second analysis type that was performed was the computation of the dynamic structural responses. Firstly, a comparison of the eigenfrequencies was made. The frequencies calculated by the simulation conducted using FAST have been benchmarked using ADAMS (Jonkman et al., 2009) for parked conditions. The frequencies obtained by GH Bladed and the DU-SWAT were calculated for a wind

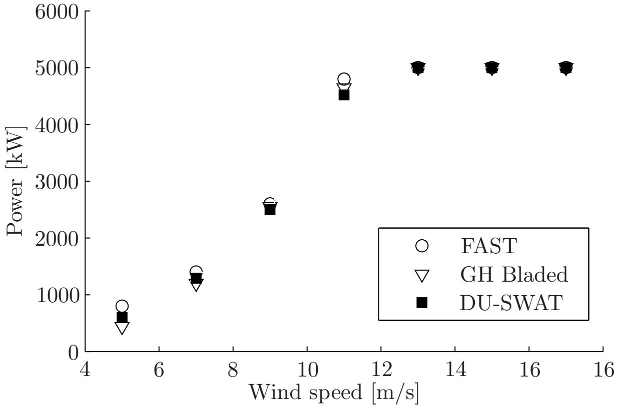

Figure 3.19: Power production comparison between FAST, GH Bladed and the DU-SWAT

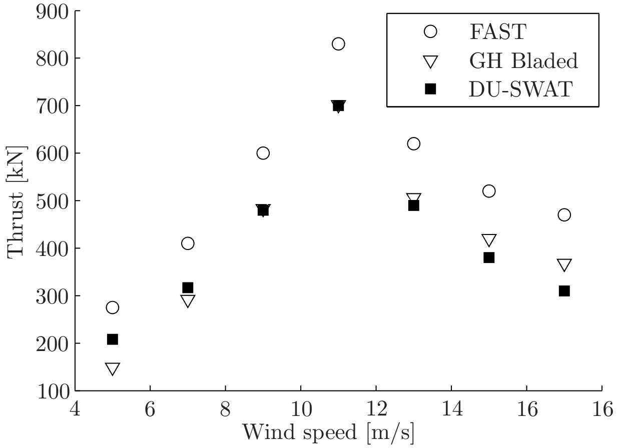

Figure 3.20: Thrust of 5MW refernce turbine comparison between FAST, GH Bladed and the DU-SWAT

speed of 7.0 m/s, which corresponds to a pitch angle of 0 degrees and a rotational speed of 0.85 rad/s. When comparing these with the results from FAST, it has to be taken into account that the rotation of the rotor, in the analysis performed using GH Bladed and the DU-SWAT, has a stiffening effect on the wind turbine blades. This effect increases the frequencies of the eigenmodes and can be seen for the first flapwise eigenfrequency in Table 3.2, where the values obtained by GH Bladed and the DU-SWAT coincide. The eigenfrequency obtained for the same mode by FAST is slightly lower, which can be attributed to the parked conditions. For the first edgewise and the second flapwise eigenfrequencies, the difference between the results of the GH Bladed and the DU-SWAT are 7% and

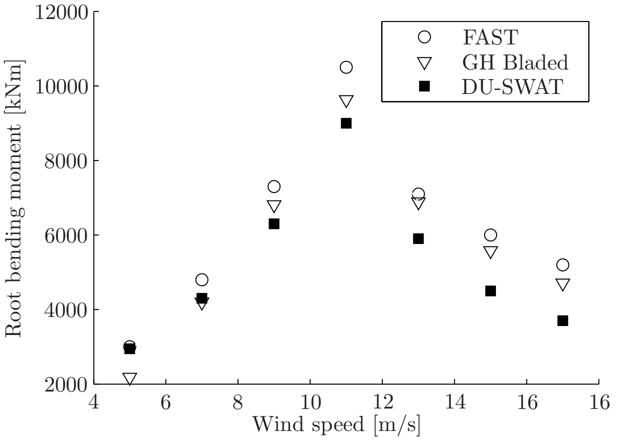

Figure 3.21: Root bending momment comparison between FAST, GH Bladed and the DU-SWAT

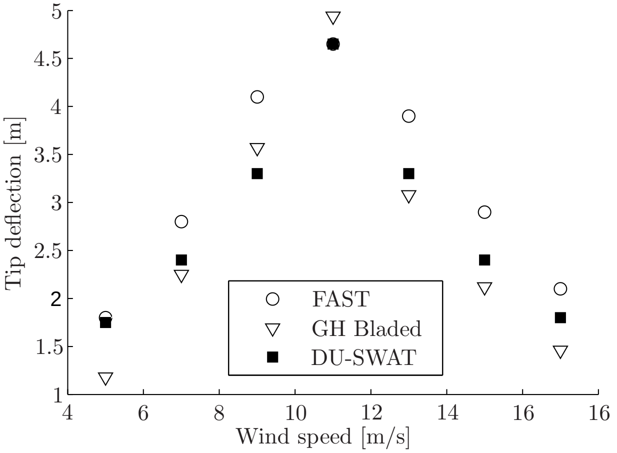

Figure 3.22: Tip deflection comparison between FAST, GH Bladed and the DU-SWAT

9%, respectively. This difference drops to 2% of the frequency value for the second edgewise eigenfrequency. In all cases, the frequencies obtained by FAST are lower than those from the analyses performed using GH Bladed and the DU-SWAT, when centrifugal forces are included, with a maximum difference of 11% for the second flapwise frequency. A similar level of accuracy was achieved for the modelling of the tower. In fact, the values of the presented code fall in between the results of GH Bladed and FAST for both fore-aft and side-to-side motion. The differences are in the order of 4% for the comparison with GH Bladed and about 10% for FAST. In the latter case, it needs to be realised that a rotating

Table 3.2: Eigenfrequencies of 5MW reference turbine

	GH Bladed	DU-SWAT	FAST (parked)
SS-Tower	0.27 Hz	0.28 Hz	0.31 Hz
FA-Tower	0.28 Hz	0.29 Hz	0.32 Hz
1st Flap	0.69 Hz	0.69 Hz	0.67 Hz
1st Edge	1.11 Hz	1.19 Hz	1.08 Hz
2nd Flap	2.06 Hz	2.26 Hz	2.02 Hz
2nd Edge	4.06 Hz	4.15 Hz	-

turbine may also slightly alter the tower eigenfrequencies.

Finally, the time history of root bending moment obtained from aeroelastic simulations performed with turbulent wind field as input are presented in Figures 3.23 and 3.24. The simulation was run at 7.0 m/s wind speed with a turbulence class of B, which corresponds to approximately a 15% turbulence level. A normal turbulence model (NTM) has been used, together with a Kaimal turbulence spectrum. The simulation length was set to 630 seconds, where the first 30 seconds where not taken into account in order to eliminate effects of the turbine start-up. Figures 3.23 and 3.24 show the Discrete Fourier Transform (DFT) of the flapwise and edgewise root bending moments from the simulations conducted with GH Bladed and the DU-SWAT. The first observation that can be made is that the vibration energy is concentrated in the low frequency part of the spectrum. This is a result of having a higher turbulence amplitude at frequencies below 2.0 Hz. When comparing the edgewise and the flapwise bending moment spectra, it can be seen that the eigenmodes are hardly damped in the edgewise case. This is found for the results of both GH Bladed and the DU-SWAT. The second observation is that the bending spectra agree very well, especially for the edgewise case. The observed eigenmodes from the two codes at 1.2 Hz, 4.2 Hz and 10.0 Hz, practically coincide both in amplitude and frequency in Figure 3.24. Also, the frequency of the 1P mode, found using both codes, is 0.2 Hz with a load amplitude of $1.5 \cdot 10^6$ Nm. GH Bladed and the DU-SWAT also predict a first eigenmode amplitude of $7 \cdot 10^4$ Nm at 0.7 Hz.

While structural damping is dominant in the case of edgewise deflections, the aerodynamic damping has a greater effect on flapwise motions. Gravitational loading, which causes a large peak in the edgewise bending moment distribution at 0.2 Hz, has a smaller impact on the flapwise bending moment spectrum. The corresponding peak can be seen at 0.2 Hz in Figure 3.23, with an amplitude of just below $2 \cdot 10^5$ Nm. Compared to the remainder of the spectrum in Figure 3.23, it will therefore not dominate the fatigue loading, especially since it occurs at low frequency. Similarly, the first eigenmode only makes a small contribution to the fatigue damage, as it occurs as a peak of $3 \cdot 10^4$ Nm at a frequency of 0.7 Hz, but peak is not very pronounced as a result of aerodynamic damping. It should be noted that the flapwise load spectra obtained by GH Bladed and the DU-SWAT coincide up to frequencies up to around 2.0 Hz. At higher frequencies, the load spectra diverge, with the spectrum of GH Bladed being lower meaning that it is more damped. This can be explained by considering that the aerodynamics of version 3.85 of GH Bladed are based on quasi-steady formulations that use lift curve data, whereas the presented code utilises unsteady aerodynamic formulations that lead to lower damping at high frequencies. Another observation that can be made is that the DU-SWAT captures also higher order modes at 2.0 Hz, 4.5 Hz and 9.0 Hz. However, those modes cannot be seen in the load spectrum obtained by GH Bladed.

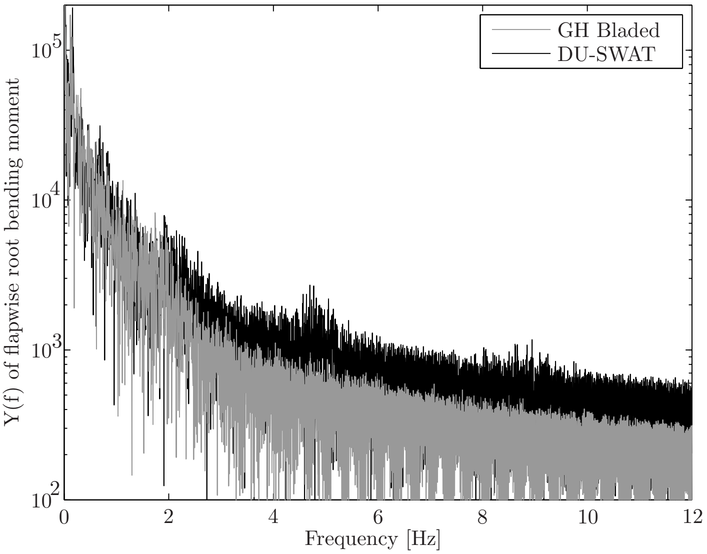

Figure 3.23: DFT of flapwise root bending moment

3.10 SYNOPSIS

A new wind turbine analysis code, the DU-SWAT, has been created. This code was developed with a focus on flap modelling and controller implementation. Standard software has been used to model any structural dynamics.

- A state-of-the-art aerodynamic modelling is used.
- This model provides highly accurate results when compared to CFD.
- Implementation in Simulink enhances the controller design possibilities.

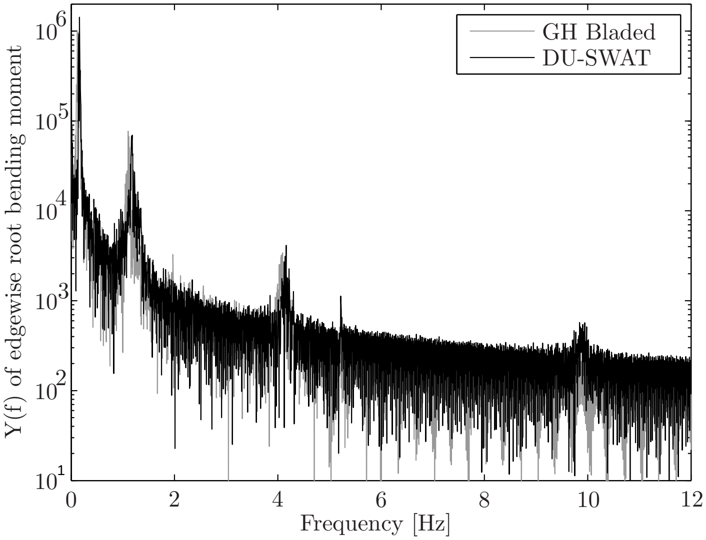

Figure 3.24: DFT of edgewise root bending moment

- Both steady and dynamic test cases provide comparable results with GH Bladed and FAST.

בישראל כדי להיות ריאליסט אתה חייב להאמין בניסים

In Israel, in order to be a realist you must believe in miracles.

David Ben-Gurion

4

Geometrically Non-Linear Modal Structural Dynamics

4.1 Introduction

The literature review in Chapter 2 has shown that while aerodynamic models have been developed for smart rotors, no efforts have been made to adapt structural models especially for smart rotors. Current concepts such as modal analysis find their limits, when local excitations of flaps or structural nonlinearities are important for the aeroelastic analysis. Another approach, which can take geometric nonlinearities into account, is constituted by beam models or multi-body formulations. However, both methods do not allow for accurate recovery of the stress field in the blades.

All of these issues are addressed in this chapter[1]. First, an overview of modelling techniques of non-linear structures is given. Then, a new, non-linear modal approach to model the structural dynamics is presented. Special attention is paid to local, impulsive excitation by using fictitious masses. The accuracy of the presented method is assessed by means of a numerical comparison with finite element results for a simple case and, finally, the application for the full wind turbine is discussed.

---

[1] This chapter is an adaptation of the journal paper 'Geometrically Non-Linear Structural Modal Analysis Using Fictitious Masses' by Bernhammer, De Breuker and Karpel (2015).

4.2 REVIEW OF MODELING APPROACHES FOR SLENDER STRUCTURES

Aeroelastic simulations of aircraft and wind turbines are time consuming, certainly when including geometric nonlinearities in a high fidelity structural model. Several software tools have been developed to model the blade structure using either multi-body formulations or beam models. One of the non-linear beam formulations is the intrinsic beam model. Hodges (2003) has first presented formulations that describe the strain-velocity relations. Inherently, beam models are one-dimensional models combined with cross-sectional properties. Asymptotic methods can be used to obtain the stiffness and mass properties of a cross-section of a slender beam (Cesnik and Hodges, 1997). Palacios obtained the cross-sectional properties based on a full linear finite element model (Palacios, 2011; Palacios et al., 2012), thereby matching the detail level from linear load models with non-linear beam models. As the formulations are strain based, the rotations and displacements which are needed for an aerodynamic analysis need to be retrieved. Quaternions allow tracing the deformation by integrating the strains along the beam axis (Palacios et al., 2012). The second approach is the flexible multi-body formulation, as incorporated in packages as MSC/Adams. Two different methods can be distinguished within multi-body codes, namely, codes employing flexible and rigid bodies. While rigid bodies are interconnected by springs, concentrating all displacements, they can only provide a very coarse structural solution. More advanced multi-body codes use elastic elements (Bachau, 2011). Mostly these simulations are based on energy formulations (Bachau, 2011). This chapter will present an alternative compact formulation, based on modal reduction, for a full geometrically non-linear aeroelastic simulation of a wind turbine.

The starting assumption is that the structural dynamics, for example of a wind turbine, can be separated into substructures such as the blades, the tower and the drive train. These substructures can be further broken down into segments, for which a modal reduction is carried out. The mode shapes and the generalised stiffness and mass matrices are then used as a basis for the aeroelastic analysis. Compatibility between two connected segments is established through displacement constraints applied to the rigid-body modes. The underlying assumption here is that large deformations and rotations are modelled by rigid-body modes in a co-rotational framework, while elastic modes serve as master coordinates for the deformations. Two intersegmental displacement compatibility types can be identified. The first one is a fixed connection, where the two sides of the connection have the same displacements and rotations. A geometrically non-linear formulation is provided in this chapter for this type of connection. An example would be the interface between multiple blade segments. The second type of connection allows relative rotational degrees of freedom between the segments. In the case of wind turbines, the pitch mechanism can be named. Selitrennik et al. (2012) provide formulations for a morphing wing-body structure with one rotational degree of freedom between the wing and body motions of an aircraft.

The structural model can be seen as a geometrically non-linear extension of the approach of Craig and Bampton (1968). Non-linear compatibility is introduced between the different segments through rotation matrices. Additionally, the modal basis is obtained using fictitious masses (Karpel and Raveh, 1996). This approach allows obtaining a set of rigid-body and elastic modes which are close to fixed-fixed condition in a single modal analysis, where all modes are orthogonal, so no orthogonalization procedure needs to be followed as in the case of the Craig-Bampton approach. The modal basis can be used as described in this chapter to model the dynamic structural response of a full wind turbine.

4.3 MODELLING ASPECTS

The modelling approach is an extension to a research campaign in which modal based formulations for geometrically non-linear structural dynamics were investigated. Selitrennik et al. (2012) have modelled morphing aircraft structures, using geometrically non-linear compatibility relations. This chapter describes the two types of connections that can connect segments with each other. A novel non-linear structural model describes in detail how fixed connections between two adjacent subsegments can be formulated, for example in the case of non-linear blade deformations, subsegments of the blade can be linked to each other. The second type of joints are morhping connections as described by Selitrennik et al. (2012).

The modelling process starts with a standard modal analysis for each segment, performed with large fictitious masses loading the boundary coordinates. The resulting modes and generalised matrices are used to perform the subsequent aeroelastic simulations. During the time-domain simulation, the compatibility is established between the segments in an iterative manner.

4.3.1 FICTITIOUS MASSES

For the modal analysis, each structural segment can be analysed individually and is integrated into the global turbine model through compatibility conditions for the boundary grid points of the segments. A full linear finite element model can be used, as will be shown in a numerical example, as a basis for such a modal reduction. For each segment the boundary grid points are defined and loaded by large fictitious masses. At each of these boundary points, two or more segments will be connected with each other. The applied fictitious masses are concentrated inertia terms that need to be large enough to introduce significant local deformations near the connecting grid points of each segment. As such, their magnitudes should be typically larger than the respective inertia of the segment under consideration, but not too large to avoid numerical ill-conditioning (Karpel and Presente, 1995). As the analysis is performed with free-free boundary conditions, rigid-body modes and elastic modes with significant local deformations are obtained. For subsequent aeroelastic analyses, the fictitious masses need to be removed from the generalised mass matrix by:

$$\bar{\mathbf{M}} = \bar{\mathbf{M}}_{\mathbf{f}} - \phi^T \mathbf{M}_{\mathbf{f}} \phi \tag{4.1}$$

where $\bar{\mathbf{M}}_{\mathbf{f}}$ is the generalised mass matrix of a segment with fictitious masses and $\mathbf{M}_{\mathbf{f}}$ has the same dimension as the full discrete mass matrix. Since only the boundary elements are loaded, the matrix containing the fictitious masses $\mathbf{M}_{\mathbf{f}}$ is non-zero only for the nodal locations of the fictitious mass. ϕ denotes the eigenvectors of the structure generated with fictitious masses. $\bar{\mathbf{M}}$ is the full generalised mass matrix of a segment to be used in the geometrically non-linear analysis. The diagonal generalised stiffness matrix is not affected by the removal of the fictitious masses.

4.3.2 EQUATION OF MOTION

The basic assumption is that the structural displacements are combinations of large rigid-body displacements and small elastic displacements. Large structural translations and rotations of each segment are modelled using rigid-body modes. The elastic modes, which can be used to analyze the strains and stresses of a given structure, are used to find small displacements in the local reference frame.

Rigid-body displacements are constrained to yield displacement compatibility between adjusting structural segments. The master-slave relation between elastic and rigid-body modes is expressed by means of a non-linear, time-dependent transformation matrix $\mathbf{T}$.

$$\xi = \left\{ \begin{array}{c} \xi_r \\ \xi_e \end{array} \right\} = \mathbf{T}\xi_e \tag{4.2}$$

where ξ is the full set of mode displacements, ξ_r are the displacements of the rigid-body modes and ξ_e the displacements of the elastic modes, as obtained with fictitious masses. $\mathbf{T}$ will be defined later for the case of fixed connections and the case of relative rotations between segments. As both mode amplitude and transformation matrix are time-dependent, the derivatives of Equation 4.2 are:

$$\dot{\xi} = \dot{\mathbf{T}}\xi_e + \mathbf{T}\dot{\xi}_e \tag{4.3}$$

and

$$\ddot{\xi} = \ddot{\mathbf{T}}\xi_e + 2\dot{\mathbf{T}}\dot{\xi}_e + \mathbf{T}\ddot{\xi}_e \tag{4.4}$$

Equations 4.2, 4.3 and 4.4 are used to express a reduced set of the modal equation of motion in state-space format:

$$\left\{ \begin{array}{c} \dot{\xi}_e \\ \ddot{\xi}_e \end{array} \right\} = \left[\begin{array}{cc} \mathbf{A} & \mathbf{B} \\ \mathbf{C} & \mathbf{D} \end{array} \right] \left\{ \begin{array}{c} \xi_e \\ \dot{\xi}_e \end{array} \right\} + \left\{ \begin{array}{c} \mathbf{0} \\ \left[\mathbf{T}^T\bar{\mathbf{M}}\mathbf{T}\right]^{-1}\mathbf{T}^T\phi^T\mathbf{F} \end{array} \right\} \tag{4.5}$$

with

$$\begin{aligned} \mathbf{A} = & \quad \mathbf{0} \\ \mathbf{B} = & \quad \mathbf{I} \\ \mathbf{C} = & -\left[\mathbf{T}^T\bar{\mathbf{M}}\mathbf{T}\right]^{-1}\left[\mathbf{T}^T\bar{\mathbf{M}}\ddot{\mathbf{T}} + \mathbf{T}^T\bar{\mathbf{K}}\mathbf{T}\right] \\ \mathbf{D} = & -\left[\mathbf{T}^T\bar{\mathbf{M}}\mathbf{T}\right]^{-1}\left[2\mathbf{T}^T\bar{\mathbf{M}}\dot{\mathbf{T}} + \mathbf{T}^T\bar{\mathbf{B}}\mathbf{T}\right] \end{aligned} \tag{4.6}$$

In Equation 4.5, $\bar{\mathbf{K}}$ and $\bar{\mathbf{B}}$ are the generalised stiffness and damping matrix. The terms $\mathbf{T}^T\bar{\mathbf{K}}\mathbf{T}$ and $\mathbf{T}^T\bar{\mathbf{B}}\mathbf{T}$ are diagonal matrices with the generalised stiffness and generalised damping of all segments on the diagonal. $\mathbf{F}$ is the vector of discrete time-dependent external and inter-segmental forces.

4.3.3 FIXED CONNECTIONS

Fixed connections are the centerpiece of the current analysis. They are used to rigidly connect the interface of two or more structural segments in a non-linear way. This type of connection is used to establish compatibility between adjacent blade or wing segments. First, the modes are separated into rigid-body modes and elastic modes. The rigid-body displacements are constraint to establish compatibility between segments. They serve as slave coordinates while the actual deformation is described by the elastic deformation. The relation between the modal amplitude of elastic and rigid-body modes is given by Equation 4.7:

$$\xi = \left\{ \begin{array}{c} \xi_{1r} \\ \xi_{1e} \\ \xi_{2r} \\ \xi_{2e} \\ \vdots \\ \xi_{nr} \\ \xi_{ne} \end{array} \right\} = \mathbf{T} \left\{ \begin{array}{c} \xi_{1e} \\ \xi_{2e} \\ \vdots \\ \xi_{ne} \end{array} \right\} \tag{4.7}$$

where the subscripts ir and ie denote the rigid-body and elastic modes of the i-th segment. The transformation matrix $\mathbf{T}$ is non-linear and time-dependent and will be constructed through compatibility relations. The fixed connection between two adjacent segments without any relative degrees of freedom implies the displacement compatibility:

$$\begin{Bmatrix} \xi_{ir} \\ \xi_{ie} \end{Bmatrix} = \begin{bmatrix} -\phi_{ir}^{-1}\phi_{ie} \\ \mathbf{I} \end{bmatrix} \xi_{ie} + \begin{Bmatrix} \phi_{ir}^{-1}\,\mathbf{R_{i,r}}\mathbf{u}_{i-1} \\ \mathbf{0} \end{Bmatrix} \tag{4.8}$$

where ϕ_{ir} and ϕ_{ie} are rigid-body and elastic modal displacements at the root of the i-th segment in local coordinates and $\mathbf{u}_{i-1}$ is a vector of translations and rotations of the boundary grid point of the previous segment in the global reference frame. The rotation matrix $\mathbf{R}$ converts displacements from the global reference frame to local coordinates. The boundary displacement vector can be obtained by:

$$\mathbf{u}_i = \mathbf{R_i^{-1}}\phi_{i,end}\mathbf{T}_i \begin{Bmatrix} \xi_{1e} \\ \vdots \\ \xi_{ie} \end{Bmatrix} \tag{4.9}$$

Equation 4.9 is given in the global coordinate system. $\mathbf{T}_i$ denotes the transformation matrix up to the segment which is considered. As the overall transformation matrix is non-linear and time-dependent, it needs to be constructed at each time step, starting at a known displacement condition. The analysis is carried out sequentially to find the global transformation matrix, starting from a segment with a known displacement. In the presented equations of motion, the structure is clamped at the root of the first segment. Theoretically, it would not be needed to introduce any rigid-body motion for the first segment if the modal reduction of the root segment was carried out with a clamped and a free end. Combining Equations 4.8 to 4.9 allows to assemble the transformation matrix specified in Equation 4.5:

$$\mathbf{T} = \begin{bmatrix} -\phi_{1r}^{-1}\phi_{1e} & \mathbf{0} & & \mathbf{0} \\ \mathbf{I} & \mathbf{0} & \cdots & \mathbf{0} \\ \tilde{\mathbf{T}}_1 & -\phi_{2r}^{-1}\phi_{2e} & & \mathbf{0} \\ \mathbf{0} & \mathbf{I} & & \mathbf{0} \\ & \vdots & \ddots & \\ [& \tilde{\mathbf{T}}_{n-1} &] & -\phi_{nr}^{-1}\phi_{ne} \\ \mathbf{0} & \mathbf{0} & \mathbf{0} & \mathbf{I} \end{bmatrix} \tag{4.10}$$

where

$$\tilde{\mathbf{T}}_i = \phi_{i+1,r}^{-1}\mathbf{R_i}\mathbf{R_{i-1}^{-1}}\phi_{n-1,end}\mathbf{G}_i\mathbf{T}_i$$

with

$$\mathbf{R_0} = \mathbf{I}$$
$$\mathbf{G}_i = \begin{bmatrix} \mathbf{0} & \cdots & \mathbf{0} & \mathbf{I} \end{bmatrix}$$

The matrix $\mathbf{G}_i$ ensures that only the displacement vector of the previous segment is used when establishing the compatibility condition. As the modal analysis is carried out in a local reference frame, a last step is needed to transform the structural displacements to the displacements in the global coordinate systems, $\mathbf{u}_{i,gl}$. In the local coordinate system the nodal locations of the deformed structure can be obtained by adding the modal deformations to the location vector of the nodes of the FEM model. As given in Equation 4.11, the inverse of the rotation matrix converts the local displacements into the global frame of reference.

$$\mathbf{u}_{i,gl} = \mathbf{R_i}^{-1} \left[\mathbf{r}_{undef,i} + \phi_i \left\{ \begin{array}{c} \xi_{ir} \\ \xi_{ie} \end{array} \right\} \right] \tag{4.11}$$

4.3.4 ROTATION MATRICES IN A CO-ROTATIONAL FRAMEWORK

The non-linear compatibility has been assessed except for the rotation matrix that needs to be used to convert the displacements from the global coordinate system to the body-attached reference frame. The formulation of rotations is one of the key problems in formulating geometrically non-linear structural models using a co-rotational framework. In this dissertation the rotational vector approach is followed (Battini, 2008) as described in Section 3.2.1 and a definition of the rotation matrix $\mathbf{R_{sub}}$ can be found in Equation 3.5. As forces, moments, rotations and displacements need to be transformed into the new reference frame, the full rotation matrix to be used per segment is given by:

$$\mathbf{R} = \begin{bmatrix} \mathbf{R_{sub}} & \mathbf{0} \\ \mathbf{0} & \mathbf{R_{sub}} \end{bmatrix} \tag{4.12}$$

While moments are passed from segment to each consecutive segment, the rotation is set to zero at the root of every segment. To ensure this condition, an additional rotation matrix is added such that rotations can be subtracted.

$$\mathbf{R_{rot}} = \begin{bmatrix} \mathbf{0} & \mathbf{0} \\ \mathbf{0} & \mathbf{R_{sub}} \end{bmatrix} \tag{4.13}$$

The non-linear transformation can thus be obtained by:

$$\mathbf{u}_{i-1,l} = \mathbf{R_i}\mathbf{u}_{i-1,g} - \mathbf{R_{rot,i}}\mathbf{u}_{i-1,g} \tag{4.14}$$

where the subscript l denotes the local coordinate system and g denotes the global coordinate system. This allows constructing a second transformation matrix $\mathbf{T}_2$ identical to $\mathbf{T}$ as given in Equation 4.10, except that all rotation matrices $\mathbf{R}$ are replaced by $\mathbf{R_{rot}}$. These are included in the second order equations of motion in modal coordinates, which become:

$$\begin{aligned} &\mathbf{T}^T\bar{\mathbf{M}}\left(\ddot{\mathbf{T}}\xi_e + 2\dot{\mathbf{T}}\dot{\xi}_2 + \mathbf{T}\ddot{\xi}_e - \ddot{\mathbf{T}}_2\xi_e - 2\dot{\mathbf{T}}_2\dot{\xi}_e - \mathbf{T}_2\ddot{\xi}_e\right) \\ &\quad +\mathbf{T}^T\bar{\mathbf{B}}\left(\dot{\mathbf{T}}\xi_e + \mathbf{T}\dot{\xi}_e - \dot{\mathbf{T}}_2\xi_e - \mathbf{T}_2\dot{\xi}_e\right) \\ &\quad +\mathbf{T}^T\bar{\mathbf{K}}\left(\mathbf{T} - \mathbf{T}_2\right)\xi_e = \mathbf{T}^T\phi^T\mathbf{F} \end{aligned} \tag{4.15}$$

The terms including $\mathbf{T}_2$ are brought to the right-hand side of the state-space Equation 4.5, which yields

$$\begin{aligned} \left\{\begin{array}{c} \dot{\xi}_e \\ \ddot{\xi}_e \end{array}\right\} &= \left[\begin{array}{cc} \mathbf{A} & \mathbf{B} \\ \mathbf{C} & \mathbf{D} \end{array}\right]\left\{\begin{array}{c} \xi_e \\ \dot{\xi}_e \end{array}\right\} \\ &+\left\{\begin{array}{c} \mathbf{0} \\ \left[\mathbf{T}^T\bar{\mathbf{M}}\mathbf{T}\right]^{-1}\mathbf{T}^T\phi^T\mathbf{F} + \mathbf{T}^T\bar{\mathbf{M}}\left(\ddot{\mathbf{T}}_2\xi_e - 2\dot{\mathbf{T}}_2\dot{\xi}_e - \mathbf{T}_2\ddot{\xi}_e\right) \end{array}\right\} \\ &+\left\{\begin{array}{c} \mathbf{0} \\ \mathbf{T}^T\bar{\mathbf{B}}\left(\dot{\mathbf{T}}_2\xi_e + \mathbf{T}_2\dot{\xi}_e\right) + \mathbf{T}^T\bar{\mathbf{K}}\mathbf{T}_2\xi_e \end{array}\right\} \end{aligned} \tag{4.16}$$

4.3.5 JOINTS

The formulation of joint connections between segments is an extension of the formulation for fixed connections. While in the case of fixed connections as described before, one segment is connected to a previous segment, in the case of a joint, a segment has multiple follower segments. The different follower segments are independent of each other and only attached through compatibility conditions at the joint. A classical example of such a connection is the hub of a wind turbine. It connects multiple blades to one shaft. The compatibility condition for each follower segment with respect to the master segment remains unaltered as described in Equation 4.8. However the transformation matrix that expresses the relation between the deformation of different segments needs to be modified. Up to the joint, the formulation given in Equation 4.10 stays unaltered. After the joint, multiple rows with the same entries in the first positions are created as shown in Equation 4.17.

$$\mathbf{T}_{joint} = \begin{bmatrix} -\phi_{1r}^{-1}\phi_{1e} & \mathbf{0} & & \mathbf{0} & \mathbf{0} \\ \mathbf{I} & \mathbf{0} & \cdots & \mathbf{0} & \mathbf{0} \\ \tilde{\mathbf{T}}_1 & -\phi_{2r}^{-1}\phi_{2e} & & \mathbf{0} & \mathbf{0} \\ \mathbf{0} & \mathbf{I} & & \mathbf{0} & \\ & \vdots & \ddots & & \\ [& \tilde{\mathbf{T}}_j &] & -\phi_{s1,r}^{-1}\phi_{s1,e} & \mathbf{0} \\ \mathbf{0} & \mathbf{0} & \mathbf{0} & \mathbf{I} & \mathbf{0} \\ [& \tilde{\mathbf{T}}_j &] & -\phi_{s2,r}^{-1}\phi_{s2,e} & \\ \mathbf{0} & \mathbf{0} & \mathbf{0} & \mathbf{0} & \mathbf{I} \end{bmatrix} \tag{4.17}$$

where the index j denotes the master segment before the joint and the indices $s1$ and $s2$ the follower segments after the joint. This can be easily extended to joints with more than two follower elements. If the slave segment has follower segments itself, the previously describes procedure holds and compatibility is just established with respect to the respective master segment.

4.3.6 MORPHING CONNECTIONS

Multiple morphing connections can be found in engineering applications. An example is the pitch mechanism in wind turbine blades. Contrary to fixed connections, morphing connections allow for rotational degrees of freedom. This modifies Equation 4.8, which yields

$$\begin{Bmatrix} \xi_{ir} \\ \xi_{ie} \end{Bmatrix} = \begin{bmatrix} \text{-}\phi_{ir}^{-1}\phi_{ie} \\ \mathbf{I} \end{bmatrix} \xi_{ie} + \begin{Bmatrix} \phi_{ir}^{-1} \ \mathbf{R_m R_i u}_{i-1} \\ \mathbf{0} \end{Bmatrix} + \begin{Bmatrix} \phi_{ir}^{-1}\boldsymbol{\Omega} \\ \mathbf{0} \end{Bmatrix} \tag{4.18}$$

where $\mathbf{R_m}$ is the associated rotation matrix defined in the local reference frame and $\boldsymbol{\Omega}$ is the displacement vector of the morphing connection.

$$\boldsymbol{\Omega} = \begin{Bmatrix} 0 \\ 0 \\ 0 \\ \varphi_1 \\ \varphi_2 \\ \varphi_3 \end{Bmatrix} \tag{4.19}$$

The variable φ_i denotes the rotations about the principle axes of the body-attached coordinate system of the current segment. These rotation angles are typically given as functions of time. As the morphing rotations do not depend on the elastic modes, Equation 4.7 is expanded to include the morphing degrees of freedom

$$\xi = \mathbf{T}\left\{\begin{array}{c} \xi_{1e} \\ \xi_{2e} \\ \vdots \\ \xi_{ne} \end{array}\right\} + \left\{\begin{array}{c} \phi_{11}^{-1}\boldsymbol{\Omega}_1 \\ \mathbf{0} \\ \phi_{21}^{-1}\boldsymbol{\Omega}_2 \\ \mathbf{0} \\ \vdots \\ \phi_{n1}^{-1}\boldsymbol{\Omega}_n \\ \mathbf{0} \end{array}\right\} = \mathbf{T}_{total}\left\{\begin{array}{c} \xi_{1e} \\ \xi_{2e} \\ \vdots \\ \xi_{ne} \\ \boldsymbol{\Omega}_1 \\ \boldsymbol{\Omega}_2 \\ \vdots \\ \boldsymbol{\Omega}_n \end{array}\right\} \tag{4.20}$$

where $\mathbf{T}_{total}$ is the transformation matrix $\mathbf{T}$, expanded to include the $\boldsymbol{\Omega}$ related terms. This formulation allows simple application of consecutive morphing connections, by repetitively applying Equation 4.18.

4.3.7 APPLIED FORCES

Since Equation 4.16 is expressed in modal coordinates defined in the local reference frame for each segment, the applied forces in $\mathbf{F}$ should be defined in the respective frames. This inherently renders the application of external forces as follower forces, which is very convenient for example for aeroelastic analyses where the lift and drag forces of a given section are defined with respect to the local coordinate system. Forces that are defined in the global coordinate system should be transformed to local coordinates using the rotation matrices presented in the previous sections.

During simulations with large structural rotations, inertial and gravitational forces play an important role. As modal formulations are used, both need special attention.

The generalised inertial forces included in $\bar{\mathbf{M}}$ in Equation 4.16 do not account for the discrete acceleration terms resulting from the rotation of the local coordinate systems. Hence, the associated inertial forces should be included in the applied force vector $\mathbf{F}$. Selitrennik et al. (2012) identified the missing inertial force terms. The inertial force terms applied to each mass point is

$$\mathbf{f}_\omega = -\mathbf{m}\frac{d\omega}{dt} \times \mathbf{r} - 2\mathbf{m}\omega \times \frac{d\mathbf{r}}{dt} - \mathbf{m}\omega \times (\omega \times \mathbf{r}) \tag{4.21}$$

where ω is the relative angular velocity vector and $\mathbf{r}$ is the location vector of the masses of the finite element model in the rotating frame. The three terms in Equation 4.21 are Euler, Coriolis and centrifugal forces. The assumptions underlying the modal approach eliminate the centrifugal forces $\mathbf{m}\frac{d\omega}{dt} \times \mathbf{r}$, whereas these assumptions do not affect the Euler forces $\mathbf{m}\omega \times (\omega \times \mathbf{r})$. The Euler forces are intrinsically included in the formulation. The Coriolis forces $2\mathbf{m}\omega \times \frac{d\mathbf{r}}{dt}$ are small for wind turbine structural dynamics and can thus be neglected. Selitrennik et al. (2012) suggest to re-introduce the centrifugal forces through an applied force vector. The angular vector can be directly obtained from the mode velocities given in Equation 4.3.

Some forces are expressed in different coordinate systems. An example of such forces are gravitational forces, which are naturally defined in the global reference frame. Therefore they need to be converted to the respective local reference frames through the rotation matrices. In these reference frames, the forces can be generalised and included in the equations of motion.

$$\mathbf{f}_g = \phi^T \mathbf{R}\mathbf{g}\left(\Psi_1, \Psi_2, \Psi_3\right)\mathbf{m}\phi \tag{4.22}$$

where $\mathbf{g}$ is the gravitational vector, $\mathbf{m}$ is the lumped nodal mass and $\mathbf{R}$ the local rotation matrix. The gravity vector depends on the orientation of the segment in time.

4.3.8 DAMPING

The common approach to include damping into the equations of motion in generalised coordinates uses a diagonal damping matrix, where the damping values are typically about 2% of the critical modal damping coefficient $B_c = 2m\omega_n$. The variables m and ω_n are the generalised mass and the natural frequency of the respective mode. However, when generalised coordinates are based on the modes generated with fictitious masses, the assignment of a diagonal damping matrix $\bar{\mathbf{B}}$ in the matrix $\mathbf{D}$ of Equation 4.7 would effectively cause coupling forces between the natural modes. Hence, it is necessary to define $\bar{\mathbf{B}}$ such that it is effectively diagonal, namely causing no coupling forces when the fictitious masses are removed by Equation 4.1 (Karpel and Presente, 1995). The process starts with solving the generalised-coordinate eigenvalue problem with the fictitious masses removed,

$$\bar{\mathbf{K}}\mathbf{\Phi} = \bar{\mathbf{M}}\mathbf{\Phi}\bar{\omega_{\mathbf{n}}}^{\mathbf{2}} \tag{4.23}$$

where $\mathbf{\Phi}$ is the eigenvector matrix and $\bar{\omega_{\mathbf{n}}}$ is a diagonal matrix with the eigenfrequencies of the system. The generalised equation of motion could be expressed in the new modal coordinates as

$$\mathbf{\Phi}^T\bar{\mathbf{M}}\mathbf{\Phi}\ddot{\xi_d} + \mathbf{\Phi}^T\bar{\mathbf{B}}\mathbf{\Phi}\dot{\xi_d} + \mathbf{\Phi}^T\bar{\mathbf{K}}\mathbf{\Phi}\xi_d = \mathbf{\Phi}^T\phi^T\mathbf{F} \tag{4.24}$$

While the generalised mass and stiffness terms in Equation 4.24 are diagonal due to the orthogonal modes, $\bar{B}$ is still to be set such that the generalised damping matrix will be also diagonal and of the standard form

$$\boldsymbol{\Phi}^T\bar{\mathbf{B}}\boldsymbol{\Phi} = 2\boldsymbol{\Phi}^T\bar{\mathbf{M}}\Phi\bar{\zeta}\bar{\omega_{\mathbf{n}}} \tag{4.25}$$

where $\bar{\zeta}$ is the assigned diagonal non-dimensional damping matrix associated with the modal coordinates of Equation 4.24. It is easy to show that in order to obtain Equation 4.25, $\bar{\mathbf{B}}$ should be

$$\bar{\mathbf{B}} = 2\bar{\mathbf{M}}\boldsymbol{\Phi}\bar{\zeta}\left[\boldsymbol{\Phi}^T\bar{\mathbf{M}}\boldsymbol{\Phi}\right]^{-1}\bar{\omega_{\mathbf{n}}}\boldsymbol{\Phi}^T\bar{\mathbf{M}} \tag{4.26}$$

4.3.9 NUMERICAL SOLVER

The following summarises the terms of the non-linear state-space equation (Equation 4.16) for cases of fixed connections between the structural segments. It is based on segmental normal modes generated with fictitious masses at the interface coordinates and expressed in local coordinate systems. The state-space matrices, defined in Equation 4.7, include the transformation matrix $\mathbf{T}$ that assures interface displacement compatibility. An additional transformation matrix $\mathbf{T}_2$, described after Equation 4.9, defines the geometric nonlinearities associated with large rotations. The matrix $\mathbf{T}_2$ is included in the forcing vector of Equation 4.16. The discrete external forces, expressed in the local coordinate, are also included in $\mathbf{F}$. In addition to specific excitation forces, $\mathbf{F}$ should also include the rotational inertial forces of Equation 4.21 and the gravitational forces of Equation 4.22, when applicable.

In the numerical examples presented in this paper, the equation of motion as presented in Equation 4.16 is solved using Simulink. The 'ode23s stiff/mod. Rosenbrock' algorithm is used for time integration with a variable step size determined by the solving algorithm and a relative tolerance of 0.01%. Every time step, the transformation matrix $\mathbf{T}$ is built starting at root condition. The boundary grid point displacement at the segment interfaces is computed. A check is carried out if the rotation angles are within -180 and 180 degrees with respect to the global reference frame. If not the values are corrected by substracting or adding 360 degrees. The resulting rotation vector is used to compute the rotation matrix $\mathbf{R}$, which is then used for the following segment. This procedure is repeated until the tip of the structure is reached and the full transformation matrix T is obtained. The time derivatives of $\mathbf{T}$ are obtained through numerical differentiation. As shown in Equation 4.16, the transformation matrix is used to compute the state-space matrix at a given time step. The time derivatives of the state vector are numerically integrated, using a Simulink integrator block for continuous time integration. The resulting state vector at time $t + 1$ serves as input to function evaluation at the next time step.

4.4 NUMERICAL EXAMPLE: A UNIFORM BEAM

The previously outlined method is applied to a test case to estimate its accuracy and demonstrate convergence for multiple segments. For the presented analysis, a uniform cantilever I-beam is considered. The properties of this beam are given in Table 4.1.

Table 4.1: Beam properties

Web and flange thickness	2 cm
Web height	40 cm
Flange width	20 cm
Elastic modulus	70 GPa
Poisson's ratio	0.3
Density	2600 kg/m^3
Beam length	30 m

All structural segments of the test case have been modelled in MSC/Nastran using shell elements and a reference line coinciding with the centroid of the cross-section has been added to be used as comparison in the non-linear simulation. The model has been loaded with fictitious masses at both ends with a diagonal mass matrix consisting of $10^5 kg$ entries for translational and $10^4 kgm^2$ for rotational degrees of freedom. This model has been created with varying segment lengths, such that it can be divided into two, three, four, five, six, eight and ten segments. The full finite element model was used for verification of the results. The cross-section in the full beam model is equivalent to the one in the segment models. The static solution and transient linear simulations were obtained using MSC/Nastran, while the static and dynamic non-linear simulations have been performed with Abaqus. Non-linear static simulations have been performed with and without follower loads and compared to the modal based solution. Figure 4.1 shows the mesh and the boundary conditions (root clamp) of the Nastran model. Figure 4.2 provides a close-up of how the forces are introduced into the structure. The total load is split and is applied at the intersection of the flanges and the web. This is done in order to prevent any twist and to ensure planar deformations.

4.4.1 LINEAR VERIFICATION

As a first test case, the presented method is benchmarked against the linear static and dynamic results of the full finite element model. The rotation matrices

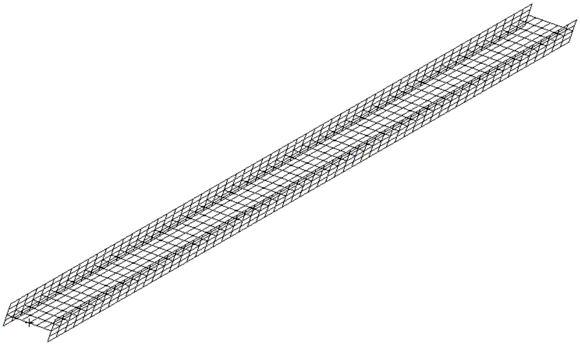

Figure 4.1: Nastran model to obtain linear and non-linear displacements

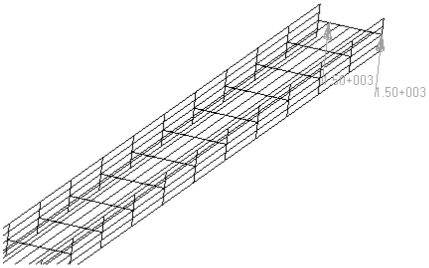

Figure 4.2: Zoom in to Nastran model and applied forces

$\mathbf{R}$ and $\mathbf{R_{rot}}$ as defined in Equations 4.12 and 4.13 are replaced by an identity matrix and a matrix only containing zero entries to eliminate the non-linear effects in the simulation. For both static and dynamic analysis, a time integration of Equation 4.16 was used. The damped out solution is used as a static comparison. High structural damping coefficients are used to enforce quick convergence of the dynamic simulation to the static results. Figure 4.3 displays the results due to an applied tip force. One can see that the analytical solution and the solution of the presented approach practically coincide. As a comparison Figure 4.3 also includes the non-linear solution with the load not following the tip deflection obtained by MSC/Nastran, but remaining in the global coordinate system. The difference between the analytical solution and the results of the mode shape based analysis is less than 0.1%.

Figure 4.4 shows the comparison of the linear time-domain simulation in MSC/Nastran (transient response) and the presented method, both for a step

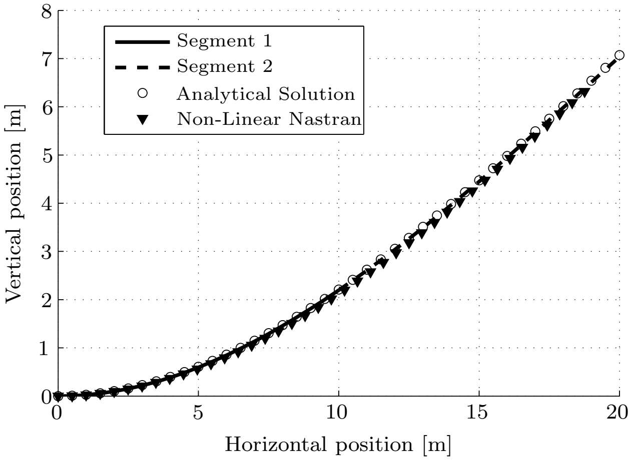

Figure 4.3: Linear static analytical solution vs modal simulation, two segments

input in force at t = 0. Again, the curves correspond very well to each other. Errors are less than 0.1% between two corresponding sets of data points. For the dynamic simulation Rayleigh stiffness proportional damping was used. The advantage is that the same damping matrix can be used also in the non-linear case, whereas modal mass proportional damping as presented in section 4.3.8 cannot conveniently be used in non-linear finite element analysis.

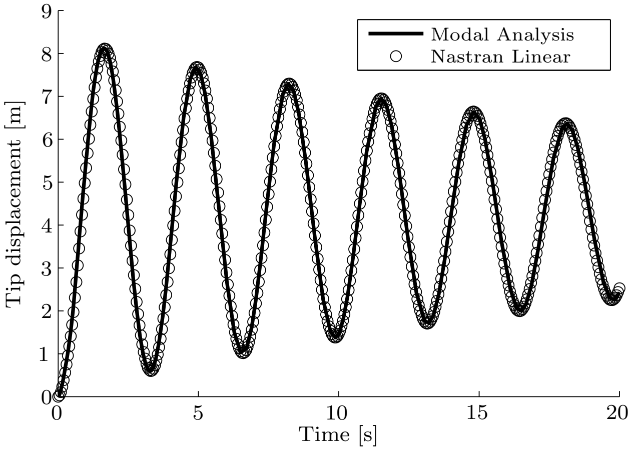

Figure 4.4: Linear simulation, Nastran vs Modal simulation: Response to step in tip load

4.4.2 NON-LINEAR STATIC VERIFICATION

As the linear modal solutions accurately reproduce the results of the linear finite element analysis, the non-linear static behavior can be evaluated in the next step. The dynamic analysis has been run including the non-linear rotation matrices until convergence to reproduce the static non-linear results obtained by Abaqus. The main objective of this chapter was to present a method that offers a compact formulation for non-linear dynamic solutions with a significant reduction in computation time compared to finite element simulations. The static solution for the Abaqus model takes about two minutes CPU time. Running a dynamic simulation with heavy damping to obtain a static solution with the presented method with two segments only takes in the order of 10 seconds. This is a speed increase of a factor of 12. Increasing the number of segments, will also increase the computational time significantly. A solution with ten segments for a strongly non-linear simulation case approaches the same CPU time as the Abaqus simulation.

Figures 4.5 and 4.6 show the results for a simulation with two segments. The continuous curve is the computed deformation using the non-linear modal approach. The figures illustrate the displacement due to a tip force of 2000 N and 5000 N, respectively. Both loads are modelled as follower forces in the local reference frame. In total four static, non-linear, full finite element simulations have been performed: A tip force of 2000 N and 5000 N both with the load as follower force and with the tip force in the global coordinate system. The dots represent the linear, analytical solution. Already for two segments, non-linear effects can be captured by the model. A clear shortening of the non-linear modal solution can be observed compared to the linear solution. While for two segments at a load of 2000 N, the error in tip deflection between the Abaqus model with the force modelled as follower force and the mode based solution is about 1.5%, the differences increase for highly non-linear deformations as shown in Figure 4.6, where the error increases to more than 13%.

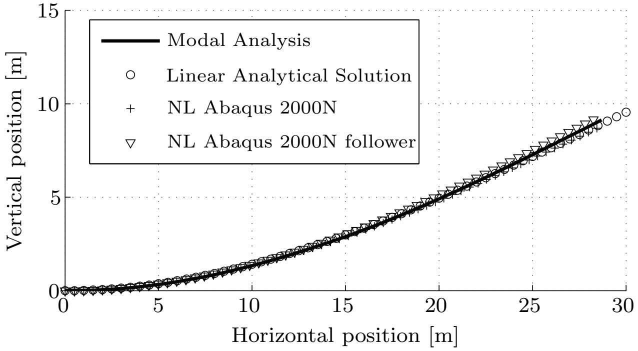

Figure 4.5: Static displacement 2000 N, two segments

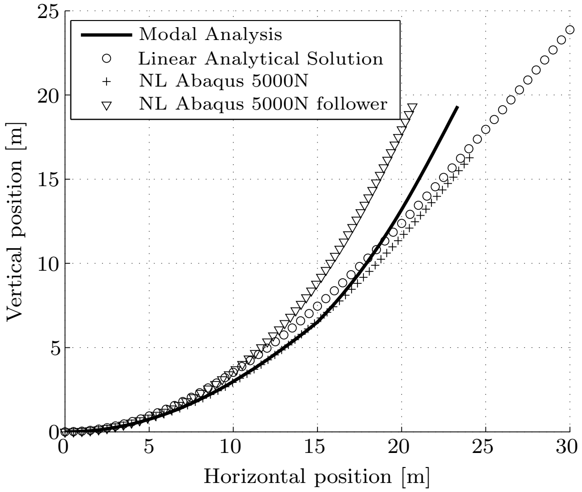

Figure 4.6: Static displacement 5000 N, two segments

To improve the accuracy of the non-linear structural modal model, the number of segments was increased to three. Figures 4.7 and 4.8 both show a strong improvement in terms of accuracy. The error for 2000 N with 25% tip deflection is in the order of 0.5%; and for the high load of 5000 N the error in tip deflection is 5%. The deflection curve is matched more accurately for both load cases. One can conclude that for weakly non-linear problems already two segments are sufficient and for highly non-linear problems of tip deflections up to 60-70% three segments are sufficient to model the beam-like structure with good accuracy.

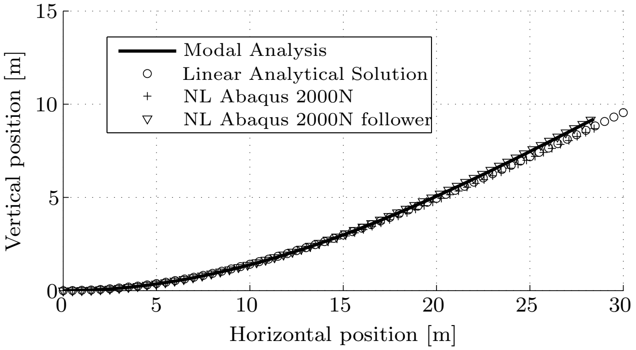

Figure 4.7: Static displacement 2000 N, three segments

Figure 4.9 displays an extension of the applicability range of the model. As an example, the rolling-up of the beam with an increasing tip moment is considered. At least five segments are needed to model a full circle, because the assumption

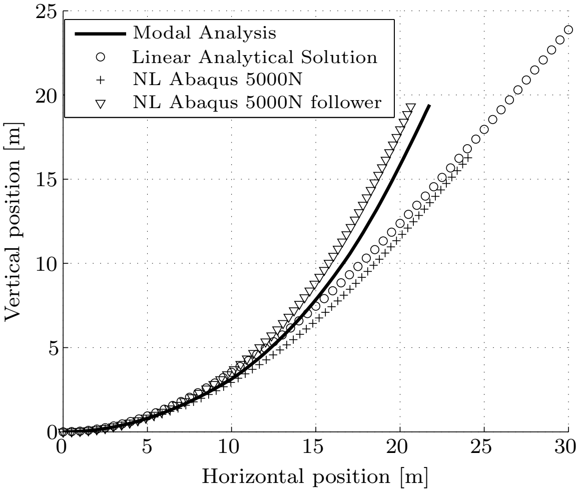

Figure 4.8: Static displacement 5000 N, three segments

of linearity for local deformations implies that rotation angles of 90 degrees and more cannot be reached for each segment. The result of the simulation with ten segments is displayed in Figure 4.9. Each curve corresponds to the static results due to an applied tip moment increasing from 50,000 Nm to 400,000 Nm in steps of 50,000 Nm. For ten linear segments, the beam can be completely rolled-up such that its tip touches the root.

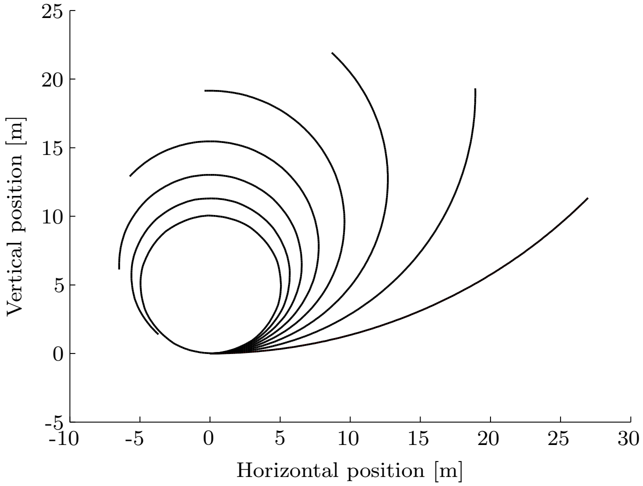

Figure 4.9: Static deflection curves for beam with tip moments from 50,000 Nm to 400,000 Nm and 10 segments

4.4.3 DYNAMIC NON-LINEAR VERIFICATION

Two simulations were performed for a non-linear dynamic comparison: a moderate step in tip force of 1000 N and a high step of 2000 N. Figures 4.10 and 4.11 display the time history of tip deflections for the step in tip force of 1000 N. Figure 4.11 shows the vertical deflection as a function of time. The simulations for both two or three segments closely approximate the deflection amplitude. The frequency of the two-segment analysis is less accurately captured with an error of about 3% compared to the finite element solution. Increasing the number of segments from two to three, improves the simulation as it reduces the frequency difference between the co-rotational framework approach and the non-linear finite element simulation. The reason for the difference in frequency can be found in Figure 4.10, which displays the horizontal tip displacement of the beam due to large deflections. Both two and three segments manage to capture the tip shortening effect, however the accuracy of the approach using two segments still needs to be improved by increasing the number of segments in the simulation. Whilst the finite element simulation gives a shortening of 1.7m, the simulations with two and three segments only shows a reduction of 1.2m and 1.5m, respectively. Increasing the number of segments further improves the prediction of the tip displacement and the frequency of the response.

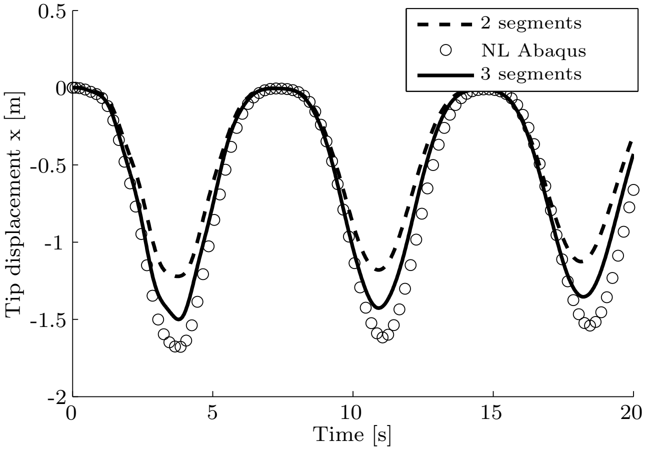

Figure 4.10: Horizontal tip displacement for a step tip force of 1000 N

Figures 4.12 and 4.13 show the results of the same simulation with a step in tip force of 2000 N. As expected the nonlinearities are significantly stronger. The maximum tip deflection approaches more than 60% of the beam length. Especially the simulation using three segments approximates the amplitude of the vertical displacement of the finite element simulation, while the model using two segments overpredicts the amplitude slightly. The vibration frequency is shifted to a higher

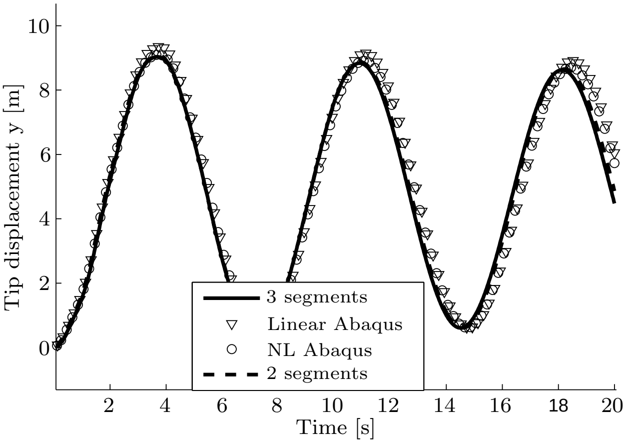

Figure 4.11: Vertical tip displacement for a step tip force of 1000 N

value, but increasing the number of segments in the co-rotational framework reduces this difference. The two-segment solution overpredicts the stiffening effect on the frequency by a factor of 2.0 compared to the finite element solution. Increasing the number of segments to three already decreases this difference to a factor of 1.7. An undesirable side effect also becomes visible. The solution using three segments produces higher harmonic oscillations, which are damped out after one cycle. These are particularly visible in Figure 4.12. The reason for those vibrations is the excitation by a step in tip force. A step excites all frequencies of a structure. In the finite element model, due to the large number of nodes, the excitation is more distributed and higher frequency modes are damped faster. In the non-linear structural modal analysis, the vibration is introduced mainly in the first two bending modes, which therefore show a higher response. Still, the presented new method captures the beam shortening, even for higher vibration amplitudes.

4.4.4 CONVERGENCE

A static solution was obtained using the modal based approach with two to ten structural segments. Figure 4.14 and Figure 4.15 show the convergence of the tip displacement and the vibration frequency, respectively. For a static tip loading of 2000 N, already two segments give a solution with less than 3% error compared to the finite element solution. When increasing the number of segments, the solution converges quickly to an accuracy that is adequate for most engineering purposes. Four segments already give a solution within less than 0.5% error compared to the Abaqus solution for tip displacments of more 30% of the beam length. The error for the high load case with 5000 N is higher and converges slower. Two segments

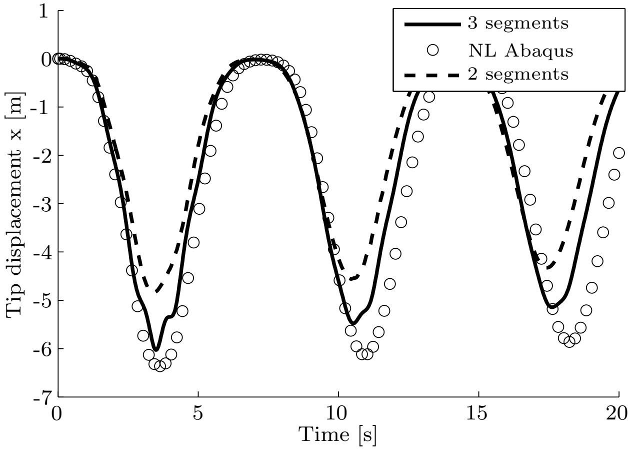

Figure 4.12: Horizontal tip displacement for a step tip force of 2000 N

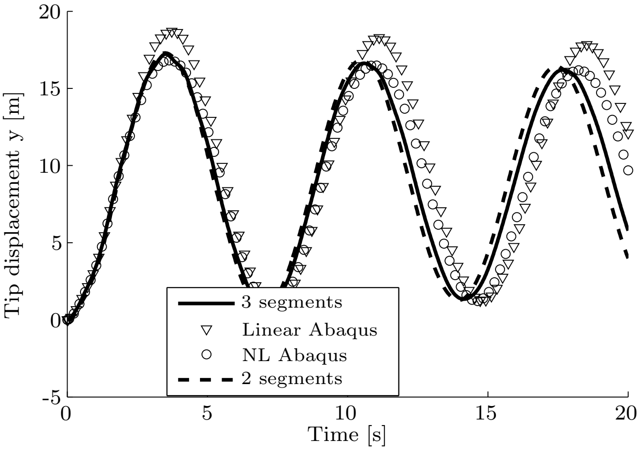

Figure 4.13: Vertical tip displacement for a step tip force of 2000 N

only give a very poor representation and produce an error of 13% in terms of tip deflection. When increasing the number of segments, the solution significantly improves and passes the 5% error margin for four segments. When doubling the number of segments again to eight, the error in tip deflection is as small as 2%. This value is sufficient for most aeroelastic analysis types.

The geometric nonlinearities introduce a stiffening effect that causes the oscillation frequency to shift from 0.1323 Hz for the linear solution to 0.1396 Hz in case of the non-linear Abaqus solution. Both cases are determined with a 2000 N step force applied. Due to this large step, the displacement significantly ex-

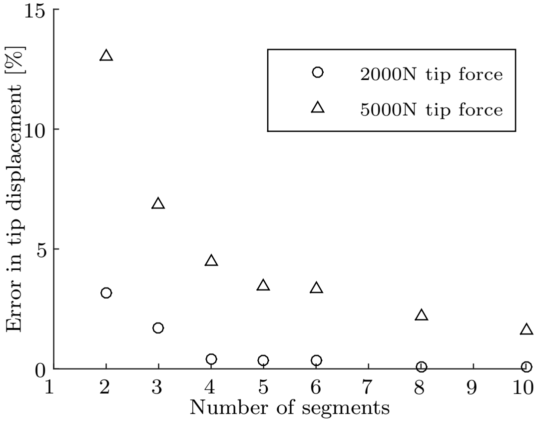

Figure 4.14: Error in tip displacement vs number of elements

ceeds the static solution and reaches maximum tip displacements of more than 55%, thereby introducing strong nonlinearities in the solution. As displayed in Figure 4.13, simulations with both two and three segments overpredict this stiffening effect by a factor of almost 2.0 and 1.7, respectively. When increasing the number of segments, this overprediction reduces and is only 17% for eight segments and 13% for ten elements, resulting in a vibration frequency of 0.1408 Hz compared to 0.1396 Hz as in the non-linear Abaqus solution.

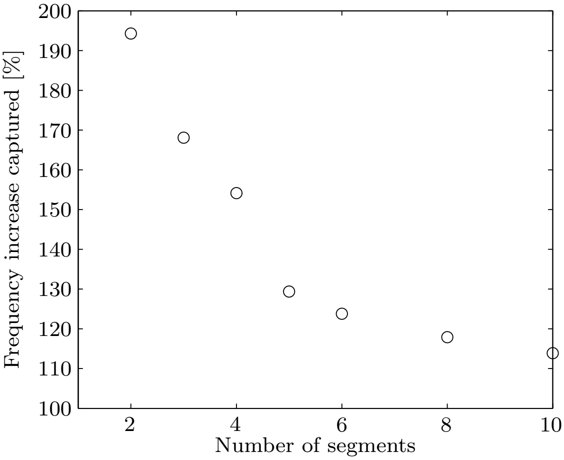

Figure 4.15: Captured non-linear stiffening effect vs number of elements

4.5 APPLICATION TO WIND TURBINES

4.5.1 BLADE AND TOWER MODEL

To show the applicability of the model to wind turbines, a linear finite element model of the NREL 5MW reference turbine is considered as a second numerical example. Based on publicly available cross-sectional data (Jonkman et al., 2009), the cross-sectional lay-out is approximated for the blade and tower in a finite element model. For that purpose the cross-section is divided into a girder section, the web, and three skin sections. From a database of material properties, the ideal configuration is determined to match the stiffness and the mass distribution. Figure 4.16 shows the resulting distributions compared to the properties of the reference turbine. Especially for the flapwise bending stiffness, an excellent approximation is achieved, a fact that can be attributed to a heavier weighting of the flapwise stiffness in the objective function. The edgewise stiffness is also approximated well. One should notice that from the root up to 10 m span, a slightly softer cross-section is modelled. The torsional stiffness is the least accurately approximated; the torsional rigidity is significantly higher than that of the reference turbine. As most deformations of a wind turbine are dominated by edgewise and flapwise deflections, a blade that is more rigid in torsion does not alter the simulation results significantly. A modal analysis has been carried out for this finite element model. Table 4.2 shows the comparison of the blade eigenfrequencies of the full linear finite element model and the reference solutions obtained by Adams and MSC/Nastran (Jonkman et al., 2009). As can be seen, the eigenfrequencies of the flapwise bending modes are closely matched with an error of 1.6% and 2.0% for the 1st and the 2nd flapwise bending mode. As the edgewise stiffness is slightly lower in the finite element model, the modal frequency for edgewise modes is lower than that of the reference turbine.

Table 4.2: Eigenfrequencies reference rotor blade

Mode	FEM model	Ref. Adams	Ref. FAST
1^{st} flapwise	0.71 Hz	0.70 Hz	0.70 Hz
1^{st} edgewise	1.01 Hz	1.08 Hz	1.07 Hz
2^{nd} flapwise	1.92 Hz	2.02 Hz	1.96 Hz

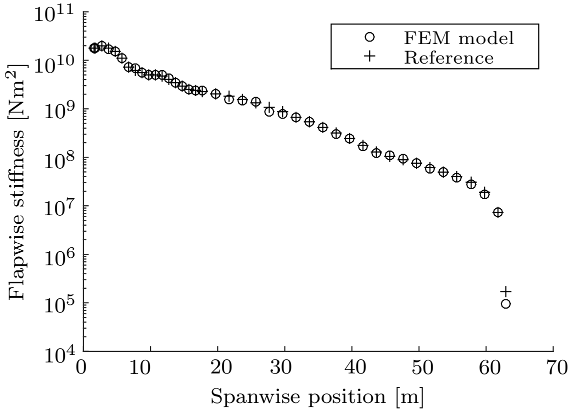

(a) Flapwise stiffness

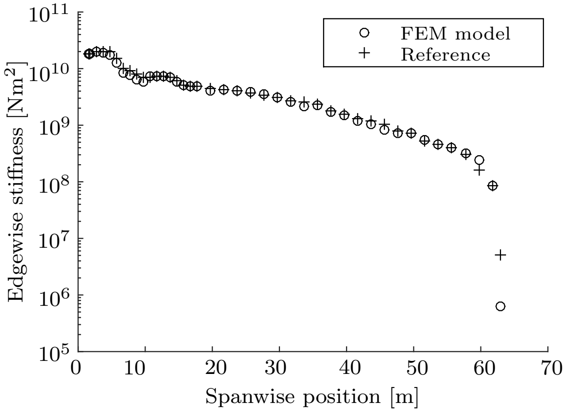

(b) Edgewise stiffness

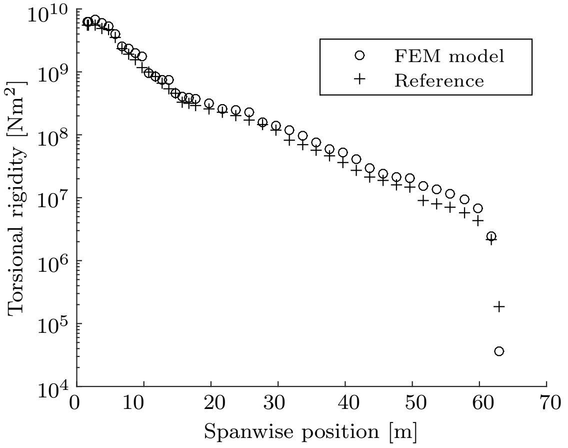

(c) Torsional rigidity

Figure 4.16: Stiffness distribution FEM model vs NREL reference turbine

4.5.2 APPLICATION TO WIND TURBINE AEROELASTIC SIMULATION

For an aeroelastic analysis using the framework presented in this chapter, a turbine can be broken down into five different substructures: the tower, the drive train and three blades. The full turbine model is shown in Figure 4.17 with the blade model as described above. A simple tower model of a tapered cylindrical beam has been modelled according to the stiffness and mass distribution of the NREL 5 MW turbine. To allow rotor rotation and pitch, morphing connections are included to introduce pitch and azimuth variations. Additionally a cone angle of 5 degrees is applied matching the description of the NREL reference turbine. This turbine system can also be easily extended to study the structural dynamics of a yawing turbine or a floating turbine, but for the presented study these degrees of freedom have not been modelled.

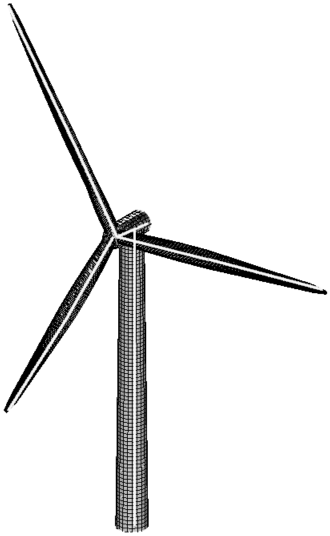

Figure 4.17: Finite element model of the NREL 5MW reference turbine

Rotor blades are most responsive to aerodynamic forces. During certain loading conditions, the blades might display geometrically non-linear effects, certainly when considering downwind turbines. In order to capture these nonlinearities, it was chosen to divide the blade into subsegments as shown in Figure 4.18. The blade is broken into two segments. For each segment a structural backbone is defined. The end points of the backbone are loaded with fictitious masses with mass entries for all translational and rotational degrees of freedom. Along the backbone a set of 20 nodes is defined, which are used to track the structural motion and to generalise the applied aerodynamic forces. Each node is connected by an RBE3 element to the nodes of the closest cross-section. RBE3 elements are interpolation elements, which describe the displacement of a slave node as a weighted average of the displacements of master nodes.

Figure 4.18: Blade Finite Element Model with segments indicated

The same procedure has been executed for the tower. The modal analysis was carried out segment per segment and the fictitious masses have been removed from the generalised mass matrices. For the presented structural dynamics analysis, seven elastic modes per segment have been taken into account. For the blade these modes are the first four flapwise bending modes, two edgewise bending modes and a torsional mode. The procedure to construct the non-linear compatibility matrix, $\mathbf{T}$, has been followed. Morphing degrees of freedom are the rotation of the blade and the cone angle the rotor forms. While the azimuth angle of the turbine is time-dependent and a function of the rotor angular speed, the cone angle is constantly 5 degree. For the aeroelastic analysis, loads have been obtained by a blade element method. The aerodynamic loads have been calculated in the DU-SWAT (Bernhammer et al., 2012; Bernhammer, De Breuker, van Kuik, Berg and van Wingerden, 2013). Neither wind shear nor turbulence are included when obtaining the loads. The time history of the aerodynamics have been calculated for wind speeds from 5.0 m/s to 17.0 m/s. These loads are applied on the geometrical non-linear structural model together with the force vector containing the gravitational and missing inertial terms as specified in Equations 4.21 and 4.22. An analysis with simplified load cases has shown that the deformations obtained with a single segment along the blade are sufficient as the displacements and rotations on the reference turbine are small. The obtained load cases have been simulated with the geometrically non-linear wind turbine model. Figure 4.19 shows the tip displacement as a function of wind speed for different wind turbine analysis tools. While both FAST and GH Bladed use linear structural formulations, the DU-SWAT exploits geometric nonlinearities by using a multi-body formulation with rigid elements and linear interconnecting springs. First of all, one can conclude that the presented method fits well within the deformations obtained by the three other codes. Especially good agreement is reached when comparing the current approach with the DU-SWAT and GH Bladed. The agreement with FAST is poorer, however the reason should not be sought in the structural dynamics, but in the aerodynamic formulations, as FAST shows a higher thrust level of the turbine as compared with the other codes (Barlas, 2011). This increase in thrust translates into an increase in tip deflection. The maximum error compared with the DU-SWAT is 6%. This difference might seems very big at first, however one should note that the DU-SWAT solves a coupled aeroelastic problem, while the modal simulation does not iterate the forces depending on the structural deformation.

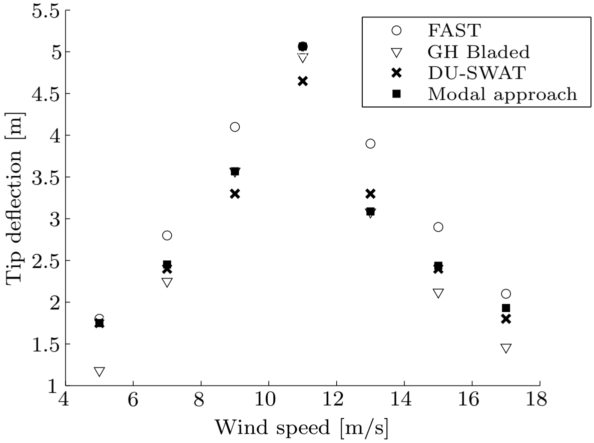

Figure 4.19: Tip displacement of the NREL 5 MW turbine, code comparison

One of the major benefits of modal formulations is that the simulations are carried out starting from the full three-dimensional model. The modal reduction is easily inverted and strains of the full blade can directly be obtained. Figure 4.20 displays the strain distribution of the windward and the leeward sides of the turbine blade when passing at an azimuth angle of 0 degree. Light shades of gray represent tensile strains, while dark shades correspond to compressive strains. One can see that the aerodynamic forces cause the entire blade to bend such that the windward side experiences tensile strain, while the leeward side is compressed. Stress concentrations are found at the double curved transition from the cylindrical root section to the airfoils at the 10 m span location. At this location, the skin of the wind turbine blade is already a lot thinner compared to the root section, such that the difference in bending stiffness is a factor of 4, while the flapwise bending moment does not change as much. Beyond this position the curvature of the beam is rather uniform as the stiffness distribution matches the bending moment distribution. Therefore, the strain level from 20 m to 50 m is rather constant before it decreases towards the tip.

As a final step, a dynamic load case was evaluated, namely a step in load from

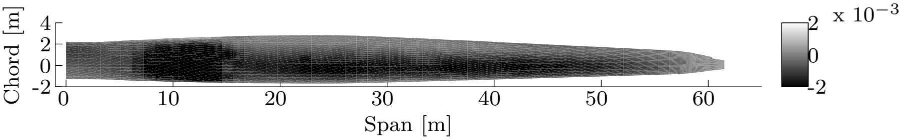

(a) 0 degree azimuth leeward side

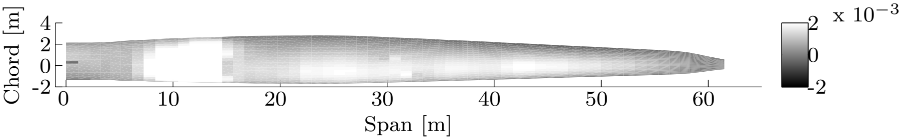

(b) 0 degree azimuth windward side

Figure 4.20: Strains in blade at different azimuth angles

the loads at 11.0 m/s as used before to 1.2 times this load. One would expect that this should trigger especially the first blade flapwise mode. The structural response to this step change in loading is shown in Figure 4.21. The step is initialised at 7.0 seconds. The step can be clearly seen in the structural response. Damping in this simulation, as in all other simulations was Rayleigh stiffness proportional damping with a coefficient of 0.03. The dominating vibration frequency of the structure is 0.7 Hz, which corresponds to the first eigenfrequency of the blade. One should notice that the structural response is distorted by the rotor blade passing through the gravitational field, reducing the tip deflection at 0 degree azimuth and increasing it for 180 degrees azimuth.

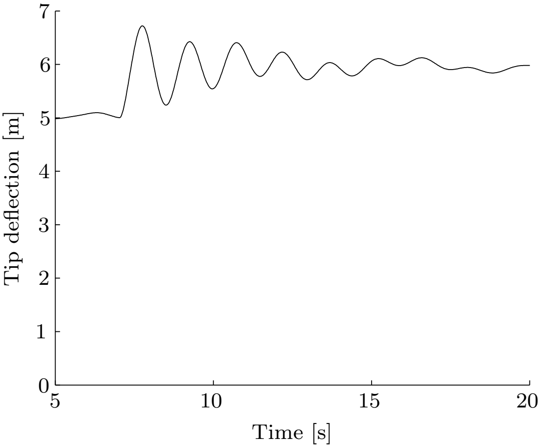

Figure 4.21: Step response of tip displacement due to load increase

4.5.3 GEOMETRICALLY NON-LINEAR BLADE DEFORMATION

While the tip displacements of the NREL 5MW turbine are far below 10% of the blade span and therefore too small to provoke significant geometric nonlinearities, an additional load case was constructed to demonstrate the non-linear modelling potential of the approach. The blade section geometry and stiffness distribution is unaltered with respect to the previous calculations, however, the applied load is reduced to a single out of plane tip force. This tip force is increased from 20,000 N to 200,000 N in steps of 20,000 N. Figure 4.22 shows the comparison between tip displacement of the blade modelled with one and two beam segments. The flapwise tip displacement is displayed versus the displacement along the beam span. While the amplitude of the deflections are not noticably influenced by the nonlinearity, the beam shows a significant non-linear shortening effect with increasing load amplitude. The explanation of this phenomenon can be found in Figure 4.23. In the non-linear model, the forces act as follower force, thereby increasing the amplitude of the tip deflection. This is manifested in the higher rotation angles that can be found at the blade tip in the non-linear case as compared to the linear analysis (one segment). Opposing this effect is the shortening of the blade in the non-linear case as compared to the linear analysis. The total blade length increases when undergoing very high deflections. The geometrically non-linear analysis does not exhibit the same lengthening effect, as large displacements and rotations are computed through rigid-body modes and non-linear compatibility. The blade span therefore does not increase by the same amount.

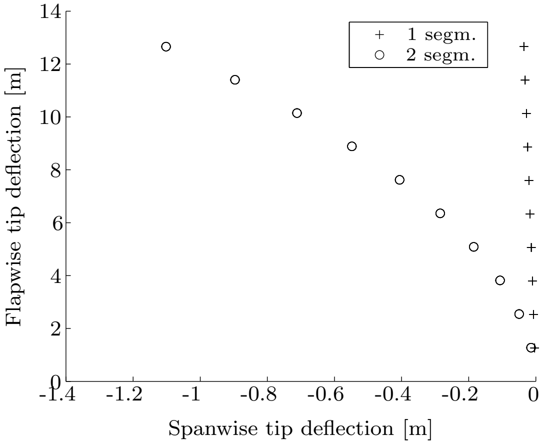

Figure 4.22: Tip motion due to tip force

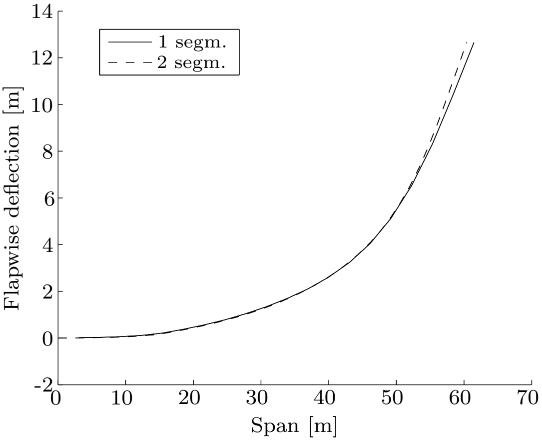

Figure 4.23: Deformation shape with tip load of 200,000 N

4.6 SYNOPSIS

In this chapter, a compact method to describe the structural dynamics of a wind turbine has been formulated based on modal reduction. The modal approach allows limiting the structural degrees of freedom to a minimum without losing accuracy in the solution.

- A structure can be broken into multiple segments. For each segment a modal analysis is performed.
- Each segment interface should be loaded by fictitious masses as they improve the deformation accuracy near the interface.
- The structure is assembled using non-linear compatibility conditions. Rigid-body modes are used to introduce large displacements.
- Typical geometric structural nonlinearities for wind energy or aeronautical applications can be accurately captured with few segments.
- Non-linearities of a slender structure with 30% tip deflection can be matched with 1% error with only three segments.
- For the 5MW reference turbine, structural nonlinearities are of minor importance.

You have to be fast on your feet and adaptive or else a strategy is useless.
Charles de Gaulle

5

DU-SWAT VALIDATION USING SANDIA NATIONAL LABORATORIES SMART ROTOR

5.1 INTRODUCTION

While the aeroelastic response of conventional wind turbines as obtained by the DU-SWAT have been compared with GH Bladed and FAST in Chapter 3, such a comparison is not possible for smart rotors as FAST and Bladed are not designed for such simulations. The Sandia National Laboratories Smart Rotor provides the possibility to physically validate the simulation results of the DU-SWAT, which is done in this chapter[1].

First, the Sandia National Laboratories (SNL) Smart Rotor experiment is presented. In a next step, load spectra of the numerical simulation and the experiment are compared. Then a time-domain analysis is performed and the response of the SNL rotor is compared to the numerical prediction of the blade strain, the

---

[1] This chapter is an adaptation of the conference paper 'Model Validation and Simulated Fatigue Load Alleviation of SNL Smart Rotor Experiment' (Bernhammer, De Breuker, van Kuik, Berg and van Wingerden, 2013) combined with the conference paper 'Aeroelastic Time-Domain Simulation of SNL Smart Rotor Experiment' (Bernhammer, De Breuker and van Kuik, 2015*a*).

hub accelerations and the power production due to step inputs in flap deflection. Finally, a controller is designed and it is shown how flaps can be used for load alleviation on smart rotors.

5.2 SANDIA NATIONAL LABORATORIES SMART ROTOR

The research overview given in Chapter 2 underlined the potential of the smart rotor to alleviate fatigue loads, but more experimental results of full-scale turbines are needed to validate the simulation results. The efforts of Delft University of Technology with a 2 m diameter proof-of-concept have been a first step towards such a validation (Barlas, van Wingerden, Hulskamp, van Kuik, Verhaegen and Bersee, 2010; Hulskamp et al., 2010; van Wingerden et al., 2010). The logical following step was to test the system on a representative turbine in terms of size and frequency. For this purpose, Sandia National Laboratories has designed and built a 115kW test turbine equipped with three individually controllable flaps on every blade. This wind turbine was the first turbine with this feature that is field tested. Information about the design, fabrication and integration has been presented by Berg et al. (2011, 2012). At the time of construction this turbine was the only utility scale smart rotor. Since then a turbine of the same size, a Vestas V27, has been updated by Vestas in collaboration with the Danish Technical University (Castaignet et al., 2014), by equipping one of the three blades with a 70 cm long flap corresponding to 5% of the blade span.

The flapped rotor designed and built by Sandia National Laboratories was tested on the SNL turbine located on the USDA-ARS site in Bushland, Texas, USA. As shown in Figure 5.1, the test turbine is a three-bladed, fixed-pitch, upwind Micon 65/13 turbine with modifications to the brakes, gearbox, generator, and blades. The rotor diameter is 20 m. The generator is rated at 115 kW and operates at 1200 rpm while the rotor turns at a nominal 55 rpm (the standard Micon 65/13 rotates at 45 rpm).

The surrounding terrain is essentially flat. Upwind of the turbine is a meteorological tower instrumented with cup anemometers at hub height (23 meters), rotor top, rotor bottom, and 2.0 m above ground level. In addition to the cup anemometers, a wind vane and ATI sonic anemometer are installed at hub height. The anemometry is located approximately 30.7 m upwind of the turbine, or roughly 1.7 rotor diameters in front of the turbine.

As detailed by Berg et al. (2011, 2012), the blades are modified versions of the CX-100 design (Berry, 2008). These 9 m blades are internally instrumented with accelerometers, fiber optic strain, fiber optic temperature, and metal foil strain gauges. The active flaps extend 20% of the chord length and roughly 20% of the blade span (starting at 7.0 m span and extending 1.83 m). Before the rotor was

Figure 5.1: SNL Smart Rotor Test Turbine

installed, each blade was characterised with three ground tests:

1. Blade pulls in flapwise and edgewise direction with the blade cantilevered to the test stand
2. Modal test with the blade cantilevered to the test stand
3. Modal test with the blade suspended in free-free boundary condition

After the rotor was installed, the flaps were actuated with various motions to excite structural dynamics while the rotor was parked. These motions consisted of sinusoidal oscillations at discrete frequencies, sinusoidal oscillations with logarithmic sweep of frequency, and step motions with amplitudes from 0 degree to 20 degrees. Finally, these flap actuations were repeated while the rotor was turning and producing power.

5.3 LOAD SPECTRA

In a first step, the aeroelastic model of the turbine has been investigated based on the transfer function from the flap angle to the blade root bending moments. Numerically this has been done through model linearisation in the DU-SWAT (Chapter 3), while the Sandia National Laboratories Smart Rotor Experiment has been investigated using a frequency sweep of the flaps.

Some modifications have been made in the numerical model compared to the SNL Smart Rotor. While the SNL Rotor has rigid flaps that rotate around a hinge axis, the flaps have been modelled as deformable trailing edges as described in Chapter 3 with a smooth transition being implemented between the undeformed airfoil and the flap to prevent flow separation. The flap angles have been set such that at the trailing edge, the flap angles of both systems are identical. The result is a slightly lower control authority on the lift coefficient.

5.3.1 NUMERICAL MODEL LINEARISATION

As a first step, the system has been linearised to obtain the numerical aeroelastic model. This has been done by adding a perturbation introduced by flap deflections to the steady state of the system. The linearisation has been done for wind speeds of 8.0 m/s. Figure 5.2 shows the Bode plots of the linearised system from flap deflection angle to blade tip deflection. The two upper plots represent the magnitude and the phase of the flapwise deflection, whereas the lower two plots correspond to the magnitude and the phase of the edgewise deflection. Periodic components are filtered out. The first resonance in the uppermost plot of Figure 5.2 occurs at 4.5 Hz for the flapwise displacement. This corresponds very well with the measurements of Sandia that obtained a first frequency at 4.4 Hz (Berg, Barone and Yoder, 2014). One can see that the elevation is relatively wide and aerodynamically strongly damped. Next to this elevation, there is a peak, at 5.7 Hz. This peak originates from edgewise motion as can be seen in the third plot of Figure 5.2. In contrast to the flapwise deflection, where motions are strongly aerodynamically damped, this type of damping does not occur for edgewise deflections. Consequently, the peak is very high, even compared to the flapwise deflections. It should be stressed that modal damping with a coefficient of 0.03 was used in the simulations and that the damping parameters can only be seen as an estimation of the damping of the real turbine. The damping was not tuned to fit the experimental results, but rather a typical value for aerospace applications was used.

5.3.2 EXPERIMENTAL FREQUENCY SWEEP

The linearisation results have been compared to the measured results of a frequency sweep of flap activity in the rotor during when producing power. Figure 5.3 shows the spectral density of the flapwise tip accelerations due to a frequency sweep of the flaps between 0.1 Hz and 6.0 Hz for the SNL rotor. This increase starts at t = 600 seconds and continues until t = 1100 seconds. Red colour in Figure 5.3 corresponds to high tip accelerations, while blue shows a low acceleration power density. A wide resonance peak can be seen centered around the first eigenmode at 4.4 Hz, while a sharp, second resonance is found between

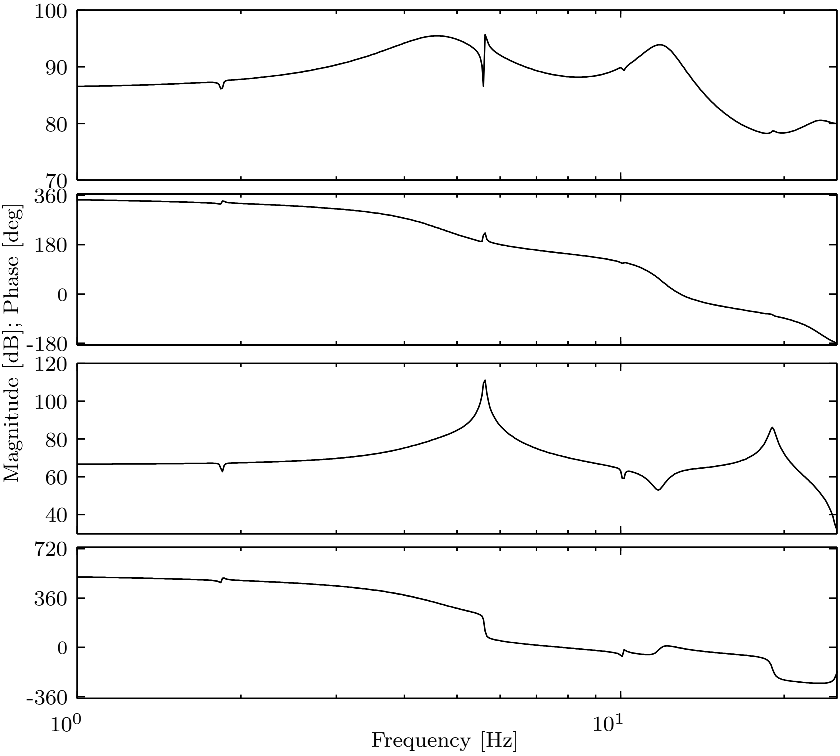

Figure 5.2: Bode plot of system: Magnitude (1st plot) and phase (2nd plot) of flapwise and Magnitude (3rd plot) and phase (4th plot) of edgewise tip deflection as a result of flap deflection

18.0 and 19.0 Hz. This compares well with the numerically obtained eigenfrequencies, which the DU-SWAT predicts to be 11.0 Hz for the second eigenfrequency in flapwise direction and 18.0 Hz for the second eigenfrequency in edgewise direction. It is expected that the weakly damped second edgewise mode is captured by the accelerometers of the SNL rotor.

In a second step, the blade tip accelerations of the numerical model are compared to the ones of the SNL test turbine as shown in Figure 5.4. The first observation is that the power spectral density of the test turbine is a lot smoother compared to the numerical simulation without control. This can be attributed to a simulation time of 100 seconds. It is assumed that the PSD will smoothen out when the simulation runs for a longer time interval. The second observation is that the numerically obtained curve corresponds well with the power spectral density of the experiment. The experimental curve peaks at a similar amplitude and frequency as the numerically obtained curve. Especially between 1.0 Hz and 10.0 Hz, the simulation and the experiment provide excellent agreement in terms of power spectral density.

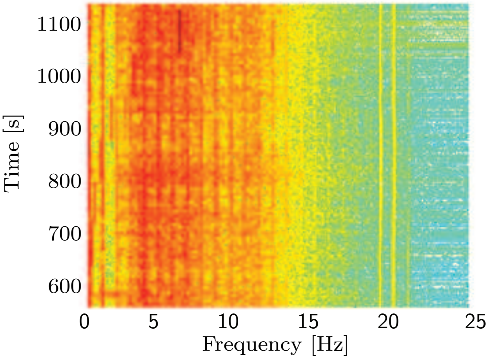

Figure 5.3: Tip acceleration response to periodic flap excitation of SNL rotor: Frequency steps from 0.1 Hz (t = 600s) to 6.0 Hz (t = 1100 s), red corresponds to a high acceleration amplitude, blue to low accelerations

At higher frequencies both power spectral densities decrease towards values of -30.0 dB/Hz or -40.0 dB/Hz. The numerical simulation shows a more pronounced second resonance frequency around 12.0 Hz. In contrast to that, the second eigenfrequency of the experiment does not find its way into the power spectral density in such a pronounced manner. The response at the second eigenfrequency is about 15.0 dB/Hz lower than the one of the first eigenfrequency, rendering the first eigenfrequency most critical to the fatigue loading.

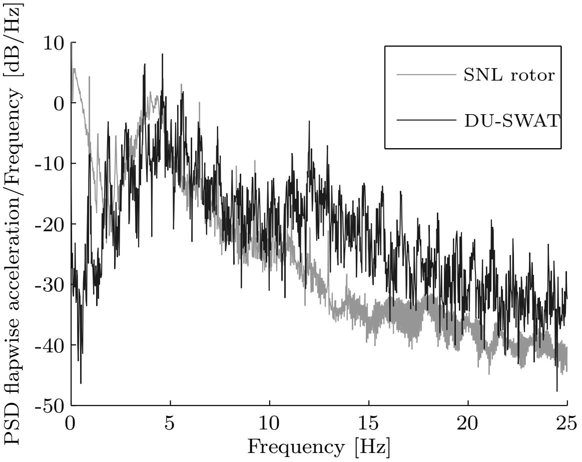

Figure 5.4: Power spectral density of local flapwise acceleration

Significant differences in the behaviour of the plots can be observed for frequencies below 1.0 Hz. While the experimentally obtained signal is perturbed by measurement noise and low frequency fluctuations in inflow velocity, the numerical simulation does not reproduce the low frequency content of the PSD diagram. Both curves show strong resonance for 1P at 0.9 Hz. A comparison of amplitudes is however difficult, as the amplitude shift might be attributed to low frequency noise of the sensor. The amplitudes for 2P and 3P of the experiment and the simulation are comparing a lot better being -6.4 dB/Hz and -3.3 dB/Hz for the SNL test rotor, while the numerical simulation results are -4.5 dB/Hz and -3.4 dB/Hz for 2P and 3P, respectively.

5.4 AEROELASTIC RESPONSE OF THE SMART ROTOR

In the next step, the aeroelastic response of the Sandia National Laboratories Smart Rotor has been analyzed using static and time-domain simulations. The static cases have been analysed using fixed flap deflections, while in the time-domain simulations step changes in the flap deflection angle were used. Strains in the blade, the turbine power and the accelerations of the tower top have been measured on the experimental rotor. The simulation results are compared to averaged measurements of the test turbine.

The most relevant difference between numerical simulation and experiment lies in the inflow conditions. Naturally, the SNL smart rotor experiments have been subject to wind fluctuations and turbulence over the rotor area. By repetitively performing the measurements and averaging of the responses, turbulence effects of the rotor response have been eliminated. For that purpose, 29 individual measurement series of 30 seconds each were taken for each step in flap deflection (Berg, Barone and Yoder, 2014). All measurement series of each step amplitude were summed independent of their average wind speed and divided by the number of repetitive measurement series. In this process, the initialisation of the flap deflection was always synchronised at 0 seconds. This way a 'mean flap response hidden beneath the stochastic wind excitation' (Berg, Barone and Yoder, 2014) was computed. One should note that this mean response only is an approximation of the exact rotor response, as this averaging approach cannot take any nonlinearities into account. In the numerical simulation a time-invariant wind field including wind shear, but no yaw, has been used such that turbulence does not pollute the numerical data.

5.4.1 COMPARISON OF BLADE LOADS FOR STATIC BLADE DEFLECTION

The numerical simulation and the smart rotor experiment are compared by investigating the static effect of smart rotors. Figure 5.5 shows the measured and numerically computed strains on the pressure side of the turbine blades at 75% of their span. While the rotor experiments have been performed between 4.0 m/s and 10.0 m/s (Berg, Barone and Yoder, 2014), the numerical analysis limits itself to wind speeds above 6.0 m/s. This decision has been made as the experimental data of wind speeds of 4.0 m/s are highly inconsistent and show strain fluctuations of more than 100% for slight changes in wind speed or flap angle.

The curves showing the strain responses for different wind speeds with 0 degree flap angle serve as a benchmark. The curves for simulation and measurements are practically identical. Only a slight variation occurs close to 10.0 m/s. Both experiment and simulation show a linear behavior with wind speed. This linearity stems from the almost linear relation between wind speed and local angle of attack at the outboard sections (Berg, Resor, Paquette and White, 2014) as the rotational speed is kept constant during power production.

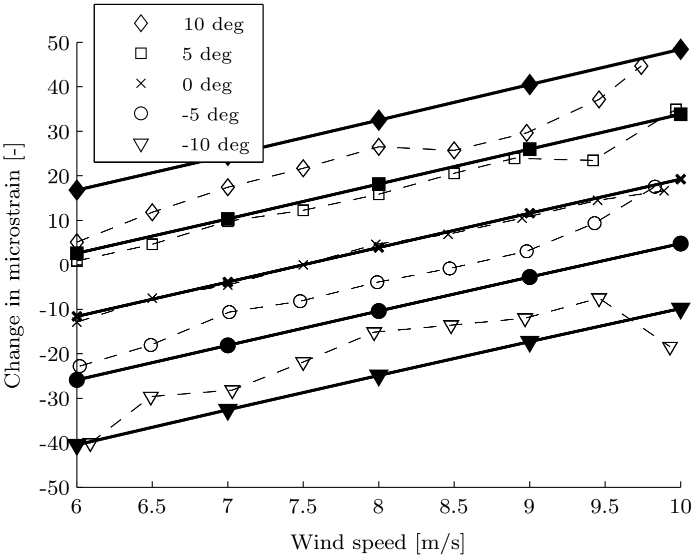

Figure 5.5: Static strain at 75% span on high pressure side: experiments (dashed) vs simulation (solid) for different flap deflection angles

In contrast to the measurement series at zero flap angle, the curves of the strains on the high pressure side for flap deflections are less linear, certainly for high wind speeds. High wind speeds correspond to high angles of attack up to 8 degrees as the turbine operates at a fixed rotor speed and is a stall controlled machine. When imposing a flap deflection, flow separation might occur. An additional problem is that, especially for low wind speeds, the delay between measured wind speeds upstream and at turbine turbine height can be up to 5 seconds. The result is an uncertain estimation of the wind velocity at the rotor. Nonetheless, the trends of simulation and experiment agree. Positive flap deflections increase the strain, while negative deflection decrease the strain. The increase is constant for all wind speeds, except for some experimental outliers such as the data point at 10.0 m/s wind speed and -10 degrees flap deflection. The numerical simulation overpredicts the change of the effect of the smart rotor on the strains by 15-20%. The blade element method assumes independent annuli. Therefore, every section is evaluated independently. However, this assumption might not be valid for smart rotors. The SNL smart rotor has discrete flaps, which are located close to the tip of the blade. Several aerodynamic phenomena can influence the loading. Firstly, discrete flaps generate a gap in the blade trailing edge which causes vortex formation as a result of flow from the high pressure side to the low pressure side. The result is a decrease in lift and a reduction of control surface effectiveness. Further studies are required to determine if the assumptions underlying BEM methods are sufficient to explain the observed differences.

5.4.2 TIME-DOMAIN RESPONSE TO STEP INPUT

Having investigated the static behavior of the blade strains, the dynamic response of the rotor to a step input is investigated next. The step deflection of the flap was initialised at t = 0.0 second and lasts 0.08 seconds. The duration of the step motion is independent of the amplitude of the motion. A slight overshoot can be observed in the flap deflections just before they reach the target deflection angle as shown in Figure 5.6. The flap motion has been modelled in the numerical simulation by a transition from a 0 degree flap angle to a final flap angle, with a $(1 - cos(\omega t))$-profile, where ω is the frequency of the motion and ωt runs from 0 to π.

The first comparison concerns the generator power as displayed in Figure 5.7. An observation that needs to be made is the large spread in measured power (grey lines). The generated power can be as low as 5kW, but can also peak to 80kW. For convenience, Figure 5.7 does not show extreme fluctuations of the power data, thereby highlighting the effect of the step input in the flap for the time-averaged signal. Besides the differences in the mean power level between the different measurement series, also the impact of turbulence on the power production during a measurement series is evident. The generator power fluctuates up to 10kW within less than 0.2 seconds due to fluctuations in the inflow. For the numerical simulations, the wind speed has been set such that the power output approximates the averaged power output of the 30 measurement series just before the step in flap response is initialised.

The averaged response in power generation agrees well with the numerical simulation for all wind speeds. The change in power production as a result of flap deflections between -15 and 10 degrees flap angles is accurately predicted. One should be notice that the wind speeds in the simulations has been matched for

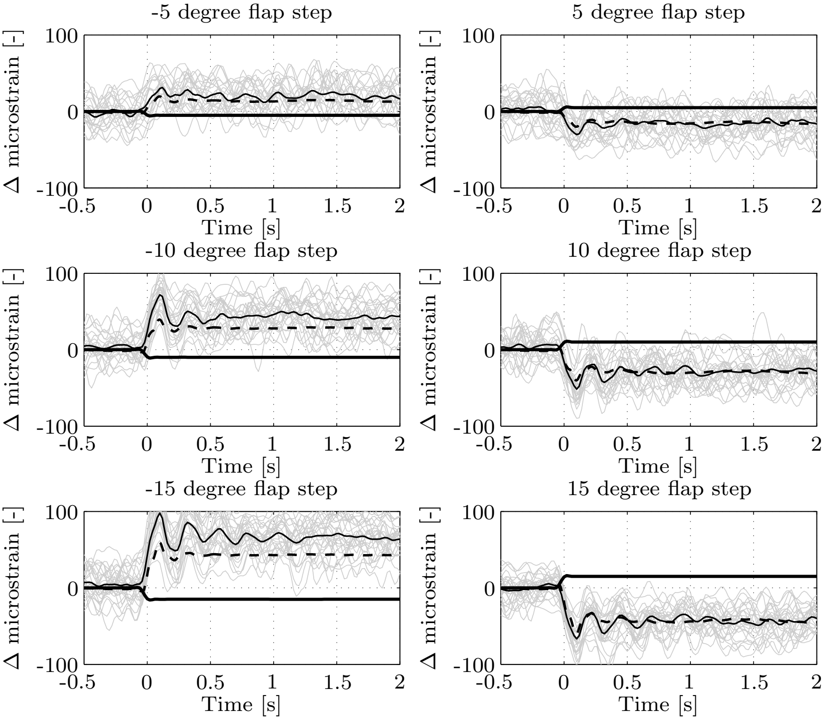

Figure 5.6: Strains at 75% blade span, high pressure side: Measured (grey), averaged (solid), flap angle (thick) and simulation (dashed)

each flap deflection series independently, resulting in a range of simulated wind speeds from 7.9 m/s in the case of the 10 degrees flap deflection to 8.6 m/s in the simulation with -5 degrees flap deflection. The curve with the poorest agreement is the 15 degrees flap angle simulation. Partially, this can be attributed to the fitting procedure of the wind speed. It is selected such that the simulated power at t = 0 corresponds to the averaged power of the 30 measurement series.

For steps in flap deflection of 15 degrees, this averaged power shows a local maximum at t = 0, probably as a result of turbulence, leading to an overestimation of the wind speed and consequently to an upward shift of the power curve by 1-2kW. Another reason is that separation might occur which is not predicted accurately by the DU-SWAT. This explanation is very likely, because at wind speeds of 10.0 m/s and and flap deflection of 15 degrees, the local flow angles close to the blade tips are around 25 degrees. This assumption is supported by a comparison to -15 degrees steps in flap deflection, which decreases the local flow angle to -3 degrees. This angle of attack is well within the linear region of the lift curve. Overall, the static results are predicted accurately.

The dynamics of the power generation are more difficult to assess. For step changes of 5 degrees in either direction, no conclusive statements can be made as the stochastic variations are almost as high as the predicted change in power. More measurement series are needed to reduce power fluctuations in the averaged signals due to turbulence. A step input of 10 degrees causes stronger oscillations in the power signal. These oscillations occur at 1.5 Hz. Therefore, they can neither be related to the structural dynamics of the turbine blades, for which the lowest eigenfrequency lies above 4.0 Hz, nor to the multiples of the rotor rotation. The rotor operates at 55 rpm, which corresponds to 0.9 Hz for 1P or 2.8 Hz for 3P. The time scales associated to flow adjustment are also different from this frequency. The time scale of local flow adjustment is 0.004 seconds and the wake response takes 1.2 seconds to reach the final state. A possible explanation for the oscillations is that the structural dynamics of the drive train are not modelled in the numerical simulation, while they might cause fluctuations in the power signal in reality.

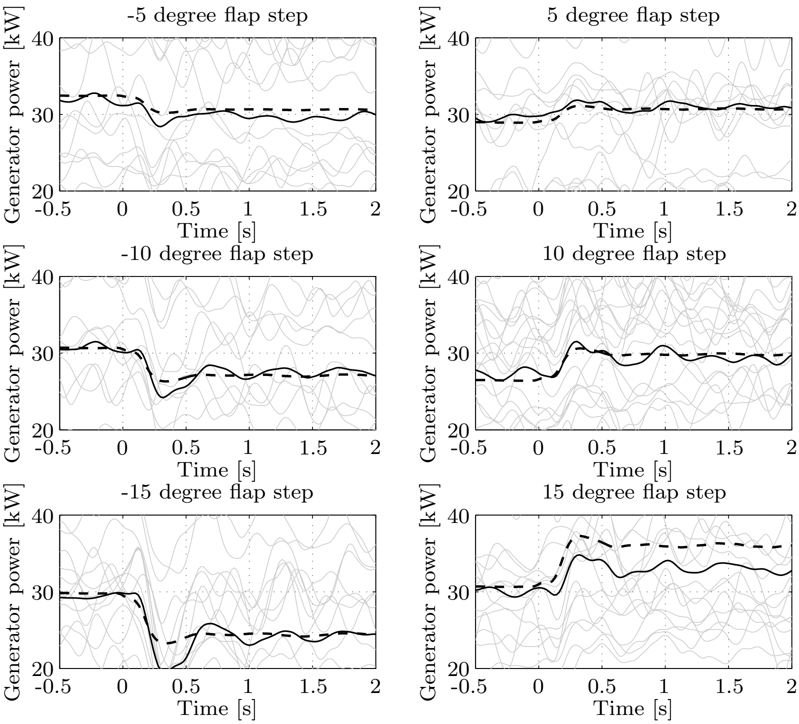

Figure 5.7: Rotor power: Measured (grey), averaged (solid) and simulation (dashed)

The oscillations increase further for the -15 degrees step change, with a strong overshoot at 0.3 seconds, which quickly damps to the amplitude level present before the step change. The DU-SWAT predicts a slight overshoot, but underpredicts the experimental overshoot. For positive flap deflections, this overshoot is not present and the numerical data approximates the change including the initial overshoot well. An expansion of the experimental data set is required to ensure that the variations are not of stochastic nature.

Figure 5.6 shows the strain measurements compared to the numerically obtained strain values. The dominant frequency in the averaged strain signals is just above 4.0 Hz, corresponding to the first flapwise bending mode. Experimentally, the first resonance frequency of the spinning rotor has been determined to be 4.2 Hz (Berg, Barone and Yoder, 2014), which corresponds well to the first flapwise eigenfrequency of 4.2 Hz, determined by spectral analysis of the numerical step response results. Also the amplitude changes are very well captured for positive flap deflections. For negative flap deflections, the strains are underpredicted. The reason for this can be found in Figure 5.8. The wind speeds of the numerical simulation have been selected such that the power production in the averaged measured signal and the numerical simulation was matched just before the step in flap deflection was applied. The fitting has been done based on the power curve with flap deflection of 0 degree. The power curves for negative flap deflection angles shifted towards much higher wind speeds. This shift is largest for -15 degrees, where the difference between curves in wind speed is more than 1.0 m/s. The result is an underestimation of the simulation wind speed. Higher wind speeds correspond to higher strains as shown in Figure 5.5, where a change in wind speed of 1.0 m/s corresponds to an increase by 10 microstrain, which is the difference between the simulation and experimental curves.

The numerical simulation also exhibits significantly higher damping than the experiment. The initial overshoot, which is caused by a combination of inertial loads due to the flap motion and aerodynamic loads, is captured well with the DU-SWAT. After that however, the blade oscillations fade quickly. The structural damping was expected to be the source for this decay. A range of damping coefficients from 0.005 to 0.04 have been studied, with the result that this hypothesis needed to be rejected as the simulation results did not show significant differences. The other damping source are aerodynamic forces. The unsteady aerodynamic performance has been studied on a two-dimensional airfoil including structural responses and controller integration (Gillebaart et al., 2014). The results do not give any reason for the assumption that the engineering model might cause a strong increase in damping. The last remaining question lies again, as for the static strain measurements, in the assumptions of the blade element momentum method like the independence of annuli. The effect of the interaction of vortices, which are shed from the flaps, and the tip vortex should be investigated by high fidelity aerodynamic analysis tools, such that the validity of the BEM assumptions can be assured.

A final comparison has been done for the tower top motion (Figure 5.9). A constant offset of 20 milli-g of the accelerations, which was observed during the

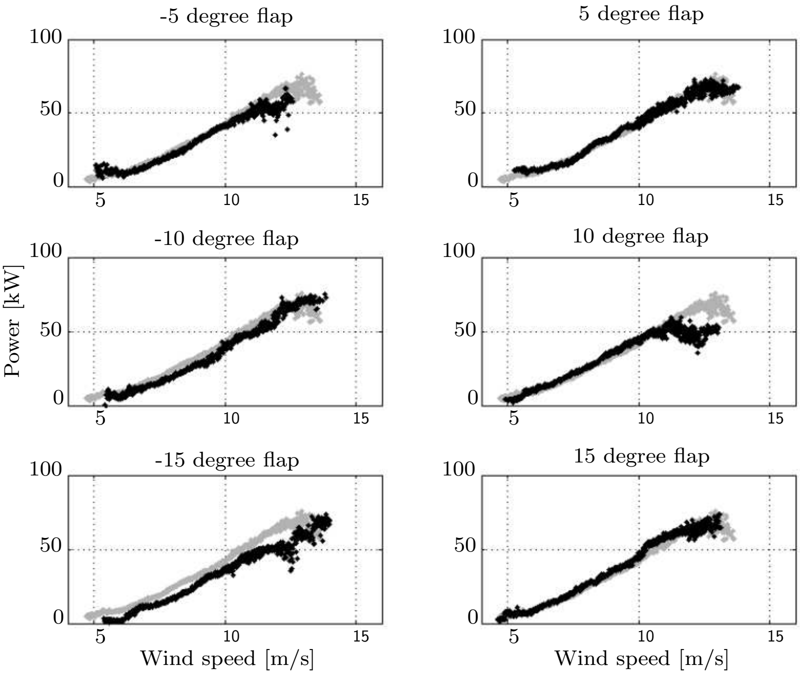

Figure 5.8: Power curve vs wind speed: flapped (black) and no flap deflection (grey)

measurements, corresponds to a misalignment of 1 degree between the accelerometer and the gravity vector. This misalignment can either be a result of the integration of the accelerometer in the structure or a result of tower deformation. The numerical results have been adjusted by this offset. The dynamic response for both numerical simulation and experiment is constituted by two separate phenomena. The first is a high frequency vibration, which is only visible in the first 0.5 seconds after the step response. This is triggered by the blade motion. The peaks in accelerations are around 0.1 and 0.3 seconds, which corresponds to the first blade frequency. In the numerical simulations, only the first peak is seen, which agrees with the analysis of the strain results as shown in Figure 5.5 that predict a quick decay of the blade vibration. In the experiment the blade vibration decays slower than in the numerical simulation. A second peak at 0.3 seconds is visible for flap deflections of 10 degrees and more. This matches with the measured strain signals, where low flap deflections only cause one visible vibration cycle before decaying to an amplitude similar to the one before the flap excitation.

The second cause of the tower top accelerations is the change in thrust level. The result is a slowly decaying tower motion. This decay is almost exclusively dependent on the structural damping of the tower. Low flap deflections of 5 degrees cause hardly any tower accelerations, similar to the very small change in power

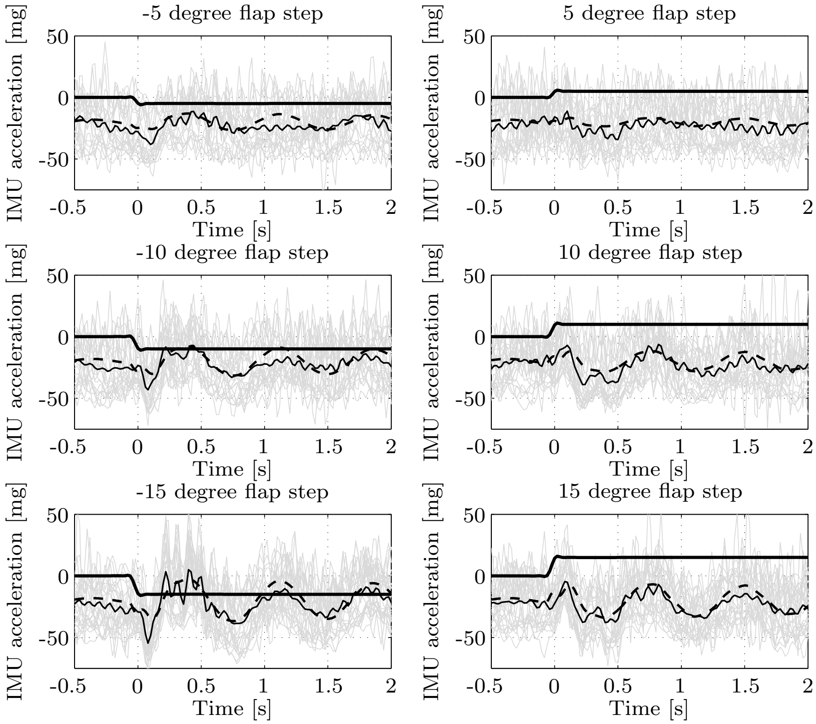

Figure 5.9: Axial accelerations inertial measurment unit (IMU) at hub: Measured (grey), averaged (solid), flap angle (thick) and simulation (dashed)

production as shown in Figure 5.7. Larger steps introduce a vibration that is well captured by the DU-SWAT, both in terms of frequency and amplitude.

5.5 INDIVIDUAL FLAP CONTROL

All of these flap excitations were open-loop, meaning that there was no feedback measurement of a blade sensor driving the flap motion. In the following sections, a closed-loop flap control strategy is proposed and simulated; however there is no closed-loop experimental data available for comparison.

The individual flap controller designed for the NREL 5MW reference turbine (Chapter 3) was adjusted for the Sandia National Laboratories Smart Rotor. The gain in Equation 3.54 has been scaled with the ratio of the average root bending moments between the NREL and the SNL turbine for wind speeds of 8.0 m/s.

5.5.1 TIME DOMAIN SIMULATION OF CONTROLLED SANDIA NATIONAL LABORATORIES ROTOR

The Individual Flap Control (IFC) controller has been designed to eliminate the periodic components (1P) of the rotor and tuned such that it also reduces the resonance associated to the first flapwise bending frequency. It was chosen to control for the periodic fatigue loading as the resonance of the root bending moment is highest for the uncontrolled load hinting towards the highest stress state. Figure 5.10 shows the PSD for uncontrolled and IFC controlled rotor simulations with a turbulent wind input. It can be seen that for the uncontrolled case the periodic deflections are dominant compared to all other deflections. Upon implementing the controller, these periodic vibrations are strongly diminished. The PSD around 0.9 Hz is strongly reduced. As the controller was tuned such that it also reduces the first resonance frequency of 4.5 Hz, a slight reduction of the deflection amplitude for the flapwise mode can be observed. This can be seen back both in Figure 5.4 and the left-hand side of Figure 5.10. The conclusion that can be drawn at this point is that individual flap control can replace individual pitch control albeit not collective pitch control for power regulation. For the current controller, where all control surfaces are fed the same signal, tuning allows load reduction of 1P without having to pay a penalty at higher frequencies. In a next step the potential of distributed control needs to be evaluated such that both the 1P component in the vibration spectrum and the resonance at the first eigenfrequency can be significantly reduced.

The right-hand side of Figure 5.10 shows that most control action is taken at 0.9 Hz. The flap deflections at higher frequencies are more than a factor of 10 lower than for 1P. This explains the relatively small impact on the PSD for the first and second eigenfrequency. At the same time, this advocates to use multiple control objectives as flaps can operate at significantly higher frequencies than IPC.

Figure 5.11 shows yet another time the potential of IFC compared to IPC. The flap deflection signals on the right hand side are clearly dominated by frequencies of 0.9 Hz. The vibration at this damping frequency are significantly reduced. It is worth to notice that the amplitude of the required flap deflection is in the order of 3 degrees. This is very desirable as a high deflection would lead to flow separation, thereby effectively causing an inversion on the desired effect on the lift coefficient. At 3 degrees, flow separation is still very modest and the gain in lift coefficient can be assumed as linear. It also demonstrates that IFC can efficiently take over the tasks of IPC certainly as only a limited range of flap deflection angles is needed. Moving from IPC to IFC reduces the actuation rate requirements on the pitch bearings and actuators, possibly leading to a less maintenance prone and cheaper system. At the same time, 1P and high frequency loads can be suppressed, reducing the overall fatigue damage.

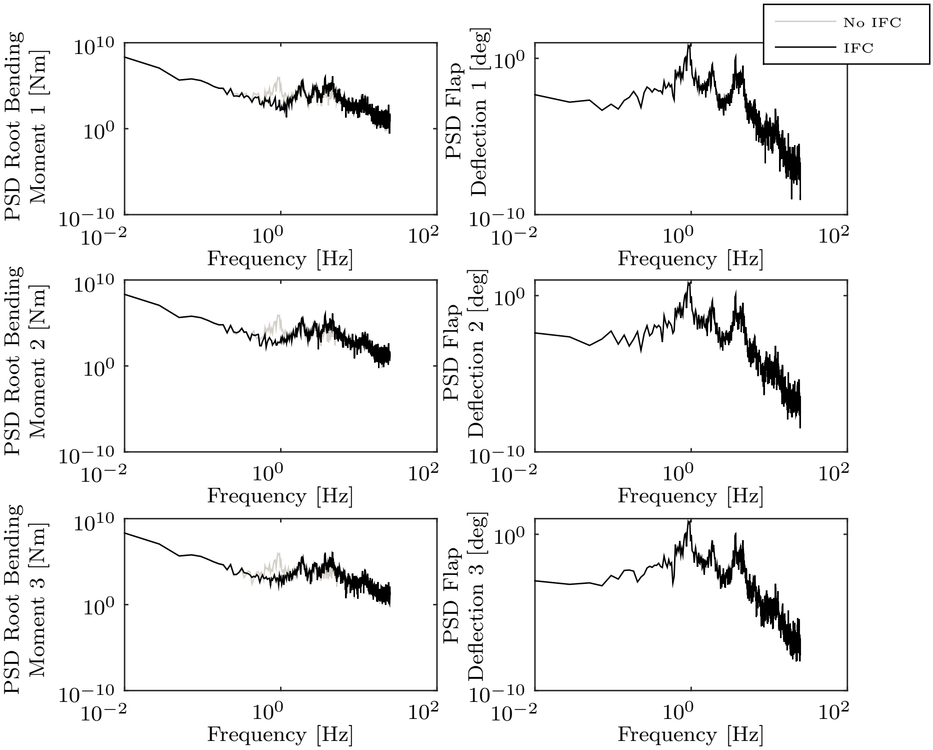

Figure 5.10: Power spectral density of root bending moment for turbulent wind speed of blades 1, 2 and 3

5.6 SYNOPSIS

A comparison study between the first utility scale smart rotor, the Sandia National Laboratories Smart Rotor, and the DU-SWAT has been conducted. The measurement data of the adapted Micon 65/13 turbine, which has been refitted with three flaps on each blade and equipped with strain gauges and accelerometers, has been used to validate the DU-SWAT:

- Frequencies and resonance of the SNL turbine have been captured both for flapwise and edgewise motion.
- The first flapwise mode produces a wide peak as a result of aerodynamic damping both for the experiment and the numerical simulation.
- The power spectral densities of the flapwise accelerations as a result of flap activity in simulation and experiment show similar behavior. For low

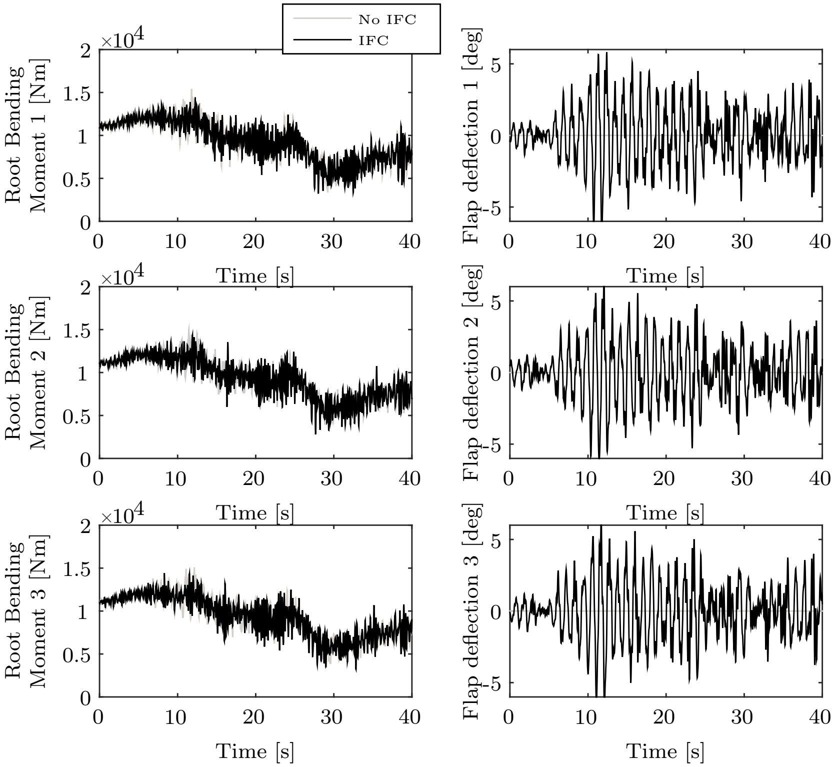

Figure 5.11: Time history of root bending moment for turbulent wind input

frequencies under 1.0 Hz, the measurement results are dominated by turbulence, which has not been included in the numerical simulations.

- Strain measurements without flap deflection could be approximated very well, while only the trend in strain measurements using flaps is correct. For high flap deflections, the numerical analysis overpredicts the effect of flaps, possibly as a result of separation modelling in the aerodynamic pre-processor Rfoil.

- The amplitude of the rotor power, the blade strains and the tower top accelerations of the DU-SWAT and of the experiment are very similar. The numerical tool, however, overpredicts aeroelastic damping for blade vibrations. The increase in damping is unclear and could neither be attributed to structural damping nor to the sectional aerodynamic model. It is recommended to study the assumptions underlying the blade element method and their validity for smart rotors.

- IFC can be efficiently done with even limited flap deflection angles.

'Now look, your grace,' said Sancho, 'what you see aren't giants, but windmills, and what seems to be arms are just their sails, that go around in the wind and turn the millstone'.
Miguel de Cervantes Saavedra, in Don Quixote

6

FULL TURBINE SIMULATIONS

6.1 INTRODUCTION

The DU-SWAT has been verified and validated in the previous chapters. A design of the individual flap control has been introduced and applied to a single load case in Chapter 5. This chapter transfers the controller design to the NREL 5MW turbine and extends the analysis basis to all failure-free load cases. In contrast to previous research, which focused on the blade root bending moment, a range of locations in the turbine are analyzed. Besides the assessment of the load alleviation potential of a smart rotor, also secondary benefits such as power generation are investigated in this chapter.

The chapter[1] starts with a brief background on previous research using smart rotors for load alleviation. This is followed by an overview of the analyzed turbine and the load cases that are taken into account. Two different aspects are investigated: fatigue and ultimate loading. In addition to a general overview of the smart rotor performance, the most significantly changing components are analyzed in more detail. The chapter is concluded by investigating how flaps can be used to increase power generation in low fatigue wind regimes.

---

[1] This chapter is an adaptation of the journal paper 'Fatigue and Extreme Load Reduction of Wind Turbine Components using Smart Rotors' by Bernhammer, De Breuker and van Kuik (2015*b*) with elements of the journal paper 'Sizing and Control of Trailing Edge Flaps on a Smart Rotor for Maximum Power Generation' (Smit et al. (2014)).

6.2 RESEARCH ON LOAD ALLEVIATION USING A SMART ROTOR

Fatigue load alleviation is so far the most investigated problem of smart rotor research. Until recently, most studies have considered only few load cases to determine the potential gain of smart rotors. Table 6.1 displays the flap dimensions and the analysed design load cases as used in peer-reviewed journal papers and Ph.D. theses. These simulations consist of the analysis of few, short period load cases such as used by Andersen (2010) or three load cases in the case of Barlas et al. (2012). Andersen reports the potential of flaps to alleviate 34% of the fatigue equivalent damage in flapwise loading, while Barlas finds slightly lower values up to 27%. While Andersen focuses on loads in the blade only, Barlas also reports a reduction potential in the tower fore-aft bending moment and the tower tip deflections. Lackner and van Kuik (2010) have expanded the approach to smart rotor control by combining flaps with individual pitch control (IPC) resulting in maximum blade root moment reductions of 22%. Bergami and Poulsen (2015) have employed a linear-quadratic controller with which they achieved a 16% fatigue load reduction of the root bending moment.

In parallel to the numerical simulations, experimental work has been performed at Delft University of Technology to prove the technical feasibility of the smart rotor concept (Hulskamp et al. (2011); van Wingerden et al. (2008)). During the wind tunnel experiments with a scaled rotor, fatigue load reductions of up to 59% have been achieved. This number, however, has to be viewed in context of the controlled wind tunnel environment with an extremely low turbulence level. Therefore, it cannot serve as an indication of the actual potential of smart rotors when considering utility sized turbines. Castaignet et al. (2014) have been the first to test a controller on a utility scale smart rotor in a field test. A Vestas V27 was retrofitted with three flaps with a span of 70 cm each on one of the blades, of which a single flap was operational during the experiment. The achieved blade root moment reduction of 14% during a 38-minute simulation is lower than the achieved values in numerical simulations of Barlas et al. (2012) or Markou et al. (2011), but one has to bear in mind that the size of the flap is significantly smaller than in all other analyses as shown in Table 6.1. Castaignet et al. (2013) also simulate the load alleviation of the full scale smart rotor experiment, but find significantly lower load reductions.

A first effort to evaluate the whole turbine with all its components has been done by Bæk (2011), who is the first to approach the load reduction potential in a more global sense. Bæk performs two types of analyses. The first one is a stochastic investigation of the effect of tubulence seeding on the load reduction results. For this purpose, he performed 100 simulations at 11.0 m/s. It is found that the standard deviation for a 10-minute simulation of load reduction in the

Table 6.1: Simulation set-up peer-reviewed papers and Ph.D. theses

Author	Flap chord ratio %	Flap width % of radius	Wind [m/s]	Shear exp.
Andersen (2010)	10.0	15.0-30.0	11.4	0.14
Barlas et al. (2012)	10.0	18.0	7.0, 11.4, 15.0	0.20
Lackner and van Kuik (2010)	10.0	20.0	8.0, 12.0, 16.0, 20.0	0.20
Bergami and Poulsen (2015)	10.0	20.0	12.0-24.0	0.20
Castaignet et al. (2013)	13.0-18.0	5.0	Field test	Field test
Castaignet et al. (2014)	13.0-18.0	5.0	Field test	Field test
Bæk (2011)	10.0	20.0	5.0-25.0	0.20

Author	Turb. Int.	DEL reduction %	Controller
Andersen (2010)	0.06	25.0-37.0	PD/HPF
Barlas et al. (2012)	0.06	10.9-27.3	MPC
Lackner and van Kuik (2010)	NTM	5.7-22.4	PID
Bergami and Poulsen (2015)	0.14-0.17	15.5 (average)	LQ
Castaignet et al. (2013)	Field test	5.0 (simulated)	MPC
Castaignet et al. (2014)	Field test	14.0 (measured)	MPC
Bæk (2011)	0.06-0.18	15.0-20.0	IBC

NTW - Normal turbulence model
PD - Proportional-derivative controller
HPF - High-pass filter
MPC - Model predictive controller
LQ - Linear quadratic controller
PID - Proportional-integral-derivative controller
IBC - Individual Blade Control

blade root bending moment is 3%.

In a second analysis step, Bæk evaluates power production load cases with a normal and extreme turbulence model for wind speeds from 5.0 to 25.0 m/s. For each wind speed a 10-minute simulation is performed. At the same time more wind turbine components are taken into account. Besides the traditionally evaluated flapwise and edgewise blade root moments, he also considers moments at the tower base, shaft torsion, hub moments, and the three moments at the tower top. Bæk carried out three distinct analyses, namely the dependency of these loads on wind class and turbulence intensity. Besides a reduction of the damage equivalent flapwise blade root bending moment of 15%, also a significant reduction of fatigue loads at the hub and the tower top were found. While being relatively independent on the wind class, the turbulence intensity proves to influence the results more significantly. Similar to Lackner and van Kuik (2010), Bæk also investigates the effect of combining individual pitch control and active flaps. He finds that, certainly for fatigue loads, the combination of individual pitch control with individual flap control (IFC) can considerably improve the performance of smart rotors, with hub fatigue load reductions of more than 40%. Extreme loads remain a site notice in Bæk's work as their results are not discussed in detail, but only presented in two subfigures. The most significant extreme load reduction is achieved for the tower top tilt moment, which gets reduced by approximately 30%.

6.3 ANALYSIS SET-UP

6.3.1 5MW REFERENCE TURBINE

The turbine, which is investigated in this chapter, is the NREL 5MW reference turbine (Jonkman et al. (2009)). This turbine has been created as benchmark model for aerodynamic and aeroelastic utility scale wind turbine computations. The 5MW reference turbine is heavily based on the REpower 5MW design with influences from publicly available conceptual turbine data such as the Dutch Offshore Wind Energy Convertor Project (DOWEC). The 5MW reference turbine has a rotor with 126 m diameter and a hub height of 90 m. In the present study the support structure under water has not been modelled. Flaps have been included without changing the structural properties as specified by the NREL. The flap length was fixed to 10% of the chord and the flaps run from 78% to 98% of the blade span. The airfoil for the entire width of the flapped section is a NACA 64-618. The deformation shape of the flaps is given in Chapter 3.

While previous studies often focused on the blade root bending moment as an indication for load reduction, in this study, loads throughout the turbine are monitored. Figure 6.1 displays the sensor locations on the wind turbine. Instead of considering only root bending moments, a full set of three forces and three moments is monitored at the blade root, the shaft, the connection between the tower and the nacelle, a location at 82 m tower height and the tower base. In case of extreme events also blade tip deflections with respect to the rotor plane have been considered.

6.3.2 EFFECT OF CONTROLLER

The control system has been implemented for the 5MW reference turbine as described in Chapter 3. The simulations were run with and without individual flap control. Figure 6.2 presents the effect of the controller on the flapwise root bending moment in a turbulent wind field at 10.0 m/s. The controller was designed to reduce fatigue loads associated with cyclic events such as wind shear or tower passing. It can be seen that the 1P frequency is efficiently reduced.

The turbine start-up load cases have been analysed starting from a wind turbine model in slow idling operation at a rotor speed of 1 RPM. As described in the NREL 5MW reference guide (Jonkman et al. (2009)), the turbine can speed up

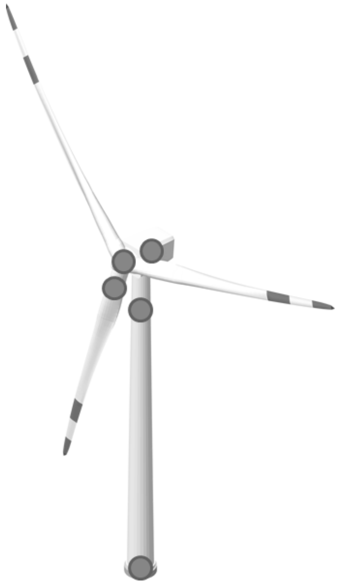

Figure 6.1: Monitored locations: Tower root, tower top, nacelle, shaft and blade root (dots)

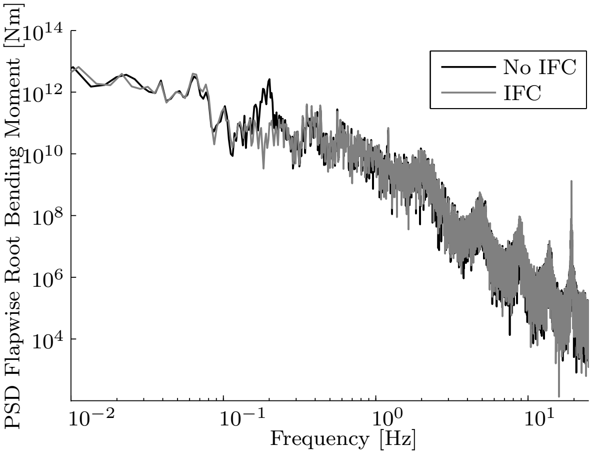

Figure 6.2: PSD flapwise root bending moment 10.0 m/s

during this control region up to 6.9 RPM at which point the turbine is connected to the grid and a resistance torque is applied. Up to a rotor speed of 8.98 RPM, this torque is ramped up, until it reaches the torque for optimal power production. The starting position of the pitch controller is 0 degree.

6.3.3 LOAD CASES CONSIDERED

The present work extends the analyses of Bæk (2011) by covering failure-free simulations as prescribed by the standards for load calculations as given by the International Electrotechnical Commission (IEC) 61400-1 (International Electrotechnical Commission (2005)). The IEC requires the analysis of eight load case groups:

1. Power production
2. Power production plus occurrence of fault
3. Start-up
4. Normal shut down
5. Emergency shut down
6. Parked
7. Parked and fault
8. Transport, assembly, maintenance and repair

The considered load cases include power production load cases with both normal and extreme wind models as well as extreme gust and extreme change of direction cases. Start-up load cases are also considered. An overview of the load cases and their respective simulation time can be found in Table 6.2. As the flap controller is dependent on the generator speed, the flaps are inactive for parked conditions, this eliminates load cases 6.1-6.4 and 7.1. It is also a fair assumption that flaps would not be used during transport, assembly, maintenance or repair, which makes running loads cases 8.1 and 8.2 unnecessary. Emergency and failure load cases have been omitted as well. These load cases correspond to 2.1-2.4 and 5.1. Load case 1.1 has been replaced by 1.3, which is allowed according to the third edition of the IEC regulations (International Electrotechnical Commission (2005)), if the blade loads during DLC 1.3 are conservative. The remainder of the load cases is analysed. All simulations have been performed according to the IEC regulations, however no safety factors have been applied on the obtained load values. As these safety factors would be applied for the simulations both with and without individual flap control, the reduction percentages are not affected.

The wind input turbulence fields were generated by by TurbSim (Jonkman (2009)) (stochastic wind fields) and IECWind (Buhl (2014)) (deterministic wind fields). The wind turbine has turbulence class of B. A power law wind shear profile with an exponent equal to 0.20 has been used. Turbulence was modelled using the von Karman turbulence model.

For the wind speed distribution a Weibull distribution with scale parameter 10.85 and shape parameter 2.15 is assumed. These parameters have been obtained by offshore measurements in the Netherlands [2].

---

[2] ECN, Meteomast IJmuiden, http://www.meteomastijmuiden.nl/, June 2013

Table 6.2: Design load cases taken into account

DLC	Wind condition	Analysis	Duration
1.2 Power prod.	NTM $V_{in} < V_{hub} < V_{out}$	Fatigue	4x10 minutes
1.3 Power prod.	ETM $V_{in} < V_{hub} < V_{out}$	Ultimate	10 minutes
1.4 Power prod.	ECD $V_r - 2m/s$, V_r, $V_r + 2m/s$	Ultimate	4x40 seconds
3.1 Start-up	NWP $V_{in} < V_{hub} < V_{out}$	Fatigue	4x40 seconds
3.2 Start-up	EOG V_{in}, $V_r - 2m/s$, V_r, $V_r + 2m/s$, V_{out}	Ultimate	4x40 seconds
3.3 Start-up	EDC V_{in}, $V_r - 2m/s$, V_r, $V_r + 2m/s$, V_{out}	Ultimate	4x40 seconds

NTW - Normal turbulence model
ETM - Extreme turbulence model
ECD - Extreme coherent gust with direction change
NWP - Normal wind speed profile
EOG - Extreme operational gust
EDC - Extreme direction change

6.4 FATIGUE LOAD ALLEVIATION

6.4.1 OVERALL SMART ROTOR PERFORMANCE

For the fatigue load analysis, design load cases 1.2 and 3.1 have been considered. The power production load case 1.2 plays a dominant role compared to the start-up load cases. Each 10-minute simulation was carried out four times with different turbulence seeds to obtain a smoother estimate of the fatigue loads. Rain flow counting has been used together with the Miner's rule to obtain fatigue equivalent loads. The exponents in the S-N curve were chosen to be 10 for blades and 3 for the remaining components. Figure 6.3 displays the ratio between the controlled and the uncontrolled fatigue equivalent loads on the different sensors. The first observation that can be made from Figure 6.3 is that the overall fatigue damage is either decreased or unchanged when applying a region of uncertainty of 2% in load changes. The vibrational load reduction is up to 25% for the blade root and up to 10% for most of the remaining components. The smart rotor uses the flaps as aerodynamic dampers that produce negative work on the wind turbine, thereby dissipating energy, which leads to a global reduction of vibrations in the turbine. In contrast to the work by Bæk, the calculated reduction potential is significantly lower for several turbine components, when carrying out an analysis for power production and start-up design load cases. Vibration reduction of more than 20%, which Bæk finds for the tower top moments, could not be reached for any other turbine component than the flapwise root bending moment.

Figure 6.3 summarises the results of (Bæk (2011)), who investigated both the load reduction based on individual pitch control and flap control based on the amplitude of the first blade mode shape. These results are compared to an overview of the results in this chapter. The first note is that the results in this chapter include many more turbine components. The load reduction potential of the individual pitch controller is almost identical to the individual flap controller, which is based on an equivalent controller architecture using the Coleman transform. The load reductions in both root bending moments, the moments at the nacelle tower intersection and the tower root moments differ by less than 1%, which lies in the stochastic accuracy range found by Bæk (2011). The modal control of Bæk sacrifices a reduction in the root bending moment for a reduction in tower moments, possibly by capturing higher harmonics of the turbine operation.

During power production, the amplitude of the flap deflection angles is increasing linearly with the wind speed above the rated wind speed (Figure 6.4). Below the rated wind speed the differences are smaller and turbulence affects the flap activity more than at high wind speeds. The maximum occurring flap deflection at 24.0 m/s is 8 degrees, which is still in a physically feasible region of flap deflection angles of existing smart rotors such as the Sandia National Laboratories Smart Rotor. Based on the wind speed distribution, the overall power production is reduced by 3.8% when the flap is active compared to the uncontrolled case.

6.4.2 BLADE LOADS

While the loads in the blade are most affected, also the rest of the turbine experiences a load reduction. The biggest changes in equivalent load are assessed in more depth.

- A fatigue load reduction of more than 24% for the flapwise blade root moment can be observed. The order of magnitude of the blade root moment fatigue reduction is in good agreement with the work of Andersen (2010) and Barlas (2011). The comparably high reduction potential can be attributed to the Wöhler exponent of 10 for composite materials used in the turbine blades, while all other components are evaluated with a Wöhler exponent of 3 for metals. This means that in the case of the wind turbine blade, only few load cycles contribute to the overall fatigue damage. These high load cycles are introduced by cyclic effects at 1P frequencies. Other components feel the effect of all three blades. The controller should therefore be extended such that it also addresses 2P and 3P frequencies. The flapwise root bending moment distribution is shown in Figure 6.5. By far the highest contribution to the equivalent flapwise bending moment is located at the rated wind speed of 11.4 m/s. A very pronounced peak can be observed in the controller-free simulation, while the controller reduces the peak significantly. To ensure that the amplitude difference is not a stochastic effect, multiple simulations have been performed. Bæk (2011) reports variations in relative fatigue of the flapwise bending moment of up to 20%. Figure 6.5 shows the average values over four simulations. It is interesting to notice, that the damage equivalent load reduction is not directly linked to the flap

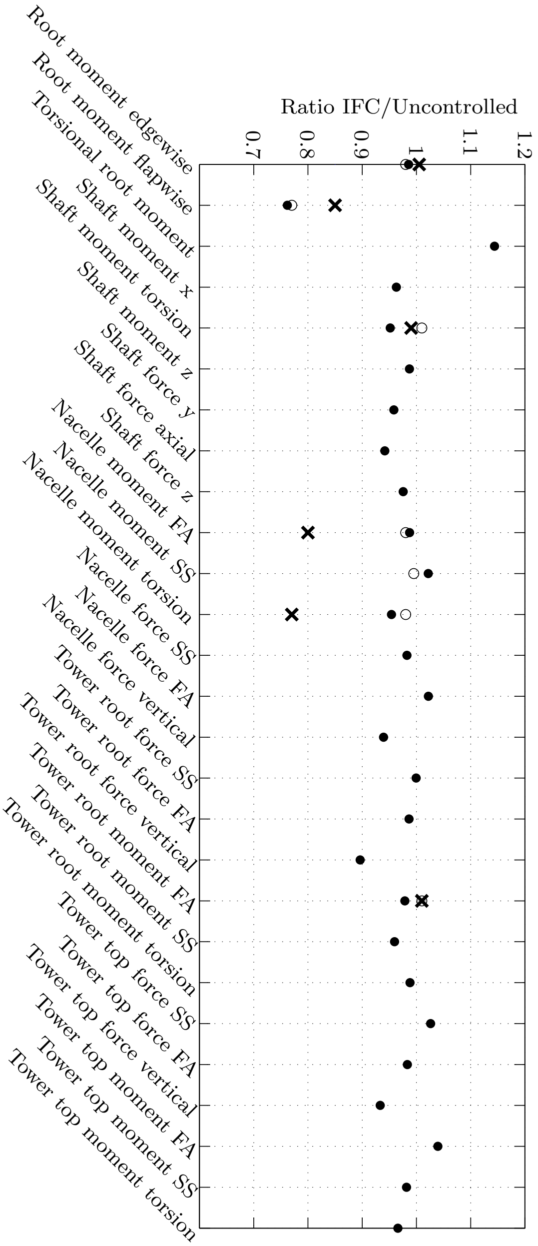

Figure 6.3: Fatigue load ratio with and without IFC, comparison of results (•) with Bæk IPC (○) and Bæk modal control (×); SS: side-side, FA: fore-aft

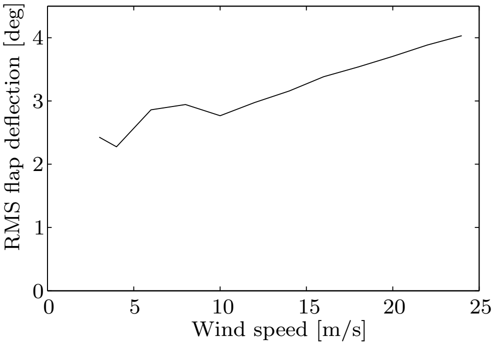

Figure 6.4: Flap activity during power production vs. wind speed

activity as shown in Figure 6.4, which reports the highest flap activity at high wind speeds. The reduction is rather linked to the alleviation of peaks around the rated wind speed, which can be realised with limited flap activity. The highest percentual decrease of the root bending moment is found at wind speeds of 20.0 and 22.0 m/s, which relates well with the high flap activity. As the damage equivalent load that is accumulated in these wind speed bins is much lower than the one around the rated wind speed, their contribution to the fatigue load alleviation is small.

- The fatigue equivalent load for the torsional blade root moment is 14% higher. Again, the major change of loads is around the rated wind speed as shown in Figure 6.6. Similarly to the flapwise moment, to the majority of the torsional fatigue load is accumulated around the rated wind speed. The increase in fatigue loads was expected. By applying a deflection at the trailing edge, one introduces a moment on the airfoil section resulting in an increase in blade torsion. It is evident that the reduction of flapwise loads comes at the expense of an increase in torsion loads. By applying a system of leading edge and trailing edge devices, this problem can be avoided.

- Gravitational loads are the major contributor to the edgewise root bending moment, while the torsional and flapwise moments are driven by aerodynamic forces. As the turbine operates, each blade rotates in the gravitational field. These forces combined with the edgewise components of lift and drag contribute to the total edgewise loading. As expected, the edgewise bending moment in Figure 6.7 shows significantly less variation depending on the wind speed. The drop of the equivalent damage at high wind speeds is related to the probability distribution of the wind speed bins. According to the computation of damage equivalent loads with Wöhler exponents, these loads are proportional to the tenth root of the number of load cycles. Wind speeds between 23.0 and 25.0 m/s occur 0.4% of the time, while wind speeds between 11.0 and 13.0 m/s occur with a probability of 12.8%. This means that the ratio of the edgewise damage equivalent loads of both wind speeds should be equal to 0.7087, which matches well with the plot presented in Figure 6.7. Despite this gravitational dominance, the smart rotor can still make a minor impact on the edgewise bending moment, by eliminating peak lift coefficients that could occur at the same time as gravitational loading. The smart rotor alleviates these loads in a uniform way over the entire wind spectrum, such that a total reduction in terms of the equivalent edgewise damage of 1.5% can be achieved.

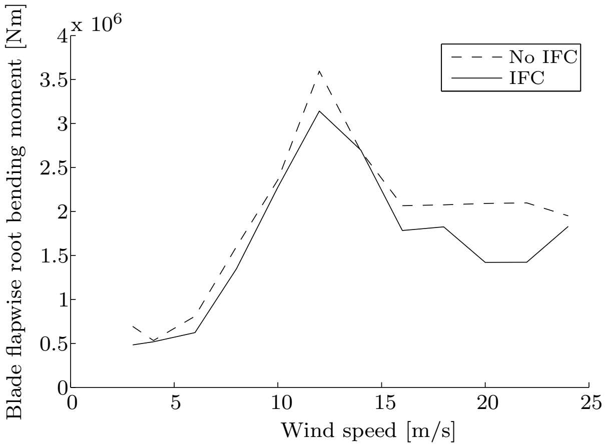

Figure 6.5: Equivalent blade flapwise root bending moment over turbine lifetime, DLC probability weighted

6.4.3 TOWER AND DRIVE TRAIN

Besides the loads in the blades, also other turbine components are affected by the smart rotor.

- Another significant reduction of equivalent fatigue damage can be found for vertical forces in the tower. Figure 6.8 shows the fatigue load reduction as a function of wind speed. The major contribution to the fatigue load is allocated around the rated wind speed of the turbine. The reason for this strong reduction potential lies in the nature of these gravitationally driven forces. Figure 6.9 shows that the forces are almost perfectly constant in time, but a small variation is introduced on top of the weight of the rotor and the nacelle. This small variation can be addressed efficiently, presumably as it originates from the variation of the lift component of all blades in vertical

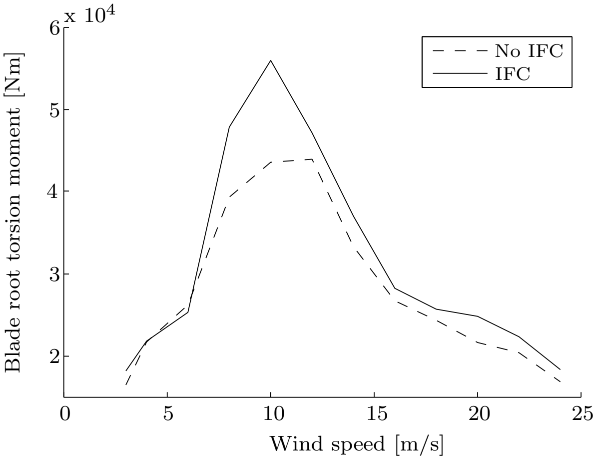

Figure 6.6: Equivalent blade root torsion moment over turbine lifetime, DLC probability weighted

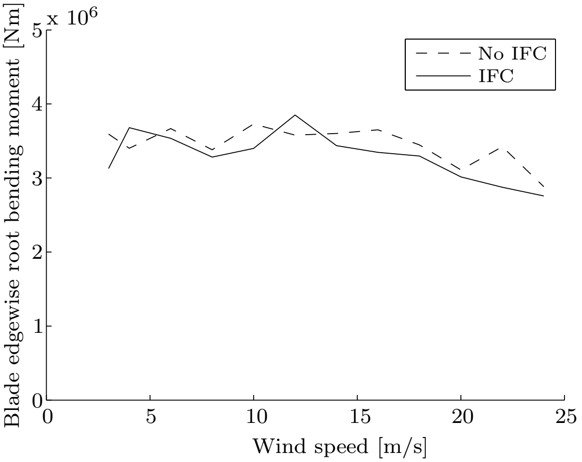

Figure 6.7: Equivalent blade edgewise root bending moment over turbine lifetime, DLC probability weighted

direction. Still, this will not alter the turbine design, as the ultimate loads and displacements are more critical for the tower design.

- Smart rotors reduce the fatigue equivalent damage in the shaft of the wind turbine. The application of smart rotors results in a smoother behavior of the power production, thereby also reducing the fatigue damage that it causes on the turbine shaft. The most significant contribution to the fatigue damage equivalent shaft torsion moments is accumulated around the rated wind speed, where the flaps help to alleviate the torsion moments most efficiently. Also for a range of wind speeds above the rated wind speed, the fatigue damage load is lowered as shown by Figure 6.10.

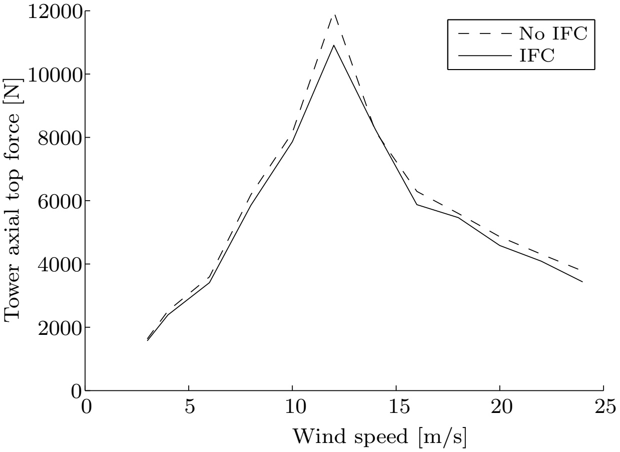

Figure 6.8: Equivalent vertical tower force over turbine lifetime, DLC probability weighted

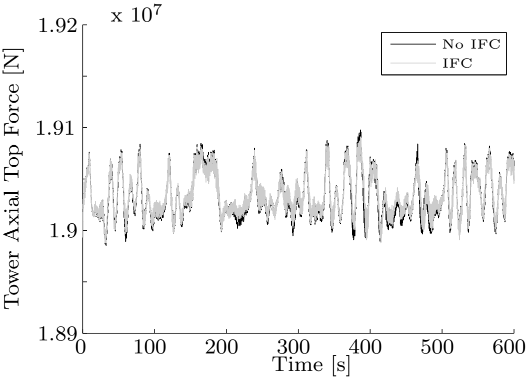

Figure 6.9: Vertical tower forces vs. time at the rated wind speed

6.5 EXTREME LOAD MITIGATION

6.5.1 OVERALL EXTREME LOAD MITIGATION

The design of blades of large wind turbines becomes more and more driven by the extreme loads instead of the fatigue load cases. A prime example thereof is

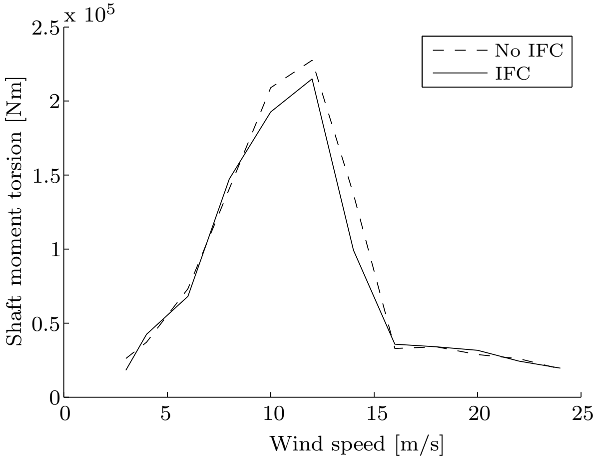

Figure 6.10: Equivalent Shaft torsional moment over turbine lifetime, DLC probability weighted

the required tower clearance as a result of large tip displacements of large wind turbine blades. It is therefore vital to also investigate the impact of smart rotors on extreme loads. It should be noted that the controller has been designed mainly for fatigue load alleviation and can be further optimised to respond to extreme events. Extreme turbulence during power production, extreme operational gusts and extreme change of wind direction cases have been investigated for start-up and power production. Figure 6.11 shows the ratio between the maximum occurring controlled loads to uncontrolled loads. This table includes the maximum value of any ultimate load case specified in Table 6.2.

A 10-minute simulation has been run per wind speed bin for the extreme turbulence load cases during power production. Multiple simulations for different azimuth angles have been performed for each ultimate load case during start-up and for the extreme change of direction with a coherent gust during power production. Bæk (2011) already identified that the effect of the fatigue load reduction strongly depends on the turbulence intensity. As the extreme turbulence model is used in these simulations, the turbulence intensity can be as high as 0.30, compared to a turbulence of 0.14 in the case of wind turbine class B that has been used in the fatigue load calculations. Bæk finds that the equivalent blade root bending moment reduction is halved from a turbulence intensity of 0.06 to 0.14. Further increasing the turbulence level causes a further reduction of alleviated load. In the extreme load simulation, most sensors deliver data that does neither hint to a significant decrease nor to a substantial increase in loads. This is expected because the controller has been set up such that it aims at reducing cyclic loads at 1P frequency. This results in a smoothening of the loads over a cycle, which helps to alleviate local peak loads. However, extreme loads could be mitigated more efficiently when a dedicated controller would be designed.

The agreement between the different simulations of the extreme loads in Figure 6.11 is poorer than for the fatigue loads. First of all, one should bear in mind that Bæk only considers power production load cases in his analysis, while the overview of results of this research also includes extreme events. The edgewise blade root moment shows a large spread in the simulations of Bæk, which find a difference in edgewise moments of more than 10% between individual pitch control and the active flap approach. This seems a large variation, especially when considering that these loads are gravity driven. The current simulations fall in the middle of these load reduction estimations. Agreements for the flapwise root bending moment are significantly better. The modal controller of Bæk and the IFC achieve the same alleviation of ultimate loads, while the individual pitch controller achieves a reduction of 5% instead of 8% as for the other two controllers. The changes in torsional moments in the shaft are small for all simulations. Very large differences can be seen in the fore-aft moment at the tower-nacelle interface and the tower torsion. While a reduction in tower torsion of 12-18% is reported for all simulations, the IPC fails to adress fore-aft moments at the tower-nacelle interface. As both flap controllers find almost the same reduction potential for other components, the small discrepancy of the fore-aft tower moment is difficult to understand. The difference are even more surprising when considering that individual pitch controllers are designed to reduce the difference in blade loads originating from wind shear, which is the driver behind this fore-aft moment.

While most components are unaffected by the smart rotor, the extreme load of certain components changes significantly.

- One of the few parameters that experience a decrease in value is the maximum flapwise root bending moment, which is reduced by 8%.
- An increase in the same order of magnitude can be seen for the torsional blade root moment.
- Four other wind turbine components display a prominent behaviour, namely the torsional moments at the interface between the nacelle and the tower, high in the tower and the tower root which all get reduced by 17%.
- An even bigger reduction is achieved for the fore-aft bending moment at the tower-nacelle interface.

The reductions in the tower moments can be explained by the nature of the controller, which eliminates cyclic effects. The moment at the interface is dominated by the difference of thrust between different blades with different azimuth. The asymmetric inflow causes this difference, but its effect is eliminated by the controller. The reduction in torsional tower moments corresponds to the same effect of eliminating cyclic loading. It is interesting to see that in spite of a strong reduction in load at the tower-nacelle interface, the tower design requirements cannot be eased as the load reduction diminishes quickly.

6.5.2 EXTREME TURBULENCE SIMULATION

To allocate where the load reductions originate from, a more detailed overview of the extreme turbulence load cases is given. Figures 6.12 to 6.15 show the ultimate loading in the tower for the power production load cases using the extreme turbulence model. Figure 6.12 displays the fore-aft moment at the interface between the tower and the nacelle. A reduction of the maximum obtained component load of more than 30% can be found. This reduction comes at a consequence of the controller design. While the controller aims to minimise the differences in the root bending moment of a blade when completing a full rotation, the loads for all azimuthal positions are equalised. The controller increases the loads on the blades in the lower shear layer, while decreasing the loads in the upper shear region. The differential between these loads causes the fore-aft bending moment at nacelle level. Unfortunately, this load reduction does not apply throughout the tower. As shown in Figure 6.15, the ultimate fore-bending moment at the root of the tower is not addressed by the individual flap controller. The reason for this is that the fore-aft root bending moment is dominated by the thrust of the rotor, while the actual moment that is passed from the rotor to the tower is more than an order of magnitude smaller. This fact is underlined by Figure 6.14 which displays the rotor thrust or fore-aft force on nacelle level. The shape of the curve both for positive and negative thrust is identical when compared with Figure 6.15. In fact, the reduction in tower bending moment has completely disappeared only 8 m from the tower top.

In contrast to the bending moments in the tower, the torsional tower moment does not change along the length of the tower. The load reduction in the tower top torsional moment can thus be directly translated in a relaxation of the design criteria. The controller balances between positive and negative torsional moments for the entire range of wind speeds. Torsional moments are a result of asymmetric inflow and mean that one of the sides of the rotor disk is loaded more heavily than the other side. Again, the controller minimises differences over one operational cycle, thereby also reducing the ultimate torsional tower moment. This ultimate load reduction cannot be found in terms of fatigue load reduction. The driving mechanism behind fatigue loads is the rate of change of the yawing inflow field, not the maximum inflow angle. As these changes are not located at the 1P frequency, the controller fails to address the fatigue load effectively. Additionally, this can be attributed to the low Wöhler coefficient, where the absolute number of cycles contributes more to the damage than the amplitude of single cycle.

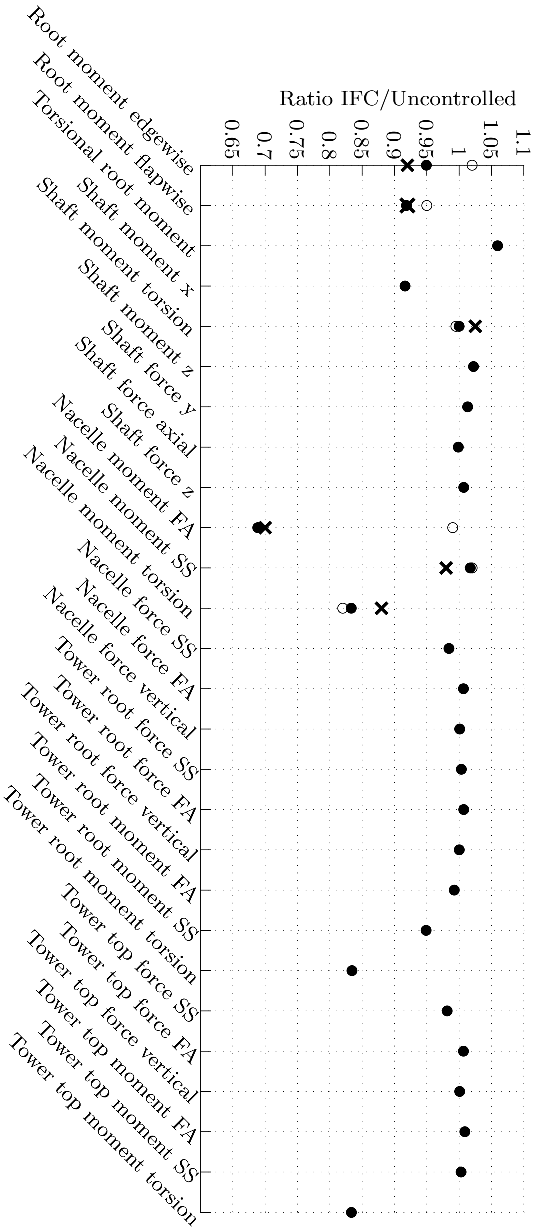

Figure 6.11: Ultimate load ratio with and without IFC, comparison of results (•) with Bæk IPC (○) and Bæk modal control (×)

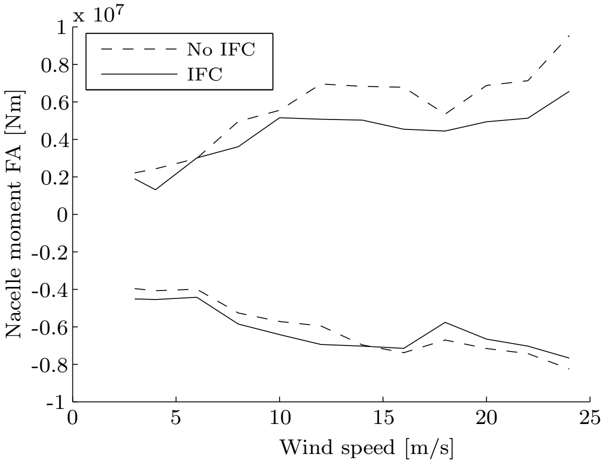

Figure 6.12: Extreme turbulence during power production: nacelle moment FA

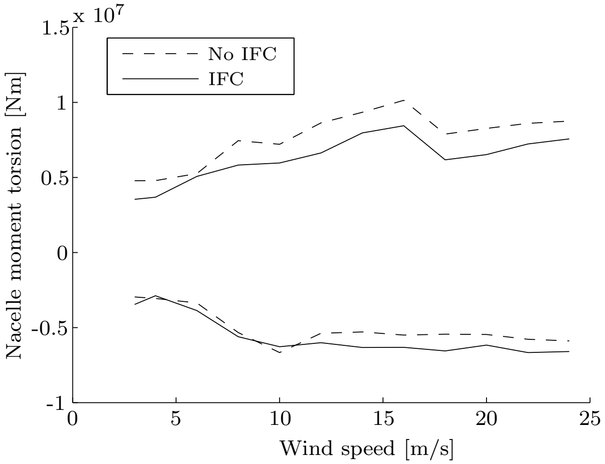

Figure 6.13: Extreme turbulence during power production: nacelle torsion

6.5.3 BLADE TIP DEFLECTION

Besides the ultimate loads, the tower clearance is one of the main design parameters for blade design. Extreme displacements during power production dominate this parameter. The extreme change of direction, which might be suspected to have a large influence, actually deflects the blades away from the tower, thereby increasing clearance. Figure 6.16 shows the maximum deflection during power production with an extreme turbulence model. As expected the highest deflections occur around the rated speed and the individual flap controller can reduce

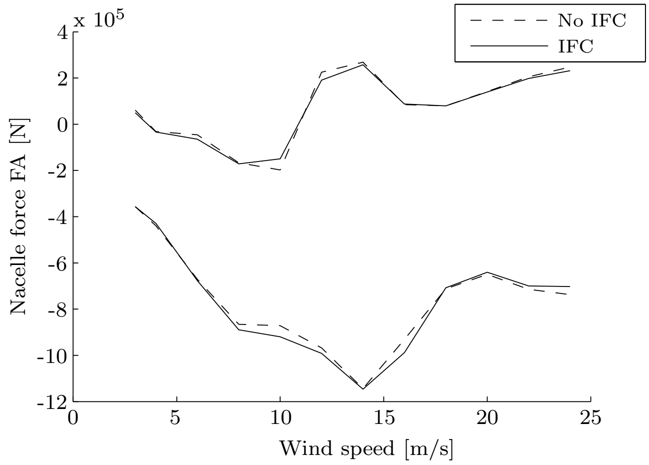

Figure 6.14: Extreme turbulence during power production: nacelle force FA

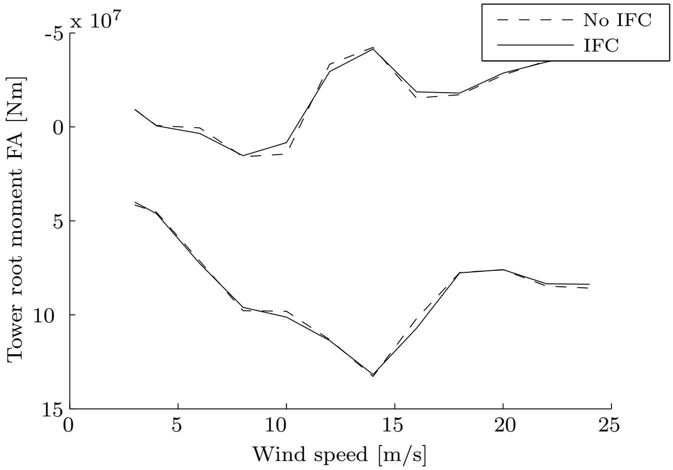

Figure 6.15: Extreme turbulence during power production: tower root FA moment

them by 6%. It is worthwhile noticing that the controller reduces the deflections below and around the rated wind speed but increases the deflection above the rated wind speed. The operation of the flaps causes an increase in drag and results in slightly lower rotational speeds for the same wind field if compared with a conventional turbine. This causes the pitch setting to be lower. It is also manifested in the pitch angle range that is a direct function of the operational speed. Figure 6.17 shows the maximum occurring pitch angle in the wind speed bins. It is worth noting, that even though the average wind speed can be below the rated speed, due to the turbulent time history, pitch activity can occur, when the turbine is hit by a gust and the instantaneous rotor velocity exceeds the turbine rating. While the highest pitch angle that is found in the simulations is only marginally reduced, the reduction of the lowest pitch angle that occurs for a certain wind speed bin is clearly visible in Figure 6.17. This lowest pitch setting corresponds to the lowest operational speed that occurs during turbine operation for a certain wind speed bin. The thrust of a turbine is highest at the rated wind speed, therefore a direct increase in bending moment throughout the blade and a higher tip deflection is to be expected above the rated wind speed, when using smart rotors. Below the rated wind speed, the reduction in rotational speed leads to a reduction in dynamic pressure and thus a decrease in thrust.

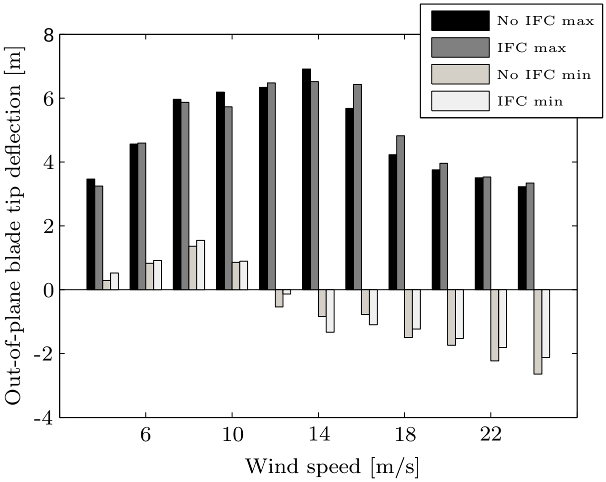

Figure 6.16: Ultimate out-of-plane tip displacement during power production in extreme turbulence

6.5.4 EXTREME GUST AND CHANGE OF DIRECTION

The extreme gust load cases during turbine start-up are not highly critical for the ultimate load determination as prescribed by the design load cases compared to the previously analyzed power production load cases with extreme turbulence. Neither is the extreme gust load case with direction change during power production. Similarly, for the ultimate loads during power production, the maximum and minimum load values of only few components are significantly affected by the smart rotor. These simulations have been repeated for different initial azimuth settings in steps of 30 degrees, such that a total of four blade positions have been investigated. The results presented in this section are the ultimate loads found during any of these simulations. Figures 6.18 to 6.23 display the components with

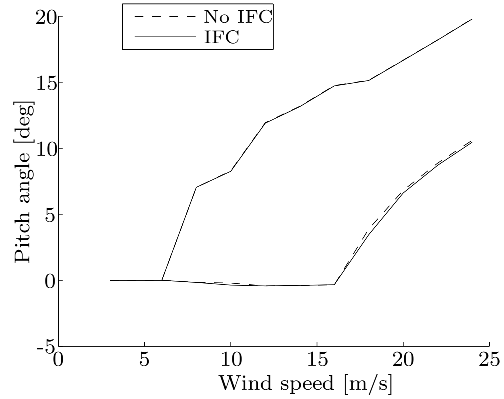

Figure 6.17: Pitch angle envelope during power production in extreme turbulence

the strongest load change.

- The blade root bending moment is neither reduced nor increased significantly.
- This is also true for the blade tip deflections.
- The torsional blade root moment is increased for all load cases.
- The ultimate torsional loads in the tower and the shaft bending moment are reduced.
- All other components are not affected by the smart wind turbine rotor.

For the bending behaviour of the turbine blade, the changes in ultimate loads and deflections are in the order of few percent as shown in Figures 6.18 and 6.19. It is critical when the gust or direction change is initialised. Already a postponement of the gust condition of 0.5 seconds can turn the reduction potential into increased loading. Figure 6.20, which displays the tip deflections during turbine start-up at the rated wind speed with extreme change of wind direction, illustrates this effect further. During the initial phase of the start-up, the blade gets excited and the vibrations at the first eigenfrequency are visible up to 5 seconds. As the rotational speed of the turbine is rather low, the dynamic pressure is correspondingly low. The resulting tip deflection is initially small, but increases with increasing rotational speed. Compared to the tip deflections of the conventional turbine, the IFC causes a steeper increase in the tip deflection from 5 to 8 seconds. During this phase, the turbine blade points downwards and passes through the lower layer of the wind shear. The controller increases the loads in this region. The turbine leaves this region at 8.0 m/s. While the blade is pointing upwards and seeing higher wind speeds as a result of wind shear, the controller starts to reduce the blade loading. Consequently, the tip deflections are lower than in the uncontrolled case. At 14 seconds, the blade is horizontal. The IFC starts to increase the loads at this location in an effort to keep the loading constant over a rotation cycle. The tip deflections increase quickly and pass the uncontrolled case. The direction change of the wind is initialised at 10 seconds, but during the first 3-4 seconds its effects are small compared to the increase in dynamic pressure that comes along with the turbine speed-up. Only at 15 seconds, the effects start to balance each other. The turbine starts to slow down as the axial component in wind speed is significantly reduced. As the slowing down starts when the blade points downwards, the IFC increases the tip deflection. Accordingly, if the change of direction would occur while the blade is pointing upwards, the ultimate tip deflection would be reduced. Indeed, for the three blades, always some of the blades experience a reduction, while others see an increase in root bending moment and tip deflection.

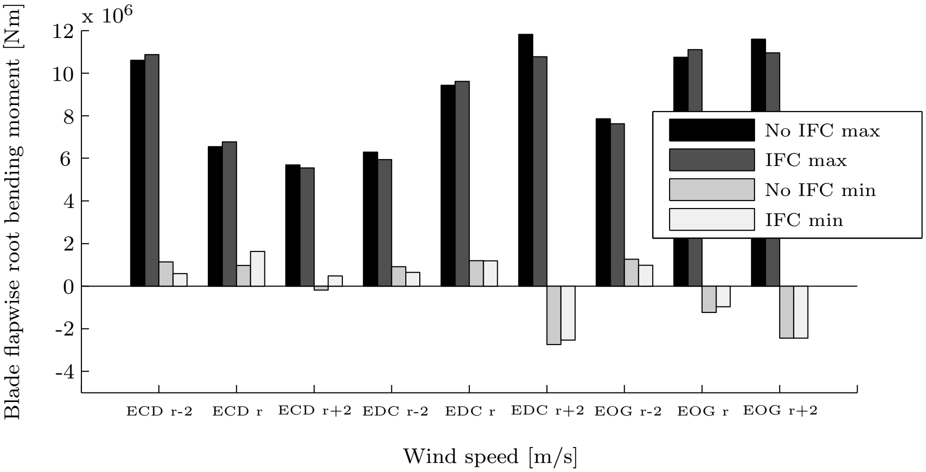

Figure 6.18: Ultimate blade root bending moment during extreme events during start-up and power production

While the picture for the bending moment and tip deflection on the turbine is ambiguous, the increase in ultimate loading for the blade root torsional moment (Figure 6.21) manifests itself in all load cases and independent of the blade orientation. The reason for this increase is the aft loading of the wind turbine blade as mentioned before. However, ultimately, the values of the extreme gust cases remain below the peak values that are reached during power production with an extreme turbulence model.

Two components experience a load decrease for practically all extreme gust load cases. The first component is the torsional moment in the tower, as shown in

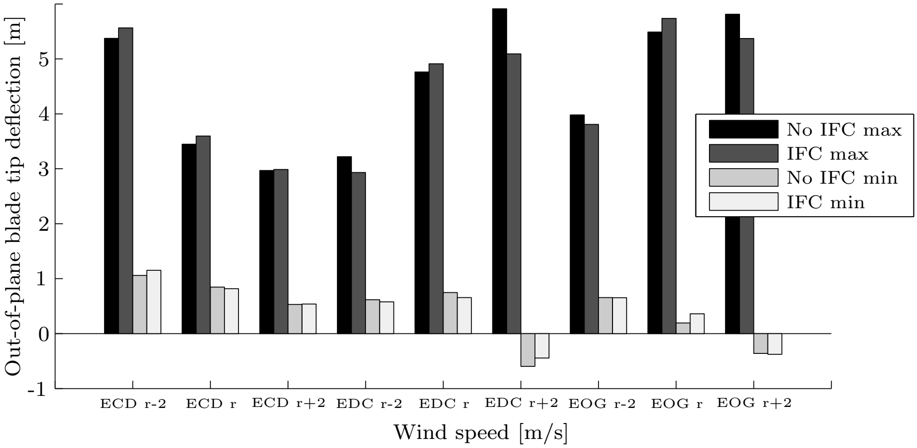

Figure 6.19: Maximum out-of-plane blade tip deflection during extreme events during start-up and power production

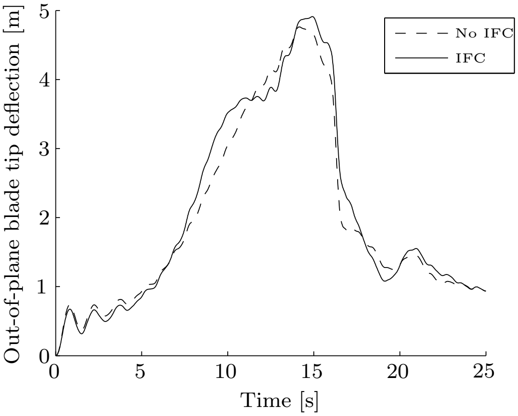

Figure 6.20: Blade tip deflection during EDC at the rated wind speed

Figure 6.22, and the second component is the shaft bending moment as shown in Figure 6.23. The torsional loads in the tower are shifted towards negative values, causing the highest loads to decrease and the negative loads to increase. As this negative component still remains lower than the positive value in absolute terms, the ultimate load is effectively decreased. For the shaft bending moment, both positive and negative values are decreased, such that an overall load reduction takes place.

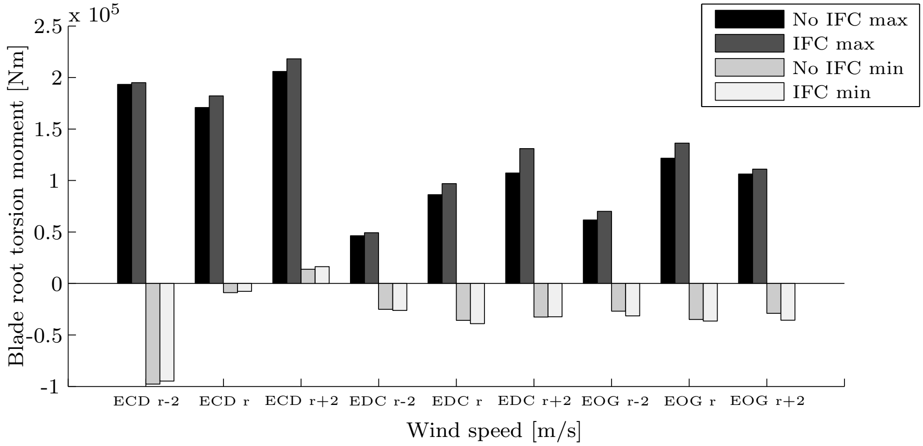

Figure 6.21: Ultimate blade root torsional moment during extreme events during start-up and power production

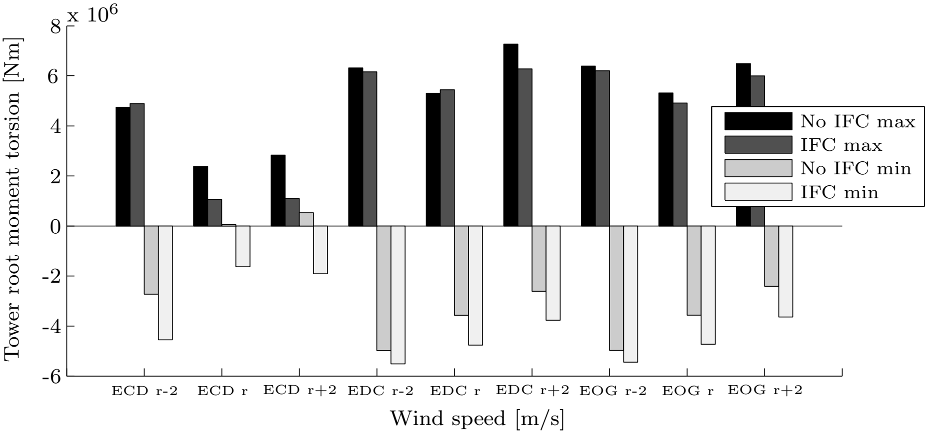

Figure 6.22: Ultimate torsional moment at tower bottom during extreme events during start-up and power production

6.6 EVALUATION OF RESULTS

The estimated load reduction in this chapter only partially reflects the potential of including smart elements in wind turbine designs. Bernhammer, van Kuik and De Breuker (2014) point out that an even further reduction in loads can be realised, when the load reduction potential of flaps is included in the design of a turbine blade.

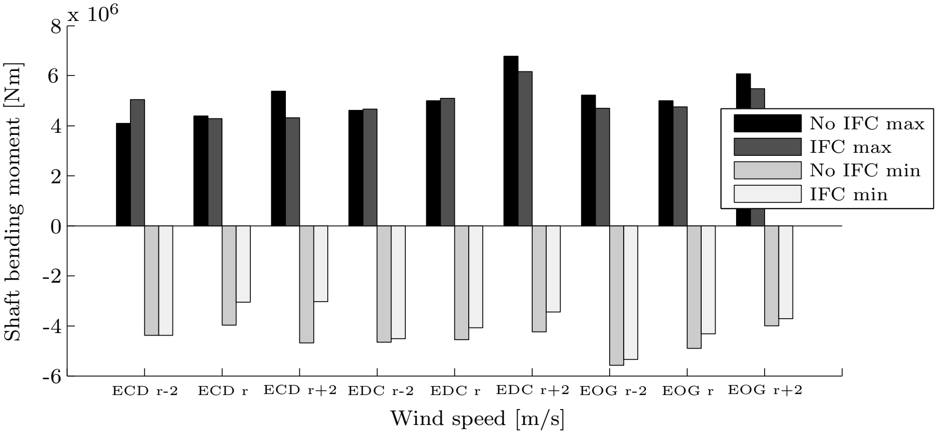

Figure 6.23: Ultimate shaft bending moment during extreme events during start-up

As has been shown in this chapter, smart rotors can reduce both fatigue and ultimate loads for several turbine components and the selection of design load cases. Flaps are applied to the turbine in this chapter without changing the blade structure to accommodate them. Two design considerations need to be taken when including smart rotors from the get-go of the turbine design. Firstly, the blade needs to be re-enforced locally such that the forces generated by the flap can be introduced into the blade structure. This will cause a locally heavier blade structure.

The second design step, however, is much more interesting. Presuming that the blade design is stiffness driven and that tower clearance and blade root moments are design drivers, the reduction in out-of-plane deflection of 6% can be directly converted into a reduction of blade stiffness requirements, assuming that the maximum deflection is not caused by resonance. The time scale of the deflections is much longer than the frequency of vibration of the first blade mode, which renders the assumption realistic. This reduction in stiffness is complemented by a reduction in the ultimate blade root stresses that are observed during all simulations of 8%. Relaxing the stiffness requirement translates into less blade mass. This in turn will reduce the edgewise bending moment as it is gravitiy driven. This means that even though the decrease in ultimate edgewise moments is marginal when including the IFC controller, upon a redesign, the load reductions will be in the same order of magnitude as for the flapwise root moment. This scaling approach holds true not only for the edgwise root moment, but also for several other turbine components, such as the shaft bending moments or the vertical tower forces.

This potential redesign of the blade would also positively affect the fatigue damage equivalent loads. In the example of the edgewise root bending moment, the damage equivalent load is directly proportional to the mass of the blade. Including this in the load alleviation reduction means that the edgewise fatigue loads can also be reduced not only by 1.5% as computed, but rather by 7%.

Finally, also some attention should be paid to the blade torsion, which is significantly increased both for the fatigue and for the extreme loads. This increase is a result of the activity of the trailing edge flap, which naturally modifies the pressure field close to the trailing edge. This variation causes a sectional moment. The increase can be kept in limits, when a more advanced flap-slat system would be designed that increases loads both at the leading and at the trailing edge, thereby distributing the control forces more evenly around the airfoil. Further studies need to show if the complexity of such a system is worth the potential reduction in blade root moments.

All these load reductions can be translated into a lighter and potentially less costly structure. The cost saving originating from the load reduction needs to be compared to costs associated with the flap system and the reduction in power production of smart rotors compared to conventional machines. Lower loads mean that a blade can be manufactured using less material and with less composite layers, which reduces the labor costs. It is also expected that a reduction in blade mass makes the installation of the turbine blades cheaper as smaller equipment can be used. An alternative way of decreasing the cost of energy would be to keep the production costs the same, but to be able to build a larger wind turbine blade, which increases the energy production.

A complete cost assessment would naturally include the production and maintenance costs of a flap system. As such systems are not yet installed on turbines, an estimation of costs therefore is difficult, as uncertain parameters as the reliability of a flap system needs to be modelled. The reliability is a key issue that has not yet been resolved for a utility scale wind turbine. Certainly for offshore turbines, the solution to this challenge is of utmost importance as the downtime of a turbine is related to failures of such a system. If blades are designed based on the loads that can be expected with smart blades, a failure of the flap system would mean that the operation of the turbine would need to be stopped.

6.7 POWER OPTIMISATION IN LOW FATIGUE REGIONS

As has been shown in Figures 6.5 to 6.10, the main contribution to fatigue loads during power production is either around or above the rated wind speed. The cumulative contribution of wind speeds below the rated wind speed to the damage equivalent flaproot bending moment is 2%. In this operational region of maximum power control, the activity of the smart rotor does not significantly add to the overall fatigue reduction. Extreme events are also more likely to occur above the rated wind speed and the use of a flap system to mitigate ultimate loads below the rated wind speed will not aid in alleviating design constraints. It therefore can be assumed that the smart rotor can be used for a secondary purpose. Such a purpose can be the quick adaptation of the rotor to react to unsteady effects to increase power capture.

Wind turbine blades are designed such that they deliver a maximum of power for a given tip speed ratio. This ratio between incoming wind and the rotational speed of the tip of a blade varies strongly as a result of turbulence and wind shear. Due to the large inertia of the rotor, the angular speed is only adapted slowly, when a change in inflow occurs. The result is that during a significant share of the operation time, the turbine operates at a suboptimal tip speed ratio. These unsteadiness in aerodynamics can be addressed by the flaps of a smart rotor, which have a high frequency bandwidth, making them particularly suitable to react to turbulence and local effects.

6.7.1 AERODYNAMIC MODEL FOR POWER OPTIMISATION

For the optimisation procedure of the ideal flap angle, an unsteady blade element momentum (BEM) tool has been developed. This code is based on the framework developed by Hansen (2008) and includes a dynamic wake model proposed by Schepers et al. (1995). As in the DU-SWAT, the ATEFlap model (Bergami et al. (2015)) is used to compute the unsteady aerodynamic airfoil forces. The model has been benchmarked against HAWC2 by Smit et al. (2014) for a range of wind speeds from 5.0 m/s to 11.0 m/s and flap deflection angles up to 8 degrees. The maximum difference between coefficients in any of these simulations was 1.5%.

6.7.2 STATIC OPTIMISATION OF POWER USING FLAPS

A first static analysis of the dependency of the power production on both pitch and flap deflections has been performed using the aerodynamic model. Power curves have been computed for a baseline case and for the ideal flap deflection, the ideal pitch deflection and combined flap and pitch angles. The optimum power curves are shown in Figure 6.24. The associated flap and pitch angles are displayed in Figure 6.25. In the optimisation, the maximum flap deflection has been limited to 10 degrees. As can be seen, the maximum power coefficient is obtained for a tip speed ratio of 8. This tip speed ratio is a design condition for the blade and can therefore be improved by neither flap deflections nor pitching of the entire blade. The velocities that are indicated in Figure 6.24 correspond to the tip speed ratios as specified by Jonkman et al. (2009) for the 5MW reference turbine. It can be seen that overall flaps are more suitable to change the power curve than pitching is. For tip speed ratios above 4.8, flaps consistently produce a higher power coefficient than pitching does. It is assumed that pitching always implies a trade-off between the power contribution of different spanwise locations, whereas flaps provide a more local and thus more efficient control approach. Almost in the entire regime of interest of tip speed ratios above 6, there is hardly any difference between the power values that can be achieved with flap deflections only or with a combined flap and pitch optimisation.

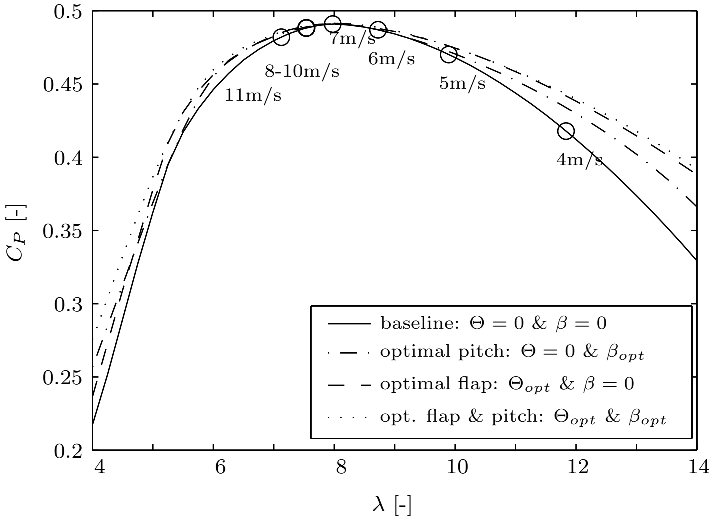

Figure 6.24: Baseline and improved power curves using flaps and/or blade pitch and corresponding control settings, with circles representing tip speed ratios for wind speeds below the rated wind speed and constant, uniform inflow

Figure 6.25 shows that indeed the only contribution on power production, which pitching of the blades can make, is a limitation of the flap activity, which however comes at the price of a significant increase in pitch activity.

6.7.3 CONTROLLER DESIGN FOR MAXIMUM POWER

Based on the insight gained from the static power curves as a function of the tip speed ratio, two controllers were developed to assess the power increase that can be realised using smart rotors.

A first control approach is a look-up table controller (LTC), which is illustrated in Figure 6.26. In this approach an instationary, local speed ratio is defined, based on the angular velocity of the rotor and the instantaneous wind and induction velocities at the flapped blade section. This local speed ratio was used to find the optimum flap angle as shown in Figure 6.25.

The second control approach is a model predictive controller, where the sys-

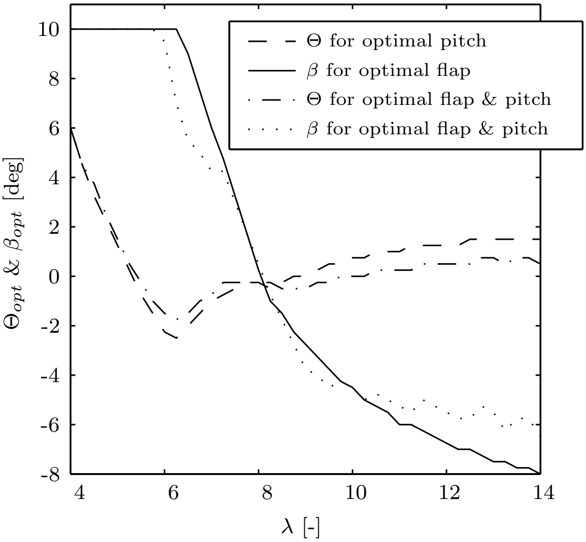

Figure 6.25: Optimum flap deflection angle and pitch angle for improved power curves

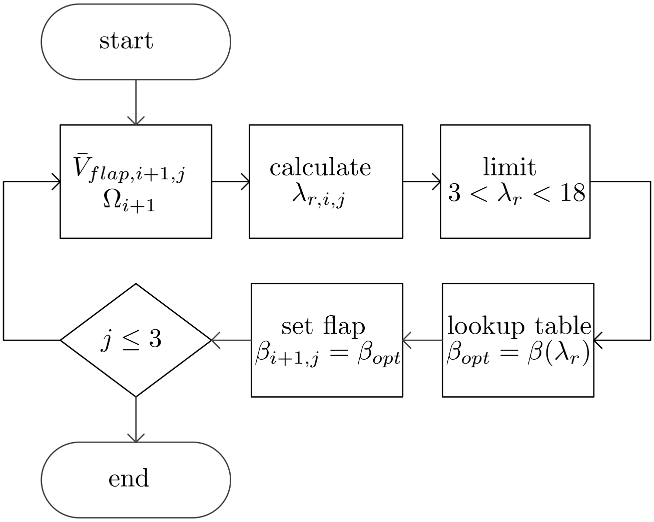

Figure 6.26: Lookup table controller (LTC)

tem output was predicted over a horizon maximizing the energy capture in this time period. Details of this approach are provided by Smit et al. (2014). The computational costs for the model predictive controller are significantly higher, certainly as a long time horizon of 2.5 seconds is required to show an improvement in power production compared to the look-up table controller as shown in Table 6.3. Table 6.3 displays the result of a controller benchmark test using a uniform wind field and wave signal as wind input. The wave signal alternates between 9.0 and 10.0 m/s. All controllers show an increase in captured power. The MPC with a prediction horizon of 0.5 seconds increases energy production for this benchmark by 0.3% but the LTC, which was computed much faster than real time, provides even better results. A MPC controller with a prediction horizon of 2.5 seconds provides the best result. However such a controller cannot be used in wind turbines. Even in combination with a simple BEM model, the computational time is too long to be used on wind turbines in a field test. Therefore it was opted to continue the simulations with the look-up table controller.

Table 6.3: Increase in power from LTC and MPC

	LTC	MPC	
		$t_{horiz} = 0.5$s	$t_{horiz} = 2.5$s
ΔP_{aero} [%]	0.30	0.25	0.40
$\Delta P_{generator}$ [%]	0.31	0.21	0.42

6.7.4 TIME DOMAIN SIMULATIONS

Time domain simulations have been performed with two different models. The first model is the aerodynamic model that has been used to optimise the flap deflections angles in Section 6.7.3. The second model is a full aeroelastic analysis in the DU-SWAT (Chapter 3). There is a distinct difference between both models. The BEM tool can only handle one-dimensional turbulence which is uniform over the rotor area, whereas the DU-SWAT can deal with spatially distributed turbulence in three directions. Computations were performed for a 5-minute time history of turbulence. The input to the BEM tool was the axial component of the wind speed at hub height. Figure 6.27 shows the increase in power for below the rated wind speed that could be realised in both simulations. The DU-SWAT consistently produces higher results than the purely aerodynamic model. To allocate the source of the differences, an analysis with only the aerodynamic module of the DU-SWAT has been performed, but including a complex, spatially distributed turbulence field. The difference in power production between the aerodynamic model of the DU-SWAT and the BEM tool was as little as 0.1%.

Therefore, difference in power is associated with structural deformations. As was concluded also for the extreme and fatigue load analysis, the trailing edge flaps introduce a significant increase in torsional moment of the blades. Figure 6.28 compares the average torsional deformation of the flapped blade section. Indeed, the active flap for power control causes consistently a lower structural twist angle. While the maximum difference of 0.1 degrees seems small, it still has a

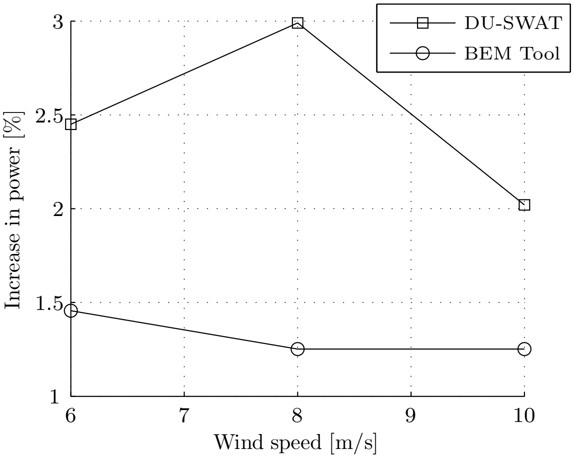

Figure 6.27: Increase in energy versus wind speed for 5-minute simulations

significant effect on the overall power production. The maximum lift-over-drag ratio of the NACA 64-618 airfoil lies around an angle of attack of 5 degrees. Indeed the simulations have shown that the for all wind speeds below the rated speed, the average angles of attack of the simulations that include flaps are closer to this angle than that of the ones without flap activity. This leads to the conclusion, that the twist distribution of the NREL 5MW turbine is not ideal for the power production below the rated wind speed and could be further optimised with aeroelastic tailoring, such that the off-rated wind speed regimes contribute more to the power generation.

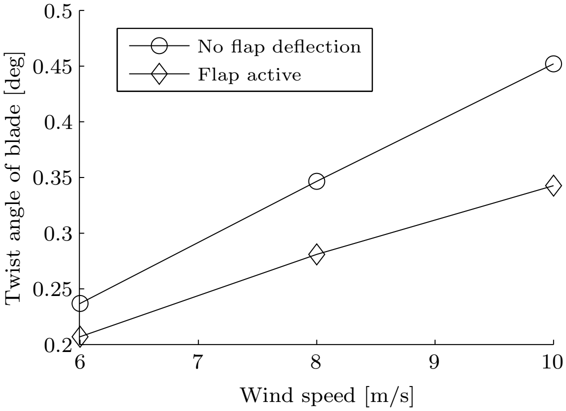

Figure 6.28: Aerodynamic and structural properties, at flapped blade section, averaged over the simulation time

Finally, the impact of the flap activity on the fatigue damage has been investigated. The increase in blade root moments is provided in Figure 6.29. The increase in the damage equivalent load is significant for the considered wind speeds, however, one needs to remember that wind speeds below the rated wind speed only contribute little to the overall damage. The resulting increases of damage equivalent loads over the turbine lifetime are 0.2% for the flapwise bending moment, but 21% for blade root torsional moments, which is in the same order of magnitude as has been found in the fatigue load analysis.

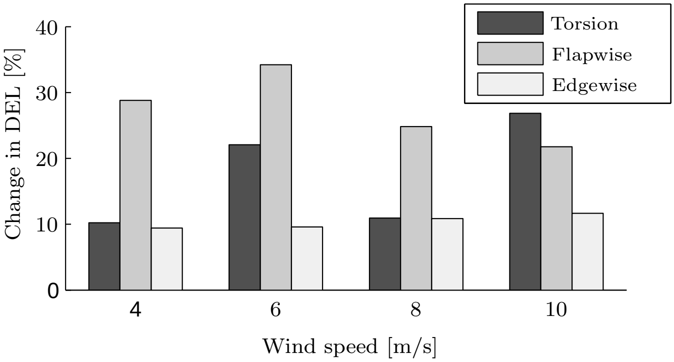

Figure 6.29: Increase in blade root moment damage equivalent loads vs. wind speed

6.8 SYNOPSIS

The load reduction potential has been assessed in this chapter for a range of turbine components, including blades, shaft and tower. Both extreme loads and fatigue damage equivalent loads have been investigated using an individual flap controller.

- The fatigue load reduction of the blade root bending moment of 24% has been benchmarked with previous analyses and found to be in agreement with the work of Barlas and the work of Anderson, but higher than the reduction found by Baek.
- Most other turbine components such as shaft, nacelle or tower experience a reduction of fatigue loads up to 10%.
- Blade root torsional loads are significantly increased.
- Extreme loads are significantly reduced in the tower. Most notable are loads that originate from the asymmetry of the inflow such as fore-aft and torsional tower moments.

- The ultimate loads of many components are hardly affected by the individual flap controller.
- The ultimate flapwise blade root moment is reduced by 8% and the maximum tip deflection is decreased by 6%.
- Most damage is accumulated either around or above the rated wind speed. The flaps can therefore be used for a secondary purpose below the rated wind speed.
- The power coefficient in the power optimised control region (region 2) varies strongly as a result of turbulence. Flaps are very suitable to increase the power because of their high bandwidth and low actuation costs.
- Flaps can increase the power production of the design tip speed ratio more than pitch control can.
- The power output below the rated wind speed can be increased by 2.5-3.0%.
- Using flaps in region 2 for power maximisation only increases the blade root moment marginally.

Part II

Smart Wind Turbine: Autonomous Flap

I believe that if one always looked at the skies, one would end up with wings.
Gustave Flaubert

7

FLAP CONCEPTS FOR WIND TURBINES

7.1 INTRODUCTION

The physical implementation of smart rotors still is one of the main remaining challenges. Research has mostly focused on increasing the lifetime of smart rotor components in a response to costly maintenance of offshore wind turbines. In this chapter an alternative approach is presented by introducing a flap concept that can be easily exchanged. This research is motivated by an analysis of the design requirements of smart rotors originated from previous studies compared with the outcome of the full turbine analysis. An overview on the physical implementations of other institutes is given. In a next step, an alternative flap concept is introduced, the free-floating flap (FFF). This flap concept has been investigated for aeronautical application, such as flutter suppression.

7.2 REQUIREMENTS DERIVED IN PREVIOUS STUDIES

Already more than a decade ago, the first evaluation of requirements on smart rotors has been made by Marrant et al. (2002), who present an almost purely qualitative list of requirements that a smart rotor system needs to fulfill. According to Marrant et al. (2002), sensors and actuators in smart rotors need to:

- be lightweight
- provide a broadband response
- provide large amplitudes
- respond with minimum destabilizing delays
- be robust with regard to large thermal gradients and radiation
- have a minimal effect on the passive system dynamics
- have a long life and low maintenance requirements (design life of 20-25 years)
- operate in harsh environment (rain, humidity, corrosion, salt, lightning)

Barlas, Lutz, Bak, Hulskamp and Apinaniz (2010) have expanded this list by including aerodynamic, structural and controller requirements. While most of the requirements are still qualitative, such as noise limits or no structural stiffness reduction, Barlas, Lutz, Bak, Hulskamp and Apinaniz (2010) are the first to quantify deflection and frequency requirements. This has been done based on the work of Barlas (2011), who did a load analysis of a conventional turbine to identify the frequencies of interest for load alleviation. All frequencies that contribute to fatigue and extreme loads for a 5MW turbine are between 0.0 and 6.0 Hz, while the 1P frequency is the most dominating load frequency. In addition to this analysis, Barlas (2011) carried out a steady aerodynamic analysis of the moment reduction that a flap can achieve on the wind turbine. To fully alleviate the loads, Barlas finds that a flap with 10% chord length would require a static deflection of 12 degrees.

7.3 REQUIREMENTS IMPOSED BY TURBINE ASSESSMENT

The requirements of the flap deflection, which are briefly addressed in Chapter 6 are further elaborated on in this section. As was shown, the root-mean square of the flap deflection amplitude during power production load cases increases almost linearly with wind speed (Figure 6.4). Still, amplitudes remain very modest up to a RMS of 4 degrees. This is confirmed in Figure 7.1, which displays the time fraction the flap deflection stays below a threshold in these simulations. In the load assessment presented in this dissertation, the individual flap controller was tuned such that around rated wind speed a maximum flap deflection of 5 degrees would be reached. Indeed, the time fraction of the flap deflection below 5 degrees is equal to or above 0.9, meaning that during most of the simulation time 5 degrees flap deflection angles were sufficient for load control around rated wind speed. This rated wind speed together with the cut-out wind speed is the main driver for the fatigue and ultimate loads for most wind turbine components as has been shown. The flap deflection angles requirements are almost constant for a broad range of wind speeds. From the cut-in wind speed of 4.0 m/s until the cut-out wind speed of 25.0 m/s, 5 degrees flap deflection are sufficient for 90% or more of the simulated time. If the maximum possible flap deflection angle is set to 6 degrees, the time fraction increases to more than 95%. A full coverage can be reached with flap deflection angles of 8 degrees. Overall, it can be said that the requirements derived by Barlas, Lutz, Bak, Hulskamp and Apinaniz (2010) have a large margin to the actual deflection amplitude as determined in the detailed load assessment. In fact, most of the load alleviation can be realised with an amplitude of 6 degrees, which is only half of the amplitude found by Barlas, Lutz, Bak, Hulskamp and Apinaniz (2010).

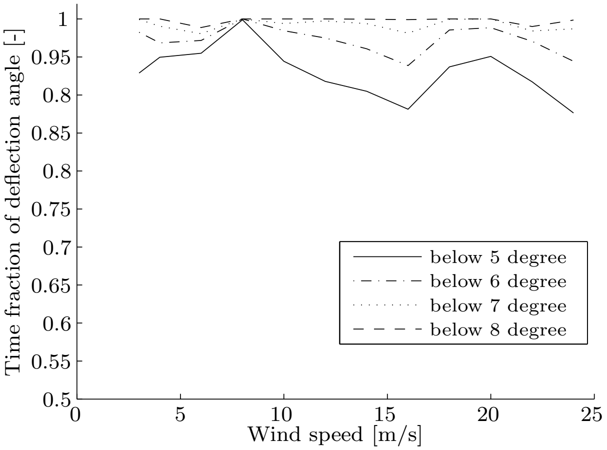

Figure 7.1: Flap activity during power production vs. wind speed

A second requirement, which follows from the load analysis of the 5MW reference turbine, is the frequency range a flap should cover. Figure 7.2 shows the frequency spectrum obtained by a Fast Fourier Transform from time-domain simulations including a three-dimensional turbulence field at rated wind speed. Remembering that in the presented analysis, the flap controller was designed analogue to the individual pitch control using a Coleman transform to eliminate the driving fatigue loads in the blades around 1P frequencies, the peak at 0.1 Hz can be explained. The flap deflections at this frequency are a factor of 100 larger than for the first flapwise eigenmode, which, for a 5MW turbine, occurs at 0.7 Hz. The amplitude of the flap oscillation at the second flapwise eigenfrequency around

2.0 Hz is yet another order of magnitude lower. Higher order eigenfrequencies cannot be identified based on the spectrum of the flap activity. Therefore, one has to conclude that the frequency bandwidth requirement of 0.0 - 6.0 Hz derived by Barlas, Lutz, Bak, Hulskamp and Apinaniz (2010) cannot be justified by load reduction purposes only. Even when addressing the the first and second flapwise eigenfrequency, a smaller control bandwidth is required. A more realistic bandwidth requirement would be 0.0 - 2.5 Hz. This value can however increase if aeroelastic stability issues were to be addressed by the system, which would originate from the interaction of a twisting mode and a flapwise mode, typically at higher frequencies.

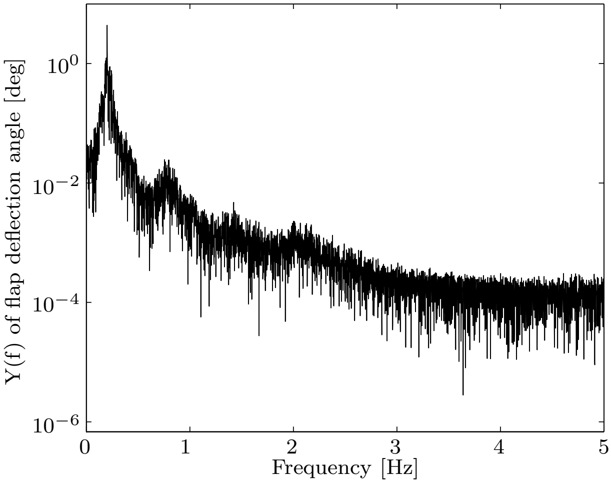

Figure 7.2: Frequency spectrum of flap activity at rated wind speed

7.4 A REVIEW OF FLAP AND MORPHING AIRFOIL CONCEPTS

The different requirements on durability and performance of the morphing section have led to a wide range of potential concepts for flaps on wind turbine blades. In this section a coarse overview is given before a concept is chosen, which will be explained in further detail. While a rough overview on different flap concepts is provided in this chapter, a more comprehensive overview on morphing concepts for both wind turbine and helicopter blades is provided by Lachenal et al. (2013) including an overview on different materials used in the morphing process. Lachenal et al. (2013) not only review flap concepts, but also give a more global overview on span extensions, planform changes, twisting and camber changes.

So far, two paths can be seen in flap design for wind turbine blades. The first approach is using classical, discrete flaps because of their simplicity of integration. The other approach is to respond to the performance requirements with seamless, morphing concepts that change the camber of a given blade section. For both concepts, the full morphing airfoil and the trailing edge flaps, but also for microtabs, the same magnitude of control forces can be generated (Barlas, 2011) with lift coefficient changes between 0.20 and 0.60. The magnitude of these changes is dependent mainly on the length of the deflecting section. The control authority of all presented concepts is similar provided that the actuation system allows to follow a specified control signal accurately. The advantage of morphing concepts is that the drag forces are lower than for discrete flaps.

The discrete flap concept has the highest technology readiness level and was therefore chosen for both field test turbines. Castaignet et al. (2014) describe the flap system on the Vestas V27 turbine as 'stiff hinged flaps', but do not specify the actuation mechanism. A similar approach is used in the Sandia National Laboratories Smart Rotor Program, in which a Micon 65/13 turbine was equipped with a rigid flap driven by electronic motors (Berg et al. (2012)). Despite the conventional layout, both experiments reported problems with the reliability of the flap system, which in the case of the V27 resulted in only one of three flaps being operational during the experimental study (Castaignet et al. (2014)).

7.4.1 PRESSURE ACTUATED CONCEPTS

The alternative concept using adaptive trailing edges has received more attention in smart rotor research over the last decade. Therefore, a great variety of concepts has been presented. A first morphing concept is the Controllable Rubber Trailing Edge Flap (CRTEF) developed by DTU Risø(Madsen et al., 2010). In this concept, a trailing edge constituted of solid rubber enclosing cavities is used as deflecting device. The cavities can be pressurised individually and due to pressure differences between the cavities a deformation is realised. These pressurised rubber flaps are a very promising concept for wind turbine blades as a smooth shape transition is achieved. Additionally, it is one of the few systems that does not rely on electrical actuation close to the tip, such that shielding against lightning strikes is not required. The obstacle with pressurised flaps is that the pressure tubes need to be long to reach the position of the most efficient location of the flaps on the blade. This introduces a time delay between the control signal and the actual control event, leading to a reduction in control efficiency or even to instabilities. Barlas and Madsen (2011) have identified the shortcoming that 'increased actuator lag considerably reduces the predicted fatigue load reduction'. Therefore, a control algorithms was investigated that includes the actuator dynamics into the modelling, resulting in less pronounced losses in the fatigue load alleviation.

A similar concept has been presented by Vos and Barrett (2011). However, instead of using a rubber flap with cavities, a honeycomb structure was employed. Figure 7.3 displays the schematics of the concept. This system has been developed for aircraft applications but the concept can be applied to wind turbines in the same manner. The torque box remains a fix geometry and carries the bending and torsional loads, while both trailing and leading edge of the airfoil are constructed of a honeycomb with a flexible skin. The cells of the honeycomb can be individually pressurised such that due to the pressure differences the structure will morph. Vos and Barrett (2011) state as distinct advantage of this system over comparable systems that are actuated by shape-memory alloys, piezoelectric materials or electrorheological fluids, the ease of certifiability as the materials used in such a set-up are well-characterised.

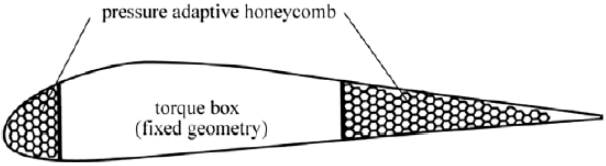

Figure 7.3: Sketch of the pressure adaptive honeycomb general arrangement with pressure adaptive nose and flap sections (Vos and Barrett (2011))

7.4.2 DISCRETE ACTUATION

Another approach, which makes use of the difference in anisotropic properties of a honeycomb structure, is presented by Daynes and Weaver (2011). In their flap configuration, a NACA 63418 was equipped with a 20% chord flap constructed of an aramid honeycomb and a silicon skin. The difference from the previous concept is that the actuation is done using a servo motor. Four flaps have been installed on a test section as shown in Figure 7.4. During the experiment trailing edge velocities of 9 deg/s could be achieved, which is high enough to satisfy the requirements derived to control 1P frequencies and the first structural mode of the reference turbine, but is lower than the Sandia National Laboratories Smart Rotor bandwidth. The maximum rotational velocities are also not high enough to satisfy the requirements derived by Barlas (2011).

Instead of using the honeycomb, Barthley-Cho et al. (2004) built a fishbone to create a structure that is flexible in camber deformations, but stiff in spanwise direction. This configuration is popular among other research groups (Campanile and Sachaul (n.d.); Woods et al. (2014)). Besides the already mentioned servo actuators, Barthley-Cho et al. (2004) also identify ultrasonic motors, piezoelectric stack actuators and shape-memory alloys as suitable actuation mecha-

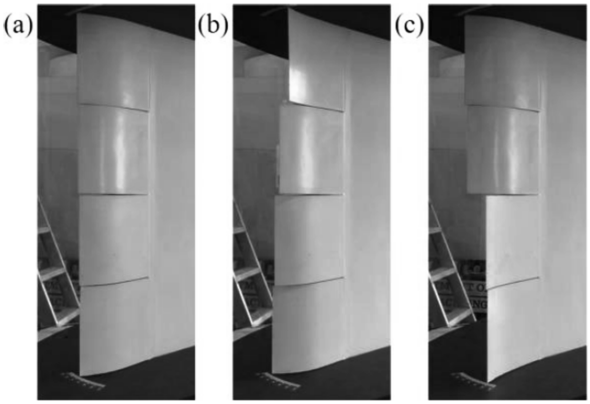

Figure 7.4: Spanwise geometries with adaptive trailing edge; (a) uniform 5 deg deflection, (b) 'twist' mode, (c) 'braking' mode (Daynes and Weaver (2012))

nisms to achieve high-rate deformations combined with large forces. The choice of Barthley-Cho et al. (2004) falls on accentuators and ultrasonic motors, while both Woods et al. (2014) and Campanile and Sachaul (n.d.) rely on cables to actuate the deformation. The cross-section of a typical fishbone configuration is displayed in Figure 7.5, showing the backbone, which will bend, and the vertical bones that ensure the shape of the airfoil during deformation. During wind tunnel tests, it was concluded that such configurations can improve the lift-over-drag ratio of the airfoil not only if the flap is deflected, but also, due to the smooth transition in the baseline configuration by 20-25% compared to rigid flaps.

7.4.3 WIND TUNNEL STUDIES

In contrast to full-scale testing, the requirements on models used in wind tunnel studies are different. Due to scaling, the bandwidth of the actuation system needs to be increased to more than 20 Hz. Other requirements like durability vanish for a proof-of-concept experiment. This leaves the bandwidth of the frequencies of interest as a major driver in the choice of the actuation system. This proof of concept of load alleviation has been done by Delft University of Technology under laboratory conditions using piezoelectric benders (Barlas, van Wingerden, Hulskamp, van Kuik, Verhaegen and Bersee (2010); Hulskamp et al. (2010); van Wingerden et al. (2010)). Such benders operate at very high frequencies, but can only generate a small amount of force, rendering them unsuitable for outdoor, full-scale experiments.

Andersen et al. (2007) have taken a similar approach to construct a flap system using piezoelectric patches as active trailing edge component as shown in Figure

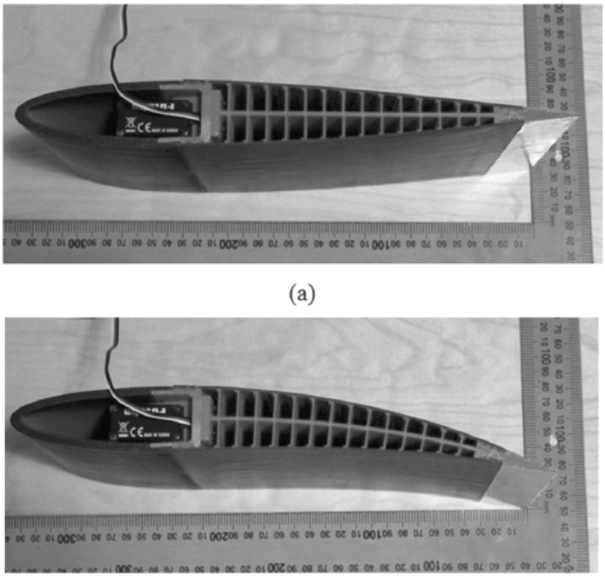

(a)

(b)

Figure 7.5: FishBAC wind tunnel model (a) baseline state and (b) deflected (Woods et al. (2014))

7.6. The piezoelectric benders are mounted on steel substrates. Structurally, these patches are clamped to the trailing edge of a rigid airfoil. In total 36 actuators are needed to cover the span of the test section.

Hulskamp (2011) made efforts to increase the frequency bandwidth of shape-memory alloys to the operational range of wind turbines by including active air cooling into the transformation process. While he succeeded to accomplish the frequency range of interest for full-scale turbines, the highest achieved oscillation frequencies that could be traced in an experimental set-up are still an order of magnitude lower than what is required for testing in a wind tunnel.

7.4.4 COMPLIANT MECHANISMS

A final option is the use of compliant structures in combination with any of the actuation systems in order to reduce the required forces that need to be generated to deflect the trailing edge flap. Saggere and Kota (1999) introduce this concept for airfoil shape control. The main design task for compliant mechanisms is to create a structural layout that can be deformed into a predefined shape with minimum energy requirements, while maintaining its shape otherwise. This task is normally accomplished by using first principles of mechanics and kinematics in

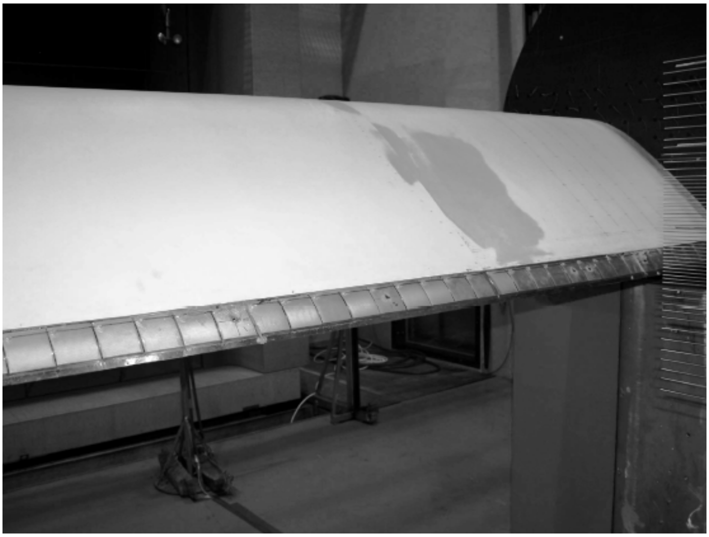

Figure 7.6: The Risoe-B1-18 airfoil equipped with the ATEG mounted in the wind tunnel stand (Andersen et al. (2007))

an optimisation routine.

For load control in wind turbine blades, two different compliant mechanisms have been proposed so far. One of these trailing edge flaps is the compliant trailing edge mechanism of Kosasih and Dicker (2014), which is based on the work of Gandhi et al. (2008), originally used in helicopter blades. Figure 7.7 shows the compliant mechanism. Vertical piezoelectric stacks serve as actuators. They are connected with crossing trusses such that a contraction will translate into a chordwise elongation of the associated trusses. Vice-versa, an elongation of the stack will cause a shortening in chordwise direction. By applying a differential between the upper piezoelectric stack and the lower stack, a bending moment can be created which leads to bending of the structure. The mechanism is covered with a flexible skin. Kosasih and Dicker (2014) used this configuration to realise changes in lift coefficient from -0.15 to 0.40.

A different route is taken by Barbarino et al. (2009), who use shape-memory alloys to actuate a rib of rigid structural elements as shown in Figure 7.8. The shape-memory alloy wires allow changing the distance between the two attachment points, thereby creating structural deformations. One disadvantage is that many rib elements are needed to ensure a smooth transition from one to another. The second disadvantage of shape memory alloys has been demonstrated by Hulskamp (2011), who showed that frequencies higher than the first eigenfrequency corresponding to flapwise blade bending, cannot be controlled, not even with active cooling of the wires. Without the cooling, even increasing the bandwidth to

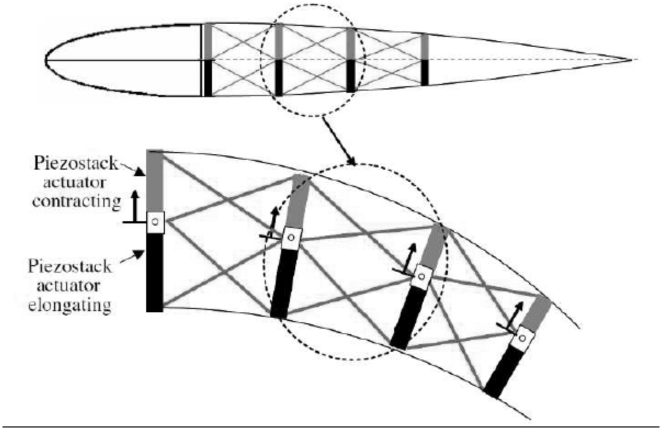

Figure 7.7: Variable camber compliant mechanism, vertical members are piezoelectric actuators (Gandhi et al. (2008))

include the first blade eigenfrequency would be a challenging design task.

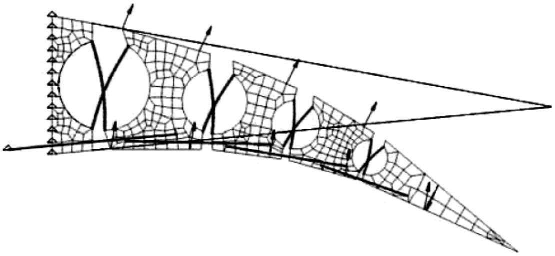

Figure 7.8: Rib morphed shape for all SMA wires activated (Barbarino et al. (2009))

These mechanisms should deflect with low actuation energy requirements, while providing strength and stiffness against all other deformation. A very suitable measure to achieve such anisotropic behaviour is tailoring of the composite skin. Gandhi and Anusonti-Inthra (2008) investigate skins with low in-plane axial stiffness, but high out-of-plane stiffness. It was shown that in camber morphing, the ideal solution is to reduce the axial stiffness to the minimum allowable such that no unacceptable camber deformation occurs under extreme aerodynamic loading.

7.4.5 AERO-MECHANICALLY ACTUATED SYSTEMS

A complete different group of flap designs can be grouped as aero-mechanically actuated systems. These systems use aerodynamic forces and moments to achieve a control force that counteracts the vibrations. This is done either in a passive or an active way. A first subgroup are bi- or multi-stable composite designs. Such an approach is described by Daynes et al. (2009) and Arrieta et al. (2014). The latter defines the structural configurations to 'allow for passively changing from a high lift generation shape to a load alleviation configuration exploiting the energy of the flow'. As such, the pressure variation around the airfoil during various operation regimes of wind turbine blade sections will cause a transition of one stable configuration to another one, thereby changing the aerodynamic forces of the section.

Instead of using the skin to achieve structural flexibility, Loth et al. (2010) segment the wind turbine blade. The segments are connected by screw sockets and a cable system as shown in Figure 7.9. The airfoil design was done such that the center of pressure is downstream of the socket axis. Therefore an aerodynamic moment is created, which, with increasing wind speed, causes the blade section to rotate to feather. One of the great disadvantages of this concept, besides the disrupted aerodynamic shape and the requirements on airfoil design, is that all loads need to be carried by a spar instead of the skin, which greatly increases the rotor mass.

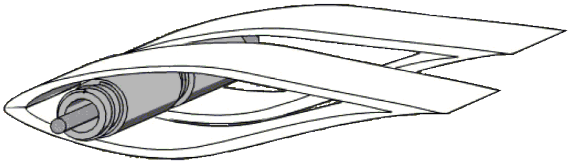

Figure 7.9: Concept of threaded socket between two blade segments: fully-wound condition for low speeds (Loth et al. (2010))

A third concept has been investigated by Lambie (2011), who mechanically links the leading edge and the trailing edge of an airfoil. Increasing pressure forces on the leading edge due to changing angles of attack cause a leading edge deflection, which is then converted mechanically into a trailing edge deflection. A sketch of this system is provided in Figure 7.10.

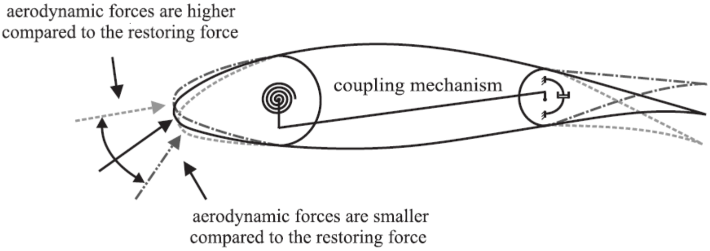

Figure 7.10: Airfoil with kinematically coupled leading- and trailing-edge flap (Lambie, 2011)

7.5 FREE-FLOATING FLAPS FOR LOAD CONTROL

7.5.1 THE CONCEPT OF A FREE-FLOATING FLAP

While all three concepts presented in section 7.4.5 are passive systems, an active system that makes use of aerodynamic forces and moments to achieve flap deflections is the concept of the free-floating flap (FFF). This system consists of a flap with a trailing edge trim tab. The flaps can rotate freely around a hinge axis and are controlled by the trailing edge tab. The forces on the tab create a moment that allows controlling the moment around the hinge axis thereby driving the flap, which generates a large control force on the blade structure. As shown in Figure 7.11, the actuation system is completely enclosed in the flap. This is of high importance, as this allows sealing both the blade structure and the flap protecting the system from harsh environmental conditions.

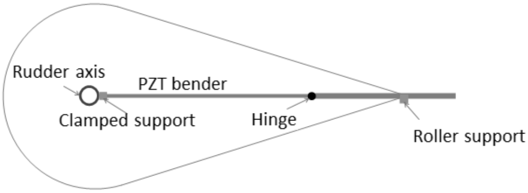

Figure 7.11: FFF design for a vertical stabiliser with tab and piezoelectric bender (Bernhammer, De Breuker, Karpel and van der Veen, 2013)

Contrary to all other flap configurations presented in this chapter, the FFF does not form an integral part of the blade structure, but is a device that can be added to any existing blade structure and is therefore easily exchangeable. This exchangeability is the key advantage of the FFF concept as it implies that complexity of repairs will be lowered compared to other flap systems, especially for those systems which employ a morphing solution. For these systems, the complete blade would need to be exchanged in case of a failure of the flap. A disadvantage is that the construction of the autonomous flap introduces several elements that can fail, thereby increasing the failure probability of the full turbine. Before implementation on a full turbine, a detailed study of the costs and risks will be necessary.

7.5.2 FREE-FLOATING FLAPS FOR LOAD ALLEVIATION AND FLUTTER SUPPRESSION

The free-floating flap is particularly suitable for the alleviation of continuous gust loads. This concept has first been introduced by Heinze and Karpel (2006) who use a single FFF for control applications on a highly flexible wing. This study was performed to overcome the disadvantages of piezoelectric actuators in control applications, namely low actuator strokes and low strains. As shown in Figure 7.12, the piezoelectric actuator is located in the main wing, contrary to a further developed concept, which encloses the actuation in the flap itself. The low stroke is addressed by aeroelastic amplification of the tab to the free-floating flap, which means that aerodynamic moments are used as a lever to achieve large flap rotations leading to a high control authority.

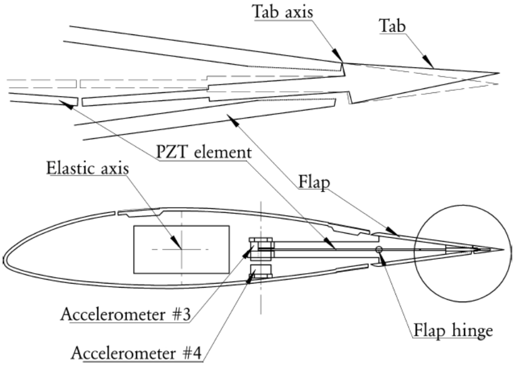

Figure 7.12: Cross-sectional view of the section with a piezo-actuated tab (Heinze and Karpel, 2006)

One of the key properties of the flap is that it is underbalanced which enhances the control response. However, it makes the system susceptible to flutter induced by an interaction of the flap oscillation with plunge displacements. This instability can however be suppressed as was shown both numerically and experimentally by Bernhammer, De Breuker, Karpel and van der Veen (2013), a property, which is used in Chapters 8 and 9.

The high control authority and high bandwidth of the FFF make them a natural candidate for load alleviation tasks. Heinze and Karpel (2006) have numerically shown the potential the FFF has when reducing the the amplitude of the response to a discrete gust. Bernhammer, De Breuker, Karpel and van der Veen (2013) have expanded this work by experimentally investigating the response of a system with two discrete flaps (rudders) on a vertical stabiliser. Besides the already mentioned capability to suppress the flutter of the system, active control based on acceleration measurements could reduce the dynamic response due to an external excitation by a factor of 2.

Finally, Pustilnik and Karpel (2013*b*) showed how limit cycle oscillations could be achieved if the flaps in the vertical stabiliser of Bernhammer, De Breuker, Karpel and van der Veen (2013) would be limited by non-linear springs that introduce a free-play zone in which the flap would be floating.

The combination of high control authority and bandwidth of the FFF as well as the simple repairability compared to structurally integrated solutions make them a good candidate for investigation as load alleviation devices, certainly for offshore wind turbines. In the following chapter the free-floating flap system will be further developed in a non-rotating environment on a wing/blade section as a technology demonstration, leading to experimental investigations of small utility scale dimensions.

7.6 SYNOPSIS

Flaps as load alleviation devices need to satisfy a large base of requirements, which has led to a variety of possible, conceptually different design solutions. An overview of flap designs has been provided in this chapter.

- The most important requirements include durability and low maintenance costs.
- Performance requirements for smart rotors based on simulation results are lower than assumed by previous studies. A frequency bandwidth of 0.0 - 2.0 Hz with a maximum amplitude of 5 degrees is sufficient to realise the complete fatigue load reduction in the case of multi-megawatt utility scale turbines.

Flap designs so far have mainly tried to address the reliability issue by seamlessly including the flap into the structure, which increases protection from the environmental conditions, however necessarily increases maintenance costs of such a flap system. A replaceable flap system such as the FFF is an ideal candidate to circumvent the maintenance issues. Therefore the implementation of free-floating flaps will be investigated further.

Ieder nadeel heb zijn voordeel.
Every disadvantage has its advantage.

Johan Cruijff

8

FREE-FLOATING FLAPS AS ENERGY HARVESTER

8.1 INTRODUCTION

Free-floating flaps are flaps that can rotate freely around a hinge axis. As has been detailed in the previous chapter, the concept has so far been used for load alleviation. In this chapter, the functionality of the FFF is extended to energy harvesting, which can be used to power sensors and actuators locally.

The chapter is divided into six sections[1]. In the first section, the energy harvesting concept is discussed, while in the second section the numerical model for the aeroservoelastic analysis of the blade section model is presented. This is followed by a stability evaluation of the system and a simulation of the power generation. The last three sections are dedicated to an experiment. The wind tunnel model is presented and two different types of limit cycle oscillations are investigated. The limit cycle is either achieved by control of the trim tabs or by structural delimiters. The measurements are finally compared to the numerical prediction.

---

[1] This chapter is an adaptation of the journal paper 'Energy Harvesting for Actuators and Sensors using Free-Floating Flaps' (Bernhammer, Karpel and De Breuker, 2015) submitted to the Journal of Intelligent Material Systems and Structures

8.2 THE CONCEPT OF AN ELECTROMAGNETIC ENERGY HARVESTER ON FREE-FLOATING FLAPS

Free-floating flaps have so far been used by Bernhammer, De Breuker, Karpel and van der Veen (2013); Heinze and Karpel (2006); Pustilnik and Karpel (2013*b*) to aerodynamically alleviate vibration loads. This chapter presents an approach to deliberately drive the flaps into a controlled flutter motion. The kinetic energy of the flap vibration associated to this flutter motion is converted into electricity that can be locally used for sensors and actuators. This is done through electromagnetic conversion of vibrational energy into electrical energy. For this process it is desired to maintain a certain vibration level, which is sufficient to charge the battery but must not exceed a maximum value to guarantee structural integrity. An option to achieve this goal has been evaluated by Pustilnik and Karpel (2013*a*,*b*), who investigated the behavior of the FFF in limit cycle oscillations (LCO), which is a type of nonlinear instability. A well-known control-surface LCO stems from free-play in the actuator connections. This free-play creates a zone in which the flaps can rotate freely around its hinge axis. These constraints are reached, when the flap deflection is large enough to be constrained by the presence of the actuator. The surface flutters within the free-play zone, but the stiffness outside the zone turns the flutter into LCO. Alternatively, the gain of the flutter suppressing control system can be tuned such that the system is neutrally stable and the amplitude of the vibrations will not increase over time.

While energy harvesting from mechanical vibrations is a well-researched topic, generating energy by exploiting aeroelastic instabilities is a young field of research. The first work in this field has been done by Bryant and Garcia (2011) and Bryant et al. (2010) who used a simple cantilevered piezoelectric bender with a free-floating flap at the trailing edge to generate flutter that can be used to harvest energy. Bryant et al. (2011) have further expanded this conceptual work by studying the influence of the system parameters on the stability. It was found that by changing component masses and stiffness, the system behavior could be significantly changed. Both models exploit a two degrees of freedom model coupled with a two-dimensional unsteady, linear aerodynamic model. Park, Kim, Kwon and Law (2012) and Park, Morgenthal, Kim, Kwon and Law (2012) use electromagnetic energy conversion instead of piezoelectric devices. Instead of exploiting a coupled flutter mechanism, a T-shaped cantilever beam is used. A magnet is attached at the end of the cantilever beam such that it sheds vortices that lead to flutter. Coils are mounted in the non-moving frame of reference. Also Bruni et al. (2014) have studied the effect of aeroelastic instabilities on energy harvesting by using embedded piezoelectric elements. Sirohi and Mahadik (2011) also use embedded piezoelectric patches to harvest electrical energy from the mechanical vibrations of triangular bar, which is attached to a cantilever beam, shedding galloping vortices.

The work presented in this chapter aims to provide an implementation of an energy harvester closer to actual aerospace applications. For this purpose, the concept of a free-floating flap (FFF) is used. The flap hinge locations are designed such that the flaps can easily be driven by the tabs and still produce flutter at low velocities. This ensures that, unless controlled otherwise, the flap responds to turbulence in the air flow and a significant amount of energy can be generated. A coil is mounted inside the flap, oscillating in a magnetic field generated by magnets which are attached to the main structure. The relative motion between the magnet and coil due to the vibration generates electricity that can be either directly used for the actuators and sensors or stored in a battery. Details of the aeroelastic design of such a flap have been presented by Bernhammer, De Breuker, Karpel and van der Veen (2013). The dimensions of the model were not altered and are given in Table 8.1. The gap indicated in Table 8.1, was present in the physical model, but is neglected for the numerical simulations. The model used by Bernhammer, De Breuker, Karpel and van der Veen (2013) was extended by installing two commercially available dynamos as shown in Figure 8.1. To limit the cycle amplitude, two structural delimiters were installed for each flap, in order to keep the amplitude of the flap deflections between 10 and -10 degrees.

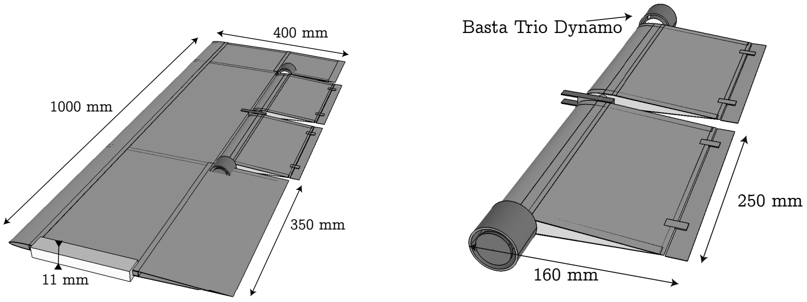

(a) CAD drawing of test configuration (b) Close-up on flaps with dynamos

Figure 8.1: Energy harvester concept

Table 8.1: Wing model details

Chord	Airfoil Thickness	Span	Gap between flaps
400 mm	11 mm	1000 mm	8 mm
Flap chord	Flap span	Dynamo	
160 mm	250 mm	Basta Trio 3320	

8.3 NUMERICAL MODEL

The numerical model was created in MSC/Nastran, where a structural modal analysis was carried out as detailed by Bernhammer, De Breuker, Karpel and van der Veen (2013). The first 15 structural modes were passed to ZAERO, which was used to extract the aeroelastic state-space time domain model that is based on rational function approximation of the unsteady aerodynamic force coefficient matrices (Karpel, 1990), however only the first three modes contribute to the unstable aeroelastic response. A modal damping coefficient of $\zeta = 0.03$ has been applied to correct for structural damping. Finally, non-linear feedback loops were introduced in Simulink to model the effect of the structural free-play zone and the electromagnetic coupling with system.

8.3.1 STATE-SPACE AEROELASTIC MODEL

The structural model was built in MSC/Nastran (Rodden and Johnson, 1994) consisting of 914 CQUAD4 elements. While originally being clamped at the root section, a spring was added to reflect the extension of the root such that it could be connected to measurement equipment. The spring was tuned to match the first bending frequency measured in the wind tunnel experiment (Pustilnik and Karpel (2013*a*)). Two additional fictitious masses (Karpel and Presente (1995)) were added to facilitate an accurate inclusion of a structural free-play zone (Karpel et al. (2013)). A modal analysis was carried out and the modal results were passed to ZAERO for constructing the frequency domain unsteady aerodynamic force coefficient matrices. The time-domain second order equations of motion in generalised coordinates can be expressed as

$$\bar{\mathbf{M}}\ddot{\xi} + \bar{\mathbf{B}}\dot{\xi} + \bar{\mathbf{K}}\xi = \mathbf{F_{aero}}\left(t\right) \tag{8.1}$$

where $\mathbf{M_{hh}}$, $\mathbf{B_{hh}}$ and $\mathbf{K_{hh}}$ are the generalised mass, damping and stiffness matrices, respectively. ξ is a vector containing the generalised displacements. $\mathbf{F_{aero}}$ is the generalised aerodynamic force vector and includes aerodynamic loads, gust inputs and control surface motion. The aerodynamic model is divided into five zones, with individual paneling, namely a root section, two flaps, the section upstream of the flaps and a tip section. The unsteady aerodynamic method of ZAERO, combined with natural modes from MSC/NASTRAN, was used for generating complex aerodynamic influence coefficient (AIC) matrices for harmonic oscillations at various frequencies. The minimum state method (Karpel, 1990) was then used to approximate the AIC matrices as rational functions of the $i\omega$. The replacement of $i\omega$ by the Laplace variable s then leads to compact time-domain state-space matrices. A stability evaluation by root-loci analysis of the resulting system matrix has been carried out to find the open-loop flutter conditions. Figure 8.2 displays the resulting aeroelastic frequency and the damping of the main modes participating in the flutter mechanism versus the velocity. Modes 1 and 2, the flap deflection modes, are heavily damped and omitted in the damping plot in Figure 8.2. Flutter occurs when the damping branch of the bending mode crosses the zero line, at 10.2 m/s with flutter frequency of 3.6 Hz. The flutter mechanism is an interaction of the first bending mode with the inboard and outboard flap deflection modes. Four snap shots of the flutter mode during a half of a cycle are shown in Figure 8.3. The control system will suppress this flutter most of the time, except for certain times when a controlled level of flutter is used to charge the batteries.

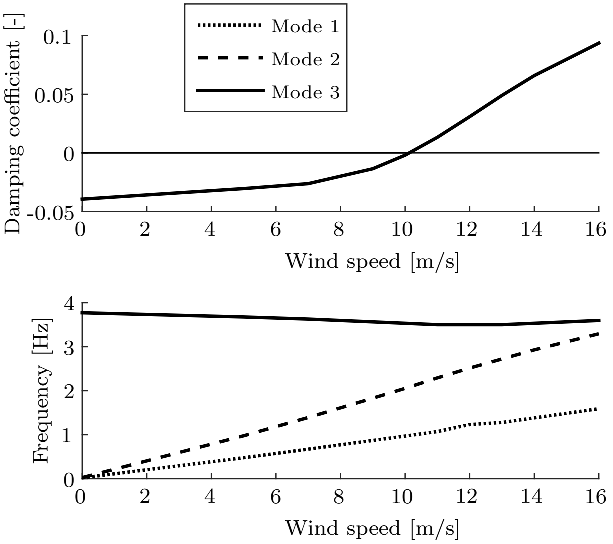

Figure 8.2: Frequency relevant modes versus velocity, damping of flutter branch

8.3.2 ELECTRONIC CIRCUIT

The electronic circuit layout was kept as simple as possible. Figure 8.4 shows the schematic layout of a simple battery charging circuit. L1 represents the coil that is rotated in the magnetic field, DB1 is a rectifier and R1 is variable resistor. For simplicity, a voltage drop over the rectifier has not been included in the model. This drop would depend on the actual circuit design and the selected low voltage rectifier. When undergoing motion, the change in the magnetic field as seen by the coil causes a current in the electric circuit. The associated open circuit voltage U_{open} created is equal to:

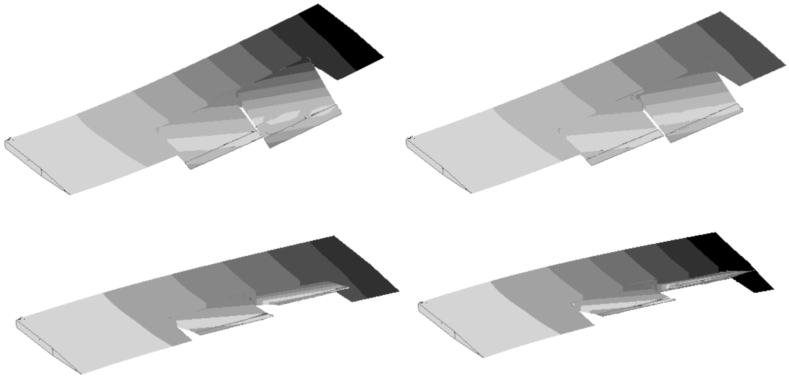

Figure 8.3: Flutter mode shape at 10.2 m/s, snapshots along a halfcycle

$$U_{open} = nl\frac{d\gamma}{dt} \tag{8.2}$$

where n is the number of coil turns, l is the length of a coil loop and γ denotes the magnetic field strength. The latter has been experimentally determined for the dynamo used during the experiment. For that purpose, an oscillation of 3.6 Hz corresponding to the frequency of the unstable mode with an amplitude of 5 degrees was prescribed, thereby representing the test conditions. The magnetic flux was computed based on these measurements. As only low coupling between structural motion and electronic excitation could be observed, the magnetic flux has been increased by a factor of 10 for the numerical simulations assuming that it can be achieved in practice. For the experiment, the magnetic flux reported in Table 8.2 was used. The increase in magnetic flux causes an increase in voltage by a factor of 10 and an increase in power by a factor of 100 in the numerical simulations. This large increase was required to show coupling effects between electronic harvesting and vibrations.

The magnetic flux coefficient is approximated by the magnetic flux multiplied by the coil length as given in Equation 8.4. The generated voltage U has to over-

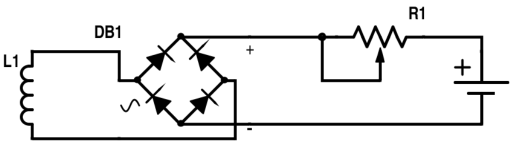

Figure 8.4: Schematic of modelled electronic circuit

Table 8.2: Properties of dynamo

# of coil turns	Length of coil loop	Magnetic flux coefficient
100	94 mm	$9.6e \cdot 10^{-3} \frac{Vs^2}{rad}$

come the voltage of the battery U_{bat}. Assuming no power loss over the rectifier, this can be separated into two cases.

$$U = \begin{cases} nl\frac{d\gamma}{dt} - U_{bat} & U_{open} > U_{bat} \\ 0 & U_{open} \leq U_{bat} \end{cases} \tag{8.3}$$

The voltage generated can be calculated based on the rotational velocity of both flaps. The effect of the battery voltage as shown in Equation 8.3 is modelled as a free-play zone with the width of the battery voltage. Note that the maximum charging voltage is not limited in the simulation. In practice the limit would be around 5-10V depending on the type of battery. As voltages above 2V do not occur in the simulation, probably a circuit to increase the voltage for the charging would be needed in the real application. Furthermore, the electrical power P that is harvested adds damping to the system. The generation of electrical power requires a mechanical power input of the same magnitude. Therefore, the equations of motion need to be expanded with a damping term that is quadratically proportional to the rotational speed of the flaps. The electromechanical power of the damping is given in Equation 8.4.

$$P = \frac{\left(nl\frac{d\gamma}{dt}\right)^2}{R_{coil} + R_{var} + j\omega L_i} \approx \frac{(nl\gamma_k)^2}{R_{coil} + R_{var}}\dot{\beta}^2 \tag{8.4}$$

where β is the flap deflection angle. Note that Equation 8.4 is approximated using a constant magnetic flux γ_k multiplied by the square of the rotational velocity. Also, the impedance $j\omega L_i$ is omitted as it is two orders of magnitude smaller than the resistance of coil (R_{coil}) and the variable resistance (R_{var}). The damping has been implemented in generalised coordinates into the state-space system together with a structural free-play zone as shown in Figure 8.5. The output of the state-space system are the tip acceleration of the blade section and the rotation angles of both flaps. The rotational velocities are obtained as output of the aeroelastic state-space system and serve as input to Equation 8.4. Based on this power, a reaction torque was computed, which was fed back as input to the aeroelastic state-space system. The circuit resistance was varied to study the effect on the aeroelastic stability as shown in Figure 8.4. The coefficients K for the structural stiffness are -1900Nm/rad, while the coefficient k of the electromagnetic damping is -0.826Nms/rad.

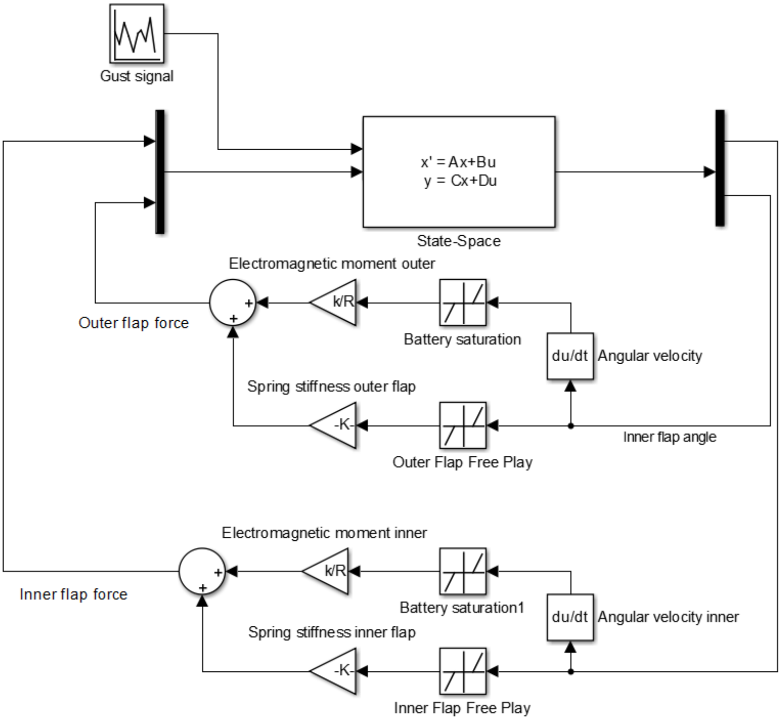

Figure 8.5: Simulink scheme of energy harvester model

Figure 8.5 also indicates a gust input. The gust force history in generalised coordinates has been computed in ZAERO for a continuous gust signal with a von Kármán turbulence spectrum for an altitude of 250 m above ground level. Only the component of the gust velocity perpendicular to the blade section was taken into account. The turbulence intensity, which is the ratio of the root mean square of the amplitude of the velocity fluctuation over the mean velocity, is 1.1%. For the gust load cases, the forces have been added to the equations of motion as given in Equation 8.1. When closing the control loop, the total state-space linear aeroservoelastic system including the linear control system that relates the tab motion to the acceleration measurements reads:

$$\begin{aligned} \dot{\mathbf{x}} &= [\mathbf{A}]\,\mathbf{x} + [\mathbf{B}]\,(\mathbf{u} + \mathbf{u_{gust}}) \\ \mathbf{y} &= [\mathbf{C}]\,\mathbf{x} + [\mathbf{D}]\,\mathbf{u} \end{aligned} \tag{8.5}$$

where

$$\begin{aligned} \mathbf{A} &= \begin{bmatrix} 0 & \mathbf{I} \\ -\bar{\mathbf{M}}^{-1}\bar{\mathbf{K}} & -\bar{\mathbf{M}}^{-1}\bar{\mathbf{B}} \end{bmatrix} \\ \mathbf{B} &= \begin{bmatrix} 0 \\ \bar{\mathbf{M}}^{-1} \end{bmatrix} \end{aligned} \tag{8.6}$$

A, **B**, **C** and **D** are the state, the input, the output and the feed-through matrices of the aeroelastic system. $\mathbf{x}$ is the state vector containing the modal displacements and velocities and aerodynamic lag states and $\mathbf{u}$ is the input vector containing the generalised force and moments due to the non-linear feedback loop. As shown in Figure 8.5, the outputs are the flap rotation angles and velocities, while the inputs are the generalised electromagnetic and mechanical moments related to the free-play zone.

8.4 SIMULATION RESULTS

The energy harvesting system using the free-floating system has been simulated in the time-domain using the state-space aeroelastic model and the non-linear structural free-play zone and electromagnetic feedback. As was outlined, the limit cycle behaviour of such a system is of the highest importance. Therefore the system has been simulated with an initial excitation and the structural response is analysed. Special attention in this analysis is paid to the transition between diverging aeroelastic responses and limit cycle oscillation. A state-space system has been identified based on every voltage time history (van der Veen et al., 2010). Eigenfrequencies and damping coefficients presented in this section were retrieved from these state-space systems. System parameters such as the resistance in the circuit and the charge level of the battery have been varied during different simulations to study their impact on the system stability and the energy harvesting performance.

In total, four sets of aeroelastic simulations have been performed numerically:

1. Time domain simulations of limit cycle oscillations
2. Stability evaluation with 0V battery voltage and varying resistance in the circuit
3. Stability evaluation with 1.2 Ω resistance and varying battery voltage
4. Gust response simulation with 0 V battery voltage and varying resistance in the circuit

8.4.1 TIME-DOMAIN SIMULATION OF LIMIT CYCLE OSCILLATION

The added damping due to the power harvester has a significant impact on the stability of the system. Figure 8.6 displays the results of a time domain simulation at 11.0 m/s wind speed, which, in very low harvesting case, is unstable as shown in Figure 8.7. The baseline operation without energy harvesting is equivalent to the 1.2 Ω case, as the power generated is not significantly contributing to damping. Both start to flutter at 10.2 m/s. This instability can be observed in the bottom plot of Figure 8.6, where only little power is generated, such that the system immediately shows an increasing oscillation. After 4 seconds a limit cycle state is reached and the voltage does not increase anymore. Decreasing the resistance leads to an increase in stability. The limit case here is a short circuit with only the resistance of the coil in the denominator of Equation 8.4. The associated structural response is very stable and damps out quickly.

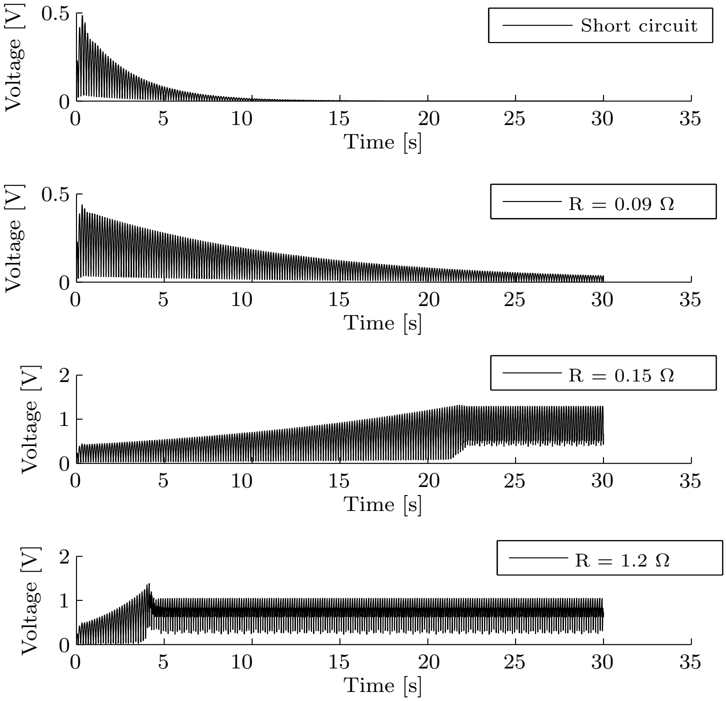

Figure 8.6: Time domain simulation with varying resistance at 11.0 m/s windspeed

A feature worth noticing is that, in the case of limit cycle oscillations as shown in Figure 8.6, the rectified voltage does not cross 0 V. Until limit cycle oscillations are reached, the voltage displays sinusoidal behavior. Figure 8.6 gives more insight into the growth of the oscillations and the transition to limit cycles. It should

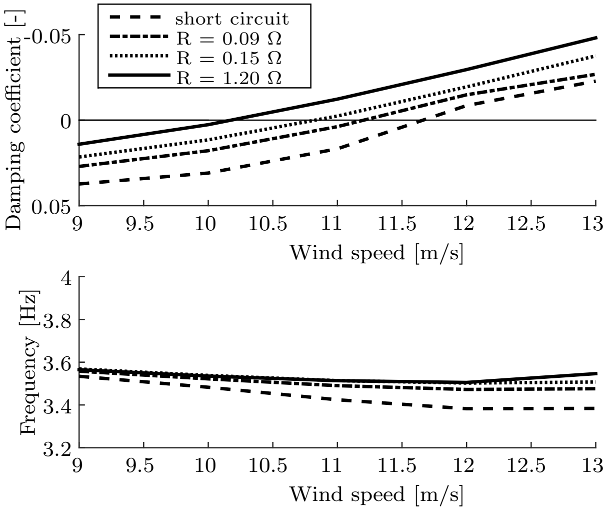

Figure 8.7: Frequency and damping of the flutter branch vs velocity depending on resistance

be noted that the reason for the limit cycle behavior is that the amplitude of the oscillations reaches the limits of the structural free-play zone. During the growth period, both flaps are oscillating in phase as shown in Figure 8.8. When the transition to the limit cycle occurs, the smooth sinusoidal behavior disappears and higher-order frequencies occur around the maximum velocity. It is assumed that this can be attributed to the interaction between the two flaps and the structural delimiters and the phase shift that develops once a limit cycle is initialised. The phase shift in angular velocity between the flaps causes the voltage always to be non-zero.

8.4.2 STABILITY EVALUATION

As was already noticed, the stability of the system strongly depends on the resistance in the circuit. The free-floating flap concept benefits from this dependence as it is possible to regulate the stability of the system by using the variable resistance as control parameter, thereby keeping the system close to neutrally stable. The power generated and consequently the resistance moment on the rotational axis decreases with increasing resistance. Figure 8.7 shows the damping coefficient and the frequency of oscillation of the flutter branch as a function of variable resistance. The baseline flutter speed was computed to be 10.2 m/s (Figure 8.2). Adding electromagnetic damping, results in an increase of the flutter speed to 11.7 m/s. Controlling the resistance in the circuit can therefore be used to keep the system marginally stable for an operational velocity range of more than 10%. Increasing the magnetic flux in the dynamo will further increase this damping

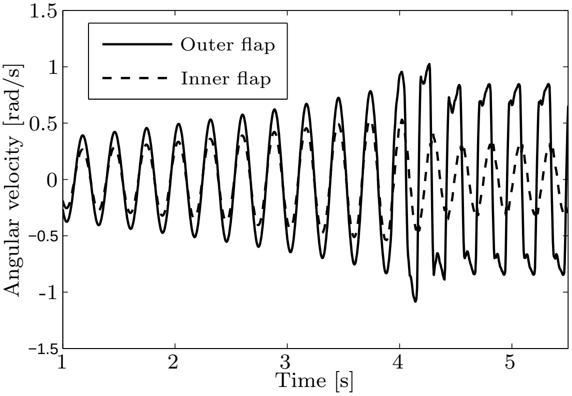

Figure 8.8: Transition to limit cycle oscillation

such that the desired wind speed region can be spanned. Furthermore, it can be seen that the change in damping coefficient between a short circuit and no electromagnetic feedback is 0.03 independent of the wind speed. While the damping is strongly influenced by the energy harvester, the frequencies stay almost unaltered. The monotonic relation between decreasing resistance and increasing damping can be attributed to the generator selection. The generator was not optimised for the power harvesting at very slow rotational velocities as observed in this study. The operating point of the generator is off the ideal condition, such that the maximum power extraction is not limited by the impedance matching condition, but rather by the variable resistance in the circuit.

The same effect can be observed when changing the battery voltage. Adding a free-play zone for the battery voltage essentially decreases the added damping of the electromagnetic system. Figure 8.9 shows the frequency and damping plots versus velocity for various voltage levels with a constant resistance of 1.2 Ω. The effect is not as pronounced as in Figure 8.7; still a decrease in flutter speed by 4% can be seen. This is a rather undesirable effect, as the resistance needs to be adjusted constantly when harvesting energy to charge the battery to keep the system neutrally stable. The charging effect reduces with increasing wind speed. The energy harvesting system can become unstable even when the battery is completely empty and no battery charging free-play is present. Aerodynamic forces and moments significantly exceed the possible damping, which was one of the reasons for numerically increasing the electromagnetic feedback. Similar to the resistance variation, changing the battery voltage hardly causes a change in vibration frequency.

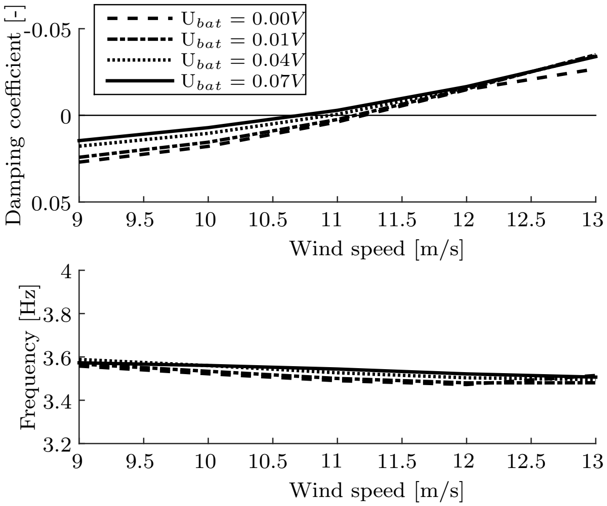

Figure 8.9: Frequency and damping of the flutter branch vs velocity depending on battery voltage

8.4.3 POWER CAPTURE

The power capture simulation has been run for a constant inflow with an initial perturbation of the model for the first bending dominated mode as shown in Figure 8.3. The time history has been calculated for 30 seconds and the average power and voltage for four different wind speeds are plotted in Figures 8.10 and 8.11. When running the simulations for 9.0 m/s, the structure damps out quickly, regardless of the resistance applied. Consequently, hardly any voltage is created and the system is not suitable as energy harvester. For 10.0 m/s the voltage is already significantly higher despite being damped, but the same trends in voltage and power still hold. Practically no power can be generated and the voltage is very low. For 9.0 and 10.0 m/s, increasing electrical resistance causes less damping, which means that the amplitude of the vibration due to an initial deflection decays slower, meaning that more energy can be extracted from the system.

Wind speeds of 11.0 m/s are the first unstable velocities evaluated. Two zones can be detected in the voltage and power curves. The first part of both curves strongly increases until a resistance of 0.3 Ω. This is the point where the blade section is neutrally stable. For lower resistances, the structure is damped and not much energy can be extracted. This changes as the oscillations decay slower with increasing resistance up to a point where the system becomes unstable and amplifies until it reaches limit cycle oscillations which are limited by the structural free-play zone. In this region of resistances above 0.3 Ω, the generated voltage is practically constant and the power is inversely proportional to the

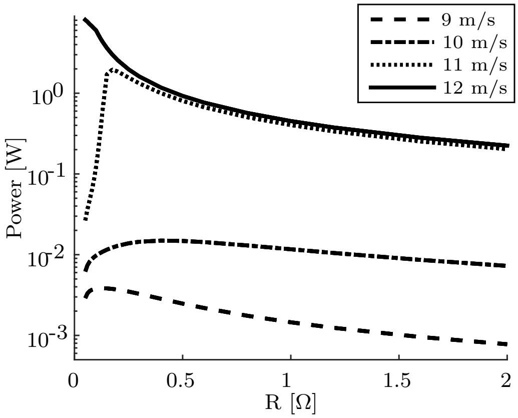

Figure 8.10: Power output vs resistance initial deflection

resistance. For 12.0 m/s, the region of increasing voltage and power disappears, as the system is unconditionally unstable regardless of the resistance as shown in Figure 8.7. Therefore, the voltage is constant throughout the resistance range. Only a discontinuity can be observed for low resistance values, where the system is just unstable. As shown in Figure 8.8, the transition mechanism produces higher angular velocities yielding a higher voltage output. In the case of 0.1-0.15 Ω, this transition takes place over multiple cycles, which explains the local rise in voltage. In the power production case, the inverse proportionality with the resistance is too dominant to visualise this variation of the voltage for low resistances.

8.4.4 GUST RESPONSE

The last simulation performed is the response of the system to a gust. The gust was modelled to be uniform over the span of the model. The simulation length was 15 seconds. A von Kármán wind spectrum was used with a turbulence intensity of 1.1%. Figures 8.13 to 8.15 show the power production in response to the gust excitation. The low turbulence amplitude was chosen to demonstrate gradual transition to limit cycle oscillations. Overall, Figures 8.12 and 8.13 agree well with the simulations with an initial deflection (Figures 8.10 and 8.11). The higher the wind speed, the more energy can be harvested. The overall amplitude of voltages is lower, as the incremental phase before reaching limit cycle oscillations contributes more. Constant voltages in the case of 11.0 and 12.0 m/s wind speeds are only reached at resistances of 0.5 and 1.2 Ω. A difference to the previous simulations can be found in the comparison of the amplitudes of Figures 8.11 and 8.12. While in the limit cycle oscillation case, the generated voltage is almost equal for 11.0 and 12.0 m/s, in the gust load case, the higher wind speed shows a much

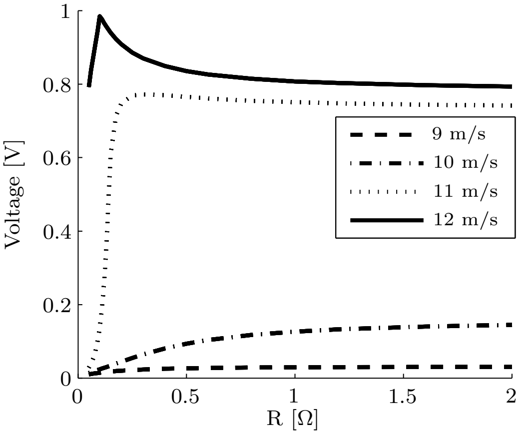

Figure 8.11: Voltage output versus resistance starting from initial deflection

higher responsiveness to the input signal, thereby tripling the output voltage. If comparing the low wind speeds to high wind speed results, a factor of 3 from 10.0 to 11.0 m/s and a factor of 5 between 11.0 and 12.0 m/s are visible. For the power production these factors increase to 9 and 25, respectively. This clearly shows the advantage of aeroelastic instabilities in energy harvesting, as the output can be increased by a factor of 225, just by crossing the flutter margin and increasing the wind speed from 10.0 to 12.0 m/s. An increase in power production in this order of magnitude strongly enhances the possibility of using energy harvesting not only for sensing, but also as power supply for active load alleviation.

In contrast to the previous simulations, a distinct peak can be observed for 0.07 Ω. This peak is accompanied by a distinct dip at 0.13 Ω. The dip occurred for both 11.0 and 12.0 m/s air speeds and is particularly visible in the power production Figure 8.13. To explain the differences a closer look needs to be taken at the time history of the vibrations, which are plotted in Figure 8.14. The low gust amplitude causes a gentle increment in voltage. It is interesting to see that the response with varying resistance changes significantly. The first observation is that with increasing resistance, there is less damping in the system and once a significant growth of the vibrations is initiated, this increase rate rises as well. This corroborates well with what has been predicted by the stability plots in Figures 7 and 8. Eventually, the time domain simulation in the subfigures for 0.13 Ω, 0.20 Ω and 1.20 Ω create stable limit cycles. The more remarkable observation, however, is that the point of initiation of the vibrations varies and causes the aforementioned dip. While the short circuit simulation grows slowly but steadily from 2 seconds onwards, all cases with higher resistance postpone the initiation point of the vibrations. For 0.13 Ω, the structure does not show any response until 5.0 seconds, increasing the resistance above this value increases the responsiveness.

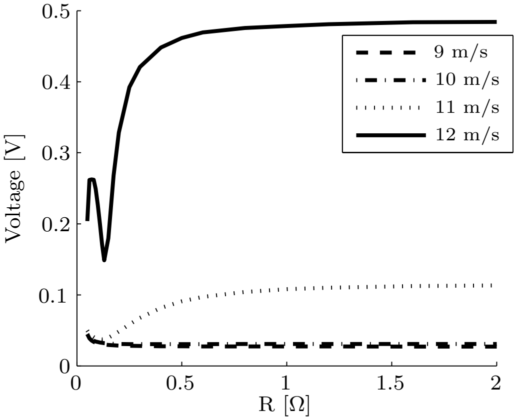

(a) All wind speeds

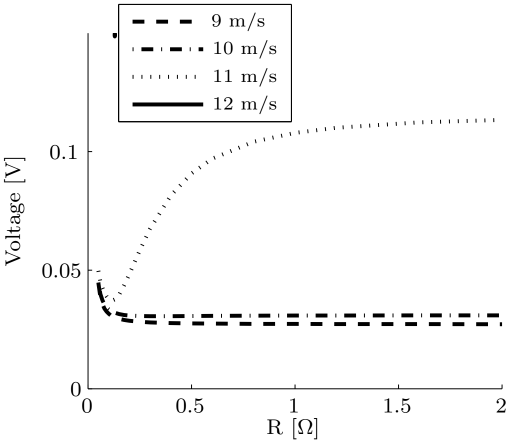

(b) Zoom in on stable configurations

Figure 8.12: Voltage output vs resistance, response to a gust

This unexpected result can be attributed to the interaction of the two flaps. Figure 8.15 shows the limit cycle amplitude of the inner and outer flap. Both flaps behave in a rather different fashion. While the outer flap has a constant limit cycle amplitude, the inner flap motion decreases with increasing resistance. For low resistance values, the inner flap becomes dominant. The electromagnetic damping has an equalizing effect on the two flaps. This is most likely to be connected with the fact that the outboard flap mode is the mode that interacts more with the bending mode in the flutter mechanism. Adding damping to the outboard flaps therefore has a stronger impact as the flutter mechanism is responsible for the power generation.

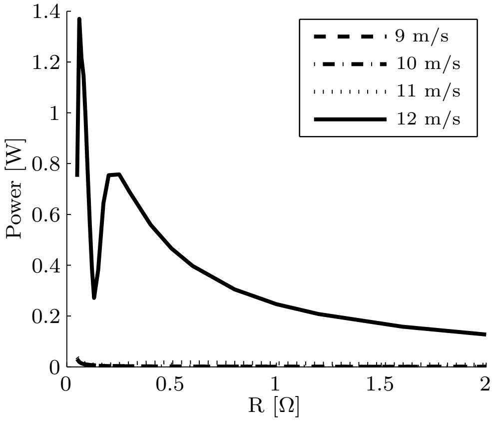

(a) All wind speeds

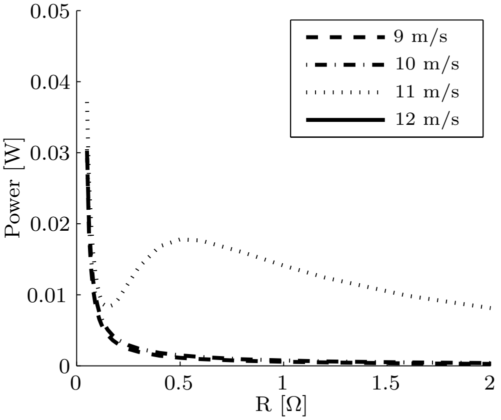

(b) Zoom in on stable configurations

Figure 8.13: Power output vs resistance, response to a gust

Figure 8.16 confirms this hypothesis. Adding electromagnetic damping changes the flutter mechanism. For high resistances, the outboard flap is the driving mechanism behind the instabilities; the flaps are almost showing identical behavior for low resistance values. When observed closely, the inner flap even shows a slightly higher amplitude in these cases. It can be concluded that this flutter mode with two equally participating flaps is more responsive to excitation, while the negative damping is smaller, as it takes longer to increase in amplitude over time. The flutter mode that is dominated by the outboard flap is less responsive, but the negative damping is higher, which causes the curves shown in Figure 8.15. Once an excitation is initialised, this flutter mode increases faster.

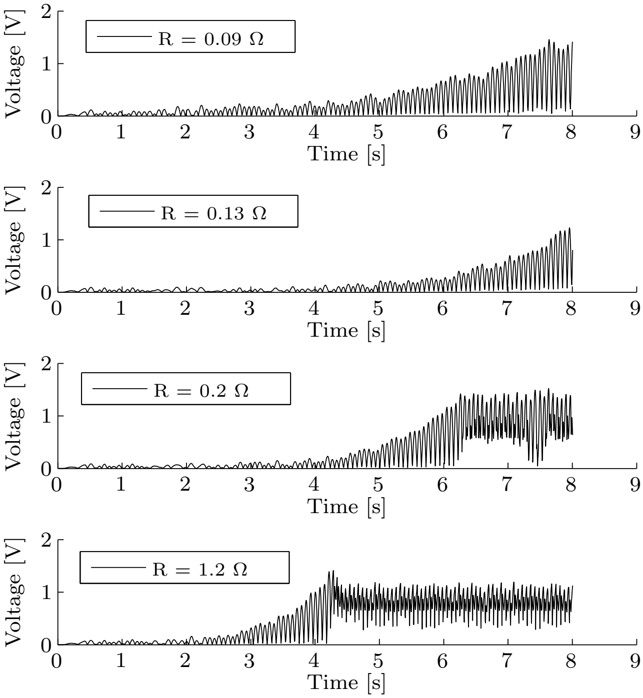

Figure 8.14: Voltage time history vs resistance due to a gust

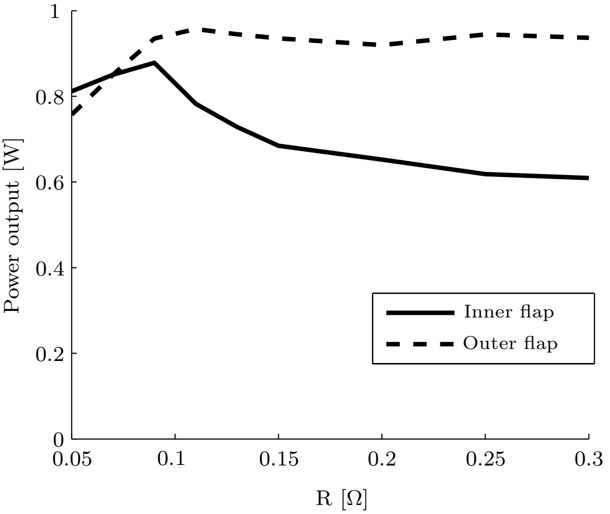

Figure 8.15: Power output vs resistance of different flaps, due to a gust

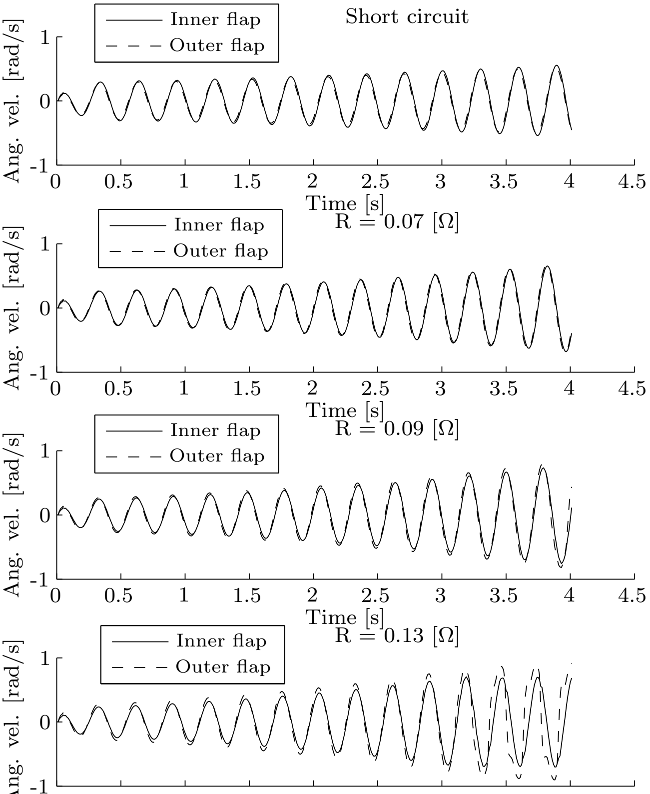

Figure 8.16: Time history of angular flap velocities due to initial impulse of bending mode

8.5 WIND TUNNEL EXPERIMENTS

The system presented in the previous section was manufactured according to the specifications given in Table 8.1. The two electromagnetic devices at the end of the flaps were connected such that the stator is magnetic and fixed to the main structure. The rotor is a coil that is co-located with the rotational axis of the flap. The aeroelastic set-up was tested in the Open Jet Facility (OJF) of Delft University of Technology. The root of the model has been connected to a six-component balance. The properties of the wind tunnel and the balance are given in Table 8.3 and the layout of the tunnel is shown in Figure 8.17. The structure was passed through an aerodynamic cover, shielding the balance from influences of the flow as shown in Figure 8.18. Two numerical results were reproduced, namely the response of the structure and the associated harvested energy as a result of an initial deflection and a continuous excitation signal. For the initial disturbance, the blade tip was loaded by a force, which was released instantaneously. The constant excitation signal was created by a disturbance signal on the inner flap. The monitoring system needed to be outside of the wind tunnel. The dynamos were thus connected by wire to the data acquisition system. Unfortunately, the resistance in the cables was too high to demonstrate a significant mechanical power extraction as has been shown numerically. Therefore, it was not possible to demonstrate stability variations by changing the resistance in the electric system as was shown numerically.

Table 8.3: Properties of the Open Jet Facility

Max. Wind Speed	Test Section	Max Load Balance
35.0 m/s	2.8 m by 2.8 m	250.0 N
Resolution Balance	Resolution Coefficients	
0.1 N	0.004 at 10.0 m/s	

The performance of the flap system was assessed before the wind tunnel tests were conducted. For this purpose, the flaps were connected to a shaker that could cause flap rotations up to 4 degrees with a maximum frequency of 10.0 Hz. Figure 8.19 shows the quadratic mean of the voltage output versus rotation angle and frequency. Equation 8.2 shows the relation between the generated voltage and the changing field strength. This linear relation can be observed for both flap deflection amplitude and flap deflection frequency as shown in Figure 8.19. Only for high deflection frequencies above 6.0 Hz, the linear relation does not hold true anymore and a reduction in voltage output can be observed.

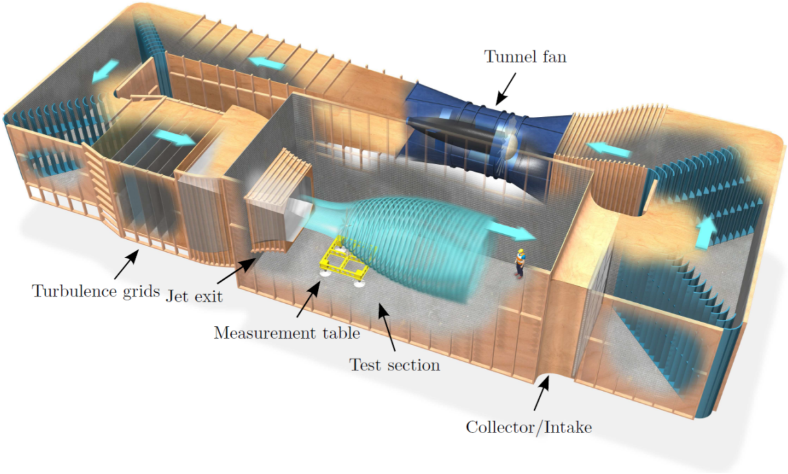

Figure 8.17: Open Jet Facility of Delft University of Technology (Sterenborg, 2014)

Figure 8.18: Test set-up of wind tunnel experiment

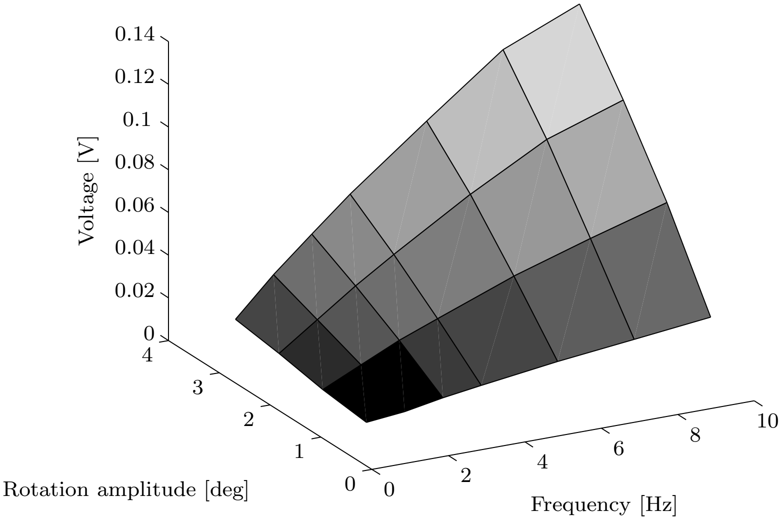

Figure 8.19: Quantification of power generation of flaps

8.5.1 LOW AMPLITUDE LIMIT CYCLES

The first step during the wind tunnel tests was to assess the aeroelastic stability of the system. Closed-loop identification (van der Veen et al., 2010) has been carried out. The controller developed for the flutter suppression experiments by Bernhammer, De Breuker, Karpel and van der Veen (2013) was used to stabilise the system above the flutter speed. Figure 8.20 shows the comparison of the identified frequency and damping to the numerical values. The experimental damping has been found by system identification using a stochastic disturbance signal on the control tab. The damping values are obtained from the state matrix of the identified system. Increasing the electrical resistance for both subfigures, the trends agree. A slight numerical underprediction of the eigenfrequency can be observed, however the difference for the first bending dominated eigenfrequency is less than 5%. Even the small dip that is obtained numerically at 11.0 m/s is reproduced. While the numerical values show a more gradual decrease to this point, the experiment shows a sharper dip, a fact that has been caused by the numerical fitting of the state-space system parameters to the measurement values. The damping plot shows excellent agreement for the first two measurement points, which are practically identical with the numerical prediction. Around the flutter point, experiment and numerical prediction diverge such that at 11.0 m/s a difference in the damping coefficient of 0.01 can be seen. This difference increases with increasing wind speed to a value of 0.025 at 13.0 m/s. While the main part of the damping below rated wind speed is caused aerodynamically, it is believed that friction in the system adds damping, which, once the system becomes unstable, contributes visibly to the overall system damping. The flutter speed obtained in both cases is between 10.5 and 11.0 m/s.

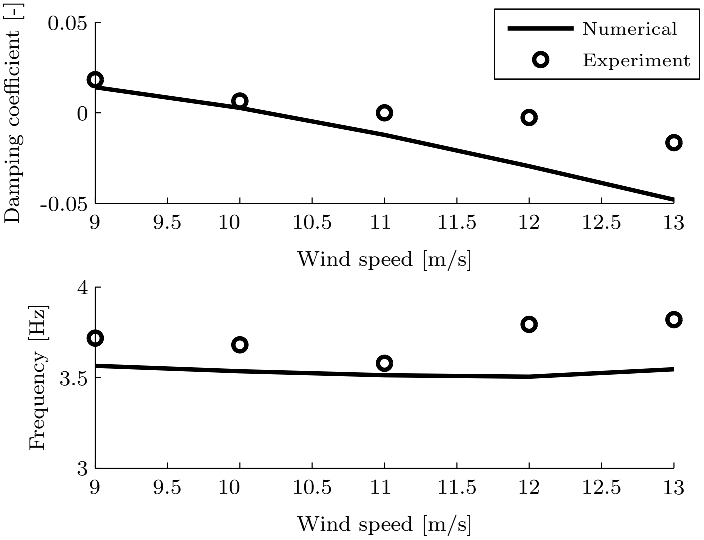

Figure 8.20: Damping and frequency plot

PERIODIC EXCITATION

To further asses the responsiveness of the system to a disturbance input, a sinusoidal signal was applied to the trailing edge tabs on both flaps. Figure 8.21 shows the measurements of the voltage response for different frequencies. The background noise in the measurements caused by turbulence in the flow results in a base voltage of 0.005 V. An excitation signal at low frequencies of 1.0 or 2.0 Hz does not change the average voltage that is obtained regardless of the wind speed. The same holds true for high frequencies of 4.0 Hz and above. Only for 3.0 and 3.5 Hz a structural response is visible. While the aerodynamic damping is still high at wind speeds of 8.0 m/s, an increase to 9.0 m/s shows already an increase in achievable voltage output of a factor of 3. When increasing the wind speed even further, the maximum response is a factor of 8 above the baseline value. Higher wind speeds in the experiment were not possible as for 11.0 m/s the system would be unstable and even a very small excitation would result in flutter. Consequently, any small excitation will result into limit cycle oscillations with a high voltage generation.

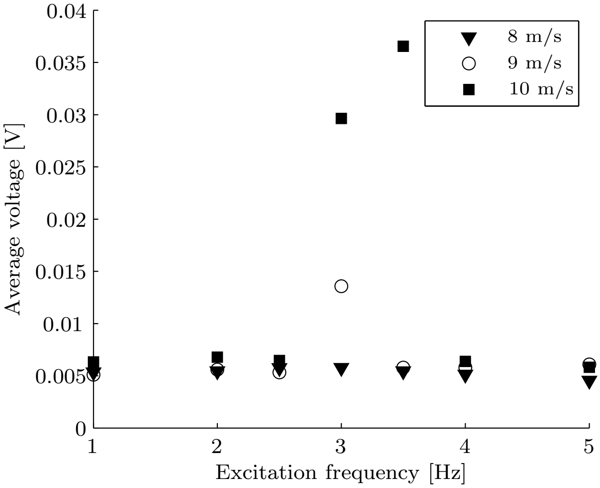

Figure 8.21: Sinusoidal excitation of trim tab for different wind speeds

SMALL INITIAL DISPLACEMENT

In a third step, the system is given a small initial disturbance. For wind speeds below 10.0 m/s, the initial perturbation is damped away relatively quickly and practically no energy can be harvested as displayed in Figure 8.22. At wind speeds of 10.0 m/s, the system is close to be neutrally stable. Any disturbance, be it initial or through turbulence, provokes a slowly fading oscillation. Consequently, the achievable power output is higher than for lower wind speeds. For 11.0 m/s, the system is unstable and the vibrations increase in amplitude. In the current experiment, the controller designed by Bernhammer, De Breuker, Karpel and van der Veen (2013), was used to keep the system neutrally stable. For this purpose, the gain in the controller was altered manually such that the tip accelerations would not exceed 2 g, where g is the acceleration due to gravity. One should notice that this is significantly below the physical delimiters of the system, which allow flap deflections up to 10 degrees. As expected, the voltage output increases by another 40% as compared to the 10.0 m/s case.

For wind speeds below the flutter speed, the energy production of both flaps is equally low. For aeroelastically triggered energy harvesting, the outer flap interacts more with the first bending dominated structural mode. The voltage generation is consequently twice that of the inner flap. Figure 8.23 shows the time history of the limit cycle oscillations for wind speeds of 11.0 m/s. The amplitude varies slightly over the cycles, which is a phenomenon that can be explained by turbulence in the inflow. The measurement data shows significant noise, which cannot be attributed to the aeroelastic response, but rather to the sensors and

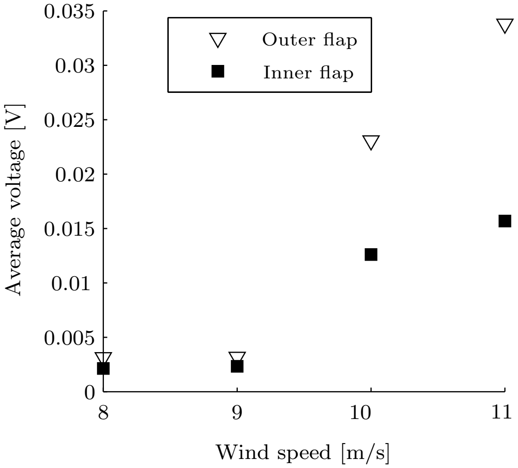

Figure 8.22: Average voltage vs wind speed of inner and outer flap

the acquisition system. It is interesting to see that despite being a limit cycle, the oscillations of both flaps are in phase. The phase shift of 180 degrees in Figure 8.23 is caused by the installation of the electromagnetic devices as shown in Figure 8.1, meaning that, when the flaps oscillate in phase, the voltage signal shows opposite signs. As the devices installed on both flaps are identical, but mirrored in orientation, a synchronous flap deflection causes opposite voltage outputs. This is contrary to the numerical findings, which show a phase shift between the flaps when in limit cycle oscillation. One should however bear in mind that in the numerical case electromagnetic coupling and structural delimiters were used to create a limit cycle, while in the experiment case, the oscillation amplitude was limited by trailing edge tab control.

The same differences with the numerical simulations can be observed in Figure 8.24. While agreement is reached concerning the damping and the decay of the oscillations for 8.0 to 10.0 m/s and the growing oscillation to limit cycle oscillations for 11.0 m/s, the synchronous nature of the vibrations of both flaps causes sinusoidal like variations in the generated voltage. Notice that in Figure 8.24 the absolute values of the voltage generation are displayed. The voltage amplitude is a factor of 10 lower than in the numerical results. This difference can be explained by the increased magnetic flux in the numerical simulations.

LIFT LOSSES

Figure 8.25 shows the lift forces measured at the root of the blade when the model was put under an angle of 3.5 degrees. While the lift in case of the fixed blade

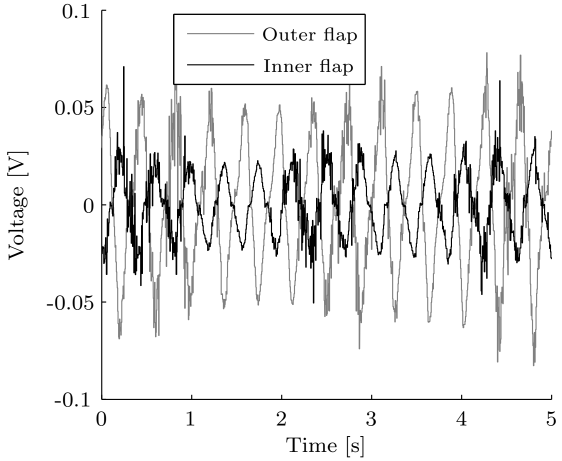

Figure 8.23: Limit cycle oscillations at 11.0 m/s

is practically constant in time and the variations are caused by low amplitude turbulence and the measurement signals, the force time history of the limit cycle oscillation shows oscillations around the value of the fixed flap case. The oscillation frequency coincides with the eigenfrequency of the first bending mode. The oscillations originate from variations of the aerodynamic forces over time and the structural dynamics associated with the flap motion. The difference in average value between the forces during the flap fixed case and the LCO case for wind speeds of 11.0 m/s is 2%, while the oscillation amplitude stays below 5% of the mean value. Unfortunately, a similar measurement for the drag could not be performed, as the differences found between the fixed flap and the LCO case are too fine to for the resolution of the load balance.

8.5.2 HIGH AMPLITUDE LIMIT CYCLE

In a final step, the controller was switched off and experiments have been performed at 11.5 m/s wind speed. The limit cycle amplitude was now not tuned manually as before, but only by the structural delimiters that allow the flaps to rotate between 10 and -10 degrees. Figure 8.26 shows the tip accelerations of the blade as the system becomes unstable. Just after 17.0 seconds in the measurement the blade starts to oscillate. While these oscillations are small at first, they grow to tip accelerations of 6 g at 22.0 seconds into the measurement, where the flaps touch the delimiters for the first time. From this point in time, sharp peaks occur in the tip accelerations history, a result of the forces that are transfered between the flaps and the blade structure. These peaks in acceleration almost

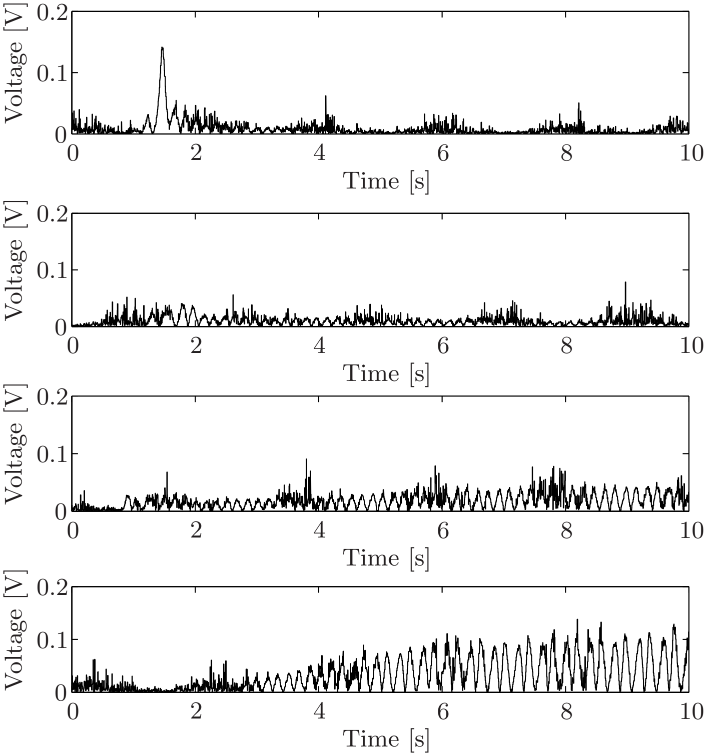

Figure 8.24: Time history of voltage generation due to impulse, 8.0 m/s (top) to 11.0 m/s (bottom)

immediately reach amplitudes above 20 g. The aeroelastic system stabilises in a limit cycle oscillation.

Figure 8.27 further elaborates on the structurally delimited oscillations as it shows the time history of the voltage generation. Up to 22 seconds, the phase of the voltages of the inner and outer flap are perfectly aligned. The noise level is relatively low and the extrema of the voltages are round. Between 22 and 23.5 seconds, the peaks become sharper and increase rapidly. This corresponds well with what has been presented in Figure 8.26. At 24 seconds, the system seems to have stabilised in the limit cycle configuration. The phase coupling between the two flaps is lost and especially the outer flap seems to suffer more from the delimiters, a fact that can be attributed to the higher interaction of the outer flap with the unstable bending mode compared to the inner flap. The deflection amplitudes are thus larger and the delimiters are reached earlier. While the frequency of the oscillation of the inner flap does not change, the frequency of

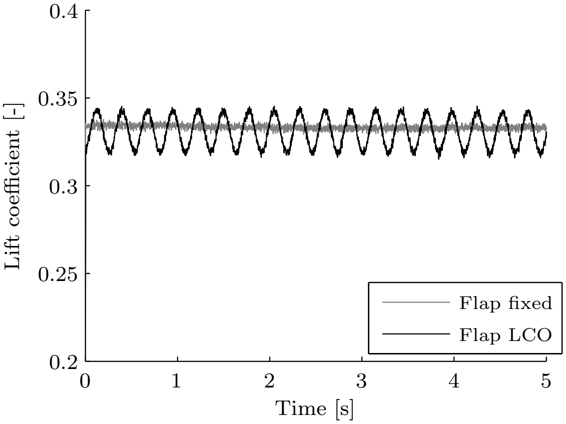

Figure 8.25: Time history of lift forces

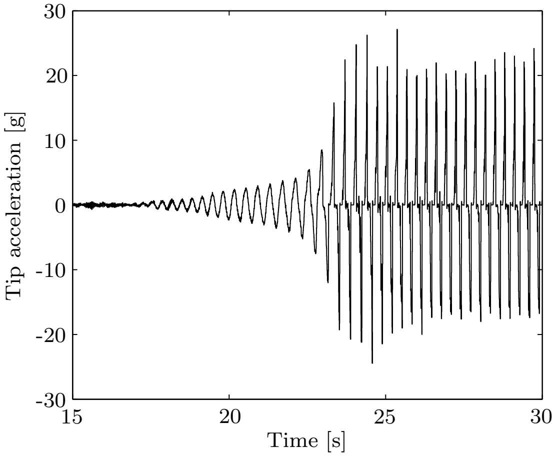

Figure 8.26: Tip accelerations during limit cycle oscillation

the outer flap triples. One dominant oscillation peak in the outer flap voltage is observed that after a transition period of 3 seconds aligns with the oscillation of the inner flap. Two additional lower amplitude cycles occur probably as a response to the impact between the outer flaps and the delimiter. The experimental results only partially confirm the numerical simulations. While the loss of phase coupling during the transition period is present both in simulation and experiment, the permanent phase shift does not manifest itself in the experiment. The difference might be connected to the hard impact the flap sees every cycle, while the delimiter amplitude was significantly smaller during the numerical simulations and thus the maximum force is also smaller as the oscillation frequencies are identical. The additional peaks that occur in the experiment can consequently not be expected to be as large in the numerical simulations and might not be visible in the voltage history.

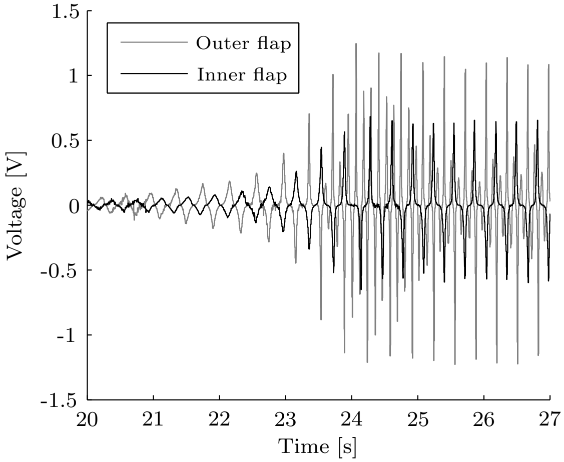

Figure 8.27: Voltage generation of flaps during limit cycle

8.6 SYNOPSIS

In this chapter, the functionality of the free-floating flap has been expanded to a secondary purpose besides load alleviation, namely the harvesting of energy from mechanical vibrations. A practical energy harvesting device has been designed, evaluated numerically, built and tested.

- The potential of exploiting aeroelastic instabilities has been demonstrated numerically and experimentally as the increment in power production can be more than a factor of 200 as compared with turbulence harvesting.
- Changing the resistance is a suitable tool to control the aeroservoelastic stability of the system as it can overcome the destabilizing effect that battery charging can have on the power production and system stability.
- A free-play zone of flap rotation with structural limiters introduces limit cycle oscillations for the numerical simulation. In this limit cycle oscillation a phase shift between the motion of both flaps occurs.
- The trends in power production could be confirmed experimentally.

- A strong relation between wind speeds and the potential energy generation has been underlined experimentally, as crossing the flutter speed yields a tenfold increase in voltage generation.
- The complex nature of the limit cycle oscillations as obtained in the numerical study could only partially be confirmed experimentally. For a controller regulated low amplitude limit cycle oscillation, no phase shift between the flaps occurred. For a structurally limited oscillation, strong peak forces and voltages occurred. During these limit cycle oscillations, the vibrations converge to a pattern, where the outer flap shows a dominant oscillation mode, which is in-phase with the inner flap. Two vibration modes with higher frequency occur for the outer flap.
- For the low amplitude oscillations, which are structurally preferred, the loss of lift of the structure is less than 2%.

Some fear flutter because they don't understand it, and some fear it because they do.
Theodore van Karman

9

THE AUTONOMOUS FLAP

9.1 INTRODUCTION

An autonomous flap combines the functionality of both operation modes of the free-floating flap, load alleviation and energy harvesting, which were presented in Chapter 7 and Chapter 8. The autonomous flap enables a relaxation of the strongest design requirement: the maintenance of a flap system on a smart turbine in offshore applications. This chapter describes a proof-of-concept experiment of such a system.

The chapter[1] is divided into a design, a numerical and an experimental part. First, the physical design of a wind tunnel demonstrator is presented. Then the time-domain response of the system is predicted using a numerical simulation. Special attention is devoted to the controller design, which is the most critical component in the autonomous flap as it needs to switch between harvesting and control modes. The experimental set-up is explained and the experimental results shown. Finally, these are compared to the numerical prediction of the autonomous flap system.

---

[1] This chapter is an adaptation of the conference papers 'Experimental investigation of an autonomous flap for load alleviation' (Bernhammer, Navalkar, Sodja, Karpel and De Breuker (2015*b*)) and 'Experimental and numerical study of an autonomous flap' (Bernhammer, Navalkar, Sodja, Karpel and De Breuker (2015*a*)).

9.2 AEROELASTIC DESIGN OF AN AUTONOMOUS FLAP

The autonomous flap concept is detailed in Figures 9.1 and 9.2. The flap is the top level component, which contains all subcomponents such as sensors, a control system, actuators, an energy harvesting device and the trailing edge tab. The most significant advantage of the autonomous flap is that it is a completely autonomous system, meaning that no connection to the wing or blade structure is needed other than an a structural attachment. It can be used as plug-and-play device on existing structures.

One or multiple sensors (accelerometers in this chapter) measure the motion of the blade-flap system. As shown in Figure 9.2 the accelerometer should be mounted close to the rotational axis of the flap such that the plunge motion of the blade section is dominant in the measured acceleration response. The obtained signal is used as input to a controller, which has been developed based on an experimental system identification of the autonomous, free-floating flap in the aeroelastic apparatus. The controller sets the deflection angle of the trailing edge tab by commanding the actuator. An aerodynamic moment is generated by the trailing edge tab that rotates the flap. This flap deflection creates an aerodynamic force that can be used for control purposes.

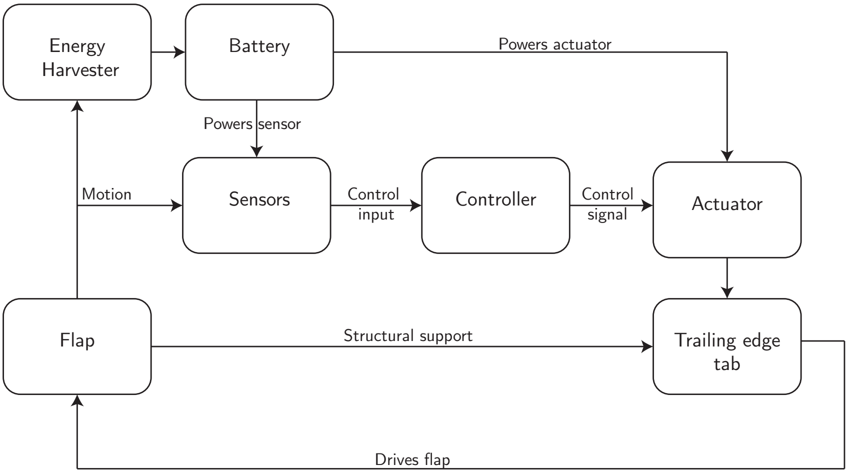

Figure 9.1: Flow chart of autonomous flap concept (Bernhammer, Sodja, Karpel and De Breuker, 2014)

The sensors, the control system and the actuation system are powered by electromagnetic harvesting of aeroelastic vibrations. As has been shown in Chapter 8, the power generation is particularly effective when the system is aeroelastically unstable. Therefore, it is highly desirable to generate controlled oscillations that can provide continuous power production without being destructive for the structure. A potential solution is to constrain the unstable oscillations into limit cycle oscillations (LCO). The amplitude of such oscillations can be limited either passively using structural delimiters or actively by a controller.

A second reason why it is desirable to have the free-floating flaps operating close to the flutter point is that the effective inertia of the flaps is reduced due to unsteady aerodynamic forces. The free-floating flap can be very efficiently controlled by the trailing edge tab as the system gain between the control input and the flap deflection strongly increases when approaching flutter speed (Chapter 8 and Bernhammer, De Breuker, Karpel and van der Veen (2013)). This high system gain reduces the required trailing edge angles and, therefore, also the power requirements of the actuators.

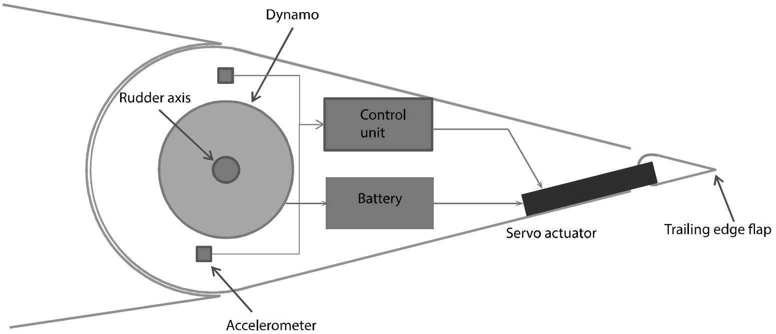

Figure 9.2: Schematic build-up of the autonomous flap (Bernhammer, Sodja, Karpel and De Breuker, 2014)

9.3 AEROELASTIC TEST SET-UP

9.3.1 WIND TUNNEL SET-UP FOR OSCILLATING AIRFOILS

The autonomous, free-floating flap concept has been integrated in an aeroelastic apparatus consisting of a blade section that can undergo pitch and plunge motion. This test set-up has been exhaustively validated for conventional flap systems using CFD data (Sterenborg, 2014). The aeroelastic apparatus is displayed in Figure 9.3. The blade section model (F) is attached by springs to a frame built of sidewalls (C) connected by beams (D). This frame is mounted on a table (B), which can be adjusted to the height of the jet exit of the open test section (A). Struts (E) on both sides are used to increase the stiffness of the frame. Plunge and pitch motion of the blade section are decoupled by having a global translating system (I), on which rotational springs are mounted, giving an additional degree of freedom as shown in Figure 9.4. The side plates are guided by a rail system to prevent motion other than pure plunge. The properties of this set-up are given in Table 9.1. The springs (H) are attached to load cells and the side plates (I) are equipped with angular sensors and accelerometers. Strain gauges are attached to the root of the blade section.

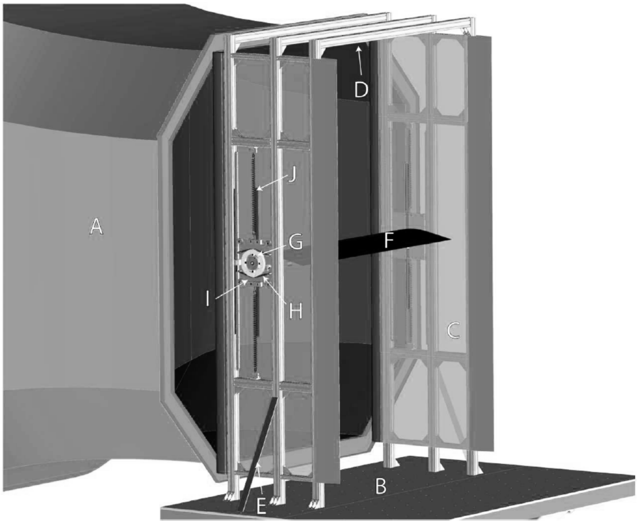

Figure 9.3: Experimental set-up in open jet facility: the jet exit (A), the table (B), two sides upright (C), connecting beams (D), struts (E) and the blade section (F). Moment sensors (G) are attached to springs (H) on movable side plates (I), drawings from Sterenborg (Sterenborg, 2014)

Table 9.1: Properties of the aeroelastic set-up

Width	1800 mm
Chord	500 mm
Airfoil profile	DU96-W-180
Flap chord	100 mm
Plunge spring stiffness	8225 N/m^2
Structural damping	77.9 kg/s
Wing assembly mass	22.7 kg
Wing mass	15.2 kg
Side plate mass	7.5 kg
Eigenfrequency	3.0 Hz

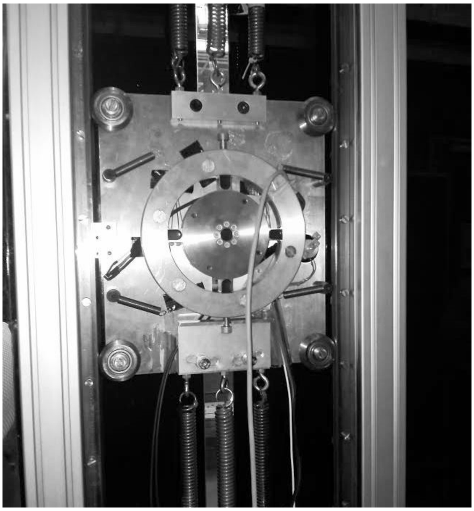

Figure 9.4: Plunge-pitch mechanism

9.3.2 MODEL DESIGN

Table 9.2 provides an overview of the equipment that has been installed in the autonomous flap. The arrangement of all components in the flap is shown in Figure 9.5. The accelerometer (A) measures motion in the plunge direction. The potentiometers (B) and the gear boxes (C) serve as hinge to the main blade section. The gear box is connected to a generator, in which the magnet is the rotor and the coil is the stator. A pair of servo-motors (D) drives the trailing edge tab (E).

Table 9.2: Flap design parameters

Material	SL-Tool STONElike
Density	1.37 g/cm^3
Young's modulus	3.5 GPa
Tensile strength	47 MPa
Skin thickness	2 mm
Servo actuator	HiTech HS-7115TH
Gear box	Apyxdyna AM022
Gear ratio	1:80
Generator	Kinetron MG 23.0
Analogue devices	ADXL78

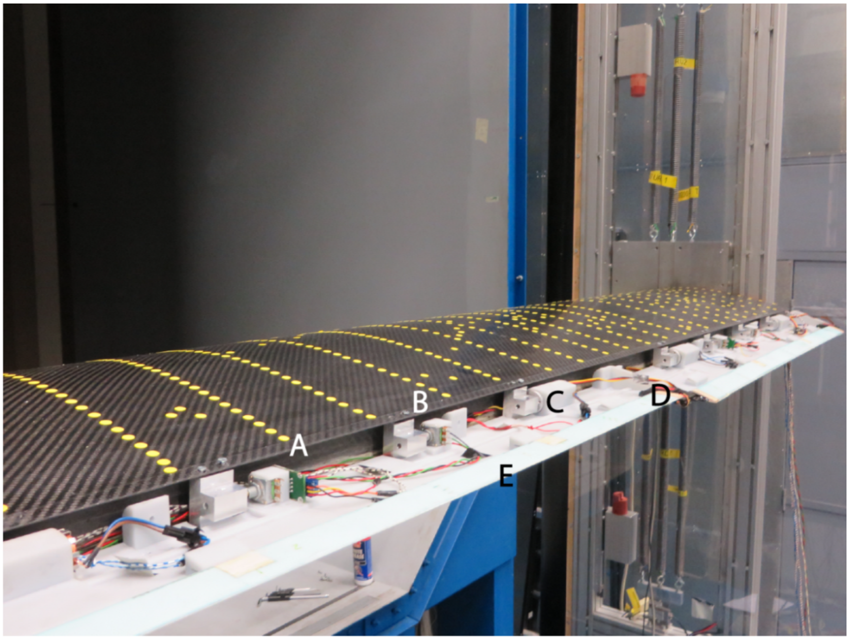

Figure 9.5: Free-floating flap with active trailing edge

9.3.3 AEROELASTIC ANALYSIS

The model has been studied both numerically and experimentally. As a first step, a flutter analysis was performed. It is very critical to operate close to the flutter speed as both the control authority of the trailing edge flaps and the power generation increase close to the flutter speed as was shown in Chapter 8 and by Bernhammer, De Breuker, Karpel and van der Veen (2013). The flutter analysis was done in MSC/Nastran using the PK-method (Rodden and Johnson, 1994). Figure 9.6 shows the relevant aeroelastic modes. The frequencies in the caption of Figure 9.6 correspond to the natural frequencies without aerodynamics. The first two modes are rigid-body modes of the free-floating flap at 0.0 Hz. The third eigenmode is a plunge dominated mode at 3.0 Hz, which also has a flap deflection component. The fourth mode of the blade section is a torsion dominated mode with a frequency of 6.8 Hz. All other elastic modes are clearly separated from the first four modes in terms of frequency. Their frequencies are more than an order of magnitude higher.

The frequency and damping plots of the aeroelastic system are shown in Figure 9.7. The frequencies of the two flap modes increase almost linearly with the wind speed. Aerodynamic stiffness is added to the flap deflection modes, which results in an increase of the oscillation frequency. The flap deflection curve with

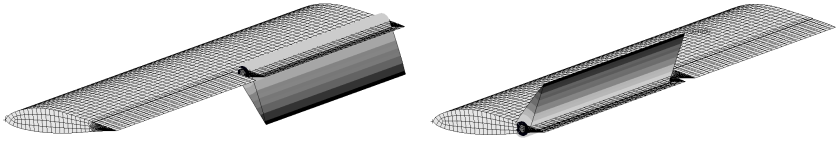

(a) 1st flap mode at 0.0 Hz (b) 2nd flap mode at 0.0 Hz

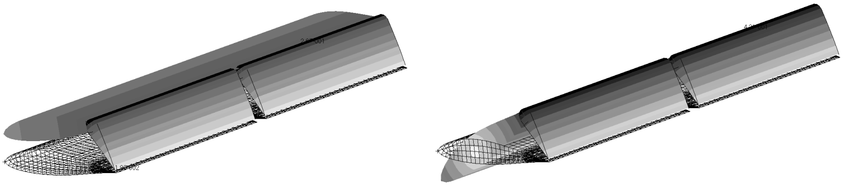

(c) 1st plunge mode at 3.0 Hz (d) 1st pitch mode at 6.8 Hz

Figure 9.6: Structural modes

the higher slope corresponds to a synchronous vibration of the two flaps, whereas the curve with the smaller slope corresponds to a 180 degrees phase difference between the two flaps. Both modes are highly damped. While the frequency of both flap deflection modes increases quickly with the velocity, the frequency of the plunge mode is constant up to 8.0 m/s. From that velocity onwards, interaction of the plunge mode with the synchronous flap deflection mode takes place and the damping of the plunge mode reduces until flutter occurs. The flutter speed can be found at a velocity of 11.0 m/s. Figure 9.8 shows four snapshots over a half-cycle of the unstable plunge mode at the flutter speed.

The frequency of the pitching mode hardly changes in the velocity window of the experiment up to 16.0 m/s. Around 30.0 m/s the frequency of the plunge mode drops from the natural frequency of 6.8 Hz to 5.0 Hz. At this point interaction with the plunge mode takes place, which has a frequency of 3.7 Hz. Both modes approach each other rapidly in terms of frequency until they have the same frequency of 4.2 Hz at 40.0 m/s. This pitch-plunge type of flutter is however outside of the scope of the investigation.

The mode shapes as obtained using MSC/Nastran have been used as basis for an aeroelastic analysis in ZAERO (Zona Technology, 2011). ZAERO has been used to obtain a state-space representation of the aeroelastic plant. The transfer functions between accelerometers and tab deflection angle have been assessed using the resulting state-space models for a velocity of 10.0 m/s. The Bode plots are given in Figure 9.9. The eigenfrequencies of both the plunge and the pitch modes are clearly visible at 2.6 Hz and 6.7 Hz, respectively. The acceleration of one of the two flaps is used as sensor. The two curves visible in Figure 9.9 correspond to trailing edge activity on the flap with the sensor and on the other

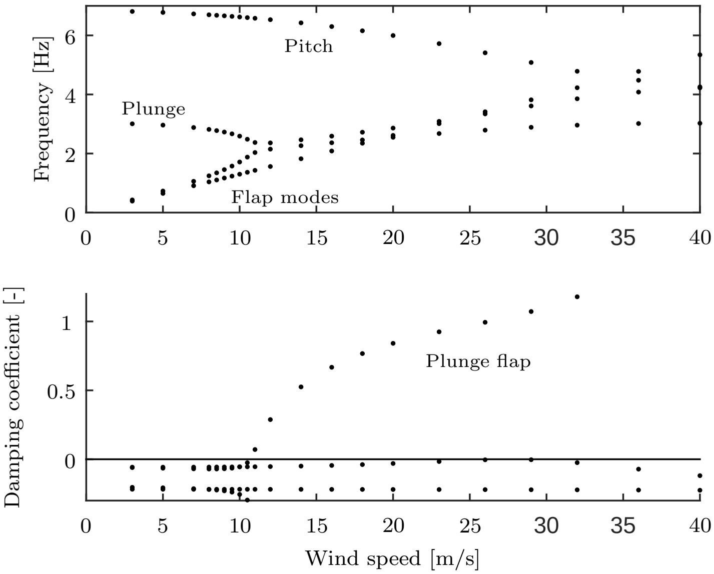

Figure 9.7: Damping and frequency plots as function of velocity

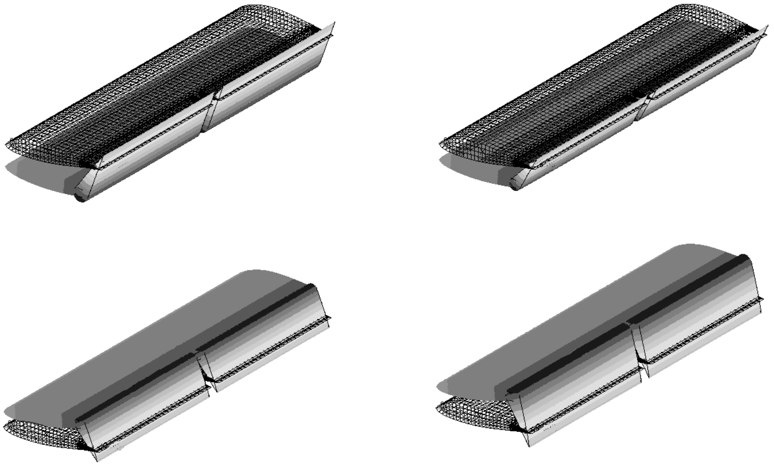

Figure 9.8: 4 snapshots of flutter mode over a half-cycle

flap. For frequencies up to 20.0 Hz, the responses are identical. This is to be expected as both plunge and pitch motion are symmetric with respect to the midplane.

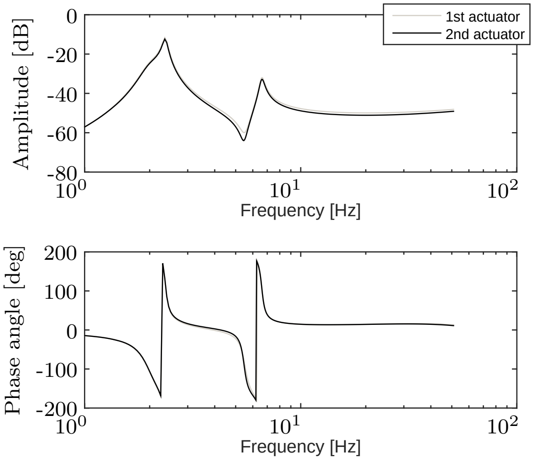

Figure 9.9: Transfer function of trim tab deflection to plunge acceleration

Compared to previous research (Bernhammer, De Breuker, Karpel and van der Veen, 2013) the control authority is reduced. The reason is that a smooth transition between the blade section and the flap was desired in order to maintain the aerodynamic properties. To achieve this, the hinge line has been moved forward to coincide with the end point of the main structure. This increases the moment arm to the aerodynamic center of the flap, thereby reducing the effectiveness of the trim tabs. Nonetheless, 1 degree of trim rotation still corresponds to 0.5 degrees of flap deflection.

9.3.4 ELECTRONIC COMPONENTS

The power requirements are driven by the tab operation. The estimated power consumption during operation is 10.5 mW per flap based on the aerodynamic moments that need to be overcome by each tab. Each generator can produce up to 70.0 mW at a nominal speed of 800 RPM, which is the average rotational speed in LCO with an amplitude of 5 degrees. This means that the system can operate 93% of the time in a control mode.

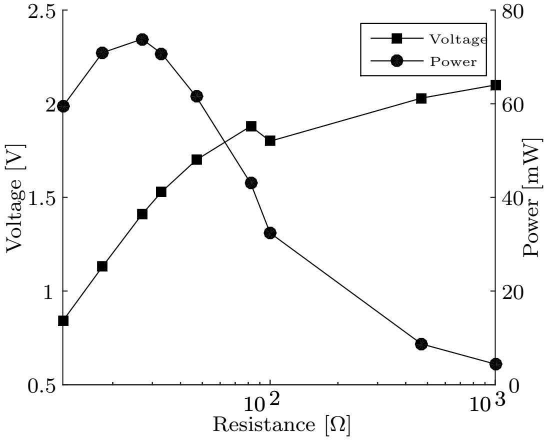

Figure 9.10: Power and voltage as a function of resistance

9.4 AEROELASTIC TIME DOMAIN SIMULATION OF THE AUTONOMOUS FLAP

The aeroelastic time-domain simulation has been implemented in Simulink and re-uses the framework developed in Chapter 8. The structural mode shapes are identical to the ones used to obtain the transfer function between tabs and flaps. The first 15 modes have been used as input to an aeroelastic analysis in ZAERO (Zona Technology, 2011). ZAERO was used to extract the aeroelastic state-space time-domain model based on the Minimum-State rational function approximation of the unsteady aerodynamic force coefficient matrices (Karpel, 1990). A modal damping coefficient of 0.057 is applied to the structural model, as identified by Sterenborg (2014) for the test set-up. The aerodynamic model is divided into five zones, one for the blade section, one for each flap and one for each trailing edge tab. Figure 9.11 shows how the state-space model is integrated into the Simulink simulations. Compared to Figure 8.5 a control feedback loop has been added. This feedback loop is additional to the non-linear feedback loops introducing the electromechanical moments and the forces generated by the structural delimiters.

Figure 9.11 also indicates a gust input. The gust force time history in generalised coordinates has been computed in ZAERO for a continuous gust signal with a low turbulence intensity using a von Kármán turbulence spectrum for an altitude of 250 m above ground level. For the gust load cases, the gust forces are added to the equations of motion. The total state-space linear aeroelastic system has been provided in Equation 8.5. The state-space matrices, $\mathbf{A}$, $\mathbf{B}$, $\mathbf{C}$ and $\mathbf{D}$, the state vector, $\mathbf{x}$, and the input vector, $\mathbf{u}$, however, have been updated compared to Chapter 8 to include the control loop.

$$
\begin{aligned}
\mathbf{A} &= \begin{bmatrix} \mathbf{A_{ae}} & \mathbf{B_{ae}} & 0 \\ 0 & \mathbf{A_{ac}} & 0 \\ 0 & 0 & \mathbf{A_c} \end{bmatrix} \\
\mathbf{B} &= \begin{bmatrix} 0 & 0 \\ \mathbf{B_{ac}} & 0 \\ 0 & \mathbf{B_c} \end{bmatrix} \\
\mathbf{C} &= \begin{bmatrix} \mathbf{C_{ae}} & \mathbf{C_{ac}} & 0 \\ 0 & 0 & \mathbf{C_c} \end{bmatrix} \\
\mathbf{D} &= \begin{bmatrix} \mathbf{D_{ac}} & 0 \\ 0 & \mathbf{D_c} \end{bmatrix} \\
\mathbf{x} &= \begin{Bmatrix} \mathbf{x_{ae}} \\ \mathbf{x_{ac}} \\ \mathbf{x_c} \end{Bmatrix}
\end{aligned}
$$

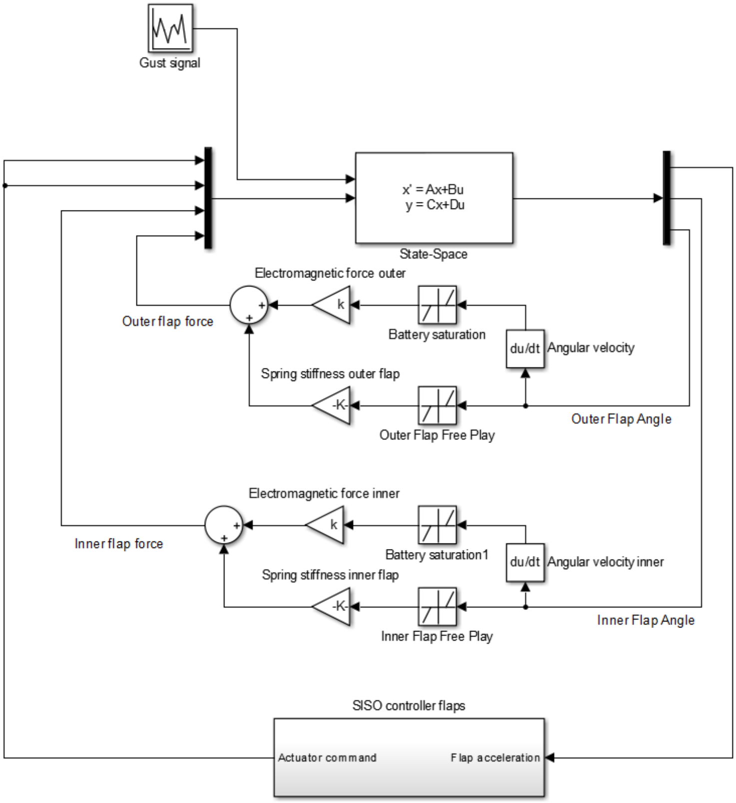

Figure 9.11: Simulink scheme of autonomous flap model

The state vector, $\mathbf{x}$, contains the modal displacements and velocities, the aerodynamic lag, the actuator states and the control states, and the input vector, $\mathbf{u}$, contains the trailing edge tab commands and the non-linear feedback hinge moments. The vector $\mathbf{u_{gust}}$ contains the gust time history. The subscripts *ae* denote the aeroelastic model, *ac* the actuator and *c* the controller. The system has been closed by including a feedback gain matrix from the output vector, $\mathbf{y}$, to the input vector, $\mathbf{u}$.

$$\mathbf{y} = [\mathbf{G}]\,\mathbf{u} \tag{9.1}$$

The electromagnetic resistance moment of the flap, which is introduced as part of the non-linear feedback hinge moment in the input vector $\mathbf{u}$, is modelled based on the electrical power of the generator. It is a function of the rotational velocity. The magnitude of the moment can be computed based on Equations 8.3 and 8.4. For the autonomous flap design, the variables of these equations have been found experimentally. The magnetic field strength has been determined by matching the generated voltage during the wind tunnel experiment. The approximation to the term $(nl\phi_k)^2$ has a value of 9.1mNms/rad and a gear ratio of 80 is applied. The resistance in the loop $(R_{coil}+R_{var})$ is chosen to be 75Ω, which corresponds to the impedance matching condition. The structural stiffness outside the free-play zone is 3800Nm/rad and the width of the free-play zone is 17 degrees in both directions, again corresponding to the experimental results.

The mechanical moments, which add to the structural damping, are implemented in generalised coordinates into the state-space system together with a structural free-play zone as shown in Figure 9.11. The outputs of the state-space system are the plunge acceleration of the blade section and the rotation angles of both free-floating flaps. The rotational velocities are also obtained as output of the aeroelastic state-space system and serve as input to Equation 8.4.

9.5 MODEL IDENTIFICATION AND CONTROLLER DESIGN

The first step in the wind tunnel experiments was system identification to obtain a low-order linear model for control system design for the autonomous flap. Due to friction in the flap mechanism of the wind tunnel model, the flutter speed increased compared to the numerical studies, such that instabilities occurred above 13.0 m/s. The exact flutter point could not be determined as the damping of the aeroelastic apparatus was highly non-linear for small vibration amplitudes. Once a vibration amplitude threshold was passed, the structural damping coefficient approached a value of 0.057, which was used in the numerical study.

In order to use the tabs to control structural vibrations, a feedback controller had to be designed. This was done in two steps: first, system identification was used to arrive at a dynamic model of the system. Next, classical loop-shaping techniques were used to design a controller that was capable of damping the plunge dominated vibrational mode of the system.

9.5.1 SYSTEM IDENTIFICATION

One of the requirements for the design of a classical feedback controller was a simple dynamic model of the system to be controlled, preferably in terms of linear differential equations. Such a model may be obtained from first principles and physical modelling, which typically requires high accuracy in experiment construction and calibration. With structural and aerodynamic non-linearities, the complexity of such physical models often renders them challenging for the purpose of controller synthesis. Further, they may involve dynamics that are irrelevant within the controller bandwidth.

An alternative approach to obtain a controller-relevant system model is to use system identification techniques, such as subspace identification (Verhaegen and Verdult, 2007). In such a method, experimental data is obtained by exciting the system and the input-output data is used directly to estimate a dynamic system model that can be used for controller design. The input data during the identification was the trim tab deflection and the sensor chosen for feedback control was the side plate accelerometer. A decision was taken to change the location of the accelerometer compared to the numerical study, as the accelerometer mounted on the side planes was delivering a measurement signal with a significantly higher signal-to-noise ratio than the accelerometers in the flaps. Consequently, system identification with less polluted data could be performed.

To simplify the identification problem, the identification experiment was conducted at a single wind speed (12.5 m/s), which is below the flutter speed, so that the system was stable and could be approximated as linear. The blade section was excited by applying a pseudo-random binary sequence to the tabs, which resulted in structural oscillations. The structural vibrations were measured by the accelerometer located on the side-plates, which was the signal that was used as feedback for the controller.

A transfer function $G(s)$ was estimated which describes the dynamics from the tab actuation angle β to the accelerometer response a_y, using the PBSID system identification technique (Chiuso, 2007).

$$a_y = G(s)\beta. \tag{9.2}$$

The frequency-domain representation of the identified system is given in Figure 9.12.

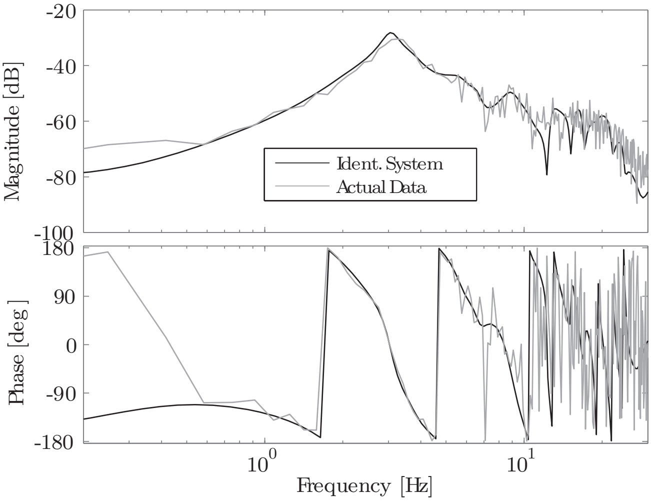

Figure 9.12: Bode plot of identified system at 12.5 m/s

The grey line is the actual frequency-domain data obtained from the experiment, while the black line shows an estimate of the underlying state-space system. As expected, a resonance peak at the first structural mode of 3.0 Hz was clearly identified in the system identification experiment. While the frequency of the unstable branch of the numerical model decreases from the natural frequency of 3.0 Hz to 2.6 Hz when approaching the flutter speed as shown in Figure 9.7, the experiment did not exhibit this behaviour. Only a slight decrease in frequency from 3.0 Hz to 2.9 Hz was observed.

Using this identified model, a classical feedback controller was designed for the system.

9.5.2 CONTROLLER DESIGN

The structural vibrations measured by the accelerometer were fed back into the controller, which generated the appropriate tab actuation signal to counteract and, thereby, damp the vibrations. Hence, there were three major considerations for the controller:

- There must be adequate gain around the first mode frequency of 3.0 Hz to be able to achieve feedback control.
- The actuation signal generated at the resonance frequency must produce an anti-phase structural response so that the vibrations are attenuated and not

enhanced.

- The resulting closed-loop system must be stable.

Taking these considerations into account, a feedback controller $K(s)$ was designed that consisted of the following three elements:

$$K(s) = K_1(s)K_2(s)K_3(s), \tag{9.3}$$

where $K_1(s) = k$ is a simple gain, $K_2(s)$ is a phase lead compensator and K_3 is an inverted notch. The filter K_2 adds an adequate amount of phase within the bandwidth to achieve the right amount of damping,

$$K_2(s) = \frac{s/\omega_1 + 1}{s/\omega_2 + 1}, \tag{9.4}$$

and K_3 enhances the feedback at a single frequency, which is the same as the resonance frequency $\omega_r = 3.0$ Hz:

$$K_2(s) = \frac{(s/\omega_r)^2 + 2(s/\omega_r) + 1}{(s/\omega_r)^2 + 2\zeta(s/\omega_r) + 1}. \tag{9.5}$$

The various tuning parameters in the controller equations are detailed in Table 9.3.

Table 9.3: Control parameters: wind tunnel experiment

Parameter	Symbol	Value
Controller gain	k	3.333
Phase lead start frequency	ω_1	0.001 Hz
Phase lead end frequency	ω_2	0.5 Hz
Resonant frequency	ω_r	3.0 Hz
Notch damping	ζ	0.5

When this controller was connected in closed loop with the plant, the structural resonance peak was damped to a large extent, as can be seen in Figure 9.13. Figure 9.13 also shows a comparison to the numerical model in both cases 0.5 m/s below flutter speed. In the experiment, the acceleration measurement had been shifted to the pitch axis of the blade section instead of being located in the flaps. Therefore the accelerometer did not capture the flap deflection modes at 1.6 Hz or the pitch mode at 6.8 Hz, which are present in the original data. The amplitude of the plunge mode was almost exactly matched in the numerical model and the experiment. A shift in frequency of the mode, however, was observed between the experimental system identification and the numerical prediction. In the experiment the frequencies did not show the same drop with increasing wind speed as is observed in Figure 9.7 for the unstable branch around the flutter point.

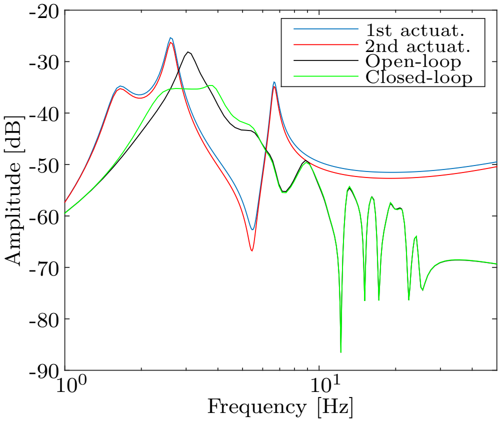

Figure 9.13: Bode plot of open-loop and closed loop system at 12.5 m/s (experiment, black and green) and 10.5 m/s (numerical model, red and blue)

The increased damping of the closed-loop system can also be seen in the time-domain results shown below, where the eigenmode oscillations decay much faster when the controller is active as shown in Figure 9.14.

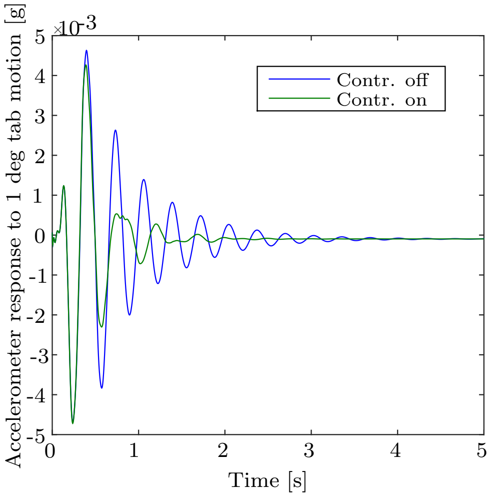

Figure 9.14: Decay of oscillation: Open-loop versus Closed-loop

Table 9.4: Control parameters: numerical simulation

Parameter	Symbol	Value
Controller gain	k	0.0016
Phase lead start frequency	ω_1	0.001 Hz
Phase lead end frequency	ω_2	0.5 Hz
Resonant frequency	ω_r	scheduled with wind speed
Notch damping	ζ	0.5

9.5.3 CONTROLLER ADAPTATION FOR NUMERICAL SIMULATION

As explained in Section 9.4, the numerical aeroelastic model has been updated compared with the methodology in Chapter 8 to include a control loop. The controller architecture is analogous to the wind tunnel experiment as presented in the previous subsection. While in the experiment, the plunge frequency remained constant for all wind speeds, numerically a drop in the frequency of the plunge mode has been observed from 3.0Hz for 0.0 m/s to 2.3 Hz at 11.0 m/s, which is the flutter speed. The notch filter in the controller design has been scheduled to match the frequency at the given wind speed. The control parameters used in the numerical simulation are provided in Table 9.4. It should be noticed that the controller gain has been adapted as well for the numerical simulations. This was needed because the controller input in the numerical simulation is the acceleration in terms of the gravitational constant, while in the experiment, the controller input is the measured accelerometer voltage.

9.6 LIMIT CYCLE OSCILLATION

As is pointed out in the introduction, for the energy harvesting it is vital to be close to, or above, the flutter speed. For that purpose, limit cycle oscillations were studied intensively during the experiment. Two different types of limit cycles were investigated, namely structurally limited cycles and limit cycles that were reached through control of the trailing edge tab. The structural limit was achieved by limiting the maximum deflection of the flaps from -20 to 30 degrees. Figure 9.15 shows the structurally limited oscillations in the wind tunnel experiment. The trailing edge tabs were used to initiate the vibration. For small oscillation amplitudes, the system was still stable as a result of friction-type non-linear damping.

A sinusoidal oscillation with a frequency of 3.0 Hz was imposed on the trailing edge tab after 7.0 seconds. This oscillation immediately caused the flap to vibrate at the input frequency. A time delay of 1.0-1.5 seconds was observed when comparing the flap oscillations and the acceleration of the plunge mode. This time delay was caused by the inertia of the blade section, which only slowly started to oscillate. Practically at the same time as the accelerometer, the load cells, which were connected to the springs, showed an oscillation in the force measurements. In contrast to the load cells, which measured an almost perfect sinusoidal signal, the accelerometers measured a dominant signal of identical frequency, but their signal also carried components of the multiples of the frequencies. The damping of the spring system might have reduced the amplitude of higher harmonics in the measurements of the vertical forces by the load cells.

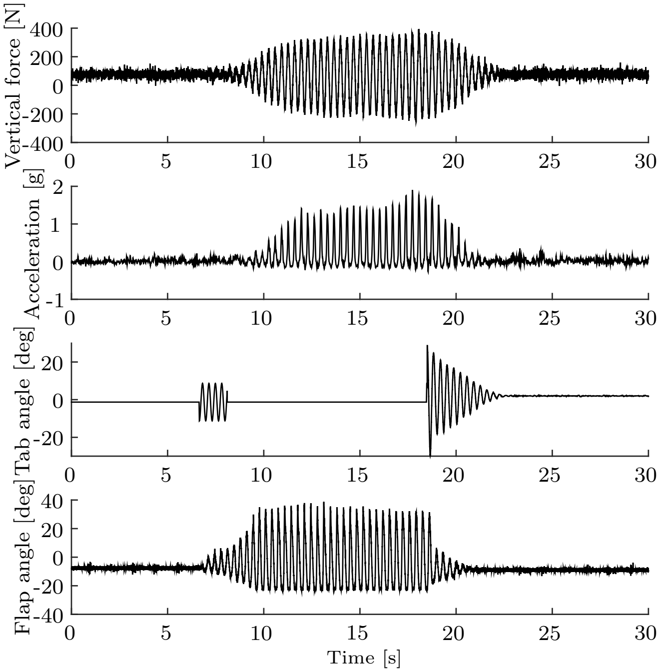

Figure 9.15: Structurally limit cycle oscillation

From 7.5 seconds until 18.0 seconds the system was unstable and the excitation signal was deactivated. At 9.0 seconds the flap deflection reached the delimiters of the flap, which caused a limit cycle oscillation. At 18.0 seconds the controller was switched on. Almost instantaneously, the amplitude of flap deflections reduced to 10 degrees, from which point it slowly decayed. This shows the stabilization effect the trailing edge tabs have on the flaps. The oscillations of the complete system decayed slower and reached a static position at 22.0 seconds.

The second possibility to achieve limit cycle oscillations is to actively use the controller to limit the cycle amplitude. The same controller as described above was used, however an on/off condition was included, namely that the controller was only active if the amplitude of the flap deflection over the previous oscillation cycle had exceeded a specified threshold. The initialization of the limit cycle was identical to the previously described structurally limited oscillations. A sinusoidal oscillation was imposed as seen in the second subfigure of Figure 9.16. Again, the oscillations started to grow even when the excitation signal was stopped. Flutter caused the oscillations to increase until the flaps reached their structural limits. This oscillation was maintained until the controller was activated at 11.0 seconds. The controller reduced the amplitude of the oscillations, but the high inertia of the plunge mode caused its oscillations to decay slowly. In that phase the controller was mostly active until the system reached a steady state. Around 17.0 seconds a stable pattern developed and the controller was only active 11% of the experimental time. The control activity almost immediately eliminated the vibration of the flaps. For three to four cycles, the controller stayed inactive, while the flap vibrations rebuilt. When flap vibrations exceeded a tunable limit, the controller was reactivated until the vibrations decayed below this limit. The inertia of the system caused the accelerations of the blade section to decay much slower than the flap deflections when the controller was active. Thus, a practically constant limit cycle oscillation was reached at a lower amplitude, with a maximum flap deflection of 15 degrees.

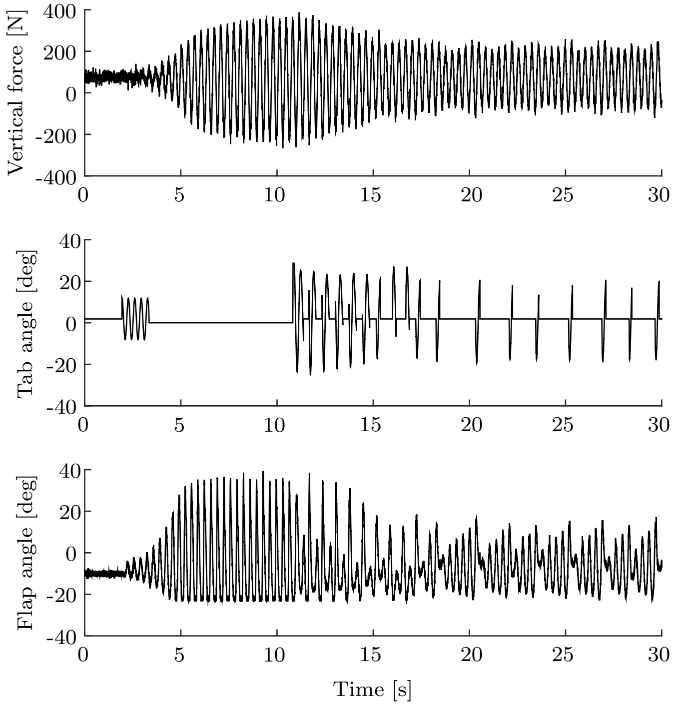

Figure 9.16: Controlled limit cycle oscillation

9.7 POWER BALANCE

The second task of the autonomous, free-floating flap is to generate power in order to be self sustained. As mechanical friction in the system was high, the power that was generated by the flaps could not directly be measured. This mechanical friction is mainly a problem of downsizing the system as small generators need higher rotational velocities than large generators. Consequently, the gear ratio to drive the flaps needed to be very high. A doubling of the generator diameter allows a doubling of the poles and, therefore, a reduction of the rotational velocities to generate sufficient power. As a collateral effect of increasing the rotational velocity by a factor of 80 (the gear ratio), the apparent frictional torque on the flap was also increased by a factor of 80. Hence, the near-flutter vibrations were required to overcome a significantly higher frictional resistance in this experiment than would be encountered at full scale. The low test speeds in the wind tunnel dramatically reduced the moment that could be generated to overcome these forces. A full-scale wind turbine operates at tip speeds of 60.0 m/s, compared to the wind tunnel test velocities of around 12.0 m/s. Additionally, the chord of the wind turbine airfoils close to the tip is four times largeree than the experimental blade section. This results in a moment on the hinge axis that would be 400 times larger than the moment on the wind tunnel model.

The measurements presented in Figure 9.17 have been obtained by imposing a flap oscillation at the first flutter frequency corresponding to the limit cycle oscillations. As can be seen in the first subfigure of Figure 9.17, the frequency of

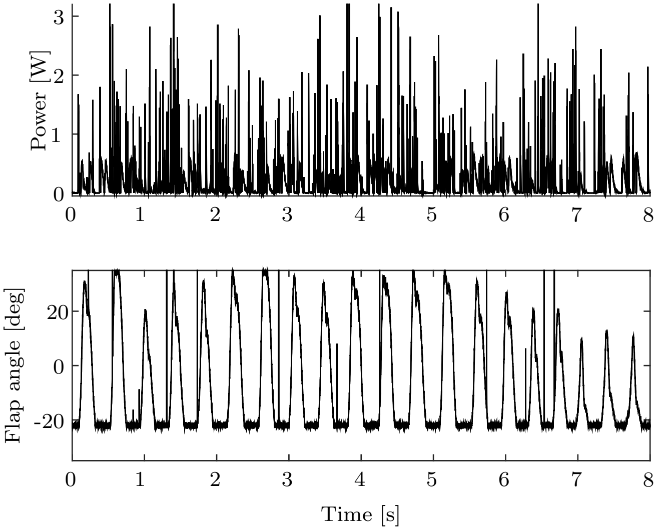

Figure 9.17: Power production of generators during sinusoidal oscillation at 3.0 Hz

the signals was much higher than the flap oscillation frequency of 3.0 Hz. This was a result of the gear ratio. The power signal shows a high noise component. The source of the noise was mechanical friction in the rotation due to which a smooth rotation could not be achieved and peaks and troughs in the rotational speed were observed. The power that could be reached in the presented configuration was measured over a resistance of 35.0 Ω. Figure 9.17 displays the sum of all four generators that have been installed in the aeroelastic apparatus. The mean power that could be achieved during the equivalent limit cycle oscillations is 313.3 mW or a root mean square power of 564.0 mW.

The harvested energy should be sufficient to power the actuators and the accelerometers. The latter has a very low power requirement of less than 1 mW such that in practice, the drivers of power requirements are the actuators that drive the trim tabs. Figure 9.18 shows an overview of the power consumption of all actuators. The top subfigure displays the current that was drawn for the actuator motion. The actuation system was powered by an external constant voltage source. The voltage that was supplied is shown in the middle subplot of Figure 9.18. Up to 4.0 Hz, the voltage demand could be matched exactly. Above this frequency, a drop in voltage output was observed, however the tabs still remained operational.

The biggest share of the power consumption stemmed from the operation of the actuators themselves. The additional power requirement by including aerodynamic loads was small compared to the free oscillation. The difference in power is provided in the lower subfigure. This curve includes the difference in power consumption for all actuators combined. Around 3.0 Hz, this difference was highest at just above 0.4W. At higher frequencies, the power source failed to deliver the demanded power. Both, with and without aerodynamics, the maximum power was drawn, such that the difference between both cases amounted to 0 V. One needs to bear in mind that the actuators only needed to be active 11% of the time to achieve a constant limit cycle amplitude. The averaged power consumption due to aerodynamic resistance moments therefore dropped to 0.0427 W, which is 14% of the generated power. When including the actuator power requirements, the average consumption increased to 0.440 W, which is 41% higher than the power production, however the actuators were overdimensioned such the trim tab could be actuated even if one of the actuators failed.

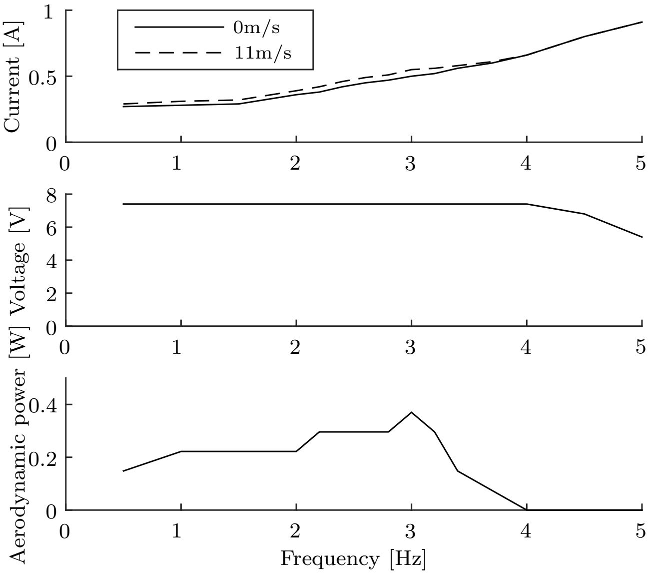

Figure 9.18: Power consumption of actuation system as function of actuation frequency and wind speed for 20 degrees tab amplitudes

9.8 COMPARISON BETWEEN NUMERICAL AND EXPERIMENTAL RESULTS

9.8.1 LIMIT CYCLE OSCILLATION

The controller design of the experiment has been tuned to the numerical simulation to account for the frequency shift as described before. Figure 9.19 displays the time history of the limit cycle oscillation and the subsequent controller activity. The results aim to reproduce the experimental counterpart, which is presented in Figure 9.15. In contrast to the experiment, the vibration in the numerical results is not initiated by tab activity, but by a small initial deflection of the plunge mode that yields identical LCO. The perturbation post flutter speed leads to a diverging motion until the flaps reach their structural limit. When the controller is activated after 5.0 seconds, the system stabilises and the vibrations damp out. The time scale in the numerical simulation associated to the damping is longer than in the experiment. This can be attributed to the lower tab deflections with a maximum of 10 degrees, while in the experiments, the maximum values reached were up to 20 degrees. This results in a lower damping of the flap motion and consequently a longer decay time.

The second comparison study concerns the controlled limit cycle through tab

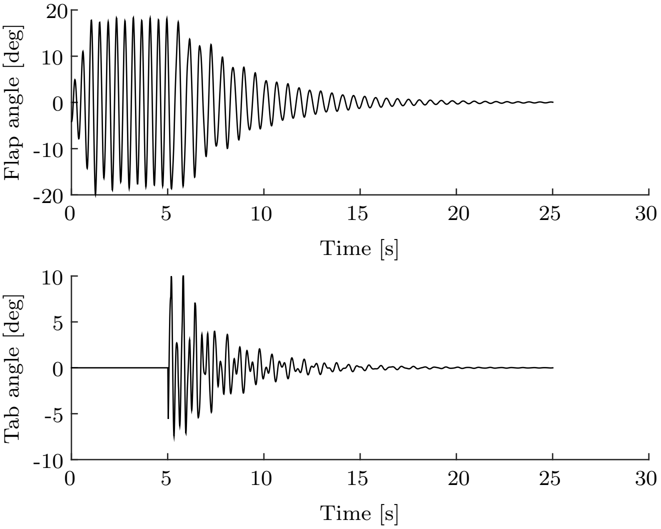

Figure 9.19: Structural limit cycle and active control

activity. The numerical results are shown in Figure 9.20. The corresponding experimental results are presented in Figure 9.16. The numerical procedure is identical to the methodology for obtaining Figure 9.19, except that a controller on/off condition is included based on the recent time history of the flap oscillation amplitude. Figures 9.20 and 9.16 are similar until the first time the controller is switched off because the flap oscillation amplitude has dropped below 10 degrees. The controller activity causes the flaps to enter a stable limit cycle with a flap amplitude of 10 degrees, similar to the experimental results (Figure 9.16). However, two differences in the results can be observed. The first difference is that the control activity during the experiment causes an immediate drop in flap oscillation amplitude from 15 to 5 degrees, while in the numerical simulation this drop is much lower. The reason is again, that the tab deflections set by the controller are around 5 degrees, while in the experiment they reach 20 degrees. The result is a more continuous control activity. In the experiment the time fraction, the controller was active, was 11%, while in the numerical simulations this time fraction is above 60%. The energy requirements on the flap are however lower, as the power consumption of the flaps is proportional to the rotational velocity of the tab and the aerodynamic forces on the flap, which are proportional to the amplitude when assuming that the lift is a linear function of the angle of attack. Decreasing the tab amplitude by a factor of 4 would yield a decrease in actuation requirements by a factor of 16.

The second difference is that the repetitive pattern observed in the experimental results is not reproduced by the numerical simulation. In the experiments, the strong drop in flap amplitude caused by control activity, recovered over several cycles before the amplitude surpasses the specified limit. Due to the small drop in flap oscillation amplitude in the numerical simulations, the oscillation might or might not grow to the specified amplitude within a single cycle.

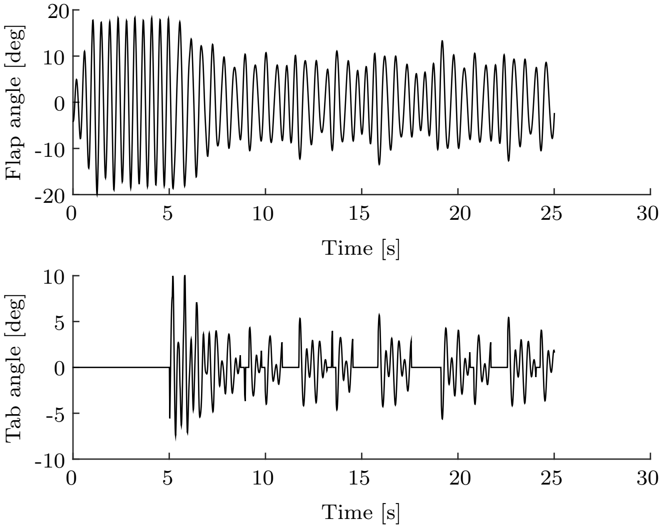

Figure 9.20: Limit cycle structure and control

9.8.2 NUMERICAL SIMULATION OF POWER PRODUCTION

In a final step, the power production of the autonomous flap system has been analyzed. Figures 9.21 and 9.22 show the time history of flap rotation and voltage production. The voltage provided in Figure 9.22 is the sum of the voltages of all four actuators as if they were connected in series. While the first three wind speeds correspond to aeroelastically stable systems, for 12.0 m/s the autonomous flap system is operating past the flutter point. The first three cases produce a small voltage at the beginning, due to the vibrations introduced by the initial conditions. For 10.0 m/s the flap deflection amplitude reaches 7.5 degrees at which point the controller becomes active for a very short period, which causes the results with and without controller to be different. For wind speeds of 3.0 and 8.0 m/s, controlled and uncontrolled results are identical. For 12.0 m/s the open-loop results are confined by the structural limit, while in the closed-loop case, the controller sets the limit cycle amplitude.

The flap vibrations are converted into electrical energy. The fraction of the extracted energy is small, such that the electromechanical damping effect remains negligible. Due to the lower amplitude of the controlled limit cycle, the voltage

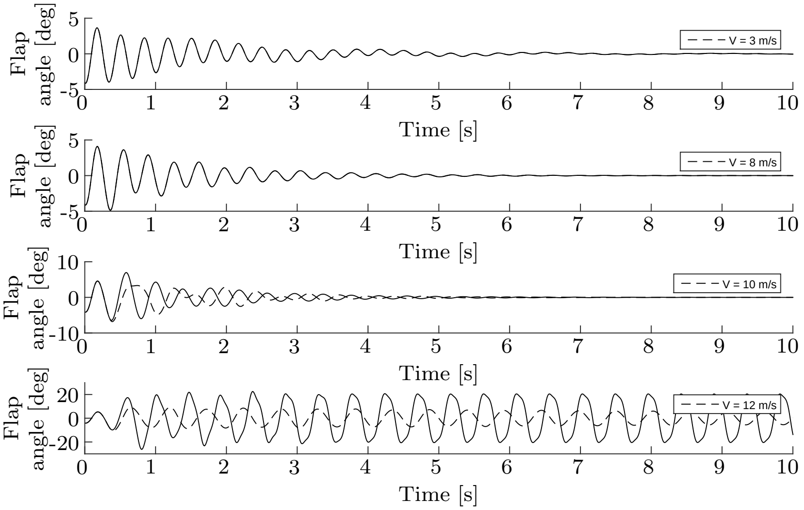

Figure 9.21: Rotation angles open- (-) and closed-loop (- -)

output of the system is reduced in the closed-loop case.

In a final step, the average power production using different limit cycle amplitudes was computed for a range of wind speeds. During the experiment, a mean power per flap of 313.3 mW was produced. Figure 9.23 shows the total power of both flaps combined due to the initial conditions with a small amplitude in plunge mode. The time results include the incremental phase of the oscillation, such that the actual power production during LCO, certainly for 11.0 m/s, which is only slightly unstable, will be slightly higher. By far the highest power production is achieved for the structural limit cycle. For a wind speed of 12.0 m/s a value of 510.0 mW is reached, which corresponds well with the experiment, certainly when considering that the LCO production in the numerical simulation should be slightly higher than the reported value. The controlled limit cycles with an amplitude of 10 degrees produce 111 mW, while for 5 degrees, the average power is 29 mW.

9.9 SYNOPSIS

In this chapter the concept of an autonomous, free-floating flap has been presented and a wind tunnel model designed. The flap system was retrofitted into an aeroelastic plunge and pitch apparatus. Numerically, the flutter speed was predicted to be 11.0 m/s, but due to friction in the flap system, the flutter speed was 13.0 m/s during the experiment. Two autonomous flaps were installed on

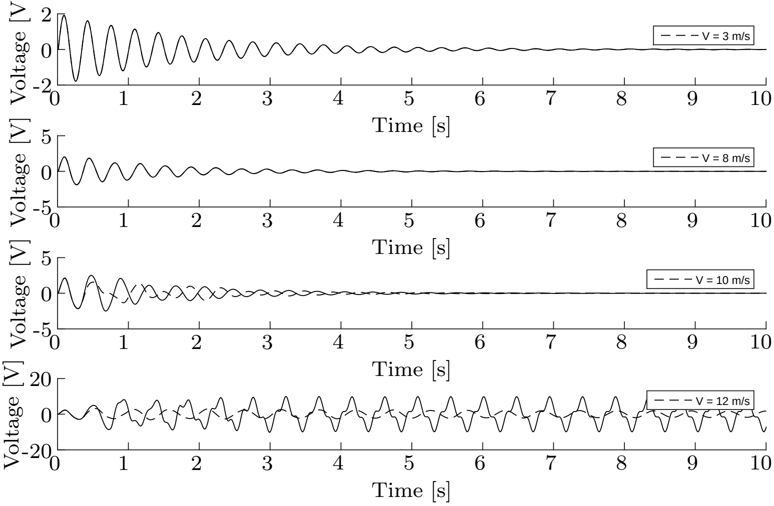

Figure 9.22: Voltage open (-) and closed loop (- -)

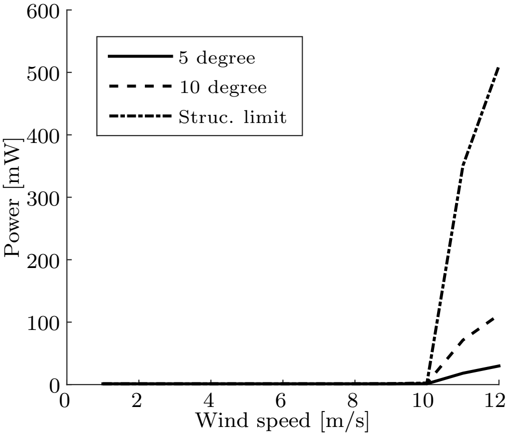

Figure 9.23: Power production of generators due to an initial impulse

a blade section. Each system included two actuators, two generators and an accelerometer. Additional sensors such as load cells were installed on the frame.

During the experiment, the transfer function of the tab command to an accelerometer command was identified. The obtained model agreed well with the numerical model, except for a drop in frequency of the numerical model close to the flutter speed, which was not observed during the experiment. It was experimentally shown that

- The system flutters in a combination of plunge and flap deflection motion.
- The controller is able to yield a lower limit cycle than the structural limit.
- An average energy production of 313.3 mW could be achieved, while the consumption is only 42.7 mW.
- The system is therefore self-sufficient.

The experimental campaign has confirmed the findings of the numerical study. The major difference between simulation and experiment lies in the control activity, which was lower in the numerical model than in the experiment. Therefore, damping of the flap caused by the trailing edge tab was reduced compared to the experimental study. The result is a more continuous control activity with lower power requirements.

Prediction is very difficult, especially about the future.
Niels Bohr

10

CONCLUSIONS AND RECOMMENDATIONS

In this dissertation, the concept of a smart rotor was studied numerically and experimentally. Additionally, an autonomous flap system has been designed and tested. This chapter presents the conclusions and recommendations drawn from the main body of this dissertation. The structure of this chapter therefore follows the structure of this thesis, by first evaluating the results of the smart rotor simulations and the comparison with the smart rotor experiment. Thereafter, the results of the autonomous flap experiment are evaluated. The conclusion of the dissertation will be discussed based on the main research question formulated in Chapter 1. The chapter is rounded of by recommending steps for future research.

10.1 EVALUATION OF RESULTS

Previous studies by Andersen (2010), Bergami (2013) or Bæk (2011) have mainly focused on the aerodynamic implementation of suitable aerodynamic models, while Barlas (2011) has focused on controller design. This dissertation forms a complementary piece of research, as the developed sectional aerodynamic models are integrated into an aeroservoelastic analysis tool for horizontal axis wind turbines. This tool was benchmarked against commercial software (GH Bladed) or open-source software (FAST). Additionally, together with the work by Castaignet et al. (2014), the first numerical study of a full-scale experimental wind turbine, the Sandia National Laboratories Smart Rotor, was presented. The results of these time-domain simulations, including flap activity, show that the aeroelastic tool, DU-SWAT, can capture the main characteristics of the structural response and the loads in the wind turbine. These characteristics include response amplitude, but also structural frequencies present in the response. The numerical model is especially accurate for moderate steps in flap deflection up to 5 degrees, but looses accuracy for large step inputs in flap deflection. The discrepancy for high flap deflections was attributed to the assumption of independence of annuli underlying the blade element momentum method. As the flaps are located close to the tip, this assumption might not be valid, as the vortices shed by the flap activity might interact with the tip vortex, which might decrease the stability of the wake. Compared to the numerical model, the Sandia National Laboratories Experiment demonstrated increased damping in the blades. As a variation of structural damping parameters showed that this damping could not be numerically achieved through structural damping, the source could be aerodynamic damping.

Besides the comparison study with the Sandia National Laboratories Rotor, a numerical investigation of the NREL 5MW reference turbine has been performed. This analysis is more detailed then any previous analysis, as components throughout the turbine are monitored; also extreme load cases with extreme turbulence and start-up simulation are performed. The fatigue load reduction results of Bæk (2011) could be reproduced. Fatigue load reductions were not only found for the blade root bending moments, but also for several load components in the shaft, hub and tower. With the exception of the blade root torsion moment, all fatigue loads are either decreased when using the smart rotor or stay unaltered. For most turbine components, the effect of the smart rotor on extreme load reduction is smaller than the fatigue load reduction. This can be explained by the type of controller, which was used in the analysis, namely an individual flap controller analogous to an individual pitch controller. It has been intentionally decided to use a simple control scheme, which would be likely to be applied in a wind turbine, rather than a controller which is based on information of non-traditional, additional sensors such as inflow sensors or distributed strain measurements. Such controllers might be able to enhance the extreme load reductions, but most likely will only be seen on wind turbines in the very long term. The most significant reductions are found for the blade root bending moment and the tower torsional moment. The high reduction in fore-aft tower bending moment close to the tower top, which was shown by Bæk (2011), was reproduced, but disappeared very quickly for lower tower locations.

A secondary purpose of smart rotors next to the load alleviation was established, namely the active increase of power output through flap deflections. A numerical study has shown that the power in control region 2 could be enhanced, when the smart rotor responds to unsteady aerodynamic effects caused by the wind inflow. As the rotor inertia is large, it only adapts slowly to the ideal rotor speed, causing the rotor to operate off its design point. Deflecting the flaps can help to increase the power capture below the rated wind speed.

Another contribution of this dissertation is the non-linear structural model. The assumption of small strains, while undergoing large deformations, allows to construct non-linear modal equations of motion based on a full finite element model, thereby allowing a matching of stress information obtained by linear models and the possibility to capture non-linear effects. The definition of different connections between structural segments makes the method a very versatile approach that is not only suitable for the simulation of wind turbines, but also for aircraft structures. Employing fictitious masses at the interface of the elements ensures accurate implementation of discrete forces and moments, which is very desirable for smart rotors as their forces are less uniform than conventional rotors.

The second part of this thesis is devoted to a flap concept, the autonomous flap. While all proposed smart rotor flap concepts aim at high reliability by integrating the flap seamlessly into the structure, the autonomous flap concept makes flaps easily interchangeable. The system includes energy generation, motion sensing and actuation integrated in a free-floating flap, which is controlled by a trailing edge tab. This set-up has several advantages compared to traditional flap concepts. The trailing edge tab controls the moment around a hinge axis of the main flap; the aerodynamic forces serve as a lever. Consequently, the actuation energy is very small. Sufficient energy to power the actuation and control system can be generated in limit cycle oscillations as has been shown numerically and experimentally. As the flap operates at the edge of aeroelastic stability, it is very responsive and can be effectively used to alleviate loads or to suppress flutter of a wind turbine blade. The experiment has shown that a controller enforced limit cycle oscillation generates sufficient energy to power both actuation system and sensors.

10.2 CONCLUSIONS

The main research questions of this dissertation were if smart wind turbines can overcome the limits of upscaling and how to design a suitable flap system for offshore application. Based on the numerical analysis of the smart wind turbine and the autonomous flap experiment these questions can be partially answered.

10.2.1 SMART WIND TURBINE ANALYSIS

As was shown by the comparison between the Sandia Smart Rotor Experiment and the DU-SWAT, the code is able to capture the relevant aeroelastic phenomena and can thus be used for analysis and design studies. Certainly for small deflection angles, the tool is accurate. High flap deflections of 15 degree and more are not required to eliminate the 1P frequency. Additionally, such deflections would come at costs of a high drag increase, which is undesirable. The limitations for the presented concepts are therefore of no practical relevance, except for the blade damping.

Loads throughout the turbine are reduced. These loads can be translated into a lighter structure or an increase in rotor size. The most significant load reduction can be achieved for the turbine blades and the tower. As blade designs are stiffness driven, the load reduction can postpone the limits of upscaling. Increases in size and load reduction can help in reducing the cost of energy.

Bending loads in the tower are mostly driven by the rotor thrust. The smart rotor hardly affects this parameter such that the tower cannot be made much lighter. The only load component that is reduced in the tower is the torsional moment.

For commercial multi-megawatt turbines, the load reduction and tip displacement control still remain the most important function of the flaps. It has not yet been shown how a smart rotor concept performs, if the flap system fails. Secondary functions such as the increase in energy capture make such a system more interesting, but do not justify the usage by itself as the increase in possible power production is small compared to the additional complexity of a flap system. In all simulations, flutter was not a problem that needed to be solved, but might occur when turbines are scaled-up further.

10.2.2 AUTONOMOUS FLAP

The autonomous flap concept has taken its first steps to improve its technology readiness level. The system has been demonstrated experimentally. It is particularly efficient in actuation and easy in integration into the main wing. It can satisfy the performance requirements in terms of load authority and frequency bandwidth needed to suppress the variation of the blade root moment at 1P frequency.

The system is scalable, in fact, a lot of the difficulties encountered in the research originate from the minimisation of the harvester layout for the wind tunnel experiment. As the chords at the airfoil sections will be four times longer than during the wind tunnel experiment, the generator size can be significantly increased and its gear ratio lowered. The size requirement of the generator in combination with the commercial availability proved to be one of the main constraints of the autonomous flap design.

10.3 RECOMMENDATIONS

The numerical and experimental studies presented in this dissertation serve as a contribution in the development of smart wind turbines. However, several steps still need to be taken before the smart rotor reaches industrial maturity.

10.3.1 SMART WIND TURBINE ANALYSIS

Further studies are required to provide a solid explanation of the increased aerodynamic damping of the wind turbine blades. The study of the aerodynamic properties using high fidelity aerodynamic methods, such as vortex methods or CFD, which can capture any interaction between section and tip vortices is a logical and required next step in smart rotor research.

All studies on load alleviation assume that the smart capabilities are added to an existing rotor. The reductions in blade root bending moments could however be translated into a lighter blade structure, which would also reduce gravitational forces. It is thus vital to incorporate smart rotors in a full design cycle before the actual reductions in blade, tower and drive train loads can be found. The reductions in component loads should be coupled to a cost model. The resulting decrease in component costs should be balanced against the additional complexity of a smart rotor system and the reduction in power production found in this theses. Combining these parameters will lead to a more accurate estimation of the impact on cost of energy a smart rotor can have.

A balance between the load reduction and the power capture control objectives will be a next step in control research. Additional research is required on the robustness of a control scheme. For the load reduction analysis, only failure-free load cases have been considered, however for a turbine certification, it has to be shown, that the application of flaps on a rotor is not detrimental for other load cases.

The non-linear structural model has been described and verified in this dissertation. Follow-up studies should evaluate the validity of the assumption of small strain while undergoing large deformations, and if necessary develop correction methods to include the effect of warping on the stress and strain fields when undergoing large deformations.

10.3.2 AUTONOMOUS FLAP

The autonomous flap concept has been tested on a reduced scale in a controlled wind tunnel environment. The demonstration during a field test still needs to be done. This should preferably be done in a rotating frame, which could be a follow-up research project of this dissertation.

The overall balance for the load reduction on a wind turbine blade still has to be made. The flap vibration introduces oscillations into the blade, however it can be used to counteract high amplitude deflections, which contribute most heavily to fatigue loads and are the driver for extreme loads. It is also needed to address wind turbine specific aerodynamic characteristics, such as non-uniform flow, when assessing the suitability of autonomous flaps for wind turbine applications.

The autonomous flap experiment can be improved by making the flap fully autonomous. Id est that the power produced by the generators is used directly to feed the actuation and sensor system, instead of having an external energy source and comparing the generated power to the consumed power. This autonomous system should be equipped with an on-board data storage possibly with a Wi-Fi connection to an external computer. A second point of improvement lies in the high gear ratio that was used in the experiment in order to produce sufficient power output. A customised electromagnetic generator that delivers high voltages and power at lower rotational speeds would reduce the gear ratio and mechanical losses in the system. Additionally, the actuators could be matched better in terms of required torque on the trim tab, such that the power balance is shifted in favor of the harvested energy.

BIBLIOGRAPHY

Andersen, P. B. (2010), *Advanced load alleviation for wind turbines using adaptive trailing edge flaps: sensoring and control*, DTU Risø, Roskilde, Denmark. Ph.D. Thesis.

Andersen, P. B., Gaunaa, M., Bak, C. and Buhl, T. (2007), Wind tunnel test on wind turbine airfoil with adaptive trailing edge geometry, *in* 'Proceedings of the 45th AIAA/ASME', Reno, USA.

Andersen, P. B., Gaunaa, M., Bak, C. and Hansen, M. H. (2009), 'A dynamic stall model for airfoils with deformable trailing edges', *Wind Energy* **12**(8), 734–751.

Arrieta, A. F., Kuder, I. K., Rist, M., Waeber, T. and Ermanni, P. (2014), 'Passive load alleviation aerofoil concept with variable stiffness multi-stable composites', *Composite Structures* **116**, 235–242.

Ashuri, T. (2012), *Beyond Classical Upscaling: Integrated Aeroservoelastic Design and Optimization of Large Offshore Wind Turbines*, TU Delft, Delft, Netherlands. Ph.D. Thesis.

Bachau, O. (2011), *Flexible multibody dynamics*, Springer, New York, USA.

Bæk, P. (2011), *Unsteady flow modeling and experimental verification of active flow control concepts for wind turbine blades*, DTU Risø, Copenhagen, Denmark. Ph.D. Thesis.

Barbarino, S., Recora, R., Lecce, L., Concilio, A., Ameduri, S. and Calvi, E. (2009), 'A novel SMA-based concept for airfoil structural morphing', *Journal of Materials Engineering and Performance* **18**, 696–705.

Barlas, T. K. (2011), *Active Aerodynamic Load Control On Wind Turbines*, TU Delft, Delft, Netherlands. Ph.D. Thesis.

Barlas, T. K., Lutz, T., Bak, C., Hulskamp, A. W. and Apinaniz, S. (2010), Requirements for smart rotor technology, Technical Report Upwind Project.

Barlas, T. K. and Madsen, H. A. (2011), Influence of actuator dynamics on the load reduction potential of wind turbines with distributed controllable rubber trailing edge flaps (CRTEF), *in* 'Proceedings of the 22nd International Conference on Adaptive Structures and Technologies', Corfu, Greece.

Barlas, T. K., van der Veen, G. J. and van Kuik, G. A. M. (2012), 'Model predictive control for wind turbines with distributed active flaps: incorporating inflow signals and actuator constraints', *Wind Energy* **15**(5), 757–771.

Barlas, T. K. and van Kuik, G. A. M. (2010), 'Review of state of the art in smart rotor control research for wind turbines', *Progress in Aerospace Science* **46**(1), 1–27.

Barlas, T. K., van Wingerden, J. W., Hulskamp, A. W., van Kuik, G. A. M. and Bersee, H. E. N. (2013), 'Smart dynamic rotor control using active flaps on a small-scale wind turbine: aeroelastic modeling and comparison with wind tunnel measurements', *Wind Energy* **16**(8), 1287–1301.

Barlas, T. K., van Wingerden, J. W., Hulskamp, A. W., van Kuik, G. A. M., Verhaegen, M. and Bersee, H. E. N. (2010), Smart dynamic rotor control: part 2: aeroelastic analysis, *in* 'Proceedings of Science of Making Torque from Wind', Heraklion, Greece.

Barthley-Cho, J. D., Wang, D. P., Martin, C. A., Kudva, J. N. and West, M. N. (2004), 'Development of high-rate, adaptive trailing edge control surface for the smart wing phase 2 wind tunnel model', *Journal of Intelligent Material Systems and Structures* **15**, 279–291.

Battini, J. M. (2008), 'Large rotations and nodal moments in corotational elements', *Computational Modeling in Engineering and Sciences* **33**(1), 1–15.

Berg, D. E., Berg, J. C., Wilson, D., White, J., Resor, B. and Rumsey, M. (2011), Design, fabrication, assembly and initial testing of a SMART rotor, *in* 'Proceedings of the 49th AIAA Aerospace Sciences Meeting', Orlando, USA.

Berg, D. E., Wilson, D., Resor, B. R., Barone, M. F., Berg, J. C., Kota, S. and Ervin, G. (2009), Active aerodynamic blade load control impacts on Utility-Scale wind turbines, *in* 'Proceedings of Windpower 2009', Chicago, USA.

Berg, J. C., Barone, M. F. and Yoder, N. C. (2014), SMART wind turbine rotor: data analysis and conclusions, SAND2014-0712, Albuquerque, USA.

Berg, J. C., Berg, D. E. and White, J. R. (2012), Fabrication, integration and initial testing of a SMART rotor, *in* 'Proceedings of the 50th AIAA Aerospace Sciences Meeting', Nashville, USA.

Berg, J. C., Resor, B. R., Paquette, J. A. and White, J. R. (2014), SMART wind turbine rotor: design and field test, SAND2014-0681, Albuquerque, USA.

Bergami, L. (2013), *Adaptive Trailing Edge Flaps for Active Load Alleviation in a Smart Rotor configuration*, DTU Risø, Roskilde, Denmark. Ph.D. Thesis.

Bergami, L. and Gaunaa, M. (2010), 'Stability investigation of an airfoil section with active flap control', *Wind Energy* **13**(2-3), 151–166.

Bergami, L. and Gaunaa, M. (2012), ATEFlap aerodynamic model, a dynamic stall model including the effects of trailing edge flap deflection, Risø-R-1792(EN).

Bergami, L., Gaunaa, M. and Heinz, J. (2013), 'Indicial lift response function: an empirical relation for finite thickness airfoils, and effects on aeroelastic simulations', *Wind Energy* **16**(5), 681–693.

Bergami, L. and Poulsen, N. K. (2015), 'A smart rotor configuration with linear quadratic control of adaptive trailing edge flaps for active load alleviation', *Wind Energy* **18**, 625–641.

Bergami, L., Riziotis, V. A. and Gaunaa, M. (2015), 'Aerodynamic response of an airfoil section undergoing pitch motion and trailing edge flap deflection: a comparison of simulation methods', *Wind Energy* **18**, 1273–1290.

Bernhammer, L., Karpel, M. and De Breuker, R. (2015), 'Energy harvesting for actuators and sensors using free-floating flaps', *Journal of Intelligent Material Systems and Structures* **accepted**.

Bernhammer, L. O., De Breuker, R. and Karpel, M. (2015), 'Geometrically nonlinear structural modal analysis using fictitious masses', *AIAA Journal* **submitted**.

Bernhammer, L. O., De Breuker, R., Karpel, M. and van der Veen, G. J. (2013), 'Aeroelastic control using distributed floating flaps actuated by piezoelectric tabs', *Journal of Aircraft* **50**(3), 732–740.

Bernhammer, L. O., De Breuker, R. and van Kuik, G. A. M. (2012), DU-SWAT: a new aeroelastic horizontal axis wind turbine analysis tool, *in* 'Proceedings of the 8th PhD Seminar on Wind Energy in Europe', EAWE, Zurich, Switzerland.

Bernhammer, L. O., De Breuker, R. and van Kuik, G. A. M. (2015*a*), Aeroelastic time-domain simulation of snl smart rotor experiment, *in* 'Proceedings of the 33rd ASME Wind Energy Symposium', American Institute of Aeronautics and Astronautics, Kissimee, USA.

Bernhammer, L. O., De Breuker, R. and van Kuik, G. A. M. (2015*b*), 'Assessment of fatigue and extreme load reduction of HAWT using smart rotors', *Journal of Wind Engineering and Industrial Aerodynamics* **submitted**.

Bernhammer, L. O., De Breuker, R., van Kuik, G. A. M., Berg, J. C. and van Wingerden, J. W. (2013), Model validation and simulated fatigue load alleviation of SNL smart rotor experiment, *in* ‘Proceedings of the 51st AIAA Aerospace Sciences Meeting’, AIAA, Grapevine, Texas, USA.

Bernhammer, L. O., Navalkar, S. T., Sodja, J., Karpel, M. and De Breuker, R. (2015*a*), Experimental and numerical study of an autonomous flap, *in* ‘Proceedings of the International Forum of Aeroelasticity and Structural Dynamics’, St. Petersburg, Russia.

Bernhammer, L. O., Navalkar, S. T., Sodja, J., Karpel, M. and De Breuker, R. (2015*b*), Experimental investigation of an autonomous flap for load alleviation, *in* ‘Proceedings of AIAA SciTech’, Kissimmee, USA.

Bernhammer, L. O., Sodja, J., Karpel, M. and De Breuker, R. (2014), Design of an autonomous flap for load alleviation, *in* ‘Proceedings of the 25nd International Conference on Adaptive Structures and Technologies’, The Hague, Netherlandes.

Bernhammer, L. O., van Kuik, G. A. M. and De Breuker, R. (2014), ‘How far is smart rotor research and what steps need to be taken to build a full-scale prototype?’, *Journal of Physics: Conference Series* **555**, 1–8.

Berring, P., Branner, K., Berggreen, C. and Knudsen, H. W. (2006), Torsional performance of wind turbine blades - part i, *in* ‘Proceedings of the 16th International Conference on Composite Materials’, Kyoto, Japan.

Berry, S. D. (2008), Blade system design studies phase 2: final project report, SAND2008-4648, Albuquerque, USA.

Bir, G. and Jonkman, J. (2007), ‘Aeroelastic instabilities of large offshore and onshore wind turbines’, *Journal of Physics: Conference Series* **75**(1), 012069.

Bossanyi, E. (2003*a*), ‘Individual blade pitch control for load reduction’, *Wind Energy* **6**(2), 119–128.

Bossanyi, E. A. (2000), ‘The design of closed loop controllers for wind turbines’, *Wind Energy* **3**(3), 149–163.

Bossanyi, E. A. (2003*b*), GH Bladed theory manual, Garrad Hassan and Partners Ltd. 282/BR/009.

Bossanyi, E. A. (2009), Controller for 5MW reference turbine, Project upwind report 11593/BR/04.

Bottasso, C. L., Cacciola, S. and Croce, A. (2013), ‘Estimation of blade structural properties from experimental data’, *Wind Energy* **16**(4), 501–518.

Bottasso, C. L., Campagnolo, F., Croce, A., Dilli, S., Gualdoni, F. and Nielsen, M. B. (2014), 'Structural optimization of wind turbine rotor blades by multilevel sectional/multibody/3D-FEM analysis', *Multibody System Dynamics* **32**(1), 87–116.

Bottasso, C. L., Campagnolo, F. and Petrovic, V. (2014), 'Wind tunnel testing of scaled wind turbine models: beyond aerodynamics', *Journal of Wind Engineering and Industrial Aerodynamics* **127**, 11–28.

Bottasso, C. L., Croce, A., Sartori, L. and Grasso, F. (2014), 'Free-form design of rotor blades', *Journal of Physics: Conference Series* **524**(1), 012041.

Bottasso, C. L., Croce, A., Savini, B., Sirchi, W. and Trainelli, L. (2006), 'Aero-servo-elastic modeling and control of wind turbines using finite-element multibody procedures', *Multibody System Dynamics* **16**(3), 291–308.

Bruni, C., Cestino, E., Frulla, G. and Marzocca, P. (2014), Developement of an aeroelastic wing model with piezoelectric elements for gust load alleviation and energy harvesting, *in* 'Proceedings of the ASME 2014 International Mechanical Engineering Congress and Exposition', Montreal, Canada.

Bryant, M., Fang, A. and Garcia, E. (2010), 'Self-powered smart blade: helicopter blade energy harvesting', *Proceedings of the SPIE* **7643**, 764317–1:10.

Bryant, M. and Garcia, E. (2011), 'Modeling and testing of a novel aeroelastic flutter energy harvester', *Journal of Vibration and Acoustics* **133**, 011010–1:10.

Bryant, M., Wolff, E. and Garcia, E. (2011), 'Aeroelastic flutter energy harvester design: the sensitivity of the driving instability to system parameters', *Smart Materials and Structures* **20**(125017).

Buhl, M. L. (2014), RunIEC User's Guide, National Renewable Energy Laboratory USA.

Buhl, T., Bak, C., Gaunaa, M. and Andersen, P. B. (2007), Load alleviation through adaptive trailing edge control surfaces: ADAPWING overview, *in* 'Proceedings of the European Wind Energy Conference and Exhibition', Milan, Italy.

Burton, T., Sharpe, D., Jenkins, N. and Bossanyi, E. A. (2001), *Wind Energy Handbook*, John Wiley & Sons, London, UK.

Campagnolo, F., Bottasso, C. L. and Bettini, P. (2014), 'Design, manufacturing and characterization of aero-elastically scaled wind turbine blades for testing active and passive load alleviation techniques within a ABL wind tunnel', *Journal of Physics: Conference Series* **524**, 012061.

Campanile, L. F. and Sachaul, D. (n.d.), 'The belt-rib concept: a structronic approach to variable camber'.

Capellaro, M. (2012), Design limits of bend twist coupled wind turbine blades, *in* '53rd AIAA/ASME/ASCE/AHS/ASC Structures, Structural Dynamics and Materials Conference', Honolulu, USA, Honolulu, USA.

Castaignet, D., Barlas, T. K., Buhl, T., Poulsen, N. K., Wedel-Heinen, J. J., Olesen, N. A., Bak, C. and Kim, T. (2014), 'Full-scale test of trailing edge flaps on a Vestas V27 wind turbine: active load reduction and system identification', *Wind Energy* **17**(4), 549–564.

Castaignet, D., Couchman, I., Poulsen, N. K., Buhl, T. and Wedel-Heinen, J. J. (2013), 'Frequency-weighted model predictive control of trailing edge flaps on a wind turbine blade', *IEEE Transactions on Control Systems Technology* **21**(4), 1105–1116.

Castaignet, D., Poulsen, N. K., Buhl, T. and Wedel-Heinen, J. J. (2011), Model predictive control of trailing edge flaps on a wind turbine blade, *in* 'Proceedings of the American Control Conference (ACC), 2011', pp. 4398–4403.

Cesnik, C. and Hodges, D. H. (1997), 'VABS: a new concept for composite rotor blade cross-Sectional modeling', *Journal of the American Helicopter Society* **42**(1), 27–38.

Chiuso, A. (2007), 'The role of vector auto-regressive modelling in predictor based subspae identification', *Automatica* **43**, 1034–1048.

Corbetta, G. and Miloradovic, T. (2014), *Wind in power - 2013 European Statistics*, EWEA, Brussels, Belgium.

Craig, R. R. and Bampton, C. C. (1968), 'Coupling of substructures for dynamic analysis', *AIAA Journal* **6**(7), 1313.

Daynes, S. and Weaver, P. (2011), Adaptive trailing edge geometry for load alleviation on wind turbine blades, *in* 'Proceedings of the 22nd International Conference on Adaptive Structures Technologies', Corfu, Greece.

Daynes, S., Weaver, P. M. and Potter, K. D. (2009), 'Aeroelastic study of bistable composite airfoils', *Journal of Aircraft* **46**, 2169–2173.

Daynes, S. and Weaver, R. M. (2012), 'Design and testing of a deformable wind turbine blade control surface', *Smart Materials and Structures* **21**, 1–10.

de Vries, H. (2013), *On Synthetic Jet Actuation for Aerodynamic Load Control*, University of Twente, Enschede, Netherlands. Ph.D. Thesis.

Drela, M. (1989), XFOIL: an analysis and design system for low reynolds number airfoils, *in* 'Low Reynolds Number Aerodynamics', Lecture Notes in Engineering, Springer Berlin, pp. 1–12.

Fedorov, V. and Berggreen, C. (2014), 'Bend-twist coupling potential of wind turbine blades', *Journal of Physics: Conference Series* **524**(1), 012035.

Gandhi, F. and Anusonti-Inthra, P. (2008), 'Skin design studies for variable camber morphing airfoils', *Smart Materials and Structures* **17**, 1–8.

Gandhi, F., Frecker, M. and Nissly, A. (2008), 'Design optimization of a controllable camber rotor airfoil', *AIAA Journal* **46**, 142–153.

Gaunaa, M. (2006), Unsteady 2D potential-flow forces on a thin variable geometry airfoil undergoing arbitrary motion, R-1478(EN), DTU Risø.

Gaunaa, M. (2007), 'Unsteady two-dimensional potential-flow model for thin variable geometry airfoils', *Wind Energy* **13**(2), 167–192.

Gillebaart, T., Bernhammer, L. O., van Zuijlen, A. H. and van Kuik, G. A. M. (2014), 'Active control on an aeroelastic turbine airfoil in gust conditions using both CFD and an engineering model', *Journal of Physics: Conference Series* **524**, 1–10.

Gœzcue , M. O. and Kayran, A. (2014), 'Investigation of the effect of bending twisting coupling on the loads in wind turbines with superelement blade definition', *Journal of Physics: Conference Series* **524**, 012040.

Hansen, M. O. L. (2008), *Aerodynamics of Wind Turbines*, Routledge, London, UK.

Hegberg, T., De Breuker, R. and van Bussel, G. J. W. (2013), Nonlinear static aeroelastic design case studies of large offshore wind turbine blades, *in* 'Proceedings of the EWEA conference', Vienna, Austria.

Heinz, J., Sœrensen, J. N. and Zahle, F. (2011), 'Investigation of the load reduction potential of two trailing edge flap controls using CFD', *Wind Energy* **14**(3), 449–462.

Heinze, S. and Karpel, M. (2006), 'Analysis and wind tunnel testing of a piezoelectic tab for aeroelastic control applications', *Journal of Aircraft* **43**(6), 1799–1804.

Hodges, D. H. (2003), 'Geometrically exact, intrinsic theory for dynamics of curved and twisted anisotropic beams', *AIAA Journal* **41**(6), 1131–1137.

Houtzager, I., van Wingerden, J. W. and Verhaegen, M. (2011), Rejection of periodic wind disturbances on an experimental "smart" rotor section using lifted repetitive control, *in* 'Proceedings of the IEEE International Conference on Control Applications (CCA)', pp. 264–271.

Houtzager, I., van Wingerden, J. W. and Verhaegen, M. (2013), 'Wind turbine load reduction by rejecting the periodic load disturbances', *Wind Energy* **16**(2), 235–256.

Hulskamp, A. W. (2011), *The Smart Rotor Concept on Wind Turbines: Actuators and Structures*, TU Delft, Delft, Netherlands. Ph.D. Thesis.

Hulskamp, A. W., Champliaud, H., van Wingerden, J. W., Barlas, T. K., Bersee, H. E. N., van Kuik, G. A. M. and Verhaegen, M. (2010), Smart dynamic rotor control: part 1, design of a smart rotor, *in* 'Proceedings of Science of Making Torque from Wind', Heraklion, Greece.

Hulskamp, A. W., van Wingerden, J. W., Barlas, T. K., Champliaud, H., van Kuik, G. A. M., Bersee, H. E. N. and Verhaegen, M. (2011), 'Design of a scaled wind turbine with a smart rotor for dynamic load control experiments', *Wind Energy* **14**(3), 339–354.

International Electrotechnical Commission (2005), Wind turbines - part 1: design requirements, IEC 61400-1 ed.3.

International Renewable Energy Agency (2012), *Renewable Energy Technologies: Cost Analysis Series - Wind Power*, Bonn, Germany.

Johnson, S. J., Baker, J. P., Dam, C. P. v. and Berg, D. E. (2010), 'An overview of active load control techniques for wind turbines with an emphasis on microtabs', *Wind Energy* **13**, 239–253.

Johnson, S. J., van Dam, C. P. and Berg, D. E. (2008), Active load control techniques for wind turbines, Technical Report SAND2008-4809, Albuquerque, USA.

Jonkman, B. J. (2009), TurbSim user's guide, National Renewable Energy Laboratory USA.

Jonkman, J. and Buhl, M. L. (2005), FAST user's guide, Technical Report NREL/EL-500-38230, Boulder, USA.

Jonkman, J., Butterfield, S., Musial, W. and Scott, G. (2009), Definition of a 5-MW reference wind turbine for offshore system development, TP-500-38060, NREL.

Karpel, M. (1990), 'Time domain aeroservoelastic modeling usingweighted unsteady aerodynamic forces', *Journal of Guidance, Control and Dynamics* **13**, 30–37.

Karpel, M. and Presente, E. (1995), 'Structural dynamic loads in response to impulsive excitation', *Journal of Aircraft* **32**(4), 853–861.

Karpel, M. and Raveh, D. (1996), ‘Fictitious mass element in structural dynamics’, *AIAA Journal* **34**(3), 607–613.

Karpel, M., Shousterman, A., Maderuelo, C. and Climent, H. (2013), Dynamic aeroservoelastic response with nonlinear structural elements, *in* ‘Proceedings of the 54th AIAA/ASME/ASCE/AHS/ASC Structures, Structural Dynamics, and Materials Conference’, Boston, MS, USA.

Kosasih, B. and Dicker, M. (2014), ‘Trailing edge deformation mechanism for active variable - camber wind turbine blade’, *Applied Mechanics and Materials* **493**, 444–449.

Lachenal, X., Daynes, S. and Weaver, P. M. (2013), ‘Review of morphing concepts and materials for wind turbine blade applications’, *Wind Energy* **16**, 287–307.

Lackner, M. A. and van Kuik, G. A. M. (2010), ‘A comparison of smart rotor control approaches using trailing edge flaps and individual pitch control’, *Wind Energy* **13**, 117–134.

Lambie, B. (2011), *Aeroelastic Investigation of a Wind Turbine Airfoil with Self-Adaptive Camber*, TU Darmstadt, Darmstadt, Germany. Ph.D. Thesis.

Larsen, T. J. and Hansen, A. M. (2012), How 2 HAWC2, the user’s manual, Risø-R-1597(ver. 4.3)(EN).

Leishman, J. G. (1994), ‘Unsteady lift of a flapped airfoil by indicial concepts’, *Journal of Aircraft* **31**(2), 288–297.

Leishman, J. G. and Beddoes, T. S. (1986), A generalized model for airfoil unsteady aerodynamic behaviour and dynamic stall using indicial method, *in* ‘Proceedings of the 42nd Annual Forum of the American Helicopter Society’, Washington D.C., USA.

Loth, E., Selig, M. and Moriaty, P. (2010), Morphing segmented wind turbine concept, *in* ‘Proceedings of the 28th AIAA Applied Aerodynamics Conference’, Chicago, USA.

Madsen, H. A., Andersen, P. B., Andersen, T. L., Bak, C., Buhl, T. and Na, L. (2010), The potentials of the controllable rubber trailing edge flap (CRTEF), *in* ‘Proceedings of the 44th AIAA Aerospace Sciences Meeting’, Reno, USA.

Manwell, J., McGowan, J. and Rogers, A. (2003), *Wind Energy Explained*, John Wiley & Sons, London, UK.

Markou, H., Andersen, P. B. and Larsen, G. C. (2011), ‘Potential load reductions on megawatt turbines exposed to wakes using individual-pitch wake compensator and trailing-edge flaps’, *Wind Energy* **14**(7), 841–857.

Marrant, B. (2007), Aeroelastic modelling of smart wind turbines, Technical report duwind.

Marrant, B. A. H., Hinnen, K., van Holten, T. and van Kuik, G. A. M. (2002), Smart dynamic rotor control of large offshore wind turbines - inventory of present techniques, TU Delft - Duwind 2002.011.

McAlister, K. W., Lambert, O. and Petot, D. (1984), Application of the ONERA model of dynamic stall, AVSCOM Technical Report 84-A-3, NASA Technical Paper 2399.

Namik, H. (2008), Using Simulink and Matlab with FAST, Technical repository University of Aukland.

Ng, B. F., Hesse, H., Palacios, R., Graham, J. M. R. and Kerrigan, E. (2015), 'Aeroservoelastic state-space vortex lattice modeling and load alleviation of wind turbine blades', *Wind Energy* **18**(7), 1317–1331.

Ng, B. F., Hesse, H., Palacios, R., Graham, J. M. R. and Kerrigan, E. C. (2014), Model-based aeroservoelastic design and load alleviation of large wind turbines, *in* 'Proceedings of the 32nd ASME Wind Energy Symposium', American Institute of Aeronautics and Astronautics, National Harbor, USA.

Ng, B. F., Palacios, R., Graham, J. M. R. and Kerrigan, E. C. (2012), Robust control synthesis for gust load alleviation from large aeroelastic models with relaxation of spatial discretisation, *in* 'Proceedings of the European Wind Energy Conference EWEA 2012', Copenhagen, Denmark.

Ng, B. F., Palacios, R., Graham, J. M. R. and Kerrigan, E. C. (2013), Aeroservoelastic modelling and active control of very large wind turbine blades for gust load alleviation., *in* 'Proceedings of the EAWE 9th PhD Seminar on Wind Energy in Europe'.

Palacios, R. (2011), 'Nonlinear normal modes in an intrinsic theory of anisotropic beams', *Journal of Sound and Vibration* **330**(8), 1772 – 1792.

Palacios, R., Wang, Y. and Karpel, M. (2012), Intrinsic models for nonlinear flexible-aircraft dynamics using industrial finite-element and loads packages, *in* 'Proceedings of the 53rd AIAA/ASME/ASCE/AHS/ASC Structures, Structural Dynamics and Materials Conference', AIAA, Honolulu, USA.

Park, J., Kim, K., Kwon, S. and Law, K. H. (2012), An aero-elastic flutter based electromagnetic energy harvester with wind speed augmenting funnel, *in* 'Proceedings of the International Conference on Advances in Wind and Structures', Seoul, Korea.

Park, J., Morgenthal, G., Kim, K., Kwon, S. and Law, K. H. (2012), Power evaluation for flutter-based electromagnetic energy harvester using CFD simulations, *in* 'Proceedings of the First International Conference on Performance-based and Life-cycle Structural Engineering', Hong Kong, China.

Plumley, C., Leithead, W., Jamieson, P., Bossanyi, E. A. and Graham, M. (2014), 'Comparison of individual pitch and smart rotor control strategies for load reduction', *Journal of Physics: Conference Series* **524**(1), 012054.

Pustilnik, M. and Karpel, M. (2013*a*), Dynamic loads alleviation using active free-floating flaps, *in* 'Proceedings of the 53rd Israel Annual Conference on Aerospace Sciences', Haifa, Israel.

Pustilnik, M. and Karpel, M. (2013*b*), Loads, vibration and maneuver control using active floating flaps, *in* 'Proceedings of International Forum on Aeroelasticity and Structural Dynamics', Royal Aeronautical Society, Bristol, UK.

Resor, B. R., Berg, D. E., Wright, Z., Halse, C. and Crowther, A. (2012), Wind turbine structural path stress and fatigue reductions resulting from use of active aerodynamic load control, *in* 'Proceedings of the 50th AIAA Aerospace Sciences Meeting', American Institute of Aeronautics and Astronautics, Nashville, USA.

Rice, J. K. and Verhaegen, M. (2008), Distributed control: a sequentially semi-seperable approach, *in* 'Proceedings of the 47th IEEE Conference on Decision and Control (CDC)', Cancun, Mexico.

Rodden, W. and Johnson, E. (1994), MSC Nastran aeroelastic analysis user's guide, MSC Software Corporation USA.

Saggere, L. and Kota, S. (1999), 'Static shape control of smart structures using compliant mechanisms', *Smart Materials and Structures* **37**(5), 572–578.

Schepers, G. J., Snel, H. and van Bussel, G. J. W. (1995), Dynamic inflow: yawed conditions and partial span pitch control, ECN-C-95-056.

Selitrennik, E., Karpel, M. and Levy, Y. (2012), 'Computational aeroelastic simulation of rapidly morphing air vehicles', *AIAA Journal* **49**(6), 1675–1686.

Sirohi, J. and Mahadik, R. (2011), 'Piezoelectric wind energy harvester for low-power sensors', *Journal of Intelligent Material Systems and Structures* **22**(18), 2215–2228.

Smit, J., Bernhammer, L. O., Navalkar, S. T., Bergami, L. and Gaunaa, M. (2014), Sizing and control of trailing edge flaps on a smart rotor for maximum power generation in low fatigue wind regimes, *in* 'Proceedings of the 32nd ASME Wind Energy Symposium', American Institute of Aeronautics and Astronautics, National Harbor, USA.

Snel, H. (2001), Survey of induction dynamics modeling within BEM-like codes - dynamic inflow and yawed flow modeling revisited, American Institute of Aeronautics and Astronautics, Reno, NV, USA.

Sterenborg, J. (2014), *Experimental and numerical investigation of an aeroelastic wing*, TU Delft, Delft, Netherlands. Ph.D. Thesis.

The Math Works (2011), SimMechanics User's Guide, Technical report, Natick, USA.

Tutty, O., Blackwell, M., Rogers, E. and Sandberg, R. (2014), 'Iterative learning control for improved aerodynamic load performance of wind turbines with smart rotors', *IEEE Transactions on Control Systems Technology* **22**(3), 967–979.

van der Veen, G. J., van Wingerden, J. W. and Verhaegen, M. (2010), Closed-loop MOESP subspace model identification with parametrisable disturbances, *in* 'Proceedings of the IEEE Conference on Decision and Control', Atlanta, USA.

van Parys, B. P., Ng, B. F., Goulart, P. J. and Palacios, R. (2014), Optimal control for load alleviation in wind turbines, *in* 'Proceedings of the 32nd ASME Wind Energy Symposium', American Institute of Aeronautics and Astronautics, National Harbor, USA.

van Rooij, R. (1996), Modification of the boundary layer calculation in RFOIL for improved airfoil stall prediction, Technical Report IW-96087R, Delft, Netherlands.

van Wingerden, J. W. (2008), *Control of wind turbines with 'smart' rotors*, TU Delft, Delft, Netherlands. Ph.D. Thesis.

van Wingerden, J. W., Hulskamp, A. W., Barlas, T. K., van Kuik, G. A. M. and Verhaegen, M. (2008), 'On the proof of concept of a 'smart' wind turbine rotor blade for load alleviation', *Wind Energy* **13**, 265–280.

van Wingerden, J. W., Hulskamp, A. W., Barlas, T. K., van Kuik, G. A. M. and Verhaegen, M. (2010), Smart dynamic rotor control: part 3 advanced control design, *in* 'Proceedings of Science of Making Torque from Wind', Heraklion, Greece.

Verhaegen, M. and Verdult, V. (2007), *Filtering and System Identification: A Least Squares Approach*, Cambridge, UK, Cambridge University Press.

Vos, R. and Barrett, R. (2011), 'Mechanics of pressure-adaptive honeycomb and its application to wing morphing', *Smart Materials and Structures* **20**, 1–11.

Wolff, T., Ernst, B. and Seume, J. R. (2014), 'Aerodynamic behavior of an airfoil with morphing trailing edge for wind turbine applications', *Journal of Physics: Conference Series* **524**(1), 012018.

Woods, B. K. S., Bilur, O. and Friswell, M. I. (2014), 'Wind tunnel testing of the fish bone active camber morphing concept', *Journal of Intelligent Material Systems and Structures* **25**, 772–785.

Zayas, J. R., van Dam, C. P., Chow, R. and Berg, D. E. (2007), 'Computational investigation of small deploying tabs and aps for aerodynamic load control', *Journal of Physics: Conference Series* **75**.

Zhu, W. J., Shen, W. Z. and Sœrensen, J. N. (2014), 'Numerical investigation of flow control feasibility with a trailing edge flap', *Journal of Physics: Conference Series* **524**(1), 012102.

Zona Technology (2011), ZAERO Theoretical Manual, Scottsdale, USA.

LIST OF PUBLICATIONS

JOURNAL PUBLICATIONS

1. Bernhammer, L.O., Sodja, J., Navalkar, S.T., De Breuker, R. and Karpel, M. (2015). Experimental and numerical investigation of an autonomous flap for load alleviation, Journal of Aircraft, to be submitted.
2. Schelbergen, M., Roscher, B., Bernhammer, L.O., Ferede, E.A., Simao Ferreira, C.J. (2015), Structural optimization and scaling trends of vertical axis wind turbine rotors, to be submitted.
3. Bernhammer, L.O., De Breuker, R. and van Kuik, G.A.M. (2015). Fatigue and extreme load reduction of wind turbine components using smart rotors. Journal of Wind Engineering and Industrial Aerodynamics, submitted.
4. Bernhammer, L.O., De Breuker, R. and Karpel, M. (2015). Geometrically non-linear structural modal analysis using fictitious masses. AIAA Journal, submitted.
5. Smit, J., Bernhammer, L.O., Navalkar, S.T., Bergami, L. and Gaunaa, M. (2015). Sizing and control of trailing edge flaps on a smart rotor for maximum power generation in low fatigue wind regimes. Wind Energy, published, online first, May 2015, 1-18.
6. Bernhammer, L.O., De Breuker, R. and Karpel, M. (2015). Energy harvesting for actuators and sensors using free-floating flaps. Journal of Intelligent Material Systems and Structures, accepted with revision.
7. Bernhammer, L.O., van Kuik, G.A.M. and De Breuker, R. (2014). How far is smart rotor research and what steps need to be taken to build a full-scale prototype. Journal of Physics: Conference Series, 555(012008), 1-8.
8. Gillebaart, T., Bernhammer, L.O., van Zuijlen, A.H. and van Kuik, G.A.M. (2014). Active flap control on an aeroelastic wind turbine airfoil in gust conditions using both a CFD and an engineering model. Journal of Physics: Conference Series, 524, 1-10.

9. Bernhammer, L.O., Teeuwen, S.P.W., De Breuker, R., van der Veen, G.J. and van Solingen, E. (2014). Gust load alleviation of an unmanned aerial vehicle wing using variable camber. Journal of Intelligent Material Systems and Structures, 25(7), 795-805.
10. Bernhammer, L.O., De Breuker, R., Karpel, M. and van der Veen, G.J. (2013). Aeroelastic control using distributed floating flaps activated by piezoelectric tabs. Journal of Aircraft, 50(3), 732-740.

CONFERENCE PUBLICATIONS

1. Bernhammer, L.O., Navalkar, S.T., Sodja, J., De Breuker, R. and Karpel, M. (2015) Experimental and numerical study of an autonomous flap. International Forum of Aeroelasticity and Structural Dynamics 2015 (pp. 1-18), St. Petersburg, Russia
2. Bernhammer, L.O., De Breuker, R. and van Kuik, G.A.M. (2015). Aeroelastic time-domain simulation of SNL smart rotor experiment. AIAA Science and Technology Forum 2015 (pp. 1-10). Kissimmee, USA
3. Bernhammer, L.O., Navalkar, S.T., Sodja, J., De Breuker, R. and Karpel, M. (2015). Experimental investigation of an autonomous flap for load alleviation. AIAA Science and Technology Forum 2015 (pp. 1-16). Kissimmee, USA
4. Roscher, B., Simao Ferreira, C.J., Bernhammer, L.O., Aagard Madsen, H., Griffith, D. and Stoevesandt, B. (2015). Combined structural optimization and aeroelastic analysis of a vertical axis wind turbine. AIAA Science and Technology Forum 2015 (pp. 1-10). Kissimmee, USA
5. Bernhammer, L.O., Sodja, J., De Breuker, R. and Karpel, M. (2014). Design of an autonomous flap for load alleviation. 25th International Conference on Adaptive Structures and Technologies (pp. 1-11). Den Haag, Netherlands
6. Bernhammer, L.O. and De Breuker, R. and Karpel, M. (2014). Energy harvesting for sensors using free floating flaps wind tunnel experiments. 54th Isreal Annual Conference on Aerospace Sciences (pp. 1-11). Tel Aviv, Israel
7. Bernhammer, L.O., De Breuker, R. and Karpel, M. (2014). Energy harvesting for sensors using free-floating flaps: simulation and experiment. DeMEASS VI (pp. 1-3). Ede, Netherlands
8. Bernhammer, L.O., De Breuker, R. and van Kuik, G.A.M. (2014). The smart rotor: load alleviation and power generation. DeMEASS VI (pp. 1-3). Ede, Netherlands

9. Bernhammer, L.O., De Breuker, R. and Karpel, M. (2014). Wind turbine structural model using non-linear modal formulations. AIAA Sciences and Technology Forum 2014 (pp. 1-14). National Harbor, USA

10. Schelbergen, M., Bernhammer, L.O., Ferede, E.A. and Simao Ferreira, C.J. (2014). Structural optimization of multi-megawatt, offshore vertical axis wind turbine rotors. AIAA Sciences and Technology Forum 2014 (pp. 1-19). National Harbor, USA

11. Smit, Jeroen, Bernhammer, L.O., Navalkar, S.T., Bergami, L. and Gaunaa, M. (2014). Sizing and control of trailing edge flaps on a smart rotor for maximum power generation in low fatigue wind regimes. AIAA Sciences and Technology Forum 2014 (pp. 1-17). National Harbor, USA

12. Bernhammer, L.O., van Kuik, G.A.M. and De Breuker, R. (2013). Assessment of fatigue and extreme load reduction of HAWT using smart rotors. 9th PhD seminar on Wind Energy in Europe (pp. 1-5). Visby, Sweden

13. Bernhammer, L.O., De Breuker, R. and Karpel, M. (2013). Energy harvesting for sensors using free-floating flaps. 24th International Conference on Adaptive Structures and Technologies (pp. 1-12). Oranjestad, Aruba

14. Bernhammer, L.O., De Breuker, R. and Karpel, M. (2013). Geometrically non-linear structural modal analysis using ficticious masses. International Forum of Aeroelasticity and Structural Dynamics 2013 (pp. 1-14). Bristol, UK

15. Bernhammer, L.O., De Breuker, R., van Kuik, G.A.M., Berg, J. and van Wingerden, J.W. (2013). Model validation and simulated fatigue load alleviation of SNL smart rotor experiment. 51st AIAA Aerospace Sciences Meeting (pp. 1-11). Grapevine, USA

16. Bernhammer, L.O., De Breuker, R. and Karpel, M. (2012). Active rudder flutter suppression using distributed flaps actuated by piezoelectric tabs. 22nd International Conference on Adaptvie Structrues and Technologies (pp. 1-12). Corfu, Greece

17. Bernhammer, L.O., van Kuik, G.A.M. and De Breuker, R. (2012). Delft University Smart Wind turbine Aeroelastic Tool (DU-SWAT): A new aeroservoelastic horizontal axis wind turbine analysis tool. 8th PhD seminar on Wind Energy in Europe (pp. 1-4). Zurich, Switzerland

18. Bernhammer, L.O., Teeuwen, S.P.W., De Breuker, R., van Solingen, E. and van der Veen, G.J. (2012). Performance optimization and gust load alleviation of a UAV wind using variable camber. 23rd International Conference on Adaptive Structures and Technologies (pp. 1-12). Nanjing, China

19. De Breuker, R., Bernhammer, L.O. and Teeuwen, S.P.W. (2012). Wind tunnel experiments of aeroelatic control methods using adaptive structures. DeMEASS V (pp. 1-1). Linz, Austria
20. Bernhammer, L.O., van Kuik, G.A.M. and De Breuker, R. (2012). How far is smart rotor research and what steps need to be taken to build a full-scale prototype? The Science of Making Torque from Wind (pp. 1-8). Oldenburg, Germany
21. Bernhammer, L.O. (2011). Gust and fatigue load alleviation of smart wind turbine blades using piezo-driven tabs. The proceedings of the 7th PhD seminar on Wind Energy in Europe (pp. 131-134). Delft, Netherlands

BIOGRAPHICAL NOTE

Lars Oliver Bernhammer was born on November 29th 1985 in Gießen, Germany. He followed a generalist education program at the Johanneum-Gymnasium Herborn, which he completed in 2005 with an award as best graduate of the year. In the same year, Lars left his home country and moved to Delft, the Netherlands, to start his studies in the field of Aerospace Engineering. He obtained both his Bachelor of Sciences and Master of Science diploma with distinction from Delft University of Technology. During the course of his studies, Lars completed a research internship at École nationale suprieure de l'aéronautique et de l'espace (ISAE-Supaero) in Toulouse, France, in 2009 and an industrial internship at Alenia Aeronautica in Torino, Italy, in 2010, where he worked in the aeroelasticity department.

Since 2011, Lars has been employed as PhD researcher in a shared position between the Aerospace Structures and Computational Mechanics department and the Wind Energy department, both in the Faculty of Aerospace Engineering at Delft University of Technology. The work presented in this dissertation is the result of this employment. Lars has been a guest researcher to Technion Israel Institute of Technology in Haifa, Israel, in 2011, 2013 and 2014. In the first half of 2015, Lars performed research related to his Ph.D. at Airbus Defence and Space in Getafe, Spain. Both during his studies and during his Ph.D. research, Lars was a scholarship holder of the 'Studienstiftung des deutschen Volkes'.

When Lars does not occupy himself with aeroelasticity, he is a very passionate traveler. He loves to discover different cultures, to meet people and to sample new food. Whenever possible, he combines his journeys with diving or other water sports. Besides the travelling, Lars takes a great interest in cooking and he is constantly eager to learn new languages.